Structural Health Monitoring and Condition Based Fatigue Damage Prognosis of Complex Metallic Structures

by

Subhasish Mohanty

A Dissertation Presented in Partial Fulfillment
of the Requirements for the Degree
Doctor of Philosophy

ARIZONA STATE UNIVERSITY

May 2010

Structural Health Monitoring and Condition Based Fatigue Damage Prognosis of

Complex Metallic Structures

by

Subhasish Mohanty

has been approved

April 2010

Graduate Supervisory Committee:

Aditi Chattopadhyay, Chair
Antonia Papandreou-Suppappola
Hanqing Jiang
John Rajadas
Pedro Peralta
Seung Bum Kim

ACCEPTED BY THE GRADUATE COLLEGE

ABSTRACT

Current practice in fatigue life prediction is based on assumed initial structural flaws regardless of whether these assumed flaws actually occur in service. Furthermore, the model parameters are often estimated empirically based on previous coupon test results. Small deviations of the initial conditions and model parameters may generate large errors in the expected dynamical behavior of fatigue damage growth. Consequently, a large degree of conservatism is incorporated into structural designs due to these expected uncertainties. The current research in the area of Structural Health Monitoring (SHM) and probabilistic fatigue modeling can help in improved fatigue damage modeling and remaining useful life estimation (RULE) techniques. This thesis discusses an integrated approach of SHM and adaptive prognosis model that not only estimates the current health, but can also forecast the future health and calculate RULE of an aerospace structural component with high level of confidence. The approach does not assume any fixed initial condition and model parameters. This dissertation include the following novel contributions. 1) A Bayesian based off-line Gaussian Process (GP) model is developed, which is the core of the present condition based prognosis approach. 2) Different passive and active SHM approaches are used for on-line damage state estimation. Applications of passive sensing are shown to estimate the time-series fatigue damage states both under constant and random fatigue loading. It is found that there is a good correlation between estimated damage states and optically measured damage states. In addition, applications for both narrow and broadband active sensing approaches are presented to estimate smaller incipient damage. It is demonstrated that the active sensing techniques not only can identify smaller incipient damage but also can quantify fatigue damage during all the three stages (stages I , II,

and III) of fatigue life. 3) An integrated on-line SHM and off-line GP predictive model is developed for real-time condition based damage state estimation of complex Aluminum structures under fatigue loading. It is found that the proposed technique can forecast the future damage states well before the final failure.

To

All my family members

who have always been supporting

me to complete my PhD study.

ACKNOWLEDGMENTS

I would first like to thank my graduate advisor, Dr. Aditi Chattopadhyay, for all of her support to finish my PhD dissertation. I would also like to thank the other members of my supervisory committee, Dr. Antonia Papandreou-Suppappola, Dr. Hanqing Jiang, Dr. John N. Rajadas, Dr. Pedro Peralta and Dr. Seung Bum Kim, for their support and advice. I am also grateful to Dr. Dallas Kingsbury for actively helping me on the MTS biaxial machine and NI data acquisition system. I am also thankful to Dr. Santanu Das for his initial mentoring on my PhD research. I am also grateful to all my fellow graduate students who have made my graduate study enjoyable, specifically Albert Moncada, Sonil Soni, Kuang Liu, Chuntao Luo, Masoud Yekani Fard, Clyde Coelho, Cristobal Hiche, Yingtao Liu and Whitney Reynolds. Additionally, I would like to thank Air Force Office of Scientific Research (AOFSR) for supporting my doctoral studies through MURI grant number FA9550-06-1-0309, technical monitor Dr. David S. Stargel. Finally, I should not forget to specially thank Kay Vasley and Dr. Lynn Cozort.

TABLE OF CONTENTS

LIST OF TABLES

LIST OF FIGURES

Figure Page

CHAPTER 1

Introduction

1.1. Overview and Motivation for Structural Health Monitoring and Prognosis

Structural Health Monitoring and Prognosis (SHMP) is the process of continuously monitoring a system for degradation or damage and to forecast its future state. This method is different from non-destructive inspection (NDI) in that SHMP is done in-situ on the structure and is conducted on a near-continuous basis. A SHMP system consists of networks of sensors which are permanently attached to the structure to monitor its condition over time.

1.1.1. Motivation from catastrophic events

Structures may fail catastrophically if appropriate measures are not taken. For example, the structural failure on April 28, 1988 of a 19 year old Boeing 737, operated by Aloha airlines, was a defining event in creating awareness of aging aircraft the aviation community. This aircraft lost a major portion of the upper fuselage in full flight at 24,000 feet, near the front of the plane. Investigation by the United States National Transportation Safety Board (NTSB) concluded the accident was caused by metal fatigue [1]. It is conceivable that, if SHMP systems were installed in the Aloha airlines aircraft, then such accident could have been prevented. In another example, on February 1, 2003 the Space Shuttle Columbia disintegrated over Texas during re-entry into the Earth's atmosphere, with the loss of all seven crew members, shortly before it was scheduled to conclude its 28th mission. The cause of the accident was a breach in the thermal protection system (TPS) on the leading edge of the left wing. This breach was caused by a piece of insulating foam that separated from the left bipod ramp of the external tank as assessed by the Columbia accident investigation board [2]. A SHMP system placed in the vicinity of the leading edge of the wing

would have been useful to detect the damage caused by debris impact and provide timely warning to the crew members and NASA officials to take necessary action.

1.1.2. Motivation from mounting ageing aircraft inspection and maintenance cost

Ageing aircraft is an issue that has been discussed for more than a decade. Statistics [3] show that the number of aging aircraft (older than 15 years) has increased significantly, with around 4600 in 1997 for US and European built civil aircraft and more than 1900 aircraft older than 25 years. This number increased to 4730 ($> 15 years$) and 2130 ($> 25 years$) respectively in 1999. At present the above numbers will be much higher. The same can be seen with military aircraft, where an increasing number of aircraft (e.g. F4 fighter aircraft) now exceeding the age of 40 years of service. Looking at mid-life updates of current fighter airplanes, service lives of 50 years and more can be expected. Considering individual aircraft maintenance cost, it represents approximately 11 percent [4] of an airline's total operating expenses, becoming a large burden to both military and civilian aircraft industries. The use of real-time SHMP system will reduce the overall aircraft maintenance cost significantly by lowering the number of schedule based maintenance.

1.1.3. Motivation based on human error in aviation maintenance and inspection

Aviation safety depends on minimizing error in the entire system. While the role of flight deck human error has received much emphasis, more attention has been recently directed toward reducing human error [5] during maintenance and inspection. Aviation maintenance and inspection procedures are part of a complex organization, where individuals perform varied tasks in an environment with time constraints, sparse feedback, and

sometimes under harsh ambient conditions. These situational characteristics, in combination with generic human erring tendencies, result in varied forms of error. Sometimes simple human error results in catastrophic accidents and loss of life. For example, failure to replace horizontal stabilizer screws on a Continental Express aircraft resulted in in-flight leading-edge separation causing 14 fatalities [6]

1.2. Need for an Automated Structural Health Monitoring and Prognosis System and Current Trend

The Continental Express aircraft could have been saved if the health and the remaining life of the load bearing airframe structure would have been estimated properly. The current trend in research on real-time structural health monitoring and prognosis (SHMP) systems are to develop techniques that can detect, localize, quantify and forecast the adverse changes in a structure in real-time. Such a system can ultimately help to reduce the life-cycle cost and also to avoid catastrophic failure. Thus real-time health monitoring and prognostics are emerging as the forefront of Condition Based Maintenance (CBM) of critical structural systems. Although condition based prognosis is an integrated system of SHM and prognostics, the majority of the available literature focuses on either SHM or on prognosis separately. The following subsections presents a literature review on the current status of SHM, prognosis and condition based prognosis.

1.2.1. Current research in online structural health monitoring

Structural health monitoring (SHM) system is an automated system that can monitor the condition of a structure in real-time. Currently, SHM is an active research area not fully developed for industrial purposes, with exception of some limited success as in

the case of the Health and Usage Monitoring Systems (HUMS) program implemented on main rotor and gearbox components of large rotorcrafts [8, 9]. The HUMS system was developed based on vibration sensor measurements. An essential feature, which is a key to the limited success of HUMS, can be attributed to the fact that the rotor speed (not the torque) is maintained typically within two percent of the nominal speed for all flight regimes and there is a single load path with no redundancy. These constraints provide a basis for a stable vibration spectrum from which a change in the measured parameter is attributable to component deterioration. This ideal scenario, consisting of an easily identifiable parametric change coupled with a stable excitation source, does not exists for fixed wing aircraft subjected to complicated loading spectrum. At present, aircraft operators use NDI techniques for damage evaluation. Although SHM is different from NDI, some of the fundamental detection and quantification techniques used in SHM have been adopted from NDI techniques. A brief literature review on current NDI based damage assessment approaches used in the aerospace industry is presented in the following subsections.

1.2.1.1. *Current practice of damage condition assessment in aircraft industry*

Currently, the aircraft industry follows either the manual or automated inspection practice to assess the condition of different aircraft components at any given instant of time [3]. The conventional manual inspection procedure is based on either visual inspection or one of the different methods developed in the mid-50s and initially used in the early to mid-60s. The basic foundation for NDI was established by discoveries in classical physics made in the 19th century. However, the pioneering work in ultrasonic was done in Russia by Sokolov, Firestone in the USA, Trost in Germany and Sproule in the UK, during World War II [11, 12]. The two most established NDI methods within the aircraft industry are

ultrasonic [13] and eddy current [14] inspection. Ultrasonic is preferred to detect corrosion, bond line defects or flaws in composite structures, while eddy current is used for fatigue crack detection or detection of material thinning as a result of corrosion. An overview of the different variations in these NDI techniques applied to aircraft structures, including their estimated minimum detectable damage size, advantages, and disadvantages, has been given by Siegel, and et al. [10]. The present practice within the aircraft industry is to use these techniques manually. In many situations this practice may tedious and even error prone. Alternate approaches are also being investigated in order to automate these inspection processes using robots [3]. These robotic systems are still in research stage and one of the goals is to make the robots to automatically crawl along the aircraft skin particularly along the rivet lines. An extensive description of the state-of-the-art in robot-assisted aircraft inspection has been given by Siegel et al. [15].

Compared to NDI system, an SHM system uses the techniques of NDI to provide continuous (or on-demand) information about the state of a structure, so that an assessment of the structural integrity can be made at any time, and corrective actions may be taken as necessary. SHM systems can be broadly divided into two groups: passive sensing and active sensing SHM. The following subsections present the current trend on both passive and active sensing SHM.

1.2.1.2. *Current research in passive sensing SHM*

Passive sensing SHM refers to the use of sensors that measures structural parameters (e.g natural frequency, mode shapes, curvature, strain etc.,) without using any external source to excite the structure. During the late 1970s and early 1980s engineers and researchers, particularly in the aerospace and offshore oil industries, began to explore vibra-

tion based damage detection techniques [16]. For passive sensing SHM, the time history response of a structure can be measured by a variety of sensors (e.g. accelerometers, strain gauges, etc.). Based on this time history responses, damage sensitive parameters such as natural frequency and mode shapes are estimated. A detail assessment of passive sensing based damage estimation approaches can be found from the review papers published by Carden, et al. [30] and Montalvo, et al. [17]. SHM methods based on the change natural frequency often fall into one of two categories [17]: the forward and the inverse problem. The forward problem consists in determining what the natural frequency change due to a known damage case (which may include its location, extension and type) will be. Whereas, the inverse problem estimates the damage conditions from the changes in the natural frequencies. Compared to natural frequency damage estimation, mode shape change damage estimation techniques require estimation of mode shapes, which requires either a single excitation point and many sensors, or a roving exciter with one or more fixed sensors. Many modal analysis techniques are available for the extraction of mode shapes from data measured in the time domain [18]. Damage detection methods have been developed for the identification of damage based directly on measured mode shapes or mode shape curvatures. A commonly used mode shape damage estimation technique is Modal Assurance Criterion (MAC). The MAC value can be considered as a measure of the similarity between two mode shapes. A MAC value of 1 is a perfect match and a value of 0 means they are completely dissimilar. Thus, the reduction of a MAC value may be an indication of damage. West [19] uses MAC to determine the level of correlation between modes from the test of an undamaged space shuttle orbiter body flap and the modes from the test of the flap after it has been exposed to acoustic loading.

A drawback of most mode shape based techniques is that they are insensitive to smaller damage and the necessity of having measurements from a large number of locations. Chattopadhyay and Dragomir-Daeseu [20] proposed strain-based damage indices and modified versions of the MAC and the modal strain assurance criterion (MSAC) and the coordinated modal strain assurance criterion (COMSAC) for identifying delamination in composite plates. They observed that modal strain is a more appropriate measure of identifying the presence of delamination than classical mode shapes. Furthermore, Swann and et al. [21] proposed a damage index based on in-plane modal strain to characterize the dynamic behavior of laminated composite plates of arbitrary thickness with discrete multiple delaminations. Comparisons were also shown with two other damage indices such as MSAC and COMSAC. In their work they observed that COMSAC fails to predict the extent of damage even for moderately sized delaminations. Experimentally using strain gauges and scanning laser vibrometry [22] they had also shown that COMSAC and MSAC fail to predict damage for cases with small delaminations, where small strain changes occur between the healthy and the damaged plates. The COMSAC and MSAC also failed to predict the damage location for composite plates where the modal strain was measured at a small number of locations. In contrary, the authors showed that the strain-based damage index provides more accurate information on the damage location and extent, in all of the cases they studied. In addition to the strain based damage estimation technique, during last decade, the usages of smart materials and distributed sensors have been introduced in structural health monitoring (SHM). The vibratory response of any structure can be detected by monitoring the voltage output of surface bonded or embedded piezoelectric sensors [23, 24, 25]. Kim and et al. [26] Ghoshal and et al. [27] presented a procedure to conduct transient analy-

sis of piezoelectric smart composite plates in the presence of delamination damage. They showed that the presence of delamination damage contributes to increased amplitude and frequency shifts in the delaminated plate transient responses. Furthermore, damage estimation techniques based on accelerometer measurements were also became popular during the last decade. Williams, et al. [28] presented a time-series vibration signal based techniques to quantify bearing damage in rotating machinery. The work presented involves running new undamaged ball and roller bearings through its entire life until failure. Conventional first order statistical metrics, such as root mean square, peak value, kurtosis and crest factor, are estimated based on accelerometers and acoustic emission sensor measurements acquired throughout the test. Much later Qiu, et al. [29] presented a wavelet filter-based weak signature detection method and its application on rolling element bearing prognostics.

In general, the available literature on vibration based SHM demonstrates that there is no universal agreement as to the optimum method for using measured vibration data for damage detection, location or quantification. Furthermore, the sensitivity and measurability of the global modal parameter shifts due to localized damage is a matter of disagreement amongst the research community. However, there are still some promises if sensor measurements sensitive to local damage (as in case of strain gauge measurements) and statistical pattern recognition techniques [31] are used to extract information from time-series vibration measurements rather than just comparing the extracted natural frequency, mode shapes and/or the direct time-series sensor data. Farrar and Doebling [16] suggested that the vibration based damage detection problem is fundamentally one of statistical pattern recognition problem. In their opinion, to advance the state-of-the-art in vibration based damage detection, developments of non-model based pattern recognition techniques are

required.

1.2.1.3. *Current research in active sensing SHM*

Unlike passive sensing methods, active schemes are capable of exciting the structure in a prescribed manner. Among different active sensing SHM approaches, ultrasonic guided wave propagation technique is currently an active research area. A detailed review on guided wave based active sensing SHM is presented by Raghavan and Cesnik [32], and by Giurgiutiu [33]. One of the earliest reported experimental work on Lamb wave based guided wave is by Worlton in 1961 [34]. A novel structural health-monitoring concept, with piezoelectric wafer active sensors (PWAS) was presented by Giurgiutiu [35]. PWAS can be structurally embedded as both individual probes or as phased arrays. Hay et al. [36] presented filtered back-projection and reconstruction algorithm for probabilistic inspection of damage (RAPID) detection using guided wave active sensing. Their work compared the results between both approaches and shows that the RAPID technique is more sensitive to material loss and less susceptible to confuse noise and image anomalies with real structural damage and/or material loss. Yang et al. [37] worked to autonomously detect the degradation in mechanical integrity of the standoff carbon-carbon (C-C) thermal protection system panels. The goal was to identify the location of loosened bolts as well as to predict the torque levels of those bolts. Monnier [38] presented a guided wave based SHM approach to detect damage in a carbon/epoxy skin of an Airbus^{TM} aircraft flap. Fourier analysis was used and retained two discriminating parameters: the maximum amplitude and phase of the transmitted spectrum to estimate impact damage. Somasekhar et al. [39] presented a similar work on low-velocity impact damage in composite plates. Conventional C-scan was conducted to confirm the presence of damage, its location, and size. Ultrasonic Lamb

waves were generated and received by piezoelectric crystals, and tomographic images were reconstructed with the collected data using iterative tomographic algorithms. Zhao et al. [40] presented a guided wave based approach for detection, localization and damage growth monitoring in an aircraft Wing. A preliminary survey on the wing panel with angle beam guided wave transducers revealed the difficulties of wave propagation over long distance in the panel due to strong attenuation from paint and rivet scattering. Nevertheless, a circular sparse array of eight-element PZT discs was implemented on the inner surface of the wing to monitor any cracks or corrosion on the wing. Olson et al. [41] presented a beam forming technique using transmitting and receiving arrays applied to Lamb waves. They discussed both experimental testing and analytical modeling of Lamb wave propagation. Michaels and Michaels [42] presented a guided wave signal processing and image fusion technique for *in situ* damage localization in plates. In their work, a method of utilizing information from multiple frequencies has been proposed and implemented for improving the quality of images constructed from sparse transducer arrays attached to plate-like structures. Even though their proposed technique has implementation issues for practical applications, the results presented are significant because they demonstrate that systematic incorporation of multi-frequency information can significantly improve the detection and localization of damage. Yu et al. [43] presented an *in situ* method for detecting damage in thin-wall structures using 2-D embedded phased-arrays of PWAS. In their work, the 2-D PWAS arrays have shown the capabilities for full range damage detection in regular plate-like structures. They used genetic algorithm, which worked well for far field damage and on well-designed laboratory experiments. Kim and Sohn [44] presented a reference free damage detection technique that can be used to detect damage without referencing to

previously stored baseline data. The technique utilizes the polarization characteristics of piezoelectric wafers attached on both sides of thin metal structure. Numerical and experimental results were presented on uniform thickness plate to demonstrate the feasibility of the proposed technique to instantaneous crack detection. Qing et al. [45] investigated the survivability and functionality of a piezoelectric sensor based active SHM system under the operating conditions of typical liquid rocket engines, such as cryogenic temperature and vibration loads. The performance of different piezoelectric sensors and a low temperature adhesive under cryogenic temperature were investigated. The active SHM system for liquid rocket engines was exposed to flight vibration and shock environments on a simulated large booster LOX-H2 engine propellant duct conditioned to cryogenic temperatures to evaluate the physical robustness of the built-in sensor network as well as operational survivability and functionality. Test results demonstrated that the proposed system can withstand operational levels of vibration and shock energy under the cryogenic temperature environment. Recently Santanu and et al. [46] proposed an active sensing technique to determine in-plane locations of delaminations in composite plates. An active sensor network with optimal sensor placement was designed to characterize the existence of damage in composite plate. By incorporating the sensor certainty region and the sensing density, the developed optimal sensor network was able to provide a description of the perturbations caused by the presence of damage. Kostson and Fromme [47] presented a guided ultrasonic wave technique for monitoring fatigue crack growth in fastener holes at the second layer of multi-layered plate structures, which a common problem in aerospace industry. The multi-layered structure investigated consists of two aluminum plate strips bonded using a structural paste adhesive. This is not a pure SHM approach. Guided ultrasonic waves were excited using

multiple piezoelectric discs bonded to the surface of the multi-layered structure, and wave propagation in the tensile specimen was measured using a laser interferometer. Measurement of the guided wave amplitude change allows, in principle the detection of fatigue cracks from laser measurements close to the fastener hole. Chakraborty et al. [48] presented an advanced signal processing and classification method to classify various types of fastener failure damage. The time-varying signals collected from piezoelectric sensors are decomposed into linear combinations of highly localized Gaussian functions using the matching pursuit decomposition algorithm. Classification was then performed by matching the extracted damage features in the time-frequency plane. To further improve classification performance, the information collected from multiple sensors was integrated using a Bayesian sensor fusion approach. Results were presented demonstrating the algorithm performance for classifying signals obtained from different types of fastener failure damage in an aluminum plate. Doyle et al. [49] investigated the application of embedded ultrasonic and magneto-elastic active sensors for monitoring the integrity of bolted joints in a satellite panel structure. Two damage detection approaches were considered, the acousto-elastic method and the magneto-mechanical impedance technique. Their experimental investigations demonstrated the need of the acousto-elastic method for detecting and locating loosened bolts in a satellite structures.

1.2.2. Current research in offline fatigue damage prognosis

Fatigue life prediction is an integral aspect of aerospace structural design. One of the two major approaches currently used for the fatigue design of aerospace structures are: safe life and damage tolerant approach. The safe life approach dates back to 1924 when Palmgren [50] presented his work on linear cumulative damage in the life evaluation of

ball bearings. In 1945, Miner [51] proposed a similar concept that is applicable to the design of aircraft components. After about a decade, Jacoby [52] and Arden [53] found the linear cumulative damage rule of the safe life approach proposed by Palmgren and Miner is not suitable as the most reliable approach to predict fatigue life. Jacoby [52] in his work predicted that the lives of one-third of about 300 tests conducted on different types of structures and materials were considered to be on the non-conservative side. Similarly, Arden [53] found that the hypothetical pitch link problem formulated by the American Helicopter Society (AHS), showed variations in predicted fatigue life from 9 to 2,594 hours. To find a better and more reliable fatigue damage prediction approach, a damage tolerant philosophy was introduced in the 1960's by the U.S. Air Force [54]. This was in an attempt to prevent catastrophic accidents resulting from a less than perfect manufacturing process. A direct comparison between the damage accumulation and the damage tolerant approach can be found in the NASA report [55]. Today, damage tolerant based fatigue damage modeling approaches are widely practiced and are continuously being improved for life estimation of structural components under both constant and variable cycle fatigue loading. These models are primarily based on fracture mechanics, as far as fatigue failure is concerned. However, prediction of fatigue crack growth in complex structures is highly complex, even under constant amplitude loading. This is primarily due to the manner in which various parameters, such as loads, material properties and crack geometries, interact with each other to affect the crack propagation, which is not clearly understood [56]. Therefore, prediction of fatigue crack growth under typical service loads experienced by aircraft structures is an even more involved task because transient loading effects in fatigue crack growth rates, may affect fatigue life significantly. A vast majority of fatigue crack

growth models [57, 58], have been limited to constant-amplitude stress cycles where the crack opening stress is assumed to be constant. These models cannot be used directly for variable-amplitude service loading because they cannot capture the intrinsic dynamic behavior. The FASTRAN-II [59, 60, 61] and the AFGROW [62] models capture the dynamics under variable amplitude by incorporating the crack opening stress as a physical variable in the fatigue crack growth model. Recently, Ray and Partnakar [63, 64], Patankar and Qu [65], and Qu et al. [66] proposed different state space models to predict fatigue damage under different variable loading. The state space model presented, although based on the original physical concept of the FASTRAN model [59, 60, 61], significantly reduces the computation time and memory requirements. A detailed comparison of computational time requirements under different variable load cases for both the FASTRAN and state space models is presented in [65]. However, the above mentioned propagation physics based models are developed on standard coupon geometry, thus when using these models for damage prognosis of real-life complex structures, approximations have to be made. Iyyer et al. [67] presented the use of a damage tolerant based approach for fatigue damage prediction of Navy's P-3C Aircraft. In their approach, to estimate crack growth at different locations of the aircraft, they used a simplified standard coupon geometry such as a compact tension (CT) specimen [68]. However, as an initial condition in the damage model, the initial crack length found during the full-scale fatigue test was used. The above approximation works well some time but may not be a general purpose approach. To model fatigue damage in real-life complex geometries a finite element (FE) based approach is required. However, there is not a single finite element based approach currently available that can estimate fatigue damage effectively. The main drawbacks attributed to FE models are usually the

fact that fixed finite element mesh is used and currently there is no computationally efficient damage propagation mechanism available. On the other hand, the fatigue damage prediction approach is a time-evolving approach, which requires dynamic mesh updating or an equivalent approach with computationally efficient damage propagation mechanism. Recently Giner et al. [69] presented an implementation of the extended finite element method for fracture problems within the finite element software $ABAQUS^{TM}$. Although the proposed finite element approach currently is in its nascent stage, it is expected to be useful in predicting fatigue damage of complex geometries in future. Although the above mentioned FE damage growth models [69] can be used to model complex structures, it is not be useful in real-time on-board applications. The major drawback in FE based physics models is the high computational requirements that make it unsuitable for on-board applications. To avoid the computational problem in the FE approach, a probabilistic data driven approach can be used to model fatigue crack growth. There are numerous stochastic crack growth models those are currently available. Broadly they can be classified into two groups: Damage accumulation [99] stochastic models and damage propagation stochastic models [77, 78, 80]. Between these two approaches, the damage propagation type is more suitable for real-time SHMP system. This is because the damage propagation approach is directly based on real-time loading condition and damage state information.

1.2.3. Current research in condition based damage prognosis

As mentioned in the previous section, the aircraft industry uses safe-life, or damage-tolerant approach for fatigue damage prognosis and residual useful life estimation (RULE). These predictive algorithms are generally used offline, in particular during the design stage, to predict the life of a structural component. Also, these models are based on assumed

initial conditions and fixed loading patterns. However, for a real-life structure the initial condition varies from time to time depending on the loading conditions, the structure was subjected to. This implies the need for an automated updating of initial conditions to life prediction algorithm. The current research on SHM can lead to a paradigm shift in condition based maintenance (CBM) and RULE. Based on the SHM techniques the state of a structure can be constantly monitored and fed to prognostics algorithms in real time to obtain updated information on RULE. Schwabacher [70] presented a review paper on data driven prognosis. As stated in reference [70], for realistic systems fault detection is difficult and a robust condition based prognostic framework for predicting the remaining time until failure is much more difficult. This is because damage prognosis is a system level approach, which requires highly multidisciplinary techniques to be integrated on a single platform. Compared to literatures available on online SHM and offline damage prognosis, literature on condition based damage prognosis is very limited [71]. Till today one of the most advanced damage detection systems, which have made the transition from research to practice is integrated condition assessment of rotating machinery in US Navy ships [73] and the HUMS (health and usage monitoring systems) program implemented on main rotor and gearbox components of large rotorcraft in UK [8, 9]. However, in the two above mentioned applications and almost in all reported SHM applications condition based prognosis remains elusive. To date, one of the few attempts at integrating condition based damage prognosis with a predictive capability is also encountered in the field of rotating machinery [74]. The success of SHM and prognosis in the field of rotating machinery is in some sense can be attributed to the availability of extensive datasets. In addition, the major parameters that influence damage, the operational and environmental conditions, are often well known a

priori and do not vary significantly. In a recent review Farrar and Lieven [72] discussed the concept and future directions of condition based damage prognosis, and indicated the dearth of publications on condition based damage prognosis. This scarcity of publications indicates that this technology is still in the early developmental phase and there is a need for considerable research.

1.3. Relationship of Literature Review to Current Project

From the above literature review, the following trend can be observed

1. Majority of the literature on passive sensing based SHM is based on vibration measurements and mode shape estimation approaches. It is important to note that mode shape approach is not sensitive to smaller local damage. Also, it requires external excitation (such as using external shakers) of structures, which is essentially not a SHM approach but rather a NDI approach.

2. Majority of the researcher on active sensing based SHM demonstrates their proposed techniques on simple structures. It is to be noted that real-life structures have complex geometry. Majority of the proposed wave based approach may not work for these complex structural components. In addition, majority of wave based SHM approach do not discuss time-series fatigue damage state prediction. They only discusses, whether there is damage present or not with respect to a reference condition. Tracking the trend of damage growth with multiple damage cases, as encountered under real fatigue loading, has not been adequately addressed.

3. In addition, majority of the reported literature either focuses on online structural health monitoring or offline damage prediction. Few of these works discusses an

integrated approach of condition based damage prognosis, which is an integration of online SHM and offline prognosis model, and is necessary for condition based state awareness and RULE.

The objective of this research is to develop a fully integrated framework for structural health monitoring and damage prognosis of metallic aerospace structural components. The goal is to address some of the deficiencies in the current literature in order to develop an efficient approach for condition based fatigue damage prediction and residual useful life estimation in real time.

CHAPTER 2

Objectives

A comprehensive SHM-Prognosis framework for real-time health monitoring and prognosis of complex metallic structures under fatigue loading has been developed. The integrated framework estimates the current health of the structure but also forecast the future damage state and the associated remaining useful life. The framework comprises both offline and online models.

Offline damage prognosis model: This is a slow time scale model that works on offline or non real-time data. This model maps the slowly evolving fatigue damage state with the parameters that causes its evolution. The model is developed using a Bayesian statistics based Gaussian process approach. The Gaussian process model maps the fatigue affecting parameters such as future loading and current damage condition to the future damage state over a high-dimensional kernel transformation. The Gaussian process model is trained using damage history data either available from different test article or from the same test article. The future damage state of a structure is predicted using the trained Gaussian process model and using the anticipated future loading information.

Online state estimation model: This is a fast time scale model, which estimates the current damage state of the structure using real-time fast scale sensor measurements. Both active and passive sensor measurements are used for current damage state estimation. Based on active sensor measurements both supervised and unsupervised approaches are proposed to estimate the current damage condition. In addition, passive sensor measurements (such as from strain gauges) based different online state estimation models are also proposed to estimate the current health of the structure.

Condition based prognosis model: The above two models are integrated to perform

condition based future state prediction and to estimate the associated residual useful life. The offline model adaptively changes its initial condition based on the current damage state estimated using the online model. In addition, the offline model adaptively changes its parameters based on the new available state information (either estimated using the online model or predicted using the offline model).

The models are validated on complex geometry Al-2024/6061 cruciform and lug joint specimens subjected to various loading conditions including uniaxial, biaxial, constant, random, and FALLSTAF flight profile loading. Different research tasks are schematically shown in Figure 2.1. Following are the tasks associated with this research.

1. Chapter-3: Develop a Bayesian Gaussian process based univariate offline model to forecast damage under constant fatigue loading.

2. Chapter-4: Develop a Bayesian Gaussian process based multivariate offline model to forecast damage under random/FALLSTAF flight profile fatigue loading.

3. Chapter-5: Develop an active sensing based supervised online model to estimate the current damage condition of a structure.

4. Chapter-6: Develop an active sensing based unsupervised online model to estimate the current damage condition of a structure.

5. Chapter-7: Develop a passive sensing measurement based unsupervised online model that can estimate the current damage condition of a structure under constant cyclic fatigue loading.

6. Chapter-8: Develop a passive sensing measurement unsupervised online model that

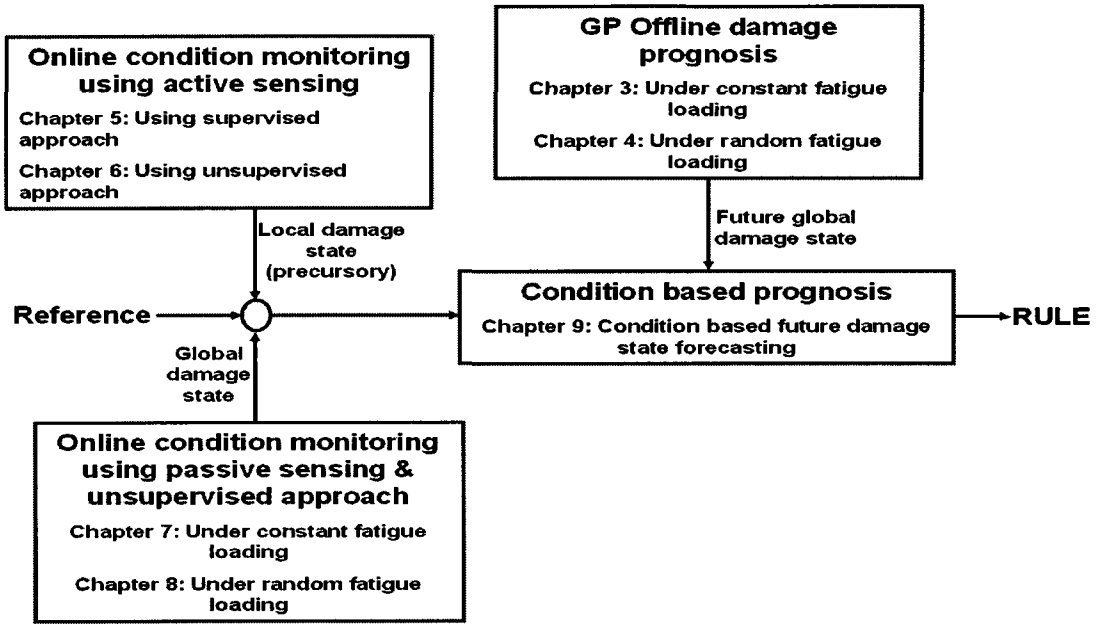

Fig. 2.1. Schematic of different research tasks.

can estimate the current damage condition of a structure under random cyclic fatigue loading.

7. Chapter-9: Develop an integrated online-offline model to forecast the future damage states of the structure based on current condition and future anticipated loading.

CHAPTER 3

Offline Damage Prediction Using Probabilistic Gaussian Process Approach

3.1. Introduction

Predictive or prognosis model is an integral part of real-time SHM-Prognosis (SHMP) framework. The goal of this prognosis model is to works in offline mode and predicts the future damage condition of a structure and the associated remaining useful life. Most reported damage (crack) growth models are based on concepts of the continuum theory with the assumption that cracks propagate in an ideal continuum media. Actual metallic materials, however, are composed of random microstructure [75] described by various micro scale parameters which can seriously affect the growth of a crack in these materials. As a result, the deterministic theories can only be accepted as an approximation of the actual random fatigue crack propagation process. The use of stochastic or probabilistic models thus becomes necessary to make predictions of crack growth more reliable. A comprehensive review of early developments on stochastic crack growth models can be found in [76]. There are basically two types of mathematical models in existence to estimate fatigue life of any metallic structure. The first employs a statistical approach in which random variables are introduced instead of the constants used in the corresponding deterministic crack growth equation. The second approach employs evolutionary methods in which the crack propagation is treated in a probabilistic or stochastic sense instead of a statistical one. The first approach needs a deterministic differential equation of the damage propagation mechanism. The expression for the deterministic differential equation varies from structure to structure. This is because of the use of a stress intensity factor that depends on the geometry of the structure. Estimating a stress intensity factor for each and every structure is not straight forward. This limits the feasibility of deterministic crack propagation based differential

equation approach for few standard geometry or coupons. For this reason majority of the available literatures on differential equation based stochastic models are limited to stochastic damage growth modeling of standard structural coupons [77, 78, 79, 80]. However, for stochastic modeling of complex structure the second approach is more suitable because the equivalent dynamics i.e., the crack propagation mechanism can be learned from the previous or history data. The history data can be obtained from previous fatigue tests data of the real complex geometry. Making use of a specific probability process, namely the Markovian process, the models with this approach strive to correlate the properties of this process with those from history of fatigue crack propagation. In this chapter a Bayesian Gaussian process [81, 82, 83, 84] approach is used, which stochastically models the damage growth dynamics using history fatigue test data. In the present chapter the proposed model will be evaluated on constant cyclic fatigue data that was obtained [80] from fatigue tests on standard coupons. However, in the next chapter the validation of the proposed approach will be performed for a complex geometry under complex state of loading.

3.2. Theoretical Approach

Fatigue damage propagation can be modeled either using a physics based approach or using a probabilistic data drive approach. The probabilistic approach is adopted in this thesis. Brief distinctions of both approaches are presented in the following subsection for completeness.

3.2.1. Physics based damage propagation model

The rate of fatigue crack propagation per fatigue cycle da/dN is governed by the stress intensity factor range ΔK and can be written in functional form (Ψ) at a future damage

level $n+1$ as

$$\begin{aligned}(\frac{da}{dN})_{n+1} &= \Psi\left\{(U_{n+1}^{max} - U_{n+1}^{min})F_n^g\right\} \\ &= \Psi\left\{(U_{n+1}^{max} - U_{n+1}^{min})\sqrt{\pi a_n}\right\} \end{aligned} \tag{3.1}$$

where $(\frac{da}{dN})_{n+1}$ is the future damage level crack growth rate, U_{n+1}^{max} and U_{n+1}^{min} are the maximum and minimum cyclic stress at the forward cycle respectively, F_n^g is the current damage level geometric function and a_n is the current damage level crack length. Paris [85] and Paris, et al. [86] were the first to formulate the expression given in Eq. (3.1). The above functional form often assumed to be a simpler power function [85, 86, 87, 88] form can be expressed as

$$\begin{aligned}(\frac{da}{dN})_{n+1} &= C(\Delta K)^m \\ &= \Psi\left\{(U_{n+1}^{max} - U_{n+1}^{min}), a_n, C, m\right\} \end{aligned} \tag{3.2}$$

For direct crack length prediction, the equivalent from of Eq. (3.2) can be written in functional form as:

$$a_{n+1} = \Psi\left\{U_{n+1}^{max}, U_{n+1}^{min}, dN_{n+1}, a_n, C, m\right\} \tag{3.3}$$

where, dN_{n+1} is the number of fatigue cycles elapsed between the current damage level (i.e., the n^{th} damage level) and the forward step damage level (i.e., the $(n+1)^{th}$ damage level). Many advanced crack growth models [59, 62, 90, 91, 63, 64, 92, 89] have been proposed in

the literature. The differences among those models are not significant; also none of them has a general applicability. Each one may be found reasonably satisfactory in a limited region or limited sets of data.

3.2.2. Generalized Bayesian data driven model for damage prediction

The lack of general applicability of available physics based crack growth model is due to the complex dependency of crack propagation on different factors such as variability due to (i) material (e.g., microstructure) (ii) geometric complexity (iii) manufacturing process (e.g., heat treatment, cold deformation) (iv) loading (v) environmental effects (e.g., temperature and humidity). To incorporate these factors in a damage propagation model, a generalized Bayesian probabilistic framework can be employed. The Bayesian framework is a data driven approach, which is not only easier to understand but also based on basic physics of damage propagation described by Eq. (3.1). The schematic of a probabilistic Bayesian framework for future step damage state forecasting is shown in Figure 3.1. The goal of a probabilistic Bayesian forecasting approach is to compute the posterior distribution of an unknown target, i.e., to predict $f\left(y_{n+1}|D=\{\mathbf{x}_i,y_i\}_{i=0,\ldots n-1,n},\mathbf{x}_{n+1}\right)$, where y_{n+1} represents either the crack length (a_{n+1}) or the crack growth rate $((\frac{da}{dN})_{n+1})$ at damage level $n+1$. The $(n+1)^{th}$ damage level distribution is obtained based on available input-output data up to the current damage level (i.e., the n^{th} damage level) $D=\{\mathbf{x}_i,y_i\}_{i=0,\ldots n-1,n}$ and future input parameter $\mathbf{x}_{n+1}$. It is noted that the input $\mathbf{x}_i$ at any fatigue damage level i is a vector and constitutes the various fatigue affecting parameters (e.g., the damage conditions a_i, maximum and minimum loading condition U_i^{max}, U_i^{min}, etc.) as discussed in section 3.2.1. Also to note that the bold faced letter used throughout this thesis represents vector. In the Bayesian framework, the predictive distribution of a target can be found

by conditioning the targets y_0,.....,y_{n-1},y_n, y_{n+1} that are affected by the corresponding random inputs $\mathbf{x}_0$,.....,$\mathbf{x}_{n-1}$,$\mathbf{x}_n$, $\mathbf{x}_{n+1}$. Now we can define a priori over the space of possible functions to model the target (crack length or crack growth rate) as $f(y|\alpha)$, where α represents parameters that account of modeling uncertainties in the form of curve fitting. It is assumed that modeling the uncertainty parameters α can account for the effect of loading interaction (e.g., retardation effect) in addition to modeling uncertainties. A *priori* noise function $f(\vartheta|\beta)$ can also be defined, where ϑ is some appropriate noise function that arises due to scatter in material micro structure and β is another set of hyperparameters used to model the uncertainty due to scatter. Now if the parameters α and β are known, the conditional probability [81, 82, 83, 84] can be expressed as

$$f\left(\mathbf{y}_n|\left\{\mathbf{x}_{i=1,\cdots,n},\alpha,\beta\right\}\right)=\int\left(\mathbf{y}_n|\left\{\mathbf{x}_{i=1,\cdots,n},y,\vartheta\right\}\right)f(y|\alpha)f(\vartheta|\beta)dyd\vartheta \tag{3.4}$$

where $\mathbf{y}_n = \{y_0, ..., y_{n-1}, y_n\}$ and ϑ denotes the underlying function which corresponds to the target functions and noise due to microstructural scattering respectively. Since y_0,.....,y_{n-1}, and y_n are conditioned random variables in the observed set of targets, the conditional distribution of y_{n+1} can be written as follows

$$f\left(y_{n+1}|D=\left\{\mathbf{x}_i,y_i\right\}_{i=1,\ldots,n},\mathbf{x}_{n+1},\alpha,\beta\right)=\frac{f\left(\mathbf{y}_{n+1}|\left\{\mathbf{x}_i\right\}_{i=1,\ldots,n+1},\alpha,\beta\right)}{f\left(\mathbf{y}_n|\left\{\mathbf{x}_i\right\}_{i=1,\ldots,n},\alpha,\beta\right)} \tag{3.5}$$

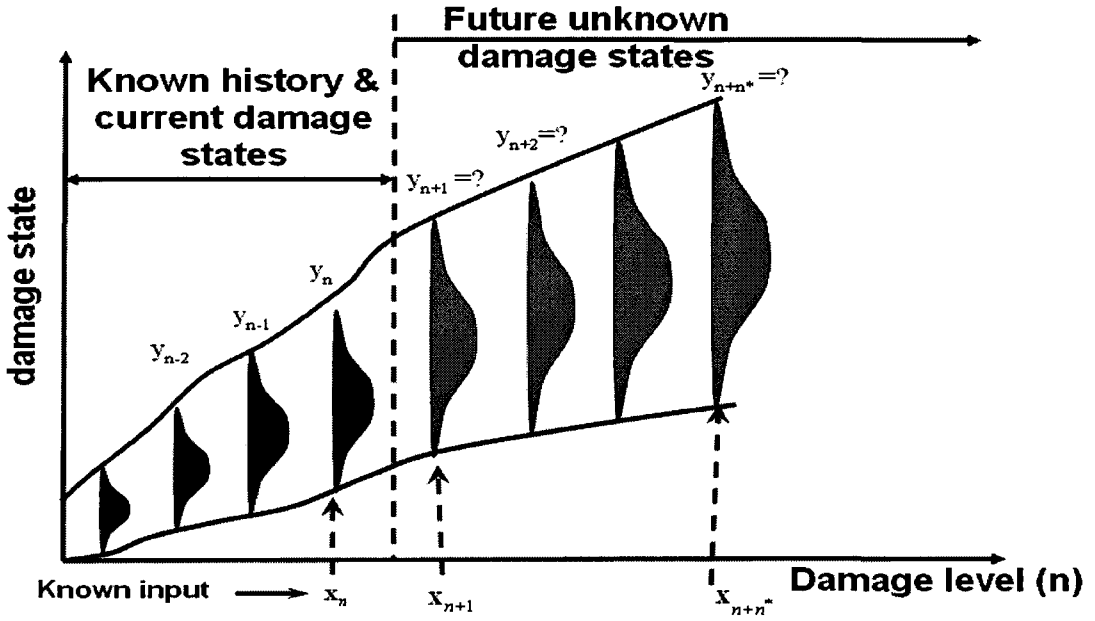

Fig. 3.1. General Bayesian probabilistic framework for future step damage state forecasting.

3.2.3. Damage prediction using data driven Gaussian Process (GP) approach

To evaluate Eq. (3.5) it is necessary to evaluate the integral given in Eq. (3.4). However in general, Eq. (3.4) is complicated to evaluate. The standard approach to evaluate the integral in Eq. (3.4) is by a method called evidence maximization [81] or by numerically integrating it by Monte Carlo simulation [93]. However, assuming the underlying function $y_{i=0,\ldots,n-1,n,n+1,\ldots}$ follows a Gaussian distribution, the exact analytical form of Eq. (3.5) can be expressed as follows

$$f\left(\mathbf{y}_n|\left\{\mathbf{x}_i\right\}_{i=1,\cdots,n},\mathbf{C}_n\right)=\frac{\theta}{(2\pi)^{n/2}det(\mathbf{C}_n)^{1/2}}exp\left(-\frac{1}{2}(\mathbf{y}_n-\boldsymbol{\mu})^T\mathbf{C}_n^{-1}(\mathbf{y}_n-\boldsymbol{\mu})\right) \tag{3.6}$$

where $\mathbf{x}_i$ is the i^{th} input, $\boldsymbol{\mu}$ is the function mean and $\mathbf{C}_n$ is a $n \times n$ covariance matrix which is function of parameters α and β. The individual elements c_{ij} of the covariance matrix C_n is a measure of "linear dependence" between the two random variables $\mathbf{x}_i$ and $\mathbf{x}_j$ and they are linked to the target function y through the parameter θ. The covariance between two random variables $\mathbf{x}_i$ and $\mathbf{x}_j$, with their respective expected values μ_{x_i} and μ_{x_j}, can be found as

$$c_{ij} = \left\langle (\mathbf{x}_i - \mu_{x_i})(\mathbf{x}_j - \mu_{x_j}) \right\rangle \tag{3.7}$$

3.2.3.1. *Covariance matrix to kernel matrix*

The expression given in Eq. (3.6) holds good if there exists a "linear dependence" between the two random variables $\mathbf{x}_i$ and $\mathbf{x}_j$. However, in general for fatigue damage modeling, the input variables $\mathbf{x}_i$ and $\mathbf{x}_j$ may not have a linear relationship. For instance, if the input-space only consists of previous level crack lengths, then the input-space variables for i^{th} and j^{th} damage level can be given as $\mathbf{x}_{i=n-1} = a_{n-1}$ and $\mathbf{x}_{j=n} = a_n$. However, it is to be noted that the relation between a_{n-1} and a_n is not always linear. The nonlinearity is more pronounced during the unstable and transient damage growth regime. In addition to crack length, if other parameters such as loading information is introduced in the input-space, the relation between input variables $\mathbf{x}_i$ and $\mathbf{x}_j$ becomes more complex. To avoid the nonlinearity problem, the expression given in Eq. (3.6) can be reformulated using a high-dimensional transformation of the original input-space. The schematic of the high-dimensional transformation Φ is shown in Figure 3.2. The high-dimensional transformation Φ [94, 95] can be performed using an assumed kernel function $k(\mathbf{x}_i, \mathbf{x}_j, \Theta)$.

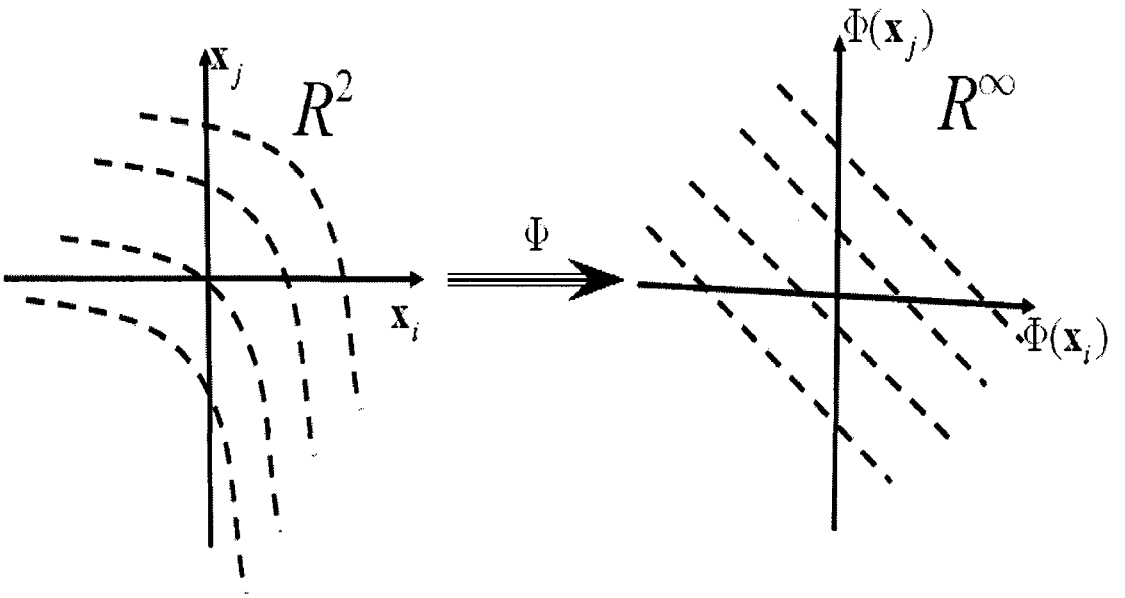

Fig. 3.2. Schematic of high-dimensional transformation of input space

With the high-dimensional transformation, the covariance matrix C_n term in Eq. (3.6) can be replaced by the kernel matrix $\mathbf{K}_n$ and Eq. (3.6) can be rewritten [81, 82, 83, 84] as

$$f\left(\mathbf{y}_n|\left\{\mathbf{x}_i\right\}_{i=1,\cdots,n},\mathbf{K}_n\right)=\frac{\theta}{(2\pi)^{n/2}det(\mathbf{K}_n)^{1/2}}exp\left(-\frac{1}{2}(\mathbf{y}_n-\boldsymbol{\mu})^T\mathbf{K}_n^{-1}(\mathbf{y}_n-\boldsymbol{\mu})\right) \tag{3.8}$$

3.2.3.2. *Mean and variance of the predicted damage at* $(n+1)^{th}$ *damage level*

The individual elements k_{ij} of the kernel matrix K_n can be found from a parameterized kernel function that will be described in the next section. Assuming a zero mean function distribution Eq. (3.8) can be written as

$$f\left(y_{n+1}|D=\{\mathbf{x}_i,y_i\}_{i=1,\ldots,n},\mathbf{x}_{n+1},k_{mn}(x_i,x_j,\Theta)_{i,j=1,2,..n+1}\right)$$
$$=\sqrt{\frac{det(K_n)}{(2\pi)det(K_{n+1})}}exp(-\frac{(y_{n+1}-\mu_{n+1})^2}{2\sigma^2_{\mu_{n+1}}}) \tag{3.9}$$

where μ_{n+1} is the predicted mean damage (of either crack length a_{n+1} or crack growth rate $(\frac{da}{dN})_{n+1}$) at $n+1^{th}$ fatigue damage level and is given by

$$\mu_{n+1}=\mathbf{k}^T\mathbf{K}_n^{-1}\mathbf{y}_n;\quad k_i=k(\mathbf{x}_{n+1},\mathbf{x}_i)_{i=1,2,\ldots n} \tag{3.10}$$

whereas σ^2_{n+1} is the associated predicted variance at $n+1^{th}$ fatigue damage level and is given by

$$\sigma^2_{n+1}=\kappa-\mathbf{k}^T\mathbf{K}_n^{-1}\mathbf{k};\quad k_i=k(\mathbf{x}_{n+1},\mathbf{x}_i)_{i=1,2,\ldots n};\quad \kappa=c(\mathbf{x}_{n+1},\mathbf{x}_{n+1}) \tag{3.11}$$

In Eq. (3.10) and (3.11), $\mathbf{K}_n$, $\mathbf{k}$ and κ are the partitioned matrix/vector of the $n+1^{th}$ fatigue damage level kernel matrix.

3.2.3.3. *Kernel function selection*

There are many possible choices of kernel functions [84]. From a modeling point of view, the objective is to select a kernel a priori, which agrees with the assumptions and mathematically represent the structure of the process being modeled. Formally, it is required to specify a function that will generate a positive definite kernel matrix for any set of inputs. In more general term the high-dimensional transformation through the assumed kernel function should satisfy Mercer's theorem of functional analysis [96]. For any two set

of input vectors x_i and x_j a kernel function used in Eq. (3.8) through Eq. (3.11) has the following form

$$k(x_i, x_j, \Theta) = k_y(x_i, x_j, \Theta) + k_{scatter}(x_i, x_j, \Theta) \tag{3.12}$$

where k_y is associated with the interpolation function y and $k_{scatter}$ is associated with the scatter model. It is to be noted that in the present case of GP damage modeling the scatter arises from micro-structural variability. Whereas for modeling the interpolation function, a neural network based multi layer perceptron (MLP) kernel is used. The MLP kernel function [97] has the following form.

$$k_y(x_i, x_j, \Theta) = \theta_p Sin^{-1}\left\{\frac{\mathbf{x}_i^T \theta_w \mathbf{x}_j}{\sqrt{(1 + \mathbf{x}_m^T \theta_w \mathbf{x}_i)(1 + \mathbf{x}_j^T \theta_w \mathbf{x}_j)}}\right\} \tag{3.13}$$

Where θ_p and θ_w respectively symbolizes process and width hyperparameter. Also in Eq. (3.12) the second term associated with the scatter model only contributes to the diagonal term of the kernel matrix and for an input independent scatter model $k_{scatter}$, it can be written in terms of a hyperparameter $\theta_{scatter}$ such that

$$c_{scatter}(x_m, x_n, \Theta) = \delta_{ij}\theta_{scatter} \tag{3.14}$$

where δ_{ij} is the Kronecker delta with value one when $i = j$ and zero when $i \neq j$.

3.2.3.4. *Hyperparameter determination*

So far we have only considered the properties of the prediction model for fixed values of the hyperparameters. In this section we will discuss how to obtain the hyperparameters

Θ for a fixed training data set $D = \{\mathbf{x}_i, y_i\}_{i=1,\ldots,n}$. Ideally, one should integrate over all possible hyperparameters in order to obtain the best possible predictions of the function value y_{n+1} at $(n+1)^{th}$ damage level. This can be written as,

$$f\left(y_{n+1}|D, \mathbf{x}_{n+1}, K(\cdot)\right) = \int f\left(y_{n+1}|D, \mathbf{x}_{n+1}, K(\cdot), \Theta\right) f\left(\Theta|D, K(\cdot)\right) d\Theta \tag{3.15}$$

The above expression is as complex as the one given in Eq. (3.4) and also difficult to evaluate for a complex problem with several hyperparameters and with multiple input-space variables. Out of the two possible approaches (e.g., the Maximum evidence [81] and the Monte Carlo [93] approach) only the use of the maximum evidence approach will be discussed. Using maximum evidence approach, Eq. (3.15) can be written in its approximate form as,

$$f\left(y_{n+1}|D, \mathbf{x}_{n+1}, K(\cdot)\right) \cong f\left(y_{n+1}|D, \mathbf{x}_{n+1}, K(\cdot), \Theta_{MAP}\right) \tag{3.16}$$

The approximation in Eq. (3.16) is based on the assumption that the posterior distribution over Θ, i.e., $f\left(\Theta|D, K(\cdot)\right)$, has a sharp peak around Θ_{MAP}. This approximation is generally good and predictions are often found very close to those obtained using the true predictive distribution [98]. To find the peak location of $f\left(\Theta|D, K(\cdot)\right)$, the posterior distribution needs to be optimized and the posterior distribution can be written as,

$$f\left(\Theta|D, K(\cdot)\right) = \frac{f\left(\mathbf{y}_n|\left\{\mathbf{x}_i\right\}_{i=1,2,\ldots n}, K(\cdot), \Theta\right) f\left(\Theta\right)}{f\left(\mathbf{y}_n|\left\{\mathbf{x}_i\right\}_{i=1,2,\ldots n}, K(\cdot)\right)} \tag{3.17}$$

In Eq.(3.17) the denominator (i.e., evidence) is independent of Θ and can be ignored in the optimization process. On the other hand, the other two terms, the likelihood $f\left(\mathbf{y}_n|\left\{\mathbf{x}_i\right\}_{i=1,2,\ldots n}, K(\cdot), \Theta\right)$ and the prior $f\left(\Theta\right)$, need to be considered in the optimization of $f\left(\Theta|D, K(\cdot)\right)$. With the assumption that all $y_{i=1,2\ldots n}$ follow a Gaussian distribution and

using Eq. (3.8), the logarithm of the objective function can be written as

$$L \equiv Log\left(f\left(\Theta|D, K(\cdot)\right)\right) = -\frac{1}{2}Log(detK_n) - \frac{1}{2}\mathbf{y}_n^T K_n^{-1}\mathbf{a}_n - \frac{n}{2}Log(2\pi) + Logf\left(\Theta\right) \quad (3.18)$$

The log-likelihood function L in Eq. (3.18) is generally multimodal and can be optimized using any multivariate optimization algorithm. In the present work the conjugate gradient method is used to optimize the log-likelihood function and to obtain the optimized hyperparameters. Note that it is common practice [98] to ignore the log prior term in Eq. (3.18) due to the lack of knowledge about Θ. The resulting solution may not be always a realistic solution, however it can be assumed that $Logf\left(\Theta\right)$ is implicitly modeled through the optimization of the log-likelihood L.

3.3. Numerical Results

Different numerical studies are performed to evaluate the GP damage prediction model. First, a constant cyclic fatigue test data set, available in the literature, is considered. It is to be noted that generation of a statistical meaningful data set for probabilistic fatigue modeling is highly time consuming and expensive. Therefore there are only few data sets available in open literature. Among them, the most famous data set perhaps is the one presented by Virkler et al. [75] more than thirty years ago. Two more recently used data sets include one reported by Ghonem and Dore [56], and the other released by the Flight Dynamics Laboratory of the US Air Force [77]. All the above mentioned data sets were generated under constant cyclic fatigue loading. Recently Wu and Ni [80] published a statistically meaningful data set based on constant cyclic fatigue loading. They presented the test data both in pictorial and tabular form. This tabular test data is considered for the

present numerical validation. Wu and Ni performed thirty replicated constant amplitude fatigue crack growth tests to generate a statistical meaningful data set. Compact tension (CT) specimens cut from a 2024-T351 aluminum alloy plate were used for the fatigue crack growth tests. The dimensions of the specimens were 50.0 mm wide (counting from the loading line to the back face of the specimen) and 12.0 mm thick. The pre-cracking test started with a crack length of 15.0 mm and extended to 18.0 mm in length. Sinusoidal signals with maximum amplitude of 4.5 kN, minimum of amplitude 0.9 kN, and frequency of 15 Hz were used as the input loads during both the pre-cracking and fatigue crack growth tests. The crack sizes were measured from the images taken by a microscope mounted on a traversing system. The specimens were tested and the corresponding measurements were taken until the specimens fractured. The numerical value of the different crack lengths up to 40 kcycles are reported [80]. The number of fatigue cycle versus crack length is shown in Figure 3.3. The equivalent crack growth rates are also estimated and plotted in Figure 3.4.

3.3.1. Input-output data for Gaussian process prediction

The crack growth and its rate data are used as the GP input-output data. It is to be noted that the GP damage prediction model is based on the assumption that crack growth and rate data follows a Gaussian distribution. For the effective use of a GP prediction model it is important to check the probability distribution of the original crack growth and rate data.

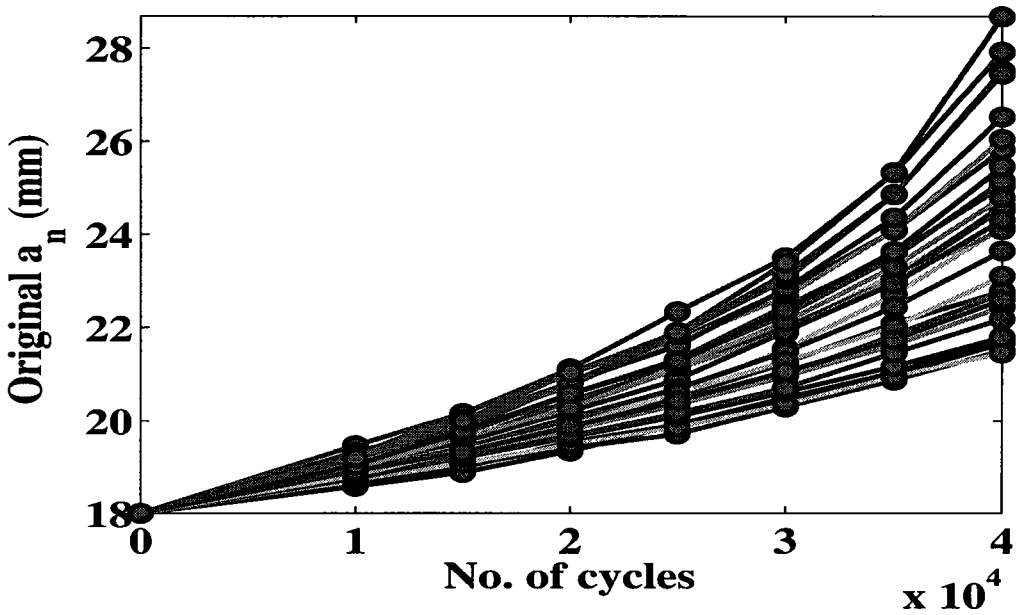

Fig. 3.3. Original crack growth data (The test data is taken from the reference by Wu and Ni [80].

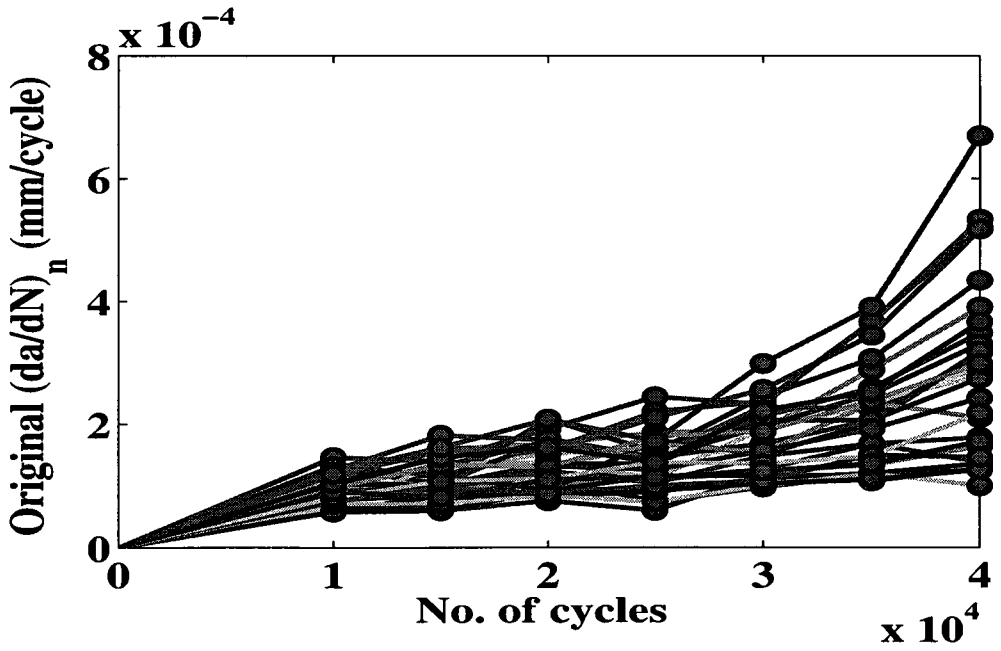

Fig. 3.4. Crack growth rate of all 30 specimens estimated based on the original crack growth data shown in Figure 3.3

3.3.1.1. *Probability distribution check of original crack growth and its rate data*

The probability distribution of crack growth and its rate at different cycles are plotted. Figure 3.5 shows the probability density function (pdf) of the crack growth data at two representative fatigue cycles, N=30000 and N=35000 cycles. Similarly, Figure 3.6 shows the probability density function (pdf) of crack growth rate data at two representative fatigue cycles, N=30000 and N=35000. From Figure 3.5, though it can be seen that the pdf distribution has an overall bell shape, which could be disguised by a Gaussian distribution, the pdf curves appear to be more flat towards the right. These right tailed pdf curves more closely resembles the pdf curves of a log-normal distribution. Similarly from the crack growth rate pdf curves shown in Figure 3.6, it can also be seen that pdf curves are flatter towards right. The above observations indicate that both crack growth and its rate data follow, more log-normal distribution than Gaussian distribution.

3.3.1.2. *Data scaling of original crack growth and its rate data*

For the effective use of GP damage prediction model it is required to perform appropriate scaling of the original data. In this work two types of scaling have been used, min-max scaling of the original data followed by then a log scaling of the scaled data. The min-max scaling is performed for better synchronization and comparison of damage states estimated using the different techniques. In the present case of crack length, the min-max scaling is performed by normalizing the original crack length against the maximum and minimum possible crack length to have a scaled crack length between 0-1. This 0-1 scaled crack length is helpful in integrating one data set with other data set measured using different

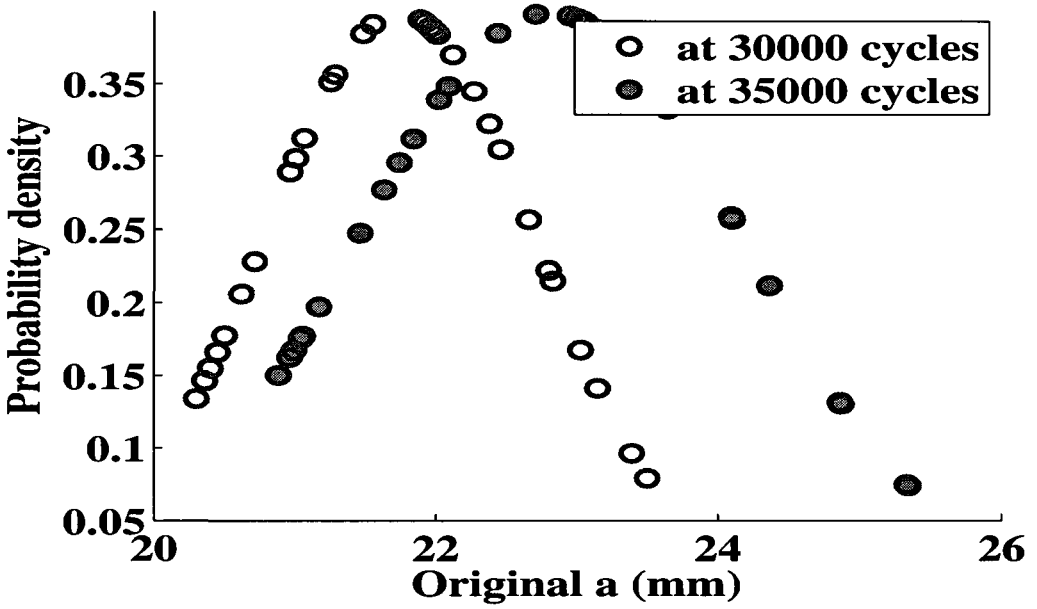

Fig. 3.5. Probability distribution of original crack growth data at N=30000 and N=35000 fatigue cycle.

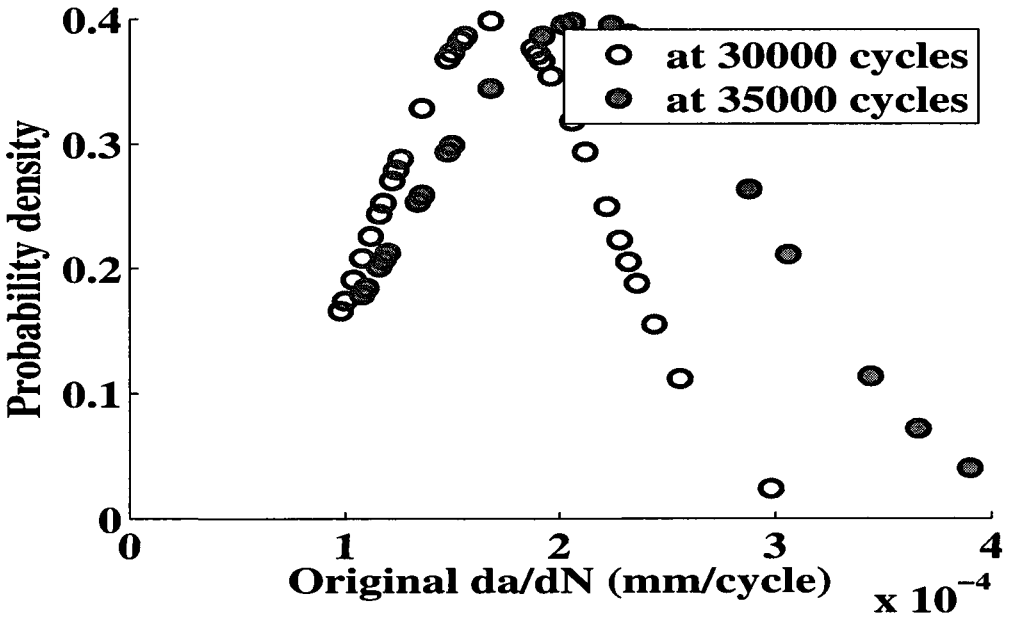

Fig. 3.6. Probability distribution of original crack growth rate data at N=30000 and N=35000 fatigue cycle.

estimation techniques and different units. In this chapter visual crack lengths are considered, which are in millimeters (it is to be noted that most of the SHM literatures presents the state estimation techniques that quantify the damage between 0-1). In the present case the original crack growth data shown in Figure 3.3 are scaled against the maximum crack length of 37.34 mm and minimum crack length of 0 mm. The min-max scaled crack growth data of the original crack lengths (refer Figure 3.3) is shown in Figure 3.7. The corresponding min-max scaled crack growth rate data are shown Figure 3.8. It is to be noted that the min-max scaling does not have any statistical significance. This can be evident from the pdf plots shown in Figure 3.9 and 3.12. The pdf curves plotted for min-max scaled crack growth data (refer Figure 3.9) resembles the pdf curves for original crack growth data (Figure 3.5). Similarly the pdf curves plotted for min-max scaled crack growth data (refer Figure 3.12) resembles the pdf curves for the original crack growth data shown in Figure 3.6. To use the proposed GP damage model it is required to convert the original data such that it follows a Gaussian distribution. This is achieved by performing logarithmic scaling of the min-max scaled data. The corresponding pdf curves of the log-min-max scaled crack growth data are shown in Figure 3.11. Comparing Figure 3.11 with Figure 3.5 it can be seen that the pdf curves of the log-min-max scale crack growth data better resembles with the bell shaped curve followed by Gaussian distributions. Similar comparison can be made between Figure 3.12 and Figure 3.6 and it can be seen that the log-min-max scaled crack growth data better resembles Gaussian distribution than the original data.

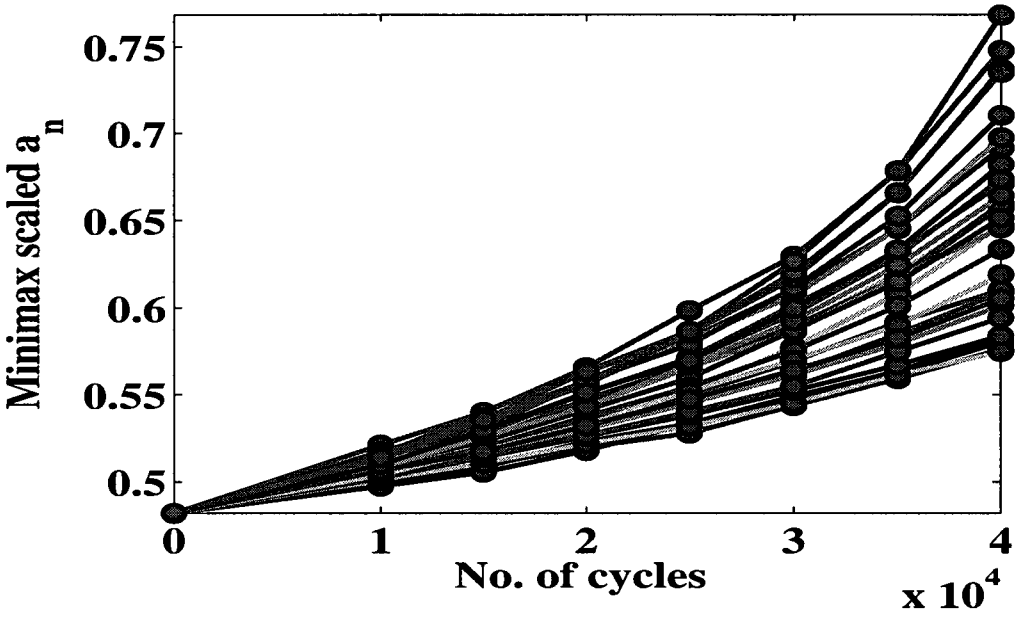

Fig. 3.7. Min-max scaled crack growth data of the original crack growth data shown in Figure 3.3.

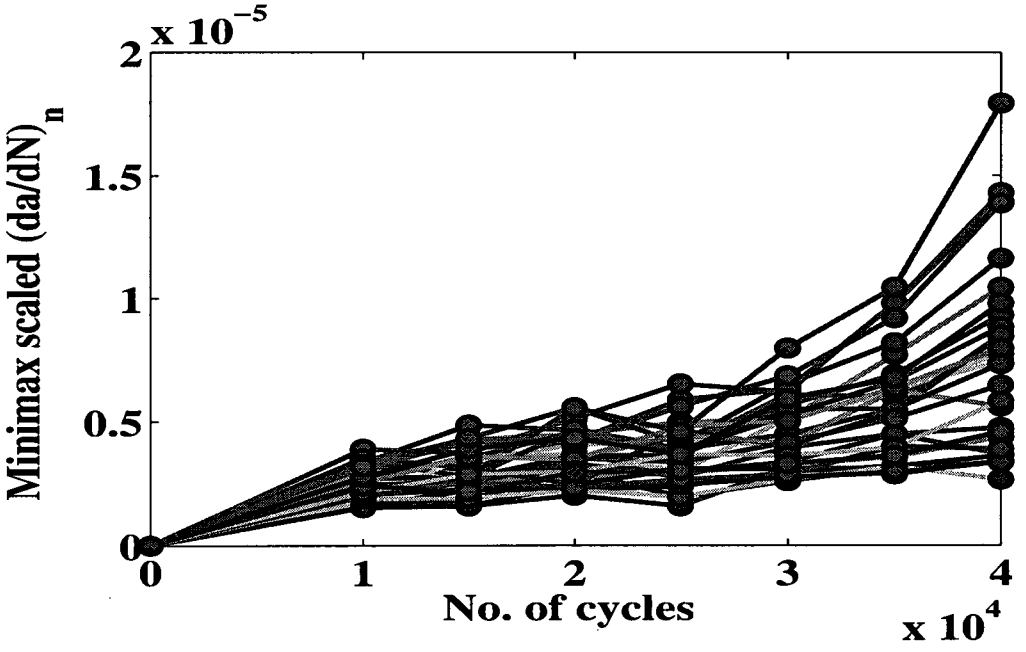

Fig. 3.8. Min-max scaled crack growth rate data of the original crack growth rate data shown in Figure 3.4.

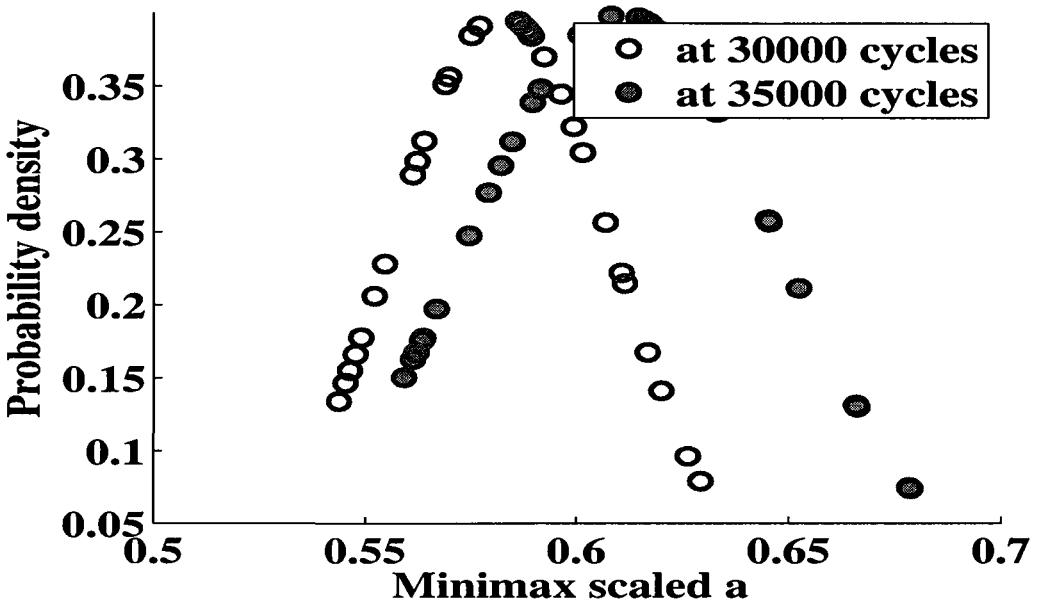

Fig. 3.9. Probability distribution of min-max scaled crack growth data shown in Figure 3.7.

3.3.1.3. *Gaussian process input-output data*

Once the log-min-max scaling is performed, the scaled data are used to make the GP input-output data set. The $(n+1)^{th}$ damage level crack length (i.e., a_{n+1}) depends on the current (i.e n^{th}) damage level crack length (i.e a_n) and future ($(n+1)^{th}$) damage level loading information (such as cyclic maximum and minimum load) and number of fatigue cycles elapsed (ΔN) between the n^{th} and $(n+1)^{th}$ damage level. Since in the present case the constant fatigue cyclic data are considered, the loading information such as cyclic maximum and minimum load remain constant. Since the loading information remains constant for statistical point of view, it is not necessary to consider the loading information in the GP damage prediction model. Hence in the present constant cyclic fatigue prediction of the direct crack length (i.e a_{n+1}), the input-space x_i of the GP model is only modeled with the previous fatigue cycle crack length and number of fatigue cycles elapsed (ΔN)

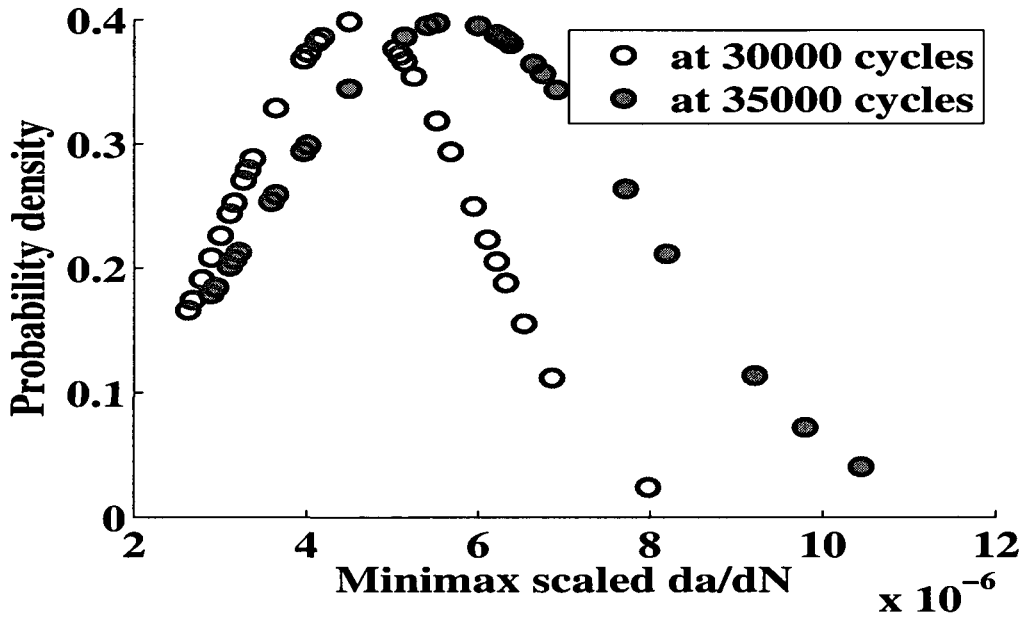

Fig. 3.10. Probability distribution of min-max scaled crack growth rate data shown in Figure 3.8.

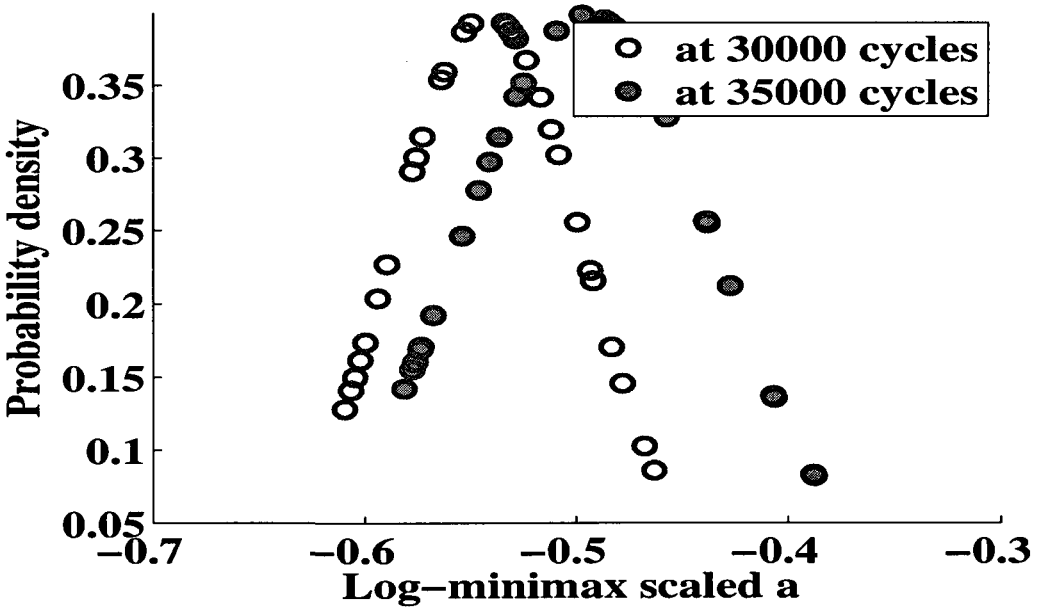

Fig. 3.11. Probability distribution of log-min-max scaled crack growth data.

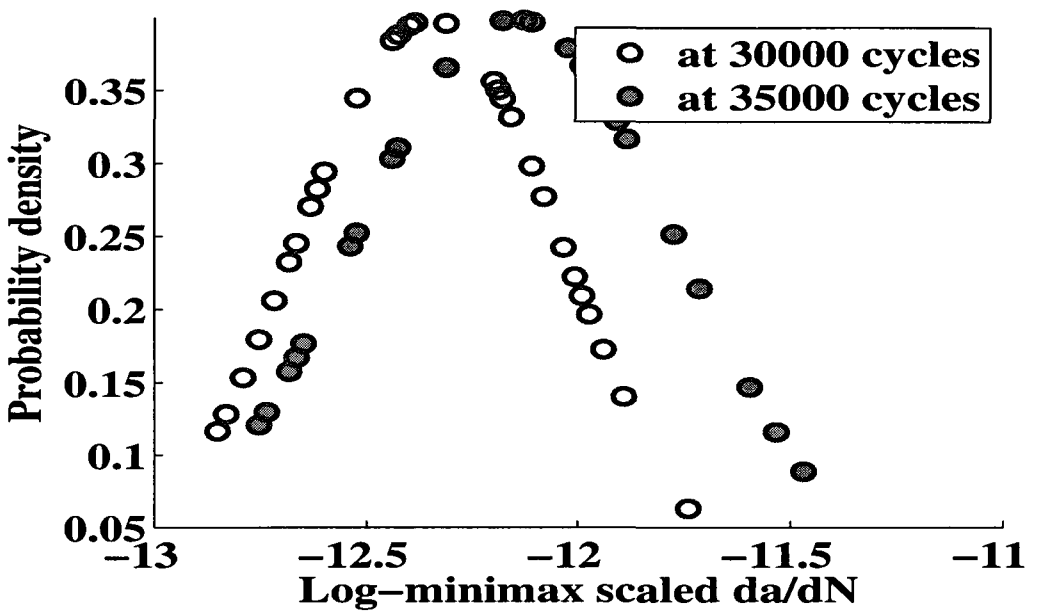

Fig. 3.12. Probability distribution of log-min-max scaled crack growth rate data.

between n^{th} and $(n+1)^{th}$ damage level. Crack growth data from different specimens are considered to train the GP model. A chart of the input-output relation for direct crack growth prediction has been depicted in Eq. (3.19).

$$\begin{bmatrix} a_{k,0} & \Delta N_{k,1} \\ \bullet & \bullet \\ a_{k,n-1} & \Delta N_{k,n} \\ a_{k,n} & \Delta N_{k,n+1} \end{bmatrix} \begin{matrix} \rightarrow \\ \rightarrow \\ \rightarrow \\ \rightarrow \end{matrix} \begin{Bmatrix} a_{k,1} \\ \bullet \\ a_{k,n} \\ a_{k,n+1} = ? \end{Bmatrix} \tag{3.19}$$

In Eq. (3.19), the first subscript 'k' symbolizes the data from different specimens. Contrary to the direct crack growth prediction, for crack growth rate prediction it is not necessary to consider the number of fatigue cycles elapsed (ΔN) between n^{th} and $(n+1)^{th}$ damage level. The equivalent input-output relation for crack growth rate prediction has been depicted in

Eq. (3.20).

$$\begin{bmatrix} a_{k,0} \\ \bullet \\ a_{k,n-1} \\ a_{k,n} \end{bmatrix} \rightarrow \begin{Bmatrix} (\frac{da}{dN})_{k,1} \\ \bullet \\ (\frac{da}{dN})_{k,n} \\ (\frac{da}{dN})_{k,n+1} = ? \end{Bmatrix} \tag{3.20}$$

3.3.2. One-step ahead future damage state prediction

One-step ahead damage state such as crack length or crack growth rate are predicted using the input-output relation depicted in Eq. (3.19) or in Eq. (3.20). Both GP interpolation and extrapolation is performed to predict future damage states. The details of the numerical results are discussed in the following subsections.

3.3.2.1. *Gaussian process interpolation: crack growth prediction inside the training horizon*

Gaussian process interpolations are performed by training the GP predictive model with fatigue test data from the entire fatigue envelope (or cycles) within which the test case prediction are performed. Two different cases are studied. First, crack growth data (up to 40 kcycles) from all the 30 specimens (Figure 3.3) are used for training the GP model and then to predict the same data set within 40 kcycles. For the second case, crack growth data (up to 40 kcycles) from specimen number 1 to 29 are used for training the GP model and then the trained GP model is used to predict the crack growth (up to 40 kcycles) of specimen number 30. The first case prediction is performed to check how efficiently the GP model can regenerate the overall scatter of the original crack growth curves. Figure 3.13 shows the corresponding overlapped prediction results from all 30 specimens. It is to be noted that in the overlapped plot there are 30 different mean crack growth predictions and their individual 2σ band around their predicted mean crack length.

The individual 2σ band includes both modeling error as well as the contribution of scatter due to micro-structural variability. The scatter from microstructural variability is modeled by the GP hyperparameter $\theta_{scatter}$ discussed previously in the theoretical sections. Without considering scatter contribution, the corresponding mean prediction and their associated 2σ error band is shown in Figure 3.14. Comparing the mean prediction and actual crack growth as shown in Figure 3.14 it can be seen that the GP model can regenerate the overall scatter of crack growth curves. Also, from the 2σ error band shown in Figure 3.14, which only includes the modeling error it can be found that (up to 40 kcycles) the modeling error is quite minimal. To further check the correctness of GP prediction a second interpolation type prediction is performed. For this purpose crack growth data from specimen number 1 to 29 (up to 40 kcycles) are considered for training the GP model and the crack growth of specimen number 30 is predicted within 40 kcycles. The predicted mean crack growth and the associated 2σ band is shown in Figure 3.15. It is to be noted that the 2σ band in this figure includes contributions from modeling error as well as contribution from estimated scatter (represented by hyper parameter $\theta_{scatter}$). The corresponding 2σ band contributed only by modeling error is shown in Figure 3.16. From this Figure it can be seen that there is a good correlation between actual and predicted crack length. In addition, it is found from the 2σ band that the modeling error contribution is minimal. It is to be noted that with difference to the previous interpolation case, where the training data set and test data set are from the same specimens, in this interpolation case the test specimen (here for specimen. number -30) is different from the training specimens (here for specimen. number -1 to 29).

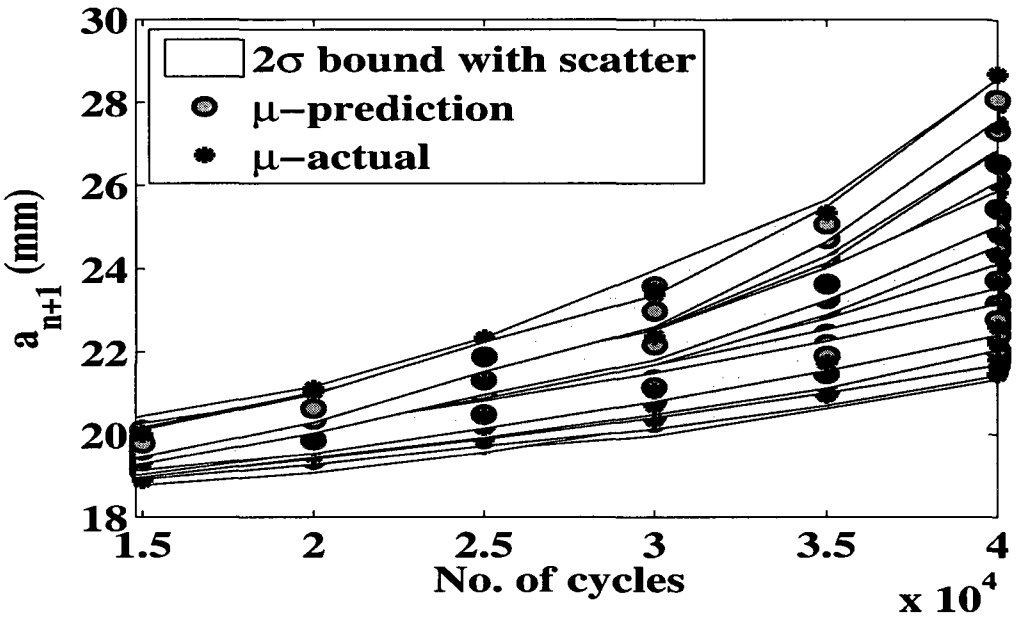

Fig. 3.13. Gaussian process prediction (up to 40kcycle) for all 30 specimen considering training data from all 30 specimens. The 2σ error bound includes contribution from both modeling error as well as from the scatter hyperparameter

3.3.3. Gaussian process extrapolation: prediction outside the training horizon

Previously GP prediction showed within the training horizon i.e., within the fatigue cycle up to which point training data was available. The extrapolation capability of the GP model beyond the training regime is presented in this section. Crack growth data up to 40 kcycles obtained from all 30 specimens are used to train a GP model. Then, using this GP model the one-step ahead prediction is performed for three different specimens beyond 40 kcycles and up to total failure. Figure 3.17 shows the corresponding mean prediction and the associated 2σ confidence band. The figure shows that the trend of the predicted mean crack length follows the actual crack growth curves. However, from the figure it can be seen that there is a larger discrepancy between predicted mean and actual crack length

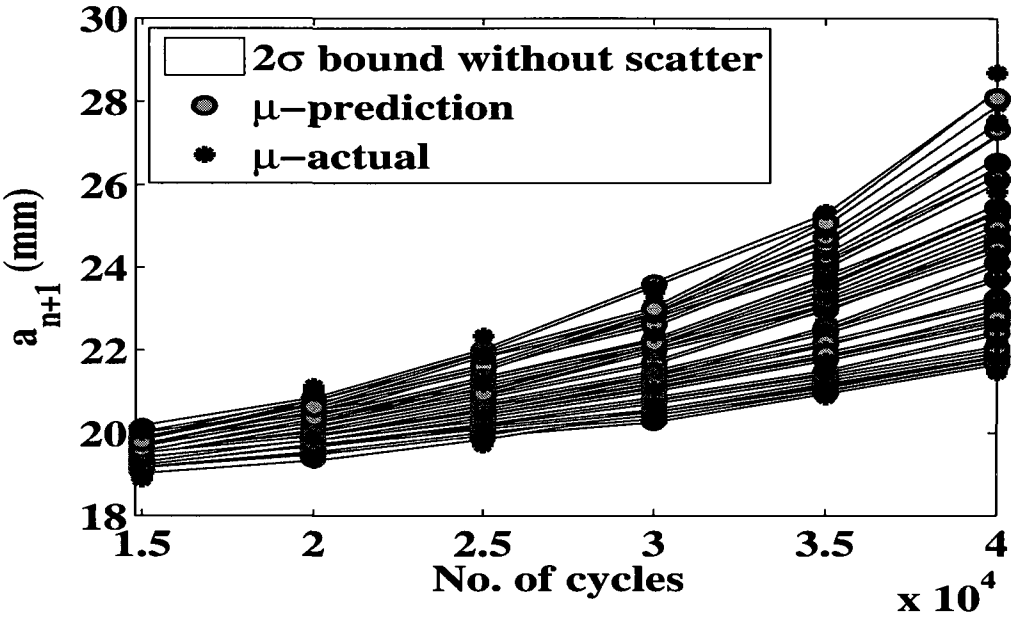

Fig. 3.14. Gaussian process prediction (up to 40kcycle) for all 30 specimens considering training data from all 30 specimens. The 2σ error bound includes contribution only from modeling error

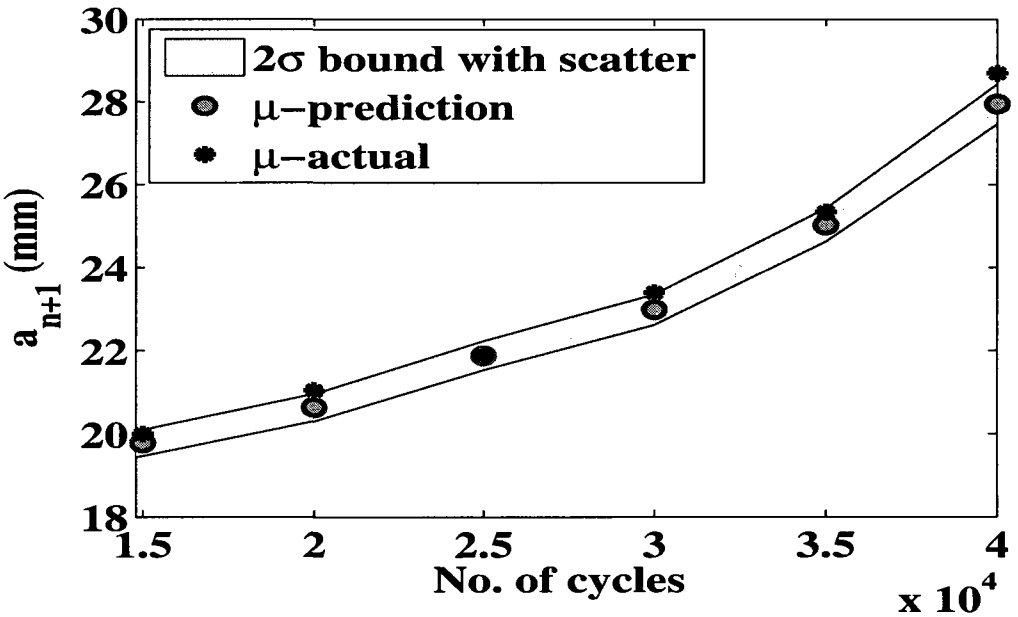

Fig. 3.15. Gaussian process prediction (up to 40kcycle) for specimen no 30 considering training data from specimen number 1-29. The 2σ error bound includes contribution from both modeling error as well as from the scatter hyperparameter

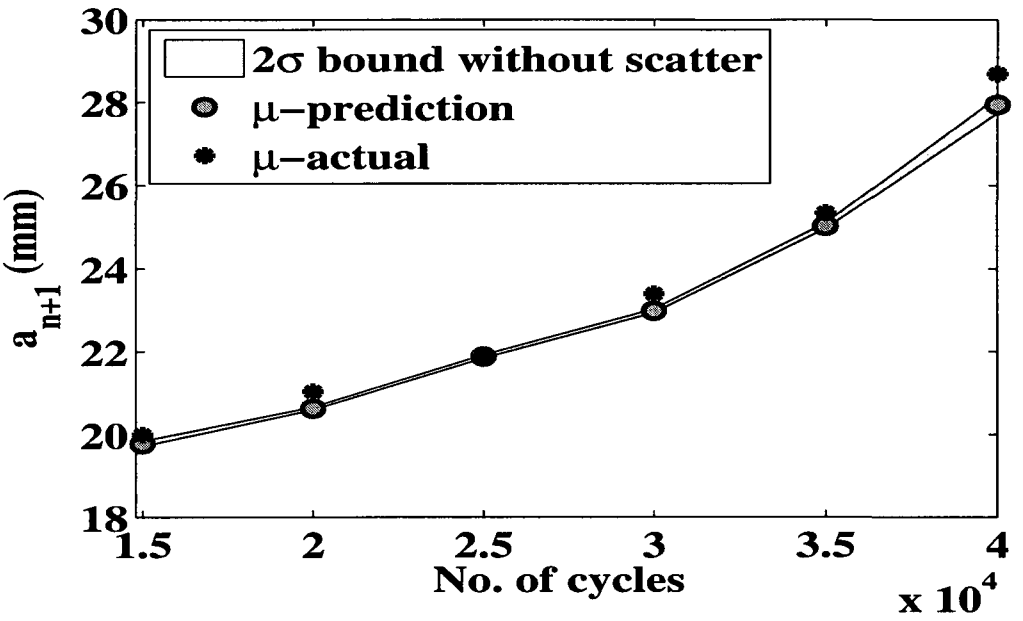

Fig. 3.16. Gaussian process prediction (up to 40kcycle) for specimen number 30 considering training data from specimen number 1-29. The 2σ error bound includes contribution only from modeling error

in the extrapolation regime than in the interpolation regime. This can be attribute to two major reasons. First, there was no training data available in the extrapolation regime, which leads to the discrepancy. The second cause is that the training data was available in a more stable or linear regime, and prediction was performed in an unstable and in a nonlinear damage growth regime without having any prior information. This is more evident from the bottom most crack growth curve shown in Figure 3.18. From the figure it can be seen that from 40 kcycles to 60 kcycles the bottom most curve follows a stable crack growth regime, and there is good correlation between predicted and actual crack growth in this regime. After 60 kcycles it is observed that damage propagation becomes more unstable and the predicted crack growth deviates increasingly from the actual value. Also, comparing Figure 3.17 with Figure 3.18 it can be seen that the width of the 2σ confidence

band does not change much in the extrapolation regime even after removing the scatter contribution from the confidence band. In other words the modeling error contributes more significantly to the 2σ confidence band in the extrapolation regime. Such discrepancy in prediction can be reduced by including at least one data set that encompasses the entire fatigue damage envelope to the training set. To verify the above claim one data set beyond 40 kcycles and up to total failure (in this case the bottom most crack growth curve shown in Figure 3.17) is added to the previously mentioned training data set. The corresponding prediction for two different specimens for their entire fatigue life is shown in Figure 3.19. This figure shows the 2σ confidence band with both modeling error and scatter contribution. The corresponding 2σ confidence band with only modeling error contribution is shown in Figure 3.20. Comparing both the figures it can be seen that not only the mean prediction better matches the actual value, but also the width of 2σ confidence band drastically reduces due to reduced modeling error. Similar approaches can be followed to predict damage in real-life situations for which at least one data set is available for the entire fatigue regime. For example, majority of aircraft manufacturers performs at least one full scale fatigue test for the study of fatigue properties of its critical components. These full scale fatigue test data can be used for on-board or real-time damage prediction.

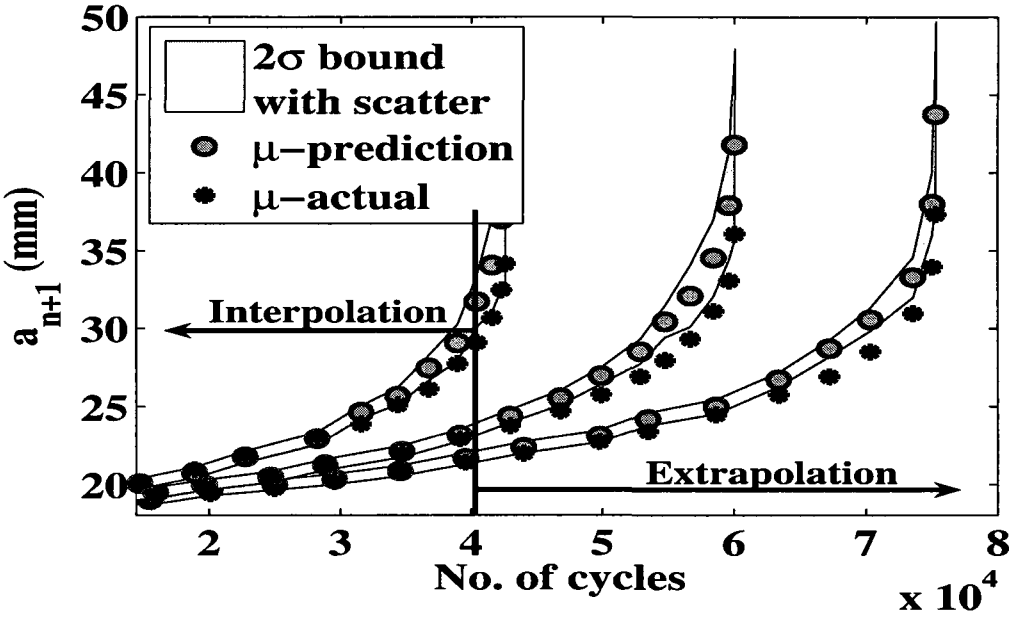

Fig. 3.17. Gaussian process prediction (before and after 40 kcycle) for 3 specimens considering training data from other 27 specimens (only up to 40 kcycle). The 2σ error bound includes contribution from both modeling error as well as from the scatter hyperparameter

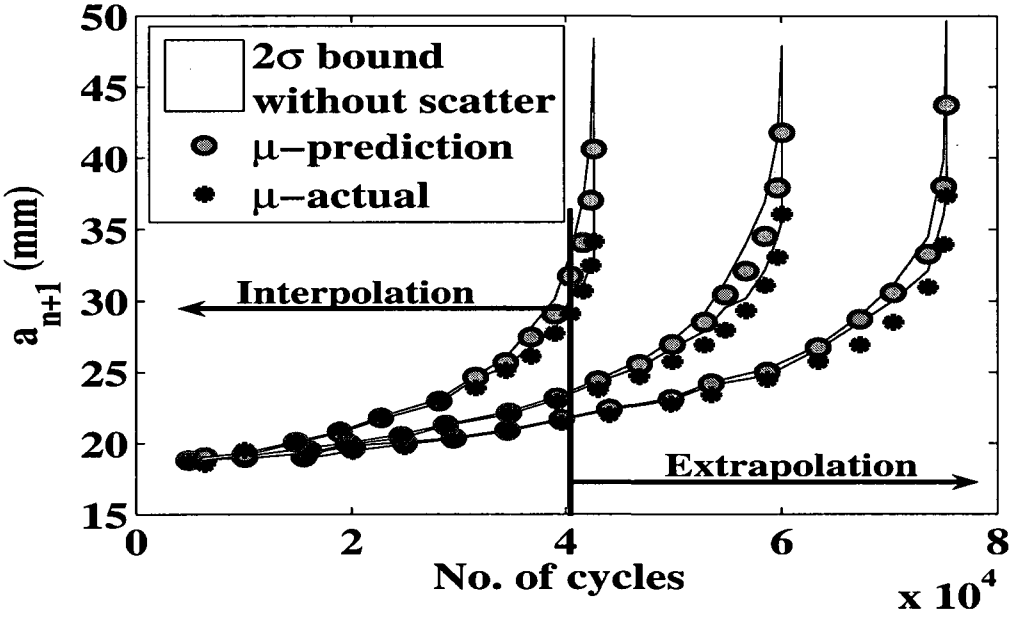

Fig. 3.18. Gaussian process prediction (before and after 40 kcycle) for 3 specimens considering training data from other 27 specimens (only up to 40 kcycle). The 2σ error bound includes contribution only from modeling error

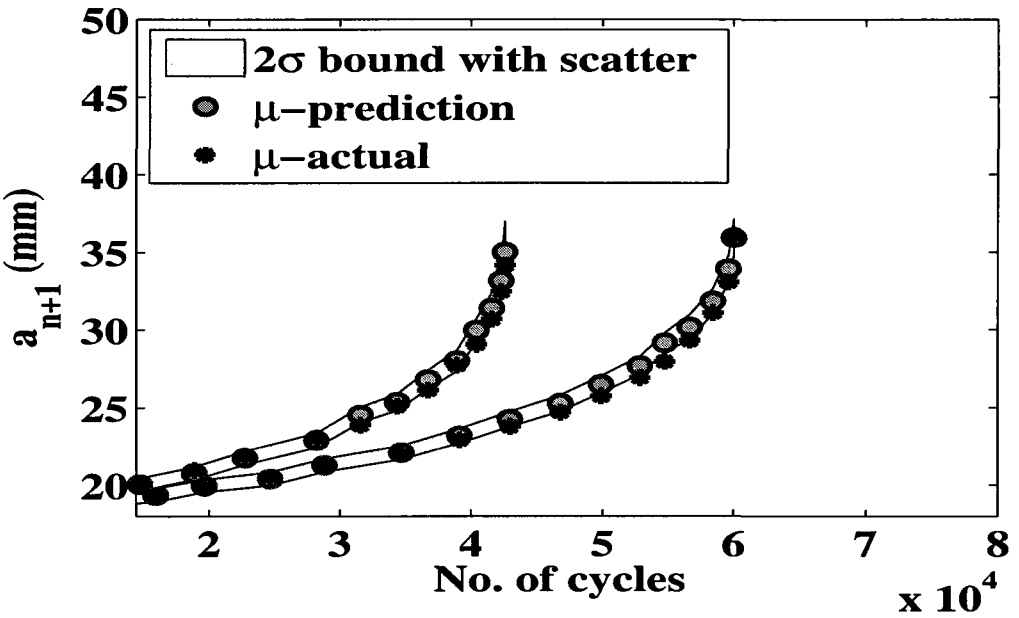

Fig. 3.19. Gaussian process prediction (before and after 40 kcycle) for 2 specimens considering training data from other 27 specimens (only up to 40 kcycle) and one specimen beyond 40 kcycle. The 2σ error bound includes contribution from both modeling error as well as from the scatter hyperparameter

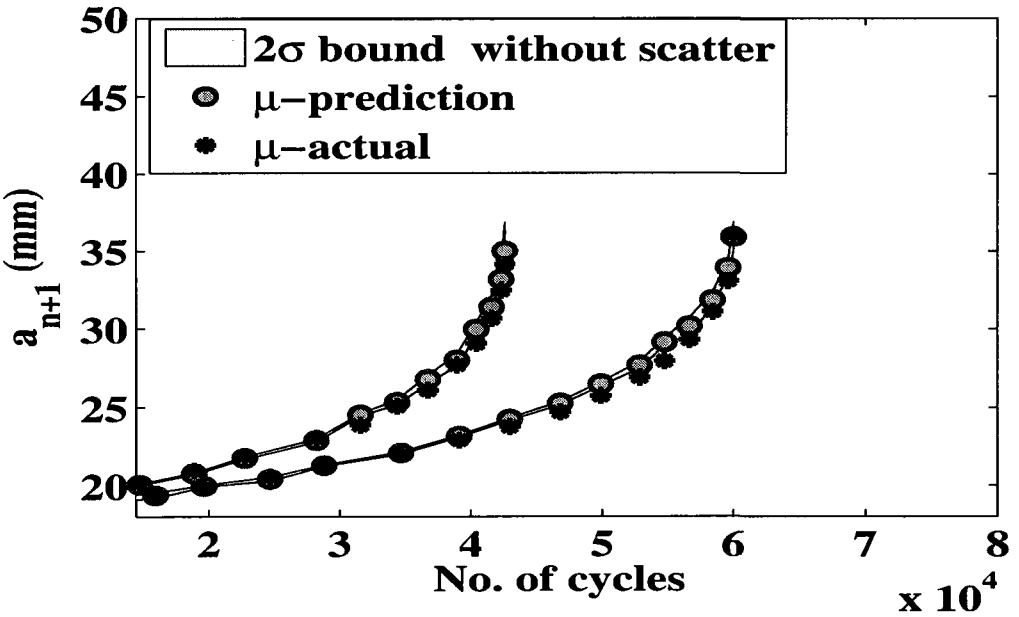

Fig. 3.20. Gaussian process prediction (before and after 40 kcycle) for 2 specimens considering training data from other 27 specimens (only up to 40 kcycle) and one specimen beyond 40 kcycle. The 2σ error bound includes contribution only from modeling error

3.3.3.1. *Crack growth rate prediction*

Similar to the direct crack growth prediction, GP model can be used to predict one-step ahead crack growth rate i.e $((\frac{da}{dN})_{n+1})$ at $(n+1)^{th}$ damage level. For crack growth rate prediction, input-output relation given by Eq. (3.20) can be used. Two crack growth rate prediction cases are discussed. First, is the GP interpolation, where the GP model is used to predict crack growth rate within the training horizon. In the second case, the GP model is used to extrapolate crack growth rate outside the training horizon. For the interpolation case the GP model is trained using the crack growth data from all 30 specimens up to 40 kcycles. The corresponding maximum crack length is approximately 28 mm (refer Figure 3.3). Using this trained GP model crack growth rates are predicted for one specimen beyond 40 kcycles up to final failure. The corresponding crack lengths (a_n) versus predicted mean crack growth rates $((\frac{da}{dN})_{n+1}))$ are shown in Figure 3.21. This figure also shows the 2σ confidence bound that includes both modeling error as well as contribution from scatter. Although from the figure it can be seen that there is a good correlation between predicted and actual rate below the crack length of 28 mm (equivalent to 40 kcycles), there are larger discrepancies in the extrapolation regime, which is beyond the crack length of 28 mm. This is more evident from the larger 2σ confidence band in the extrapolation regime as seen in Figure 3.22. It is noted that the confidence band shown in Figure 3.22 is only accounts for modeling error. Similar to the case of direct crack growth prediction, GP model capability for crack growth rate prediction can be improved by including at least one complete (up to failure) fatigue test data set in the training data set. For the present case the complete crack growth data of a specimen (in this case the bottom most crack growth curve data as seen in Figure 3.17) is added to the previously mentioned training set (that includes

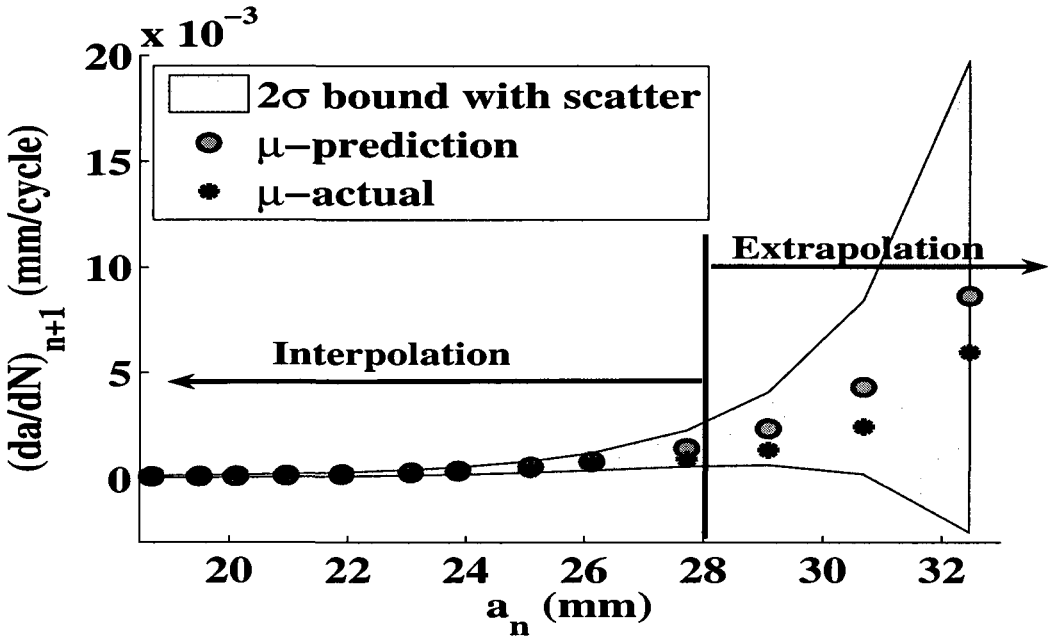

Fig. 3.21. Gaussian process crack growth rate prediction of a specimen considering training data from all 30 specimens (only up to 40 kcycle). The 2σ error bound includes contribution from both modeling error as well as from the scatter hyperparameter

crack growth data of all specimens up to 40 kcycles). The corresponding GP crack growth rate prediction is depicted in Figure 3.23. This figure also shows the 2σ confidence band with contribution from both modeling error as well as from scatter hyperparameter. The 2σ confidence band with only contribution from modeling error is shown in Figure 3.24. Comparing Figures 3.23 and 3.24 with Figures 3.21 and 3.22, it can be seen that inclusion of one full scale fatigue data drastically reduces the 2σ confidence band attributed to modeling error.

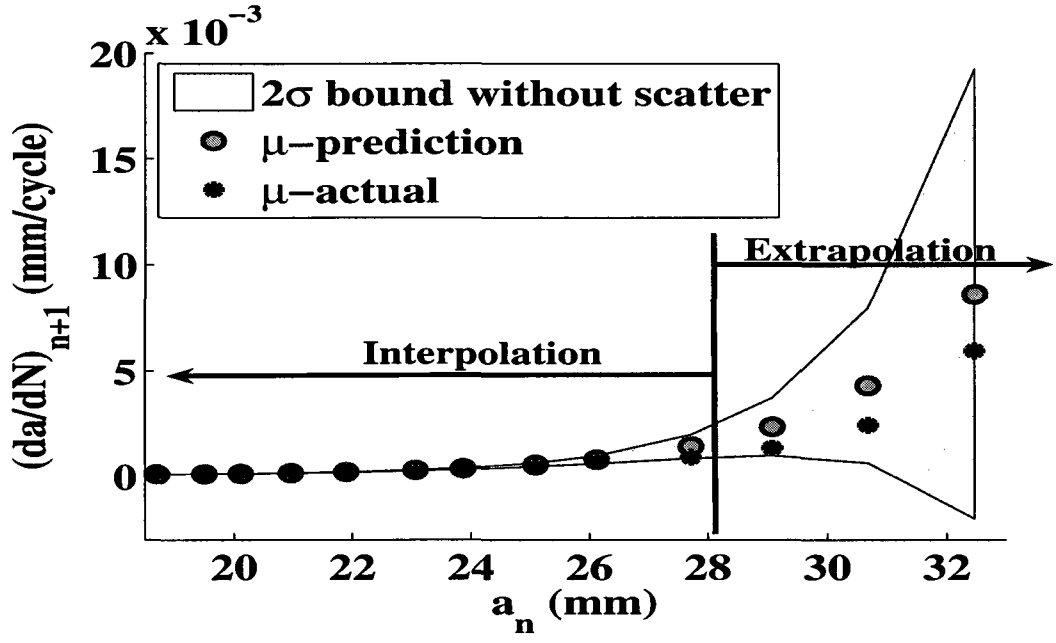

Fig. 3.22. Gaussian process crack growth rate prediction of a specimen considering training data from all 30 specimens (only up to 40 kcycle). The 2σ error bound includes contribution only from modeling error

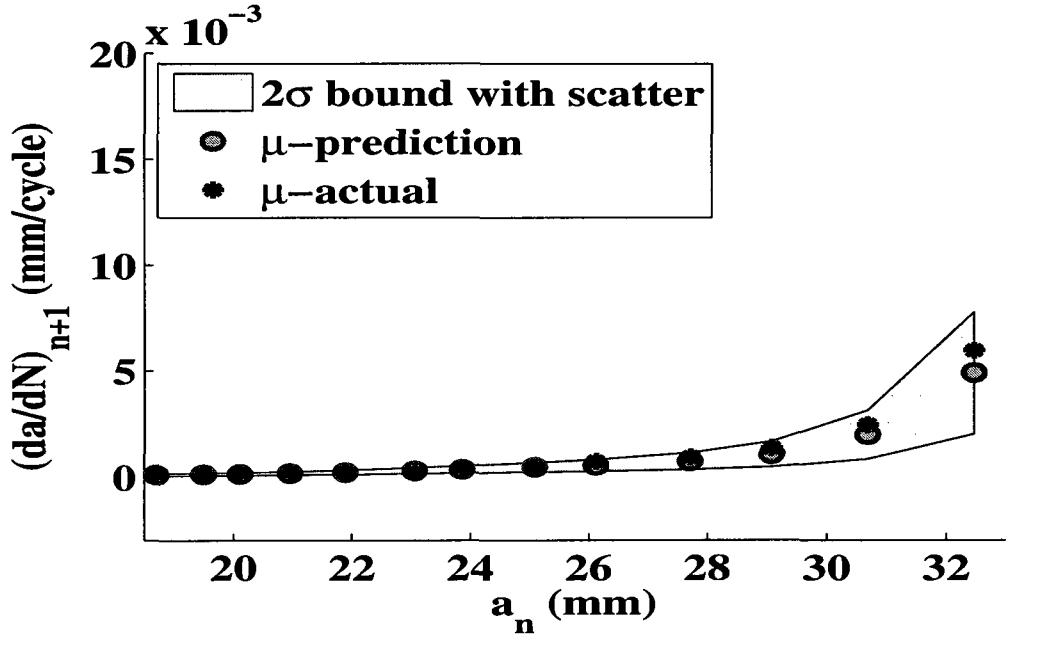

Fig. 3.23. Gaussian process crack growth rate prediction of a specimen considering training data from other 30 specimens (only up to 40 kcycle) and one specimen beyond 40 kcycle. The 2σ error bound includes contribution from both modeling error as well as from the scatter hyperparameter

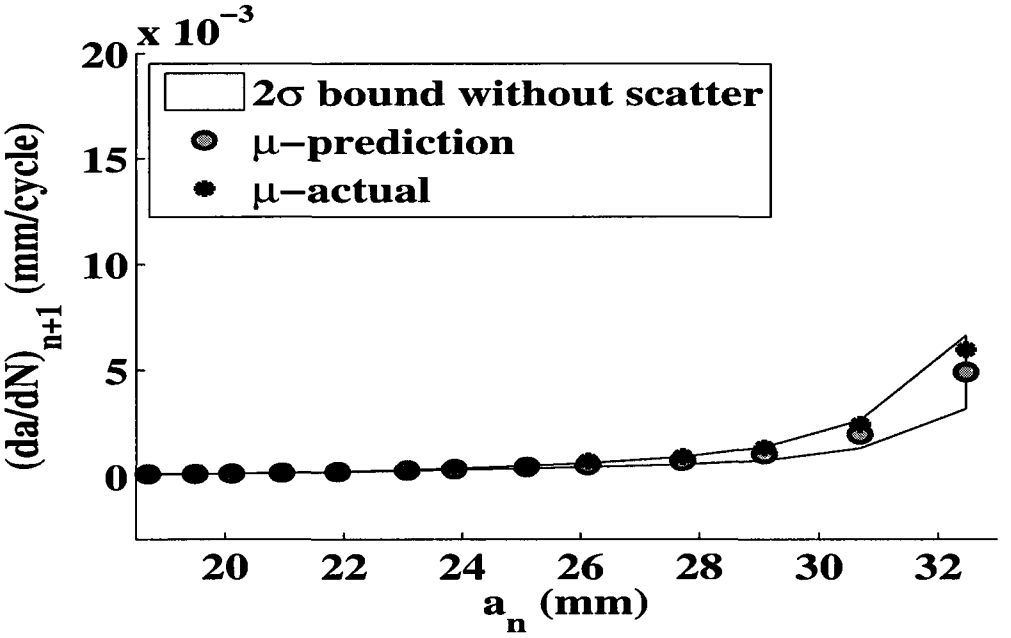

Fig. 3.24. Gaussian process crack growth rate prediction of a specimen considering training data from other 30 specimens (only up to 40 kcycle) and one specimen beyond 40 kcycle. The 2σ error bound includes contribution only from modeling error

3.4. Conclusion

A GP approach has been developed for the one-step ahead prediction of fatigue damage states. The GP model is validated on constant cyclic fatigue test data available in the literature. From the numerical study it is found that pdf of original crack growth data more resembles log-normal distribution than pdf of Gaussian distribution. Hence to suit the GP model the original crack growth data transformed to normal distribution data by performing appropriate log scaling. In addition GP model is validated for future step prediction of crack growth or its rate. From the GP prediction model it is found that there is a good correlation between predicted damage states and its actual experiment value. The prediction results indicate that the GP is able to capture the nonlinear dynamics of the fatigue crack growth propagation mechanisms. Furthermore, it is observed that, the

performance of the GP predicted can be drastically improved by including at least one data set over the entire fatigue life to the training data set. The GP model is a Bayesian statistics based model that can incorporate material scatter in the modeling process. Also being a data driven approach it can easily model complex geometry and loading condition, which will be discussed in the following chapter. Furthermore, the proposed GP model is computationally inexpensive compared to any finite element based damage model. Hence the proposed GP model can easily be implemented in on-board system for real-time damage prediction.

CHAPTER 4

Offline Damage State Prediction of Complex Structure under Complex State of Loading

4.1. Introduction

In the chapter 3 fatigue damage prediction under constant cyclic loading was discussed. However, aircraft structural components are required to achieve long lives under demanding operational conditions consisting of highly complex and variable spectrum loading. Traditionally, the design of aircraft structural components against fatigue loading has been based on an estimated load spectrum using some form of damage accumulation rule, usually a modification of Miner's rule [51]. Miner's rule is applied using S N diagram based on different constant amplitude fatigue tests. It is widely accepted that constant amplitude loading insufficiently represents the intrinsic dynamic behavior (such as transient loading effects in the fatigue crack growth rates) that occur with variable amplitude service loading [100]. For example, constant amplitude loading, can not simulate a service load history, such as for aircraft wing structures subjected to random gust load. Consequently, accurate fatigue predictions are unlikely because the available constant cycle fatigue test data are not truly representative of the in service loading. The application of flight condition tests to fatigue problems is becoming a widespread procedure both in the aircraft industry [67] and in aeronautical research laboratories [101]. For several reasons the flight condition test has replaced the conventional fatigue test with a constant mean load and a constant load amplitude (usually indicated as a 'constant amplitude test') [101]. The most important reason being the load/time history in a flight condition test can be a more realistic simulation of the load history in service. However, the definition of a load/time profile for a flight condition test is not as simple as it is for a constant amplitude test load profile and load sequences have to be specified. Two standardized load histories for aircraft wings

were developed in recent years. The load history Transport Wing Standard (TWIST) was proposed as representative of the wing tension skin of a transport aircraft [102]. Fighter Aircraft Loading STAndard For Fatigue (FALSTAFF), is typical to the wing root area of a fighter-type aircraft [103, 92]. Both of these random flight profile load histories are widely used in numerous fatigue research programs. Though a significant amount of research has been reported [89, 100, 101] on fatigue life modeling under random and flight profile loading, a majority of these models are based on standard test coupons [104]. A common practice in aerospace applications such as in the case of fatigue life modeling of C-130 aircraft [67] is to use the coupon test crack growth model, but augmented with real initial flaw size that is directly estimated either from the individual component fatigue test or from the full scale fatigue test of the entire aircraft. The crack growth models are based on stress intensity factors [57]. It is to be noted evaluation of stress intensity factor for each and every critical structure is a nontrivial task. Due to the unavailability of stress intensity factor data for a complex structure, its future life is often estimated by over simplifying the geometry. Thus the crack growth model of the real structure is approximated using the crack growth model of standard coupons. However for complex structure the damage initiation and growth pattern can be different from the coupon structure. Although finite element (FE) based crack growth model [105] can be used to model complex structures, currently there is no single FE based damage propagation model available that can be useful in real-time on-board applications. The major drawback in FE based physics models is due to the high computational requirements that make it unsuitable for on-board applications. To avoid the problem in FE based approach, probabilistic data driven approach such as Gaussian process [83, 81, 82, 84] can be used to model the fatigue damage growth. The details of the

approach are presented next.

4.2. Theoretical Approach

Damage propagation in complex structure under any real-life random loading can be modeled using the Gaussian process (GP) approach. Recall that a GP model was used to model the constant cyclic and uniaxial fatigue loading in chapter 3. However, in the present case, the same GP model is used to model the fatigue damage under variable cyclic as well as multi-axial fatigue loading. For the multiaxial (in this case biaxial) random loading case with target or function value being crack length ($a_{(\bullet)}$), the input-output relation can be expressed as follows.

$$\begin{bmatrix} a_{k,0} & U^{\max}_{x_{k,1}} & U^{\min}_{x_{k,1}} & U^{\max}_{y_{k,1}} & U^{\min}_{y_{k,1}} & dN_{k,1} & \bullet \\ \bullet & \bullet & \bullet & \bullet & \bullet & \bullet & \bullet \\ a_{k,n-1} & U^{\max}_{x_{k,n}} & U^{\min}_{x_{k,n}} & U^{\max}_{y_{k,n}} & U^{\min}_{y_{k,n}} & dN_{k,n} & \bullet \\ a_{k,n} & U^{\max}_{x_{k,n+1}} & U^{\min}_{x_{k,n+1}} & U^{\max}_{y_{k,n+1}} & U^{\min}_{y_{k,n+1}} & dN_{k,n+1} & \bullet \end{bmatrix} \rightarrow \begin{Bmatrix} a_{k,1} \\ \bullet \\ a_{k,n} \\ a_{k,n+1} = ? \end{Bmatrix} \quad (4.1)$$

In the above expression $U^{\max}_{x_{(\bullet)}}$, $U^{\min}_{x_{(\bullet)}}$, $U^{\max}_{y_{(\bullet)}}$, $U^{\min}_{y_{(\bullet)}}$ symbolize the X-axis maximum and minimum and Y-axis maximum and minimum load at different fatigue cycle, respectively. Also, $dN_{(\bullet)}$ symbolizes the number of fatigue cycles elapsed between the current and forward step damage level. Furthermore, the fatigue affecting parameters should be a measurable quantity and should be time variant. If these parameters are time invariant, from a statistical modeling perspective, there would be no need to consider these parameters. Equation 4.1 represents a generic input-output framework. Other fatigue affecting parameters such as temperature and humidity can also me modeled in to the input-output framework given by Eq. (4.1). However, in the present work, the test was performed under laboratory condition with minimal change in temperature and humidity change, and hence not considered in the

present formulation. Once the input-output variables are known, a similar procedure as discussed in chapter 3 can be used to model the multivariate fatigue damage process. The major difference between the procedure used in the previous chapter and the present chapter is the individual row of the input matrix as shown in the left side of the Eq. (4.1). In the present biaxial random loading case for example at n^{th} damage level the corresponding input vector $x_{i=n}$ is given by $x_n = \{a_n, U^{\max}_{x_{n+1}}, U^{\min}_{x_{n+1}}, U^{\max}_{y_{n+1}}, U^{\min}_{y_{n+1}}, dN_{n+1}\}$. Whereas, for uniaxial constant cyclic case since the mean load does not vary and the loading is uniaxial, the corresponding input vector is denoted as $x_n = \{a_n, dN_{n+1}\}$ in chapter 3.

4.3. Numerical Results

4.3.1. Fatigue experiment and data collection

Numerical tests are conducted and results are presented to demonstrate the validity of the developed data driven approach for any load patterns. To validate the prognosis algorithm, three fatigue tests were performed on an Al-2024-T351 cruciform specimen under biaxial loading. The loaded cruciform specimen in an MTS biaxial fatigue test frame can be seen in Figure 4.1. The specimens were subjected to either random loading or flight profile FALSTAFF [103, 92]. To generate the correct load pattern, first finite element stress analysis was performed to evaluate the yield stress. The geometry of a typical cruciform specimen and the finite element stress analysis contour plot is shown in Figure 4.2. From the stress analysis results, the yield load was found to be 7200 lbf. Based on this limiting yield load both random and FALSTAFF flight profile load patterns were generated. The original patterns were generated using MATLAB and then coded to the MTS controller. A typical one block (equivalent to 300 cycles) of original random load pattern is shown in Figure 4.3. Also a typical four block (equivalent to 308 cycles) FALSTAFF loading profile is

shown in Figure 4.4. It is to be noted that for random loading case all blocks are nonrepetitive, i.e. individual blocks are different from each other. However, for FALSTAFF loading all blocks are repetitive. The random loading patterns were generated using MATLAB random number generation command, keeping a maximum load limitation equal to 80% of the yield load (i.e. 7200 lbf) and a minimum load limitation of equal 6.6% of the yield load. For the FALSTAFF loading case the normalized FALSTAFF profile presented by Schijve, et. al. [7] is modified, keeping a maximum load limitation equal to 80% of the yield load and a minimum load limitation equal to 6.6% of the yield load. Additionally, to speed up the fatigue process the extreme low loads in original FALSTAFF profile were augmented with additional load. For this reason, in the later parts of this chapter the flight profile load patterns are referred as modified FALSTAFF loading rather than FALSTAFF loading. The biaxial machine actuator was operated with a fixed frequency of 10 Hz. Both the x-axis actuator and y-axis actuator of the biaxial frame were subjected to in-phase fatigue loading. Moreover, a hole in the center of the specimen was made to create crack initiation in the web area of the cruciform specimen. To accelerate damage growth, an EDM notch of 1 mm length was made at the bottom right quadrant of the central hole (45^o to the vertical axis). A 48 channel NI PXI system was used to collect the MTS load cell (X and Y) measurements. A high resolution SONY camera was used to visually monitor the crack growth. The data acquisition system and the computer capturing the visual image were synchronized with the biaxial machine controller to collect the time synchronized data/ image at a specified interval of 300 cycles (one block) for the random load and 308 cycles (four blocks) for the modified FALSTAFF. Three specimens (named Cruciform-7, 8, 11) were tested with Cruciform-7 and 8 under random load and Cruciform-11 under modified

FALSTAFF. Although there was a central hole and an EDM notch, all specimens were fatigued under constant amplitude loading of 480-4800lbf to further accelerate the damage process. The constant cycle fatigue tests were performed for 20-30 kcycles to achieve a precrack of 1-3 mm. For the demonstration of the prognosis algorithm crack lengths were estimated at discrete instances (fatigue cycles). Also at those instances the X and Y-axis loads were estimated from the acquired load cell signals. It is noted that in real aircraft [3] the loads can be estimated from the real-time sensor (e.g. from pressure, altitude, weight sensors) measurements. In addition, following a standardized procedure, the estimated crack length and real-time loads are respectively normalized against the maximum crack length (experimentally found to be 72mm) and yield load (obtained from FE simulation as 7200 lbf). This procedure of load normalization will during integration of the present data sets with future generated data sets with similar or different loading conditions. The normalization of crack growth is performed to replace the current approach of visual measurement (for estimating the crack length) with the online structural health monitoring (SHM) based approach. Furthermore, majority of SHM algorithms define damage indices that vary between 0-1. The SHM model integration with the offline prognosis model will be discussed in the later part of this dissertation.

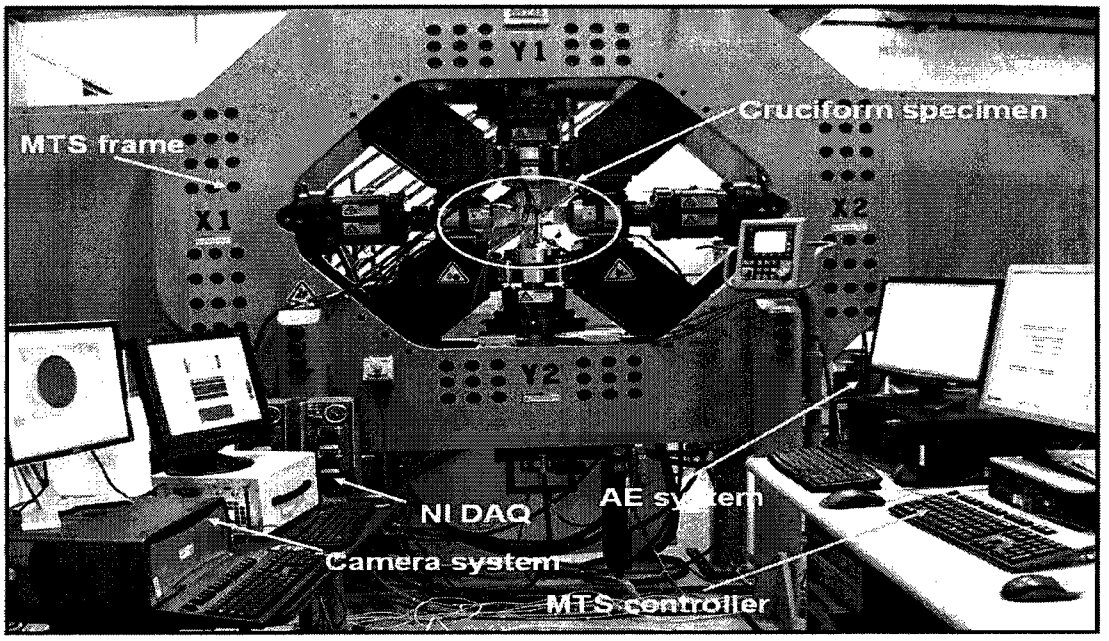

Fig. 4.1. Biaxial/Torsion Experimental set-up

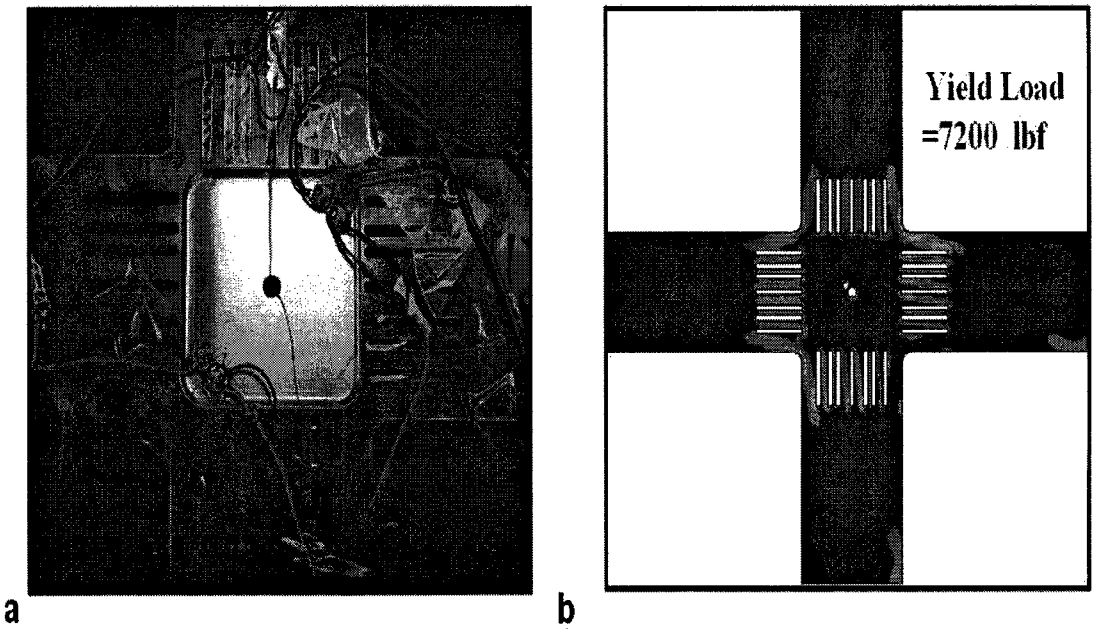

Fig. 4.2. a) Al-2024 cruciform specimen b) Stress analysis contour plot

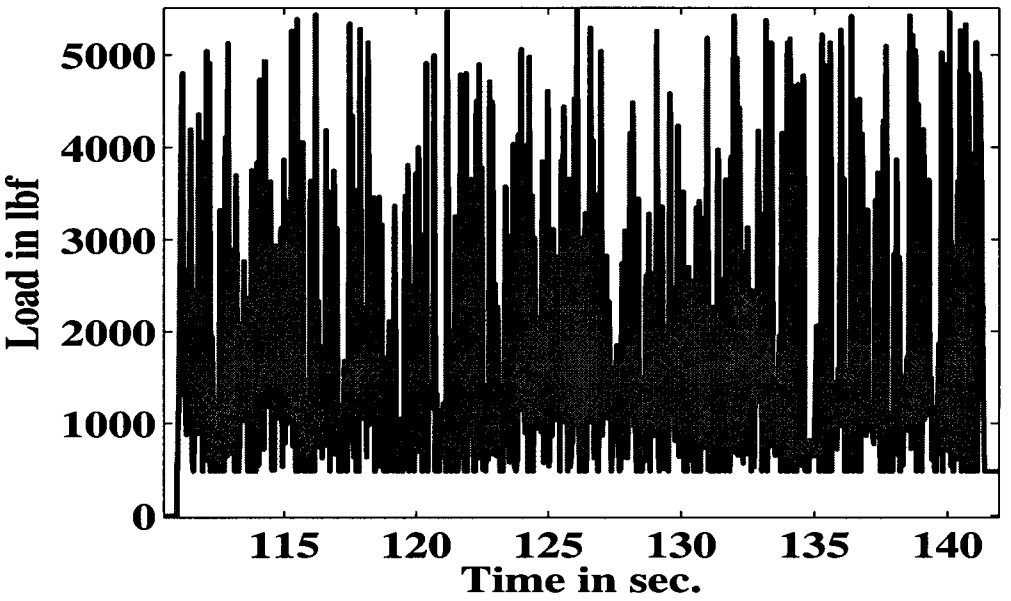

Fig. 4.3. One block (300 cycles) of random load

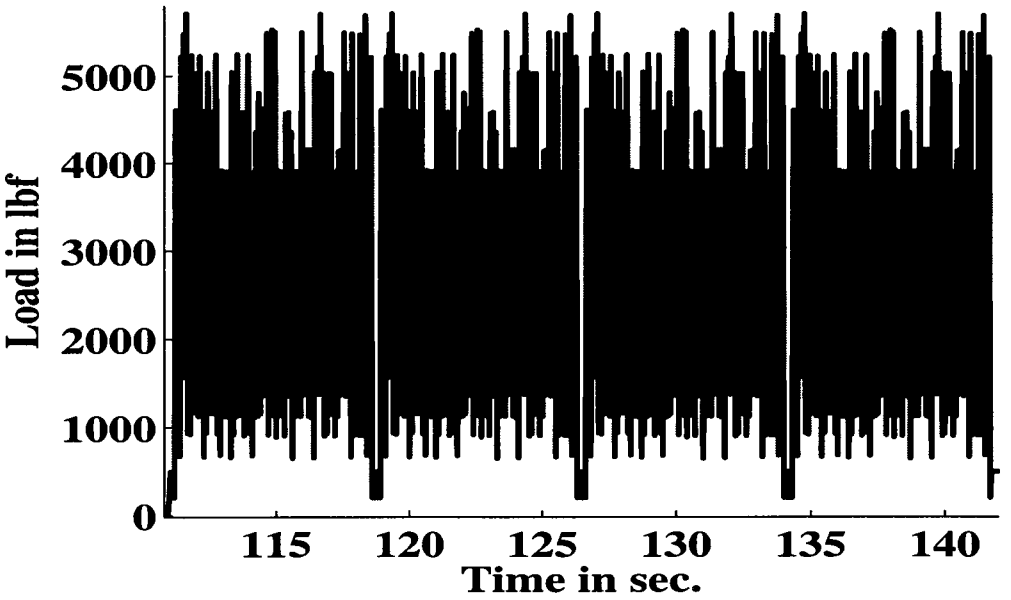

Fig. 4.4. Four blocks (308 cycles) of modified FALSTAFF load

4.3.2. One-step ahead future state prediction

The supervised Gaussian process damage predictions are performed for following three different cases.

1. Case-I: prediction under random loading with training data from a different specimen but tested under same random loading blocks.

2. Case-II: prediction under modified FALSTAFF loading with training data from a different specimen and tested under random loading.

3. Case-III: prediction under random loading with training data from a different specimen and tested under modified FALSTAFF loading.

Case-I: Two cruciform specimens (cruciform specimen 7 and 8) were tested under same random loading blocks. The fatigue test data acquired from cruciform 8 is considered for training the GP model. Whereas, data acquired from cruciform 7 is considered as test (or target) case. Figures 4.5 and 4.6 show the prediction results for cruciform 7 specimen. At individual damage instances (say at n^{th} damage level) the GP input space formed using six variables such as $n-1^{th}$ damage level damage state (a_{n-1}), n^{th} damage level X-axis maximum load ($U_{x_n}^{\max}$) , X-axis minimum load ($U_{x_n}^{\min}$), Y-axis maximum load ($U_{y_n}^{\max}$) , Y-axis minimum load ($U_{y_n}^{\min}$) and fatigue cycle interval (dN_n). The n^{th} damage level damage states, a_n, is considered as target. Also, as mentioned before, the damage states (here the crack lengths) in both input and output spaces are normalized against its maximum value i.e. approximately 72.0mm. The load measurements in input space are normalized against the yield load (i.e. 7200 lbf or 32027.2 N). Although the test data (both high resolution image and load cell measurements) are available in an interval of 300

cycles, only at discrete instances training and test cases are selected. This is because it is highly cumbersome to visually estimate the crack length from acquired images. The use of automated SHM technique, which is discussed in the later part of this dissertation, can alleviate this problem associated with manual/visual way of damage quantification. Using the trained GP model the one-step ahead predictions are performed for individual input space (or input condition) of cruciform 7. Figure 4.5 shows the training crack growth data as well the test case prediction (mean prediction). From the figure it can be seen there is a good correlation between mean prediction and mean actual crack length. All the predictions are performed in scaled domain of interval 0-1. Once the predictions are performed the damage states are scaled backed to its original scale (in mm). Figure 4.5 also shows the 2σ (95 %) confidence bound. It can be seen that all the mean predictions fall within the 2σ confidence bound. It is to be noted that the confidence bound shown in Figure 4.5 has contributions from both modeling error as well as from scatter or noise hyperparameter $\theta_{scatter}$ (refer chapter 3). Figure 4.6 shows 2σ confidence bound without considering the noise hyperparameter contribution. Comparison of Figure 4.5 and Figure 4.6 shows that the 2σ confidence bound due to only modeling error contribution is substantially less compared to 2σ confidence bound with both modeling error and noise contribution.

Case-II: The prediction is performed for cruciform specimen 11, which was fatigue tested under modified FALSTAFF loading. In this case, test data from cruciform specimen 8 was used to train the GP model. It is important to note specimen 8 was fatigued under random loading. Figures 4.7 and 4.8 show the corresponding prediction results. Figure 4.7 shows the training crack length data as well as the mean prediction and its associated 2σ (95 %) confidence bound (with both modeling error and noise hyperparameter contribution).

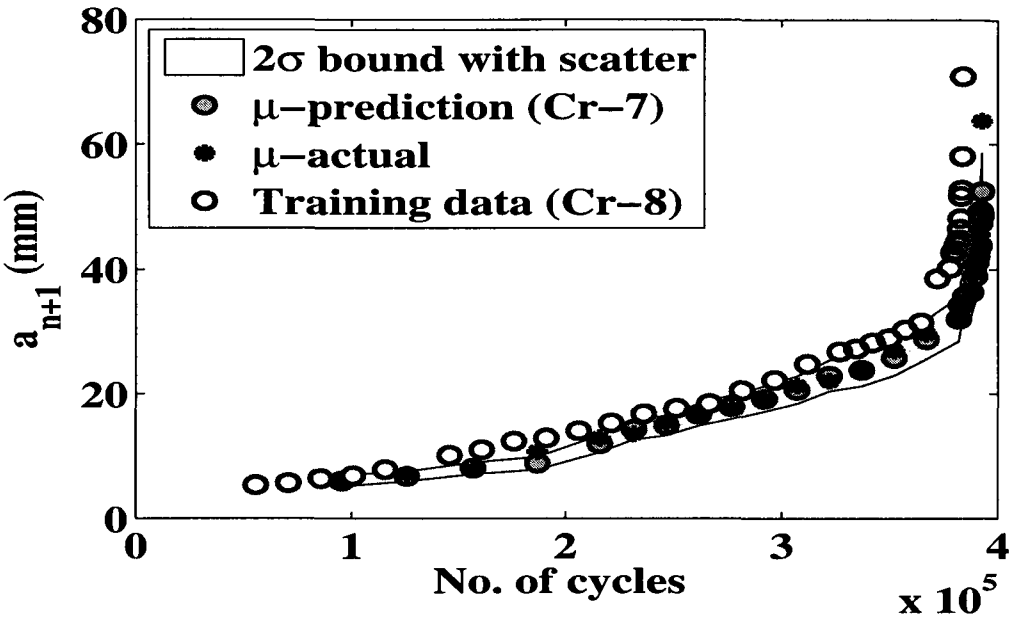

Fig. 4.5. Prediction under biaxial random loading with training data from random loading test (error bound includes the contribution from noise hyperparameter)

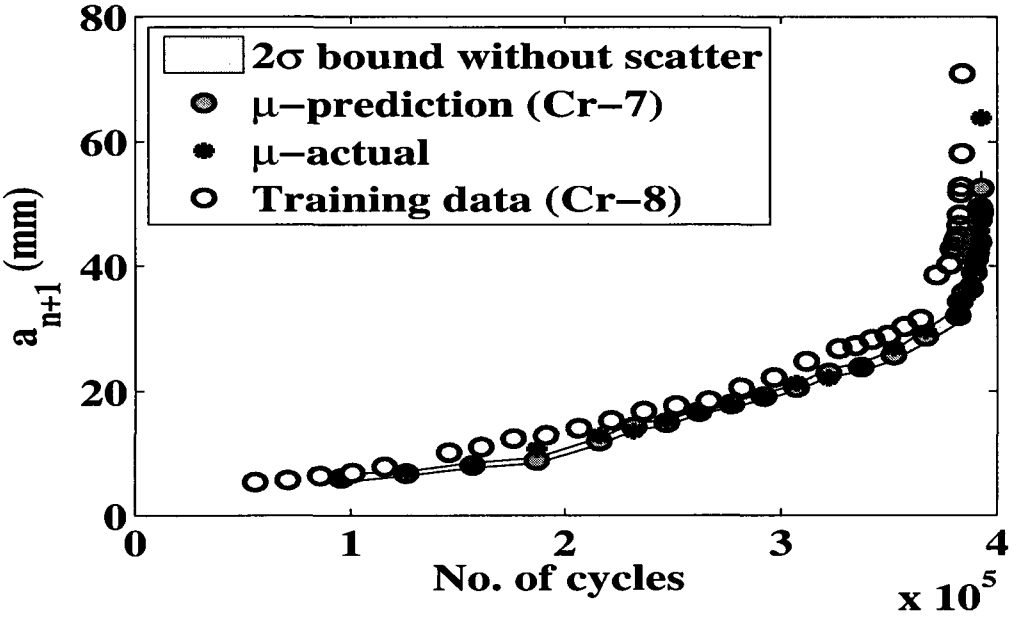

Fig. 4.6. Prediction under biaxial random loading with training data from random loading test (error bound does not include the contribution from noise hyperparameter)

Comparing the mean prediction with actual mean crack length it can be seen that there is a good correlation between actual and prediction as it was observed in the case I. Also, the 2σ (95 %) confidence bound without noise hyperparameter contribution can be seen in Figure 4.8. Comparing Figures 4.7 and 4.8 it can be seen that there is slightly narrower 2σ bound in the absence of noise compared to the case with noise contribution. However, compared to case I (for which both training and test loading cases are same), in this case the reduction in 2σ bound by removing the noise contribution is not significant. This implies modeling error mostly contributed to the 2σ confidence bound in case II. The comparatively larger modeling error contribution is due to a totally different test loading case compared to the training load case. This is closer to real-life situation, where one may not have the luxury of predicting a test case, for which a training data set that would be available. From Figure 4.8 it can be observed that though the 2σ bound is wider compared to the previous random loading prediction case, it is reasonably narrow. It can be seen that if the test loading patterns have similar loading cycles (not necessarily in the same order), as in case of training load case, the GP model is capable of predicting the unknown pattern for the test case. In the present case each block of modified FALSTAFF (refer Figure 4) has only 75 different loading cycles (or with 75 different load ratios) compared to the random loading case with much larger number of different load ratios. The random loading patterns are generated for each fatigue cycle differently by using the $MATLAB^{TM}$ random number generator. For a good GP prediction it is always better if the training data set has more number of different load patterns compared to the test case load patterns.

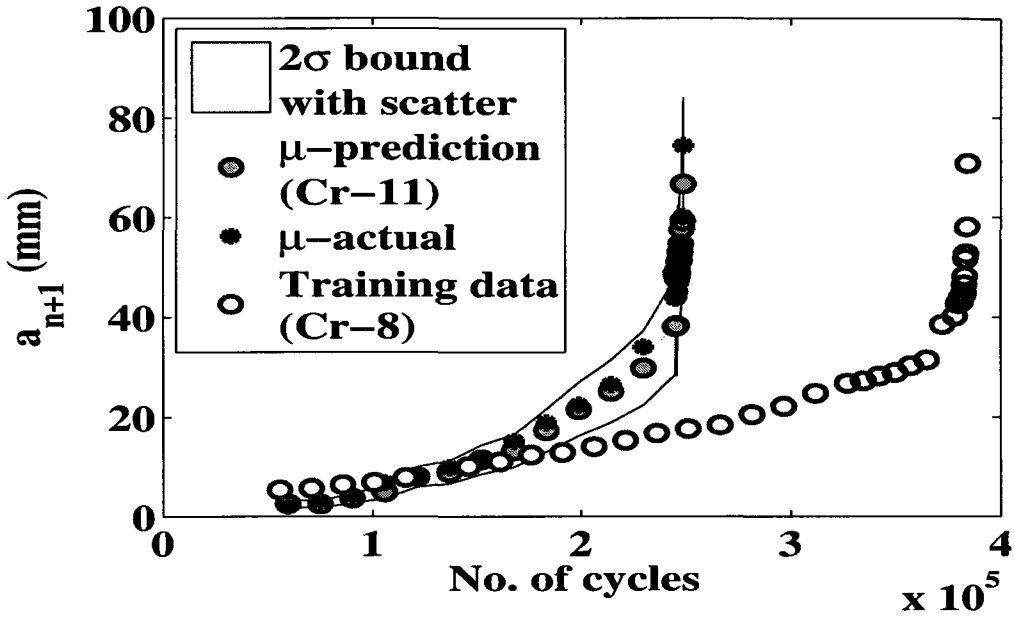

Fig. 4.7. Prediction under biaxial modified FALSTAFF loading with training data from random loading test (error bound includes the contribution from noise hyperparameter)

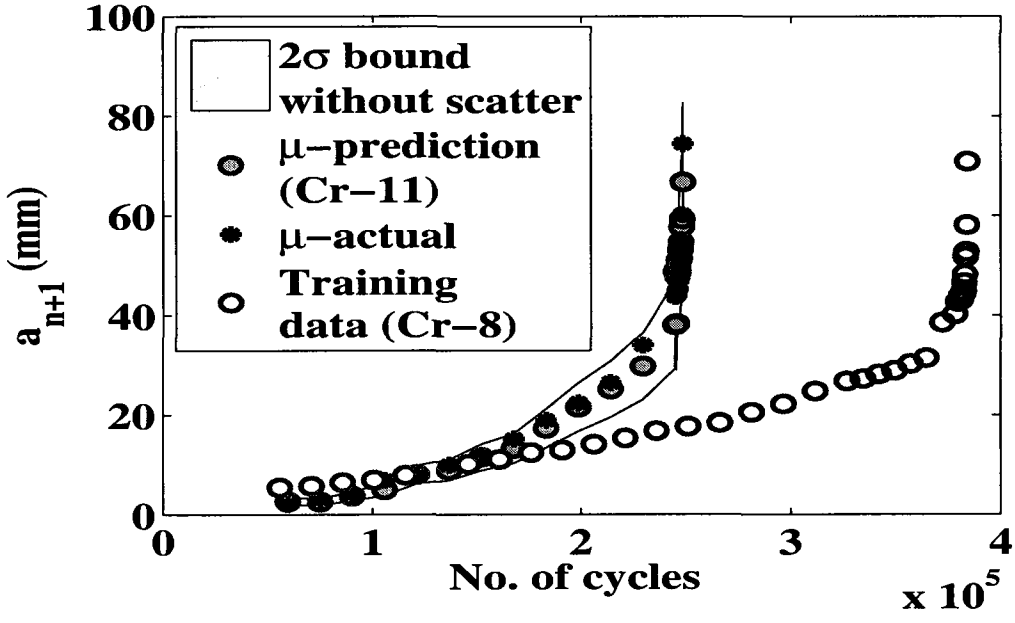

Fig. 4.8. Prediction under biaxial modified FALSTAFF loading with training data from random loading test (error bound does not includes the contribution from noise hyperparameter)

Case-III: In this case the prediction is performed for cruciform specimen 8 (tested under random loading) with training data from cruciform specimen 11 (tested under modified FALSTAFF loading). This is opposite of the previous prediction case (case II). The prediction results are shown in Figures 4.9 and 4.10. Figure 4.9 shows the training crack length data as well as the mean prediction and its associated 2σ (95 %) confidence bound (with noise hyperparameter contribution). Comparing the mean prediction with actual mean crack length it can be seen that there is not much correlation between actual and prediction as it was observed in the previous two cases. In addition, comparing prediction results for random loading case (refer Figure 4.5) and modified FALSTAFF case (refer Figure 4.7), the present prediction results (refer Figure 4.9) shows a much wider 2σ (95 %) confidence bound. The 2σ (95 %) confidence bound without noise hyperparameter contribution is shown in Figure 4.9. Comparing Figures 4.9 and 4.10 it can be seen that there is slightly narrower 2σ bound in case of without noise than with noise. This implies that the modeling error contribution in the 2σ confidences bound. is more significant. The cause for large modeling error is due to the use of modified FALSTAFF input-output data as training set data. As explained before, the modified FALSTAFF input-output data has less information compared to the random loading input-output data set. This leads to the inferior prediction of random loading damage states.

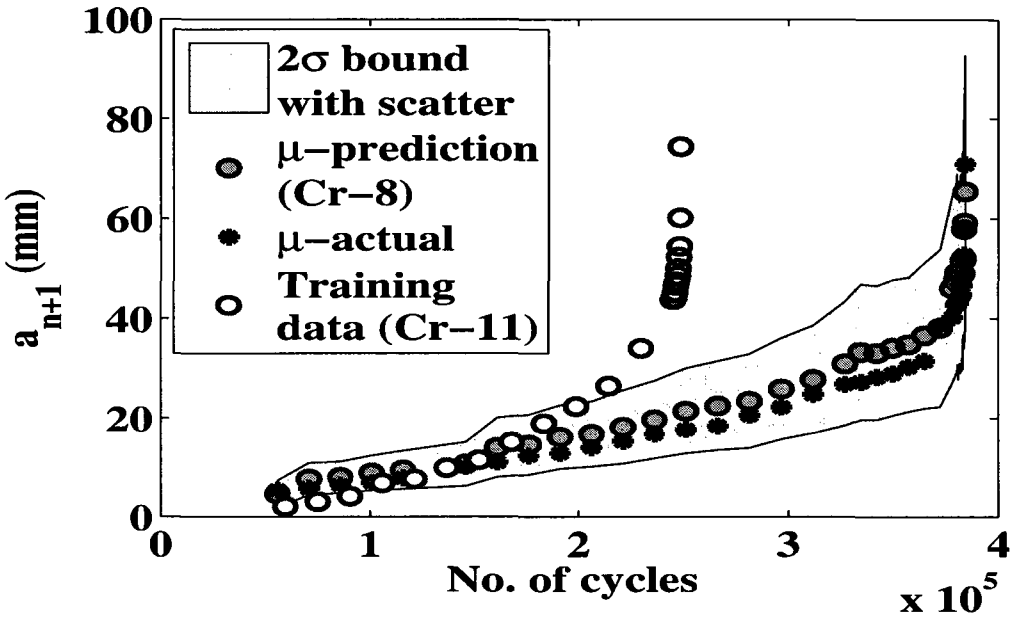

Fig. 4.9. Prediction under biaxial random loading with training data from modified FALSTAFF loading test (error bound includes the contribution from noise hyperparameter)

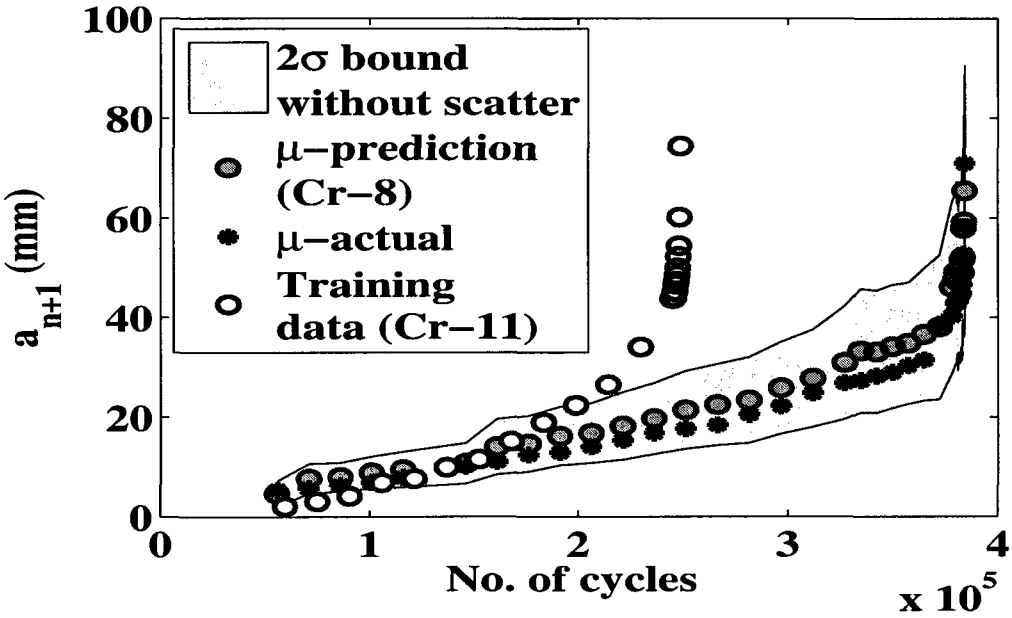

Fig. 4.10. Prediction under biaxial random loading with training data from modified FALSTAFF loading test (error bound does not include the contribution from noise hyperparameter

4.4. Conclusion

The present chapter discusses the Bayesian Gaussian process approach to predict damage in complex structure under complex biaxial state of random and flight profile fatigue loading. The multivariate GP model first trained with input-output data set obtained from previous fatigue test. For a typical output at n^{th} damage level (a_n) the corresponding GP input space $\mathbf{x}_n$ formed using six variables such as $n-1^{th}$ level damage state (a_{n-1}), n^{th} level X-axis maximum load ($U_{x_n}^{\max}$) , X-axis minimum load ($U_{x_n}^{\min}$), Y-axis maximum load ($U_{y_n}^{\max}$) , Y-axis minimum load ($U_{y_n}^{\min}$) and fatigue cycle interval (dN_n). Once the GP model is trained, it is used to predict the unknown damage state or crack length ($a_\bullet$) for a known input condition ($\mathbf{x}_\bullet$). Different training and prediction cases are studied to evaluate the performance of the proposed GP model. Following are the important observations from the present study.

1. Prediction under a particular load can be performed very accurately by training the GP model with the fatigue test data obtained from a different specimen but tested under same loading condition.

2. Prediction under a particular loading pattern can be performed fairly accurate if the GP model is trained with the fatigue test data set that has majority of the test case load patterns, not necessarily with the same order as the test case. A typical example is the prediction under a flight profile load with a training data set using random load data.

3. Poor prediction is observed if the GP model trained with the fatigue test data set that has not seen majority of the test case load patterns. A typical example is the

prediction under random load using a GP model that is trained with data obtained from modified FALSTAFF fatigue test.

CHAPTER 5

Online Damage State Estimation Using Active Sensing and Supervised Gaussian Process Approach

5.1. Introduction

In the chapter 3 and 4 it was discussed how to predict the future damage state of a structure. However, the correct prediction of future damage states depends on current damage conditions of the structure. Manual inspection of damage condition is generally uneconomical and also undermines the mission capability due to long overhauling time requirement. The current research on structural health monitoring (SHM) [106, 107] can lead to a paradigm shift in condition based maintenance (CBM) and residual useful life estimation (RULE) procedures. The use of distributed sensors, networks and novel information management techniques can lead to greater efficiency in monitoring and damage state estimation. Capability for prognostic and preventative maintenance through SHM will reduce the downtime of these critical structures, resulting in substantial savings and greater flexibility on maintaining and using the current fleet and designing the next generation air transportation system. The present chapter discusses a Gaussian process [82, 84, 98] based supervised approach for estimating the damage condition at any given damage level. This is an online model, which maps the features of a piezoelectric sensor signal to the physical damage state, in this case the crack length or the crack growth rate.

5.2. Theoretical Approach

5.2.1. Gaussian process (GP) online damage state estimation

A Gaussian process [82, 84, 98] approach that includes Bayesian uncertainty into the model is used for the online damage state estimation. It is assumed that the crack length or the damage condition at a given damage level is a random variable and follows a Gaussian

probability distribution. The GP is a combination of such Gaussian distributions over the entire fatigue life. The GP model projects the input space to an output space by inferring the underlying probabilistic nonlinear function relating the input to the output. Once the GP is trained with a known input-output data set, it can predict the unknown output crack length or its growth rate for a known input. For the online state estimation, the model input space is trained using the features obtained from sensor signals, whereas the output space is trained with the corresponding crack lengths as parameters representative of the damage state. The training data are generated using different test specimens. It is noted that to estimate the n^{th} damage level output, i.e., the crack length or its rate, the corresponding input for the online GP model are the n^{th} damage level sensor signal features. To estimate the n^{th} damage level crack length (a_n), the online GP model posterior distribution for a_n can be given as

$$f(a_n|D,\, \mathbf{K}_n(\mathbf{x}_i, \mathbf{x}_j),\, \Theta) = \frac{1}{Z} \exp\left(-\frac{(a_n - \mu_{a_n})}{2\sigma^2_{a_n}}\right) \tag{5.1}$$

It is noted that in all mathematical expressions used in this thesis, including the above equation, the bold lettering symbolizes either a vector or a matrix. Also in Eq. (5.1), Z is an appropriate normalizing constant and $D = \{\mathbf{x}_i, a_i\}_{i=1}^{n-1}$ is the training data, with $\mathbf{x}_i$ and a_i are the i^{th} feature vector and corresponding damage state, respectively. The mean μ_{a_n} and the variance $\sigma^2_{a_n}$ of the new distribution are, respectively, defined as

$$\mu_{a_n} = \mathbf{k}_n^T \mathbf{K}_{n-1}^{-1} \mathbf{a}_{n-1} \quad ; \quad \sigma^2_{a_n} = \kappa - \mathbf{k}_n^T \mathbf{K}_{n-1}^{-1} \mathbf{k}_n \tag{5.2}$$

It is noted that μ_{a_n} gives the mean of the estimated crack length, whereas the variance $\sigma^2_{a_n}$ gives the associated error in estimation. The error is attributed to the training of the GP

online model with signal features found from different specimens, which do not necessarily have the same microstructure as the specimen under consideration. In Eq. (5.2) $\mathbf{a}_{n-1}$ is the $(1 \times n-1)$ training output vector which, in this case, consists of the crack length. Also κ, $\mathbf{k}_n$, and $\mathbf{K}_{n-1}$ are the partitioned components of n^{th} instances of the kernel matrix $\mathbf{K}_n$ and they can be described as

$$\kappa = k(\mathbf{x}_n, \mathbf{x}_n) \; ; \; \mathbf{k} = k(\mathbf{x}_n, \mathbf{x}_i)_{i=1,2,\cdots,n-1} \; ; \; \mathbf{K} = k(\mathbf{x}_i, \mathbf{x}_j)_{i,j=1,2,\cdots,n-1} \tag{5.3}$$

In Eq. (5.3), k is the assumed kernel function, which transfers the nonlinear function parameter to a linear high dimensional space based on some observations. It is noted that in high dimensional space, the original nonlinear data are linearly separable. There are many possible choices of prior kernel functions [82, 84, 97, 98]. From a modeling point of view, the objective is to specify a prior kernel that contains our assumptions about the structure of the process being modeled. The kernel function used for the present problem is a combination of different kernel functions and is expressed as

$$k = k_{MLP} + k_{RBF} + k_{CONST} + k_{NOISE} \tag{5.4}$$

where, the multi-layer perceptron (MLP) kernel is expressed as

$$k_{MLP}(\mathbf{x}_i, \mathbf{x}_j) = \Theta_1 Sin^{-1}\left(\frac{\Theta_2 \mathbf{x}_i^T \mathbf{x}_j}{\sqrt{(\Theta_2 \mathbf{x}_i^T \mathbf{x}_i + 1)}\sqrt{(1 + \Theta_2 \mathbf{x}_j^T \mathbf{x}_j)}}\right) \tag{5.5}$$

In Eq. (5.4), the anisotropic radial basis function (RBF) kernel is

$$k_{RBF}(\mathbf{x}_i, \mathbf{x}_j, \Theta) = \Theta_3 \exp\left(-\frac{1}{2}\sum_{l=1}^{d} \frac{(\mathbf{x}_{l,i} - \mathbf{x}_{l,j})^2}{\Theta_l^2}\right) \tag{5.6}$$

The constant function (CONST) kernel is

$$k_{CONST}(\Theta) = \Theta_{3+d+1} \tag{5.7}$$

and the noise function (NOISE) kernel is

$$k_{NOISE}(\Theta) = \delta_{i,j}\Theta_{3+d+2} \tag{5.8}$$

In Eq. (5.6 to 5.8) d is the dimension of the sensor signal feature space, i.e., the type of sensor signal features and $\delta_{i,j}$ is the Kronecker delta. As stated earlier, for the online state estimation model the input space $\mathbf{x}_j$ in Eq. (5.3) uses sensor signal features, whereas the output space a_j corresponds to the damage state at the j^{th} damage level. For the present online estimation, the features could be normalized resonant frequencies or normalized sensor signal variances found from different sensors. Details about feature vector extraction are provided in later subsections. The hyperparameters $\Theta_{i=1,2...d+5}$ in Eq. (5.5) to Eq.(5.8) are adjusted to minimize the negative log likelihood L, given by

$$L = -\frac{1}{2}\log \det \mathbf{K}_n - \frac{1}{2}\mathbf{a}_n^T\mathbf{K}_n^{-1}\mathbf{a}_n - \frac{n}{2}\log 2\Pi \tag{5.9}$$

These hyperparameters are initialized to reasonable values and then the conjugate gradient method is used to search for their optimal values. Initially the kernel function in Eq. (5.4) is evaluated using the assumed initial hyperparameters and iterated further to find the optimal values for which the negative log likelihood L in Eq. (5.9) is minimized. In addition to estimating the direct crack length, the crack growth rate can also be estimated by modifying Eq. (5.1) as follows

$$f(\frac{da}{dn}_n | D, \mathbf{K}_n(\mathbf{x}_i, \mathbf{x}_j), \Theta) = \frac{1}{Z}\exp\left(-\frac{(\frac{da}{dn}_n - \mu_{\frac{da}{dn}_n})}{2\sigma^2_{\frac{da}{dn}_n}}\right) \tag{5.10}$$

Where, $\mu_{\frac{da}{dn}_n}$ and $\sigma^2_{\frac{da}{dn}_n}$ are the estimated mean and variance, respectively of the crack growth rate at the n^{th} damage level. Equations (5.1 to 5.10) describe the online GP model, and can be used for estimating the damage state at the n^{th} damage level.

5.2.2. Sensor signal denoising using principal component analysis (PCA)

Principal component analysis [108, 109] is an orthogonal basis transformation that can be used for sensor signal denoising and dimension reduction. PCA is a process that identifies the direction of the principal components where the variance of changes in dynamics is maximum. Assuming $\bar{M}$ different observations obtained from each sensor at a typical damage instance (say at the n^{th} damage level) and each observation with M samples, the input signal space corresponding to that particular sensor and damage level, is a $\bar{M} \times M$ matrix. It is noted that each sensor observation is a $1 \times M$ vector named y_M. Then the centered $\bar{M} \times \bar{M}$ covariance matrix of the data set $\left\{ y_p \in R^{\bar{M}} | p = 1, 2, \cdots \bar{M} \right\}$ can be found as

$$C_{\bar{M}} = \langle (y_q - \langle y_p \rangle)(y_q - \langle y_p \rangle)^T \rangle \tag{5.11}$$

The covariance matrix is diagonalized to obtain the principal components and the diagonalization can be performed by solving the following eigenvalue problem

$$\lambda v = C_{\bar{M}} v \tag{5.12}$$

The size of an eigenvalue λ corresponding to an eigenvector v of covariance matrix $C_{\bar{M}}$ equals the amount of variance in the direction of v. It is assumed that all the $\bar{M}$ sensor observations taken at a typical damage level can be converted to $\bar{m}$ equivalent observations, which contain the necessary dynamics of the structure at that damage level. The original (after using an appropriate filter) observation space $Y_{\bar{M} \times M}$ can be reduced to a $Y_{\bar{m} \times M}$ equivalent observation space by using the following transformation

$$Y_{\bar{m} \times M} = \Phi^T_{\bar{M} \times \bar{m}} Y_{\bar{M} \times M} \tag{5.13}$$

Where, $\Phi_{M\times\bar{m}}$ is the eigenvector matrix containing $\bar{m}$ eigenvectors found from the eigenvalue analysis described in Eq. (5.13). The transformed observation space $Y_{\bar{m}\times M}$ consists of $\bar{m}$ $1 \times M$ denoised sensor signals, which can be used further for feature extraction.

5.2.3. Normalized damage feature extraction

Once sensor signal denoising has been performed using PCA, the denoised sensor signal has minimal noise content, and has only information that is pertinent to the dynamics of the physical system. From the denoised signal, two types of features are extracted: one is based on resonant frequency of the denoised signal, and the other is based on the variance of the denoised signal. The scaled sensor signal features, which were fed to the GP input space of online state estimation model can be found using

$$x_{i=1\cdots,d,\ j=0,1,\cdots,n-1,n,\cdots} = \sum_{k=1}^{\bar{m}} \left(\frac{fe_{k,j} - fe_{k,0}}{fe_{k,0}}\right)^2 \tag{5.14}$$

where fe corresponds either to the resonant frequency or the variance of the denoised sensor signal; d is the dimension of the input space and is equal to the total number of features; $\bar{m}$ is the dimension of the reduced denoised signal space given in Eq.(5.13). Also the subscript 'j' in $fe_{k,j}$ and '0' in $fe_{k,0}$ respectively indicate the j^{th} and 0^{th} (or healthy state) damage level. The subscript 'k' corresponds to individual signals in the reduced denoised signal space $Y_{\bar{m}\times M}$ given in Eq. (5.13).

5.3. Numerical Results

5.3.1. Fatigue test and data acquisition

The online state estimation algorithm is validated with Al-2024 T3 lug joint specimens under constant fatigue loading of 50N-2750N. A typical test setup is shown in Figure 5.1. The test setup includes a TestResource desktop fatigue frame, a 48 channel National

Instrument PXI data acquisition system and a SONY high resolution CCD camera (with maximum resolution of 1376 x 1024) for the visual crack length measurement. Figure 5.1b also shows the magnified image of Al-2024 T3 lug joint specimen. As shown in Figure 5.1b, each lug-joint was instrumented with four piezoelectric sensors, S1-S4 and one piezoelectric actuator, A1. The sensor network was divided into two zones: Zone-1 consisting of sensors S1 and S2, and Zone-2 consisting of sensors S3 and S4. Three different lug joints labeled Sample-1 to 3 were fatigue tested. The fatigue frame was stopped at different instances and using the multi channel data acquisition system, the piezoelectric signals corresponding to a narrow band actuator input (Figure 5.2) were acquired at those stopping instances. The input signal had a central frequency of 230 kHz and sampled at 1 MHz. However, to avoid any information loss due to host structure coupling, the output sensor signals were acquired with a sampling frequency of 2MHz. Also rather than acquiring one observation per sensor at a typical stopping instance, 100 different observations were acquired for the statistical denoising of the sensor signals. To acquire individual sensor observations, each time the piezoelectric actuator was excited with the mentioned input signal, at a time interval of 5 seconds. It is noted that each observation contains 1000 samples. As the fatigue frame was stopped, high resolution pictures of the lug joint were taken to find the corresponding crack length. The observed crack lengths for all the three samples are depicted in Figure (5.3). These crack lengths are used either for the GP algorithm training or validation.

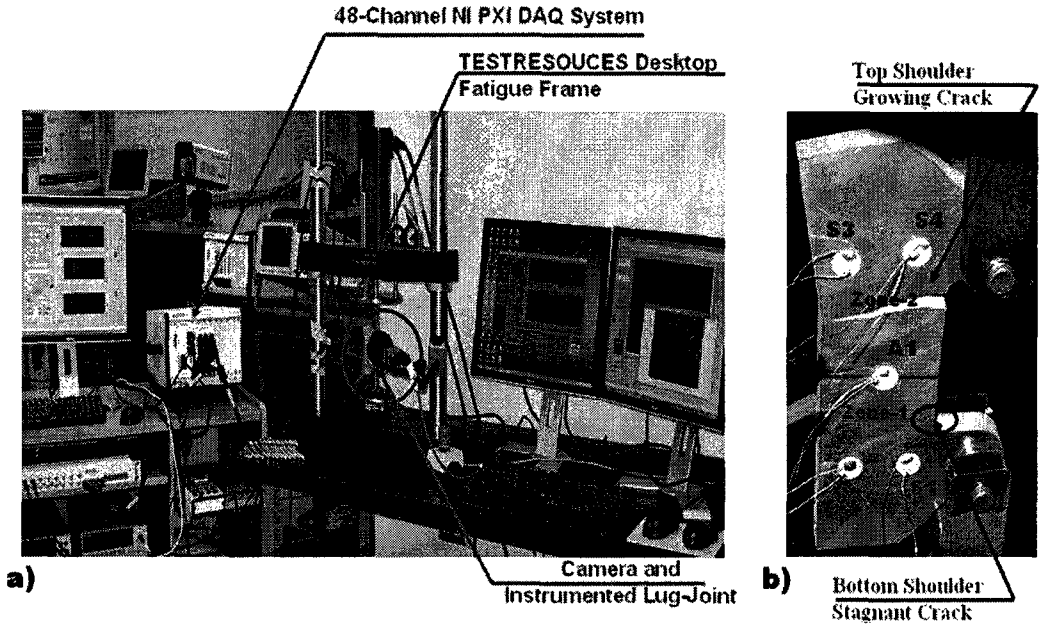

Fig. 5.1. a) Lug joint under fatigue loading b) Magnified view of instrumented Lug-joint

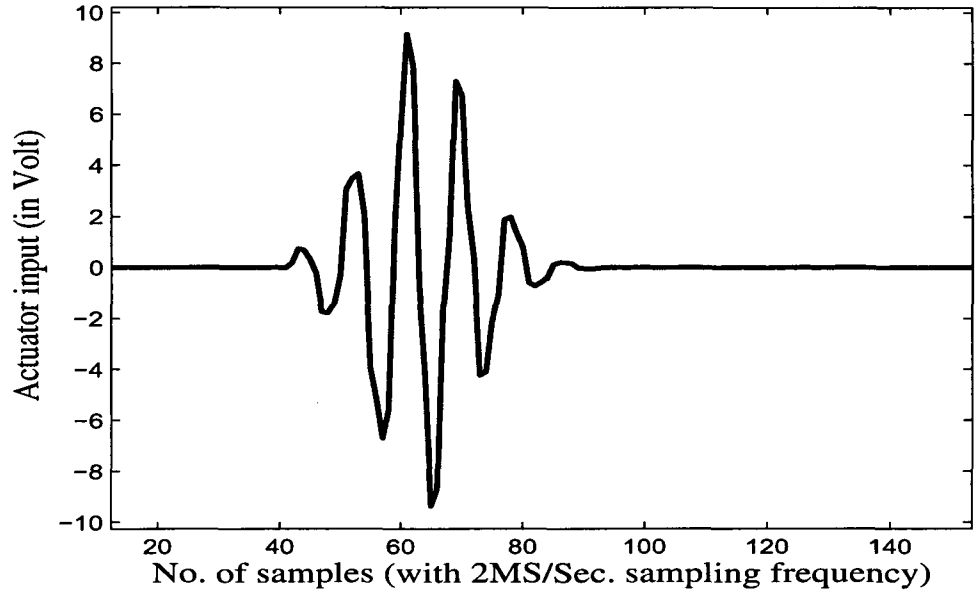

Fig. 5.2. Narrow band input signal for active sensing

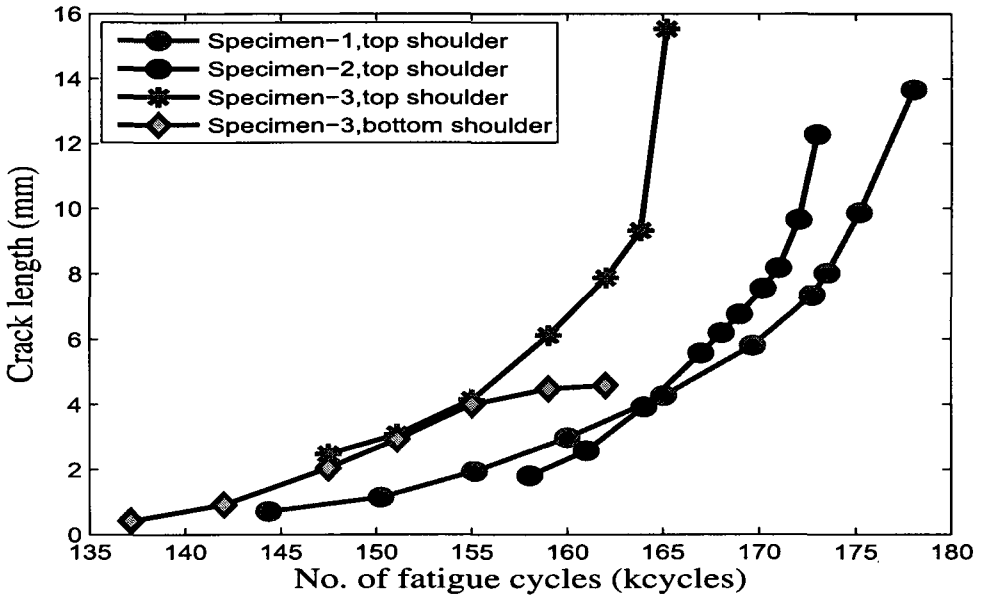

Fig. 5.3. Measured crack length using high resolution camera

5.3.2. Sensor signal normalization

As mentioned above, at each stopping instance, 100 sensor observations were acquired per sensor, against the stated input actuation. At the start of each acquisition, it is supposed that the data acquisition system would record ideally zero or nearly zero (if noise is considered) value. However, it is observed from Figure 5.4, that the starting value of individual observations do not have a zero value or approximately zero value, rather have a higher value. Also, it is observed from Figure 5.5 that the mean of each observation is not zero, rather it has some higher numbered value. This is possibly because of the static charge developed due to the static mechanical loading and any unknown ambient noise. Also, from Figure 5.4 and Figure 5.5, it is observed that as the number of observations increases, the mean (or starting point) of individual observations drifts away from its starting observation value. This is possibly due to the above mentioned causes, in addition to the

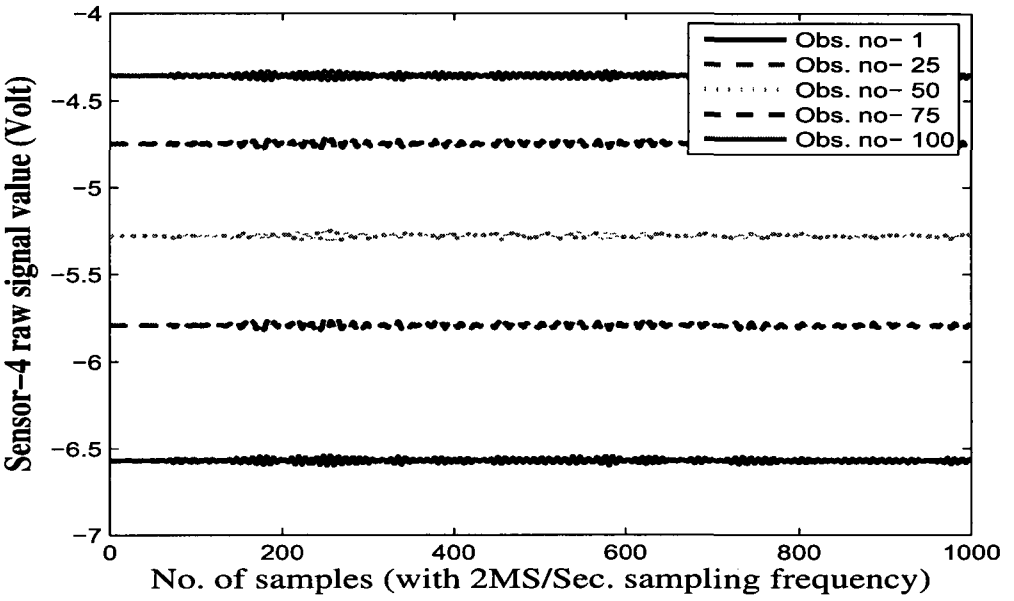

Fig. 5.4. Raw sensor signal (from sensor 4 at the healthy state of specimen 2) acquired for individual observation

possible static charge build up in sensors due to the repeated actuation in short intervals (5 seconds). The state estimation model based on this unregulated observations can lead to faulty estimations. To avoid this, before performing any other signal processing, the individual sensor observations are normalized with sample mean equal to zero. Typical mean transformed sensor observations for the observations mentioned in Figure 5.4 and Figure 5.5 are depicted in Figures 5.6 to 5.7.

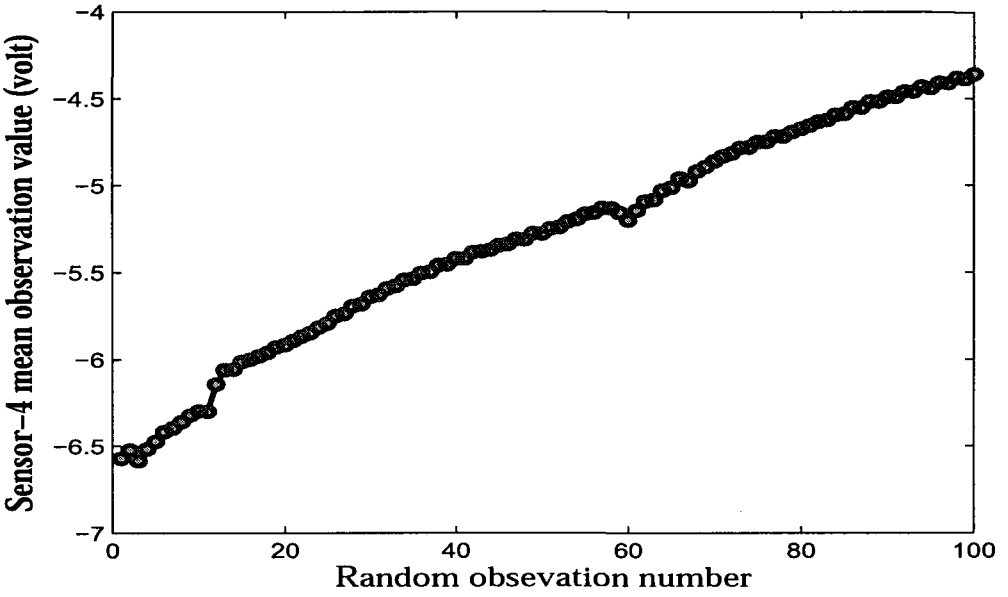

Fig. 5.5. Mean of raw sensor signal (from sensor 4 at the healthy state of specimen 2) acquired for individual observation

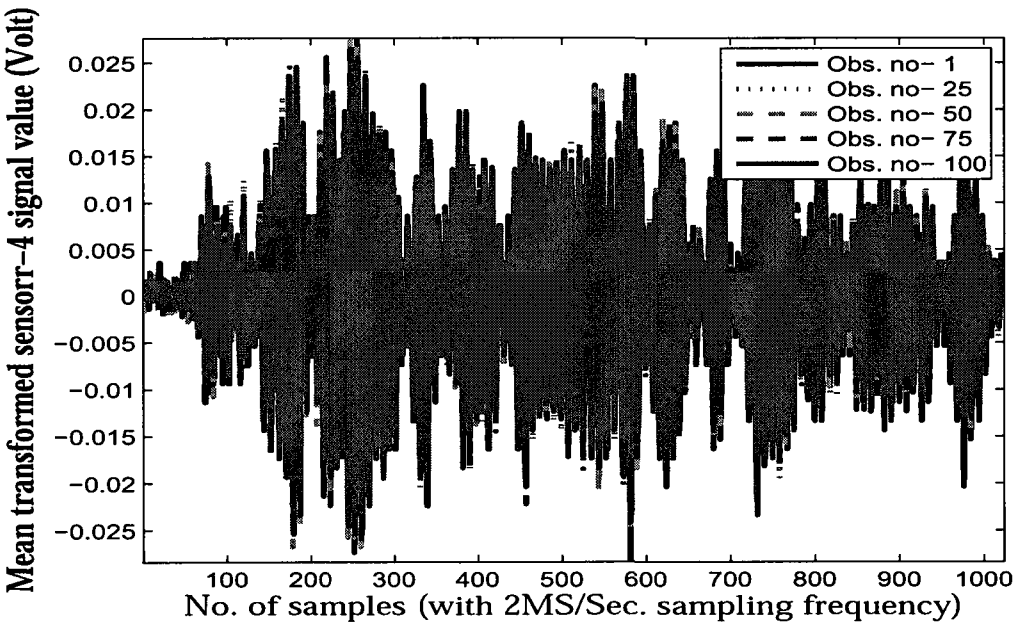

Fig. 5.6. Mean transformed sensor signal (from sensor 4) mentioned in Figure (5.4) and Figure (5.5)

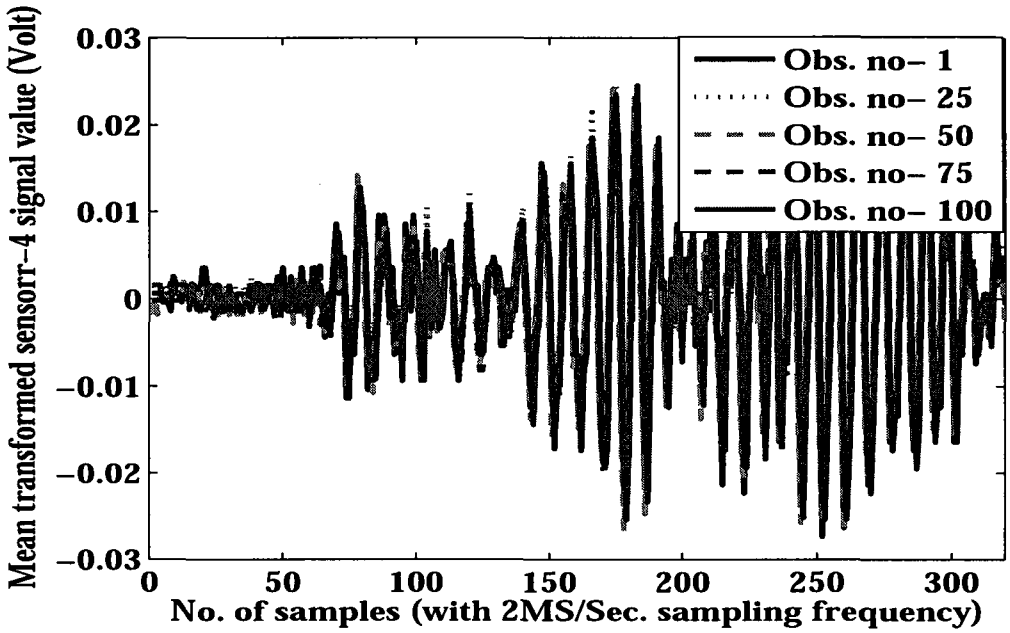

Fig. 5.7. Magnified version of Figure (5.6)

5.3.3. Sensor signal filtering and windowing

After each sensor observations are normalized using the mean transformation mentioned above, the observations are filtered from environmental noise using a band pass filter. The band pass filter has a cutoff frequency of 230±100 kHz. Where, 230 kHz is the central frequency of narrow band actuation. The selection of 100 kHz upper and lower limit for the band pass filter is based on the assumption that the maximum frequency variation of the observed signal will not cross these limits over the entire fatigue loading envelope. This also ensures that low frequency noise due to the actuator of the fatigue frame and high frequency noise due to other environmental factors are not modeled in the feature extraction process. Figure 5.8 and Figure 5.10, respectively, show the time response and frequency response comparison of unfiltered and filtered observations (from sensor 4) at any typical fatigue instance (for the present figure at the 0^{th} damage level or at the healthy

state). The magnified version of the Figure 5.8 is also shown in Figure 5.9. Although it is not clear from the time response, the magnified frequency response (Figure 5.10) clearly shows that high frequency components (frequency more than 400 kHz) were present in the sensor signal. The high frequency signal may be due to the interaction of narrowband actuation waves with piezoelectric bonding layers, or due to other physical/environmental unknown causes.

Once the low and high frequency signals (here the noise) are filtered out, it is necessary to select a proper window of samples, that does not consist of reflected signals from the geometric boundary of the specimen. For the discussed geometry, it is assumed that the direct wave from the actuator will always reach first compared to the reflected wave from the boundary. For this reason a window of sample width 80-110 is selected from the full signal of sample no. of 1-1000. The time and frequency response of the full signal (after band pass filter) is shown in Figure 5.11. From the frequency response it is seen that there are multiple peaks around the central frequency. These frequency peaks are due to the reflected waves from the boundary. The purpose of signal windowing is not to consider the reflected signal that contributes to those side lobed frequency peaks around the central frequency. The reasons for considering the lower bound of sample number 80 are the assumptions that the traveling waves from the actuator did not reach the sensor, before the 80^{th} sample (i.e., before 40 micro seconds) reached. This time lag is due to the combination of time lag caused by data acquisition itself and due to the time required by the actuation wave to travel within the structure. The higher bound of sample no. 110 is due to the assumption that after this sample the reflected wave starts reaching the sensors. The time and frequency response of the windowed signal is shown in Figure 5.12. From the

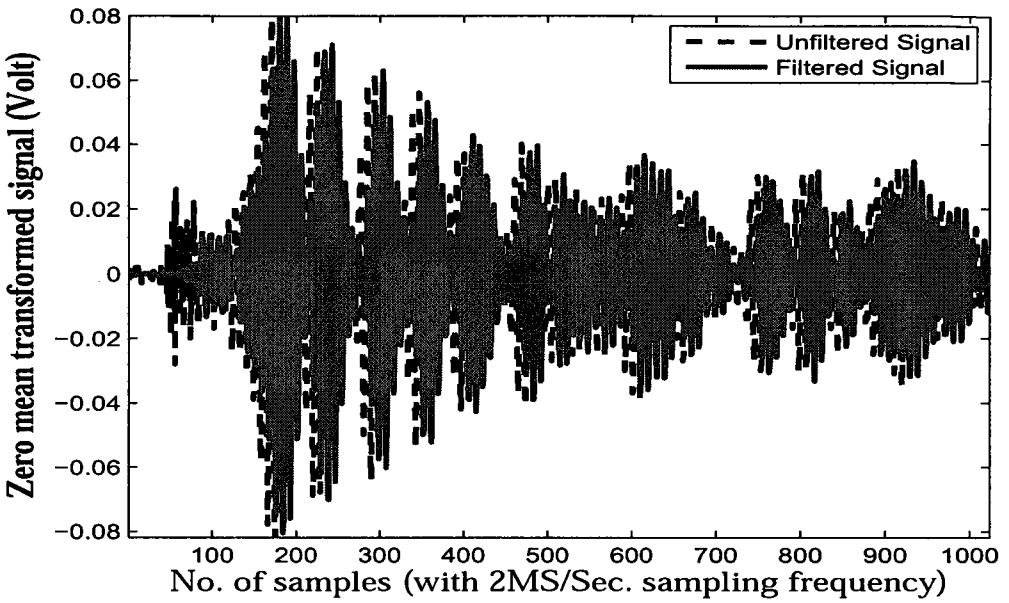

Fig. 5.8. Time response comparison of a typical unfiltered and filtered observation (from sensor 4) at the healthy state of specimen 2

frequency response, it is seen that the windowed signal has only one dominant frequency, which is expected when the sample is healthy and no frequency modulation occurs due to the boundary reflections. However, it is noted that the reflected signal (Figure 5.11) after sample no. 110 has more strength than the direct signal (before sample no. 110). The reflected signal may have more signals to noise ratio and might help in improving online state prediction accuracy, but may indicate the presence of a crack, even if there is no crack. This type of false detection might happen in the presence of multiple cracks in a single sample.

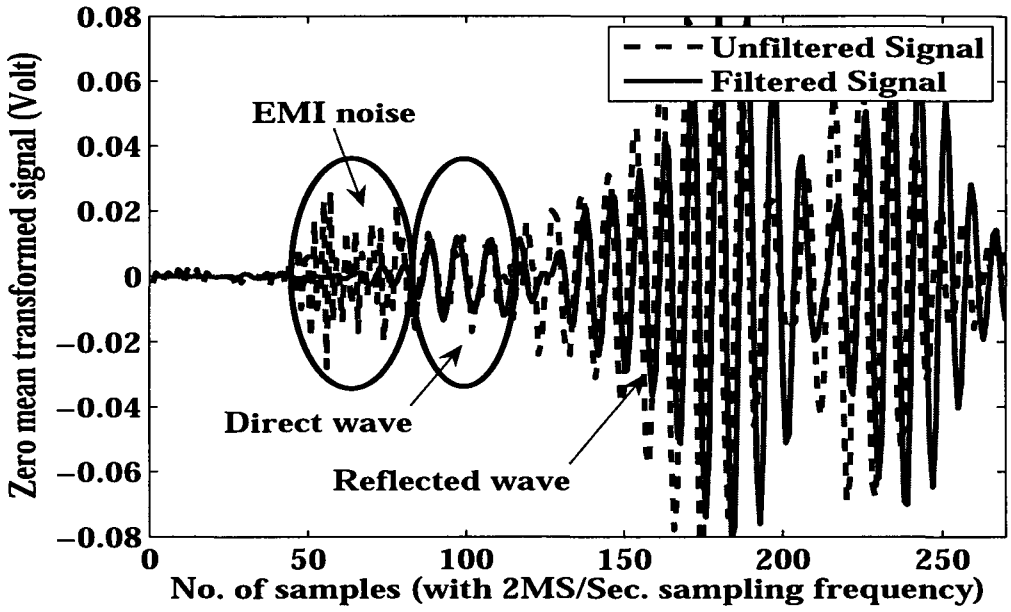

Fig. 5.9. Magnified version of Figure (5.8)

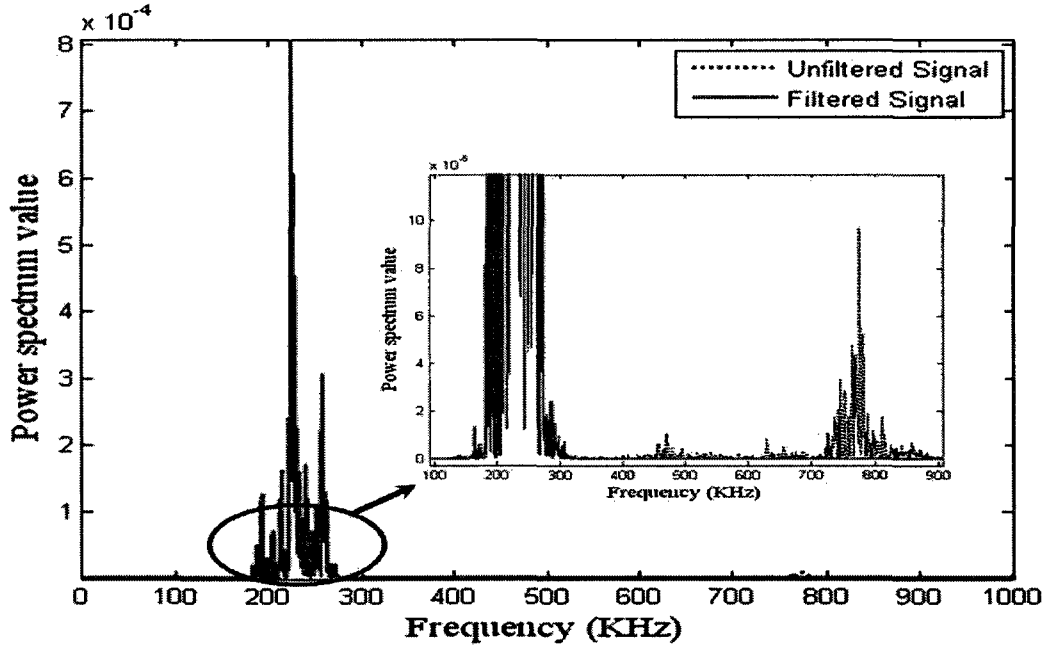

Fig. 5.10. Frequency response comparison of unfiltered and filtered observations (from sensor 4) at the healthy state of specimen 2

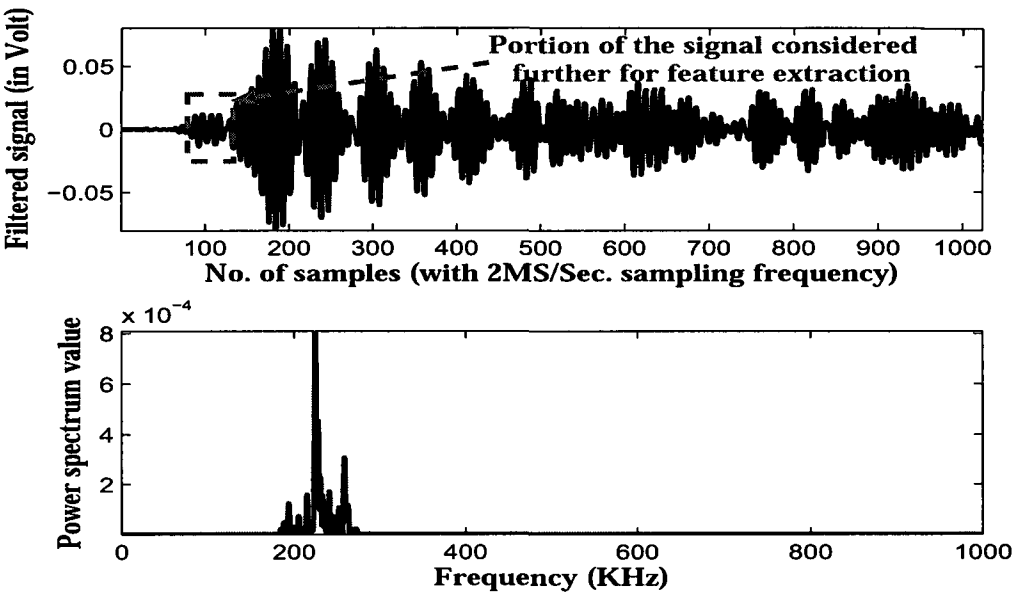

Fig. 5.11. Time and frequency response of the band pass filtered signal. The raw signal was collected from sensor 4 at the healthy state of specimen 2

5.3.4. Sensor signal denoising and dimension reduction

Even after sensor signal normalization and subsequent band pass filtering, the windowed signal mentioned above not necessarily consists only of the information pertaining to the dynamics of the physical system. There is still environmental noise present in the windowed signal. The frequencies of the noise will be in the unfiltered frequency band of 130 kHz-330 kHz. However, it is not possible to directly filter out the noise in this frequency band, as it was done before. Direct use of a filter may remove the signal features that are related to the damage features of the structure. Principal component analysis (PCA) as described before is used to remove the remaining environmental noise. For this purpose, at each damage level, (where the fatigue frame was stopped to collect the data) 100 windowed observations from each sensor are considered. It is assumed that using PCA,

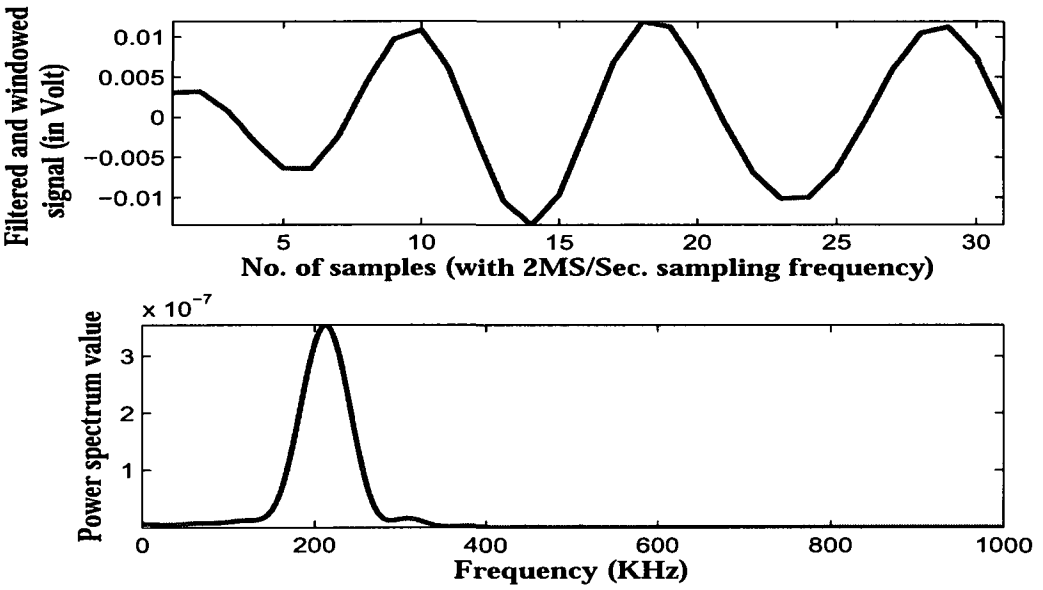

Fig. 5.12. Time and frequency response of the windowed signal (from the band pass filtered signal as shown in Figure 5.11). The single peak in frequency response shows that there is no boundary reflection

100 observations can be transformed to an equivalent single observation, which has the necessary dynamics change information. Figure 5.13 and Figure 5.14, respectively, show the covariance value of 100 observations before and after denoising. The highly noisy covariance plot of the original windowed signal confirms the presence of noise, which is not related to changes in the dynamics of the physical system. However, the covariance plot after denoising shows few clear peaks indicating that the new denoised signals set have only a few signals that contain the necessary dynamic change information. The number of denoised signals, which can be considered further, for feature extraction, can be selected based on the eigenvalue plot shown in Figure 5.15. Eigenvalues are found using the eigenvalue analysis of the original covariance matrix as described in Eq. (5.12). The eigenvalue plot clearly shows that the first eigenvalue is widely separated from the rest and the denoised

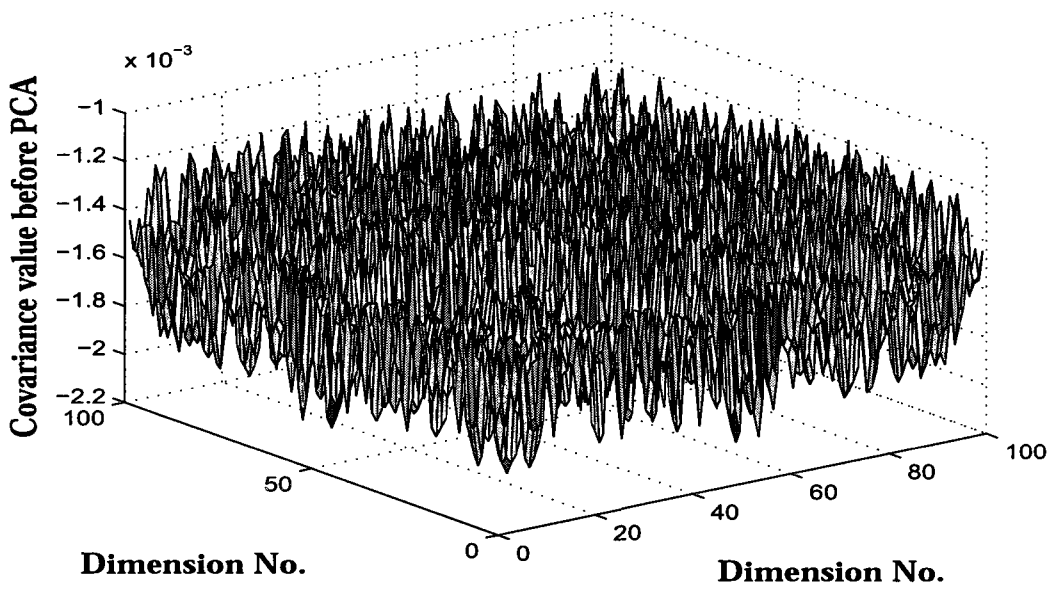

Fig. 5.13. Covariance of the windowed signal before denoising. The noisy plot shows the windowed observations has noise content, which are highly correlated

signal corresponding to the 1^{st} eigenvalue can be assumed to contain the highest dynamics change information. Hence, with the total number of signal samples considered ($M = 30$ after windowing), and the total number of eigenvectors considered ($\bar{m} = 1$), the denoised observation space $Y_{\bar{m} \times M}$ described in Eq. (5.13) reduces to a 1×30 denoised signal vector. Figure 5.16 and Figure 5.17, respectively, show the time and frequency response of a few denoised signals according to the decreasing order of sorted eigenvalue (signal variance). It is clearly seen that the signal corresponding to dimension 1 has the highest signal value and energy level, compared to the rest of the denoised signals.

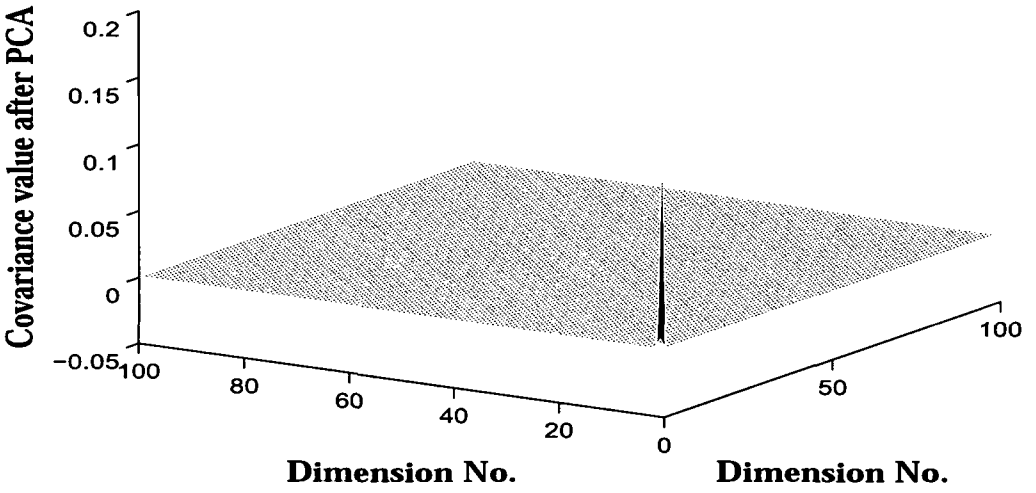

Fig. 5.14. Covariance of the windowed signal after denoising. Few clear peaks show the denoised observations have the least noise contents, and are the least correlated

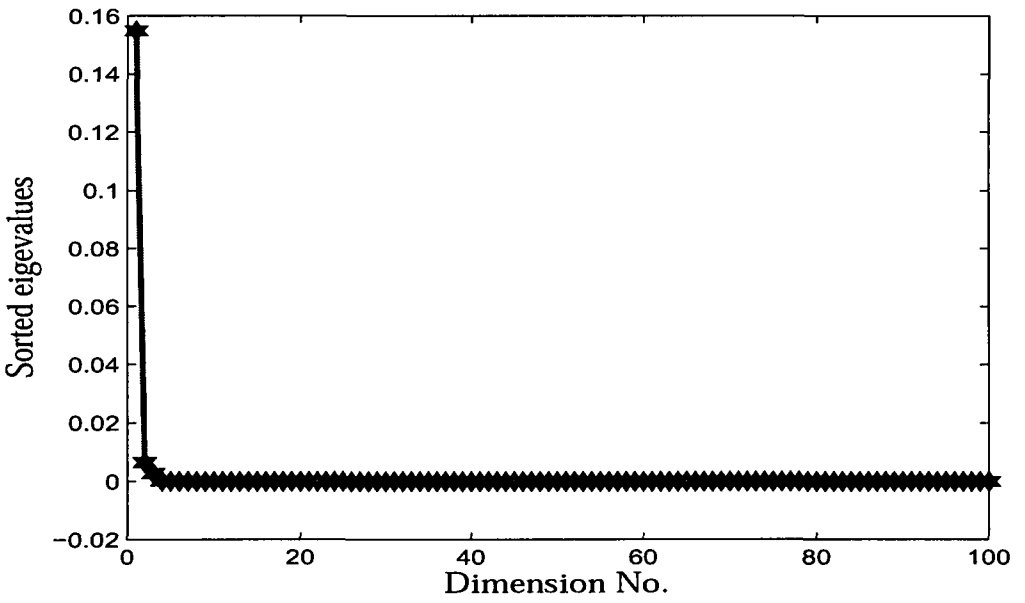

Fig. 5.15. Sorted eigenvalues indicating that the denoised signal corresponding to the first eigenvalue has the highest dynamics change information

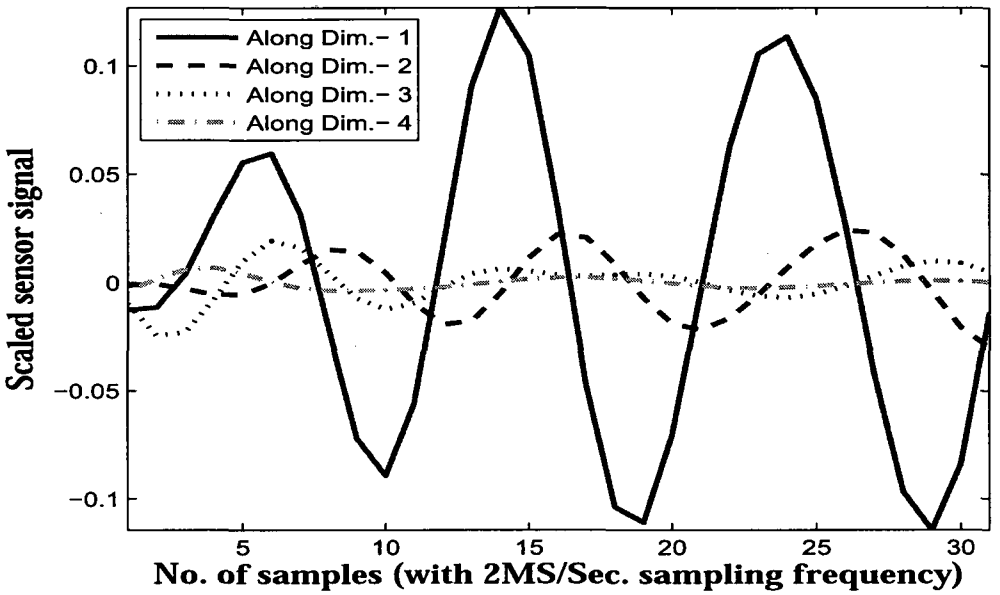

Fig. 5.16. Various denoised signals corresponding to sorted eigenvalues and their corresponding eigenvectors

5.3.5. Sensor signal feature extraction

Using the denoised signal mentioned in the previous section, the damage pertaining features are extracted using Eq. (5.14). With the dimension of the denoised signal space equal to 1×30, the value of $\bar{m}$ in Eq. (5.13) and Eq. (5.14) is 1. The normalized features as described in Eq. (5.14) are found with respect to the healthy state of the specimen, and are found at each damage level, where the sensor signals were available. Figure 5.18 and Figure 5.19, respectively, show the features based on changes in resonant frequency and changes in variance of the denoised signal at different fatigue instances. From the figure it is seen that there is a good trend in signal features for both specimen 2 and specimen 3. These features will be used further, to form the GP input space for online state estimation.

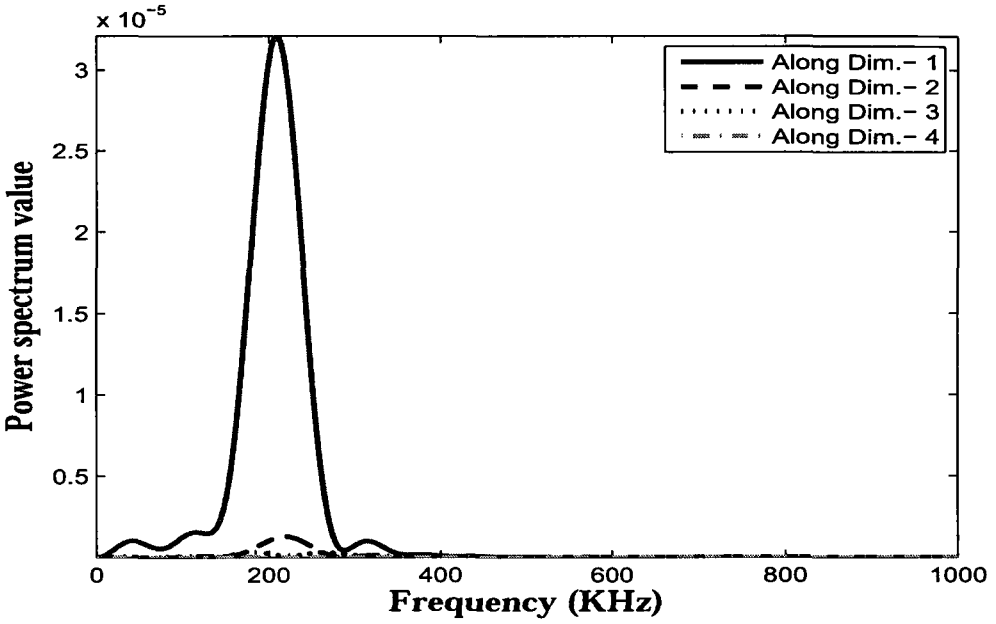

Fig. 5.17. Frequency response of the time response shown in Figure 5.16

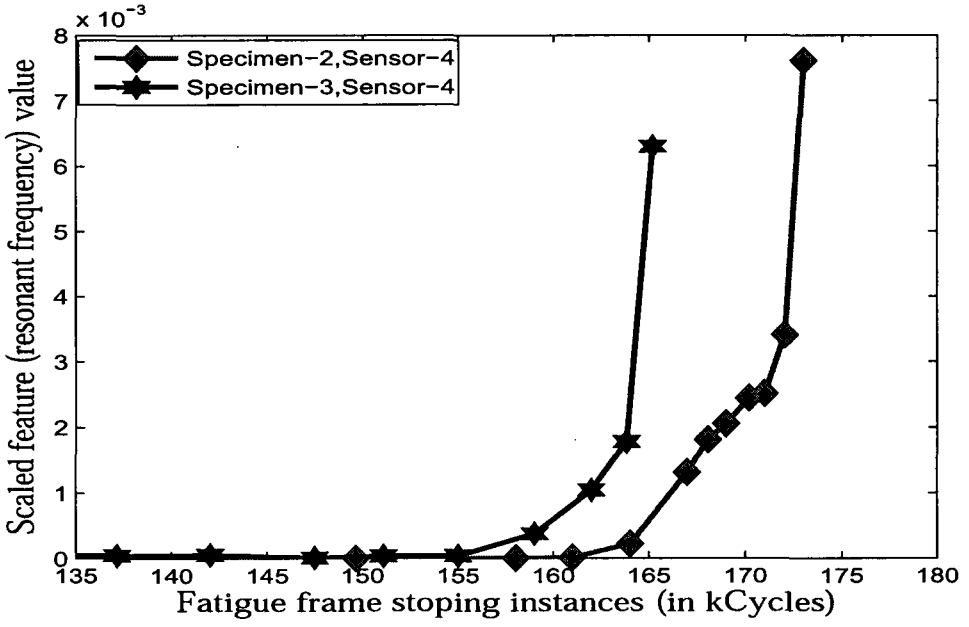

Fig. 5.18. Features based on change in resonant frequency.

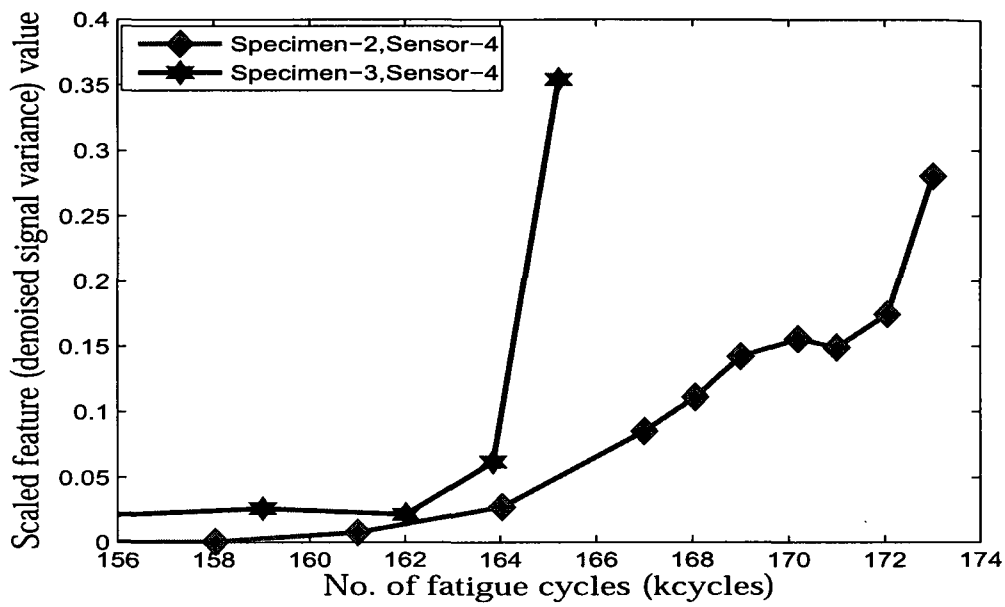

Fig. 5.19. Features based on change in denoised signal variance.

5.3.6. Damage zone localization

In a real life structure there could be multiple cracks. However, not all cracks are critical from the structural integrity point of view. For example, for the case of the present lug joint in specimen 3 there are two cracks: a stagnant bottom shoulder crack and a top shoulder crack that led to final failure. The real-time prognosis algorithm should have the ability to identify the damage propagating zone that leads to final failure. For the present symmetric lug-joint, either the bottom or top shoulder crack can lead to final failure. To identify the most critical damage zone, which consists of a critical propagating crack, the entire lug-joint is divided into two zones: zone-1, comprising the bottom half, and zone-2 comprising the top half. Zone-1 consists of sensor 1 and sensor 2, whereas zone-2 consists of sensor 3 and sensor 4. To identify the critical zone with most damage a metric is selected, which is equal to the mean of the resonant frequency based features found for the individual

sensors located in that zone. The metric is calculated for each zone at different fatigue instances, for which sensor signals were available. At a given fatigue instance, the stated metric can be compared for individual zones, and accordingly the prognosis algorithm has to be switched to a particular zone that has the highest metric value. Figure 5.20 and Figure 5.21, respectively, show the comparison of the damage zone identification metric between zone-1 and zone-2 for specimen 2 and specimen 3. For specimen 2, it is clearly seen that the damage zone identification metric has a lower value for zone-1 compared to zone-2. This can also be confirmed from the visually observed crack growth as shown in Figure 5.3, that there was no bottom shoulder crack. Similarly, in the case of specimen 3, it is seen that after 157 kcycles, the zone-1 identification metric becomes approximately constant and has consistently lower value compared to zone-2 metric. The above implies that the damage in zone-2 is growing, whereas damage in zone-1 is stagnant. This can also be seen in the observed crack lengths shown in Figure 5.3.

5.3.7. Gaussian Process input-output space

Once the feature extraction is performed for the online damage state estimation the GP input space is made using sensor signal features, discussed in the earlier section. The input vector $x_{j,\ j=0,1,\cdots,n,n+1}$ is a $d \times 1$ vector, where d is the dimension of the input space, comprising of different types of features found from different sensors placed in a particular zone of interest. For example, considering both the resonant frequency based features and signal variance based features and considering features from both sensor 3 and sensor 4, (ref. Figure 5.1b) the dimension d will be equal to 4. On the other hand, the output space at any given damage level comprises either the crack length or the crack growth rate,

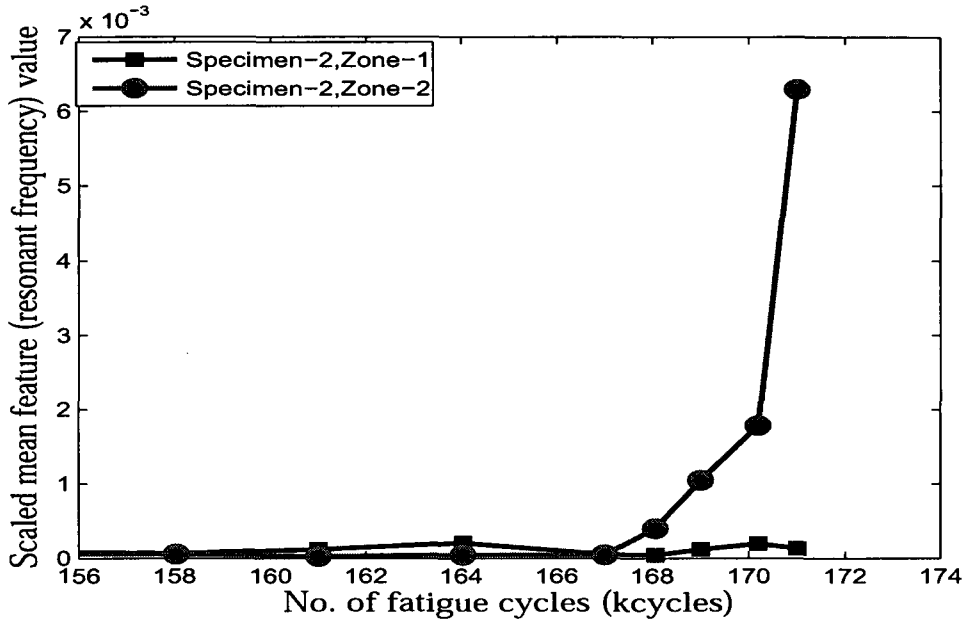

Fig. 5.20. Comparison of damage zone identifying metric for specimen 2.

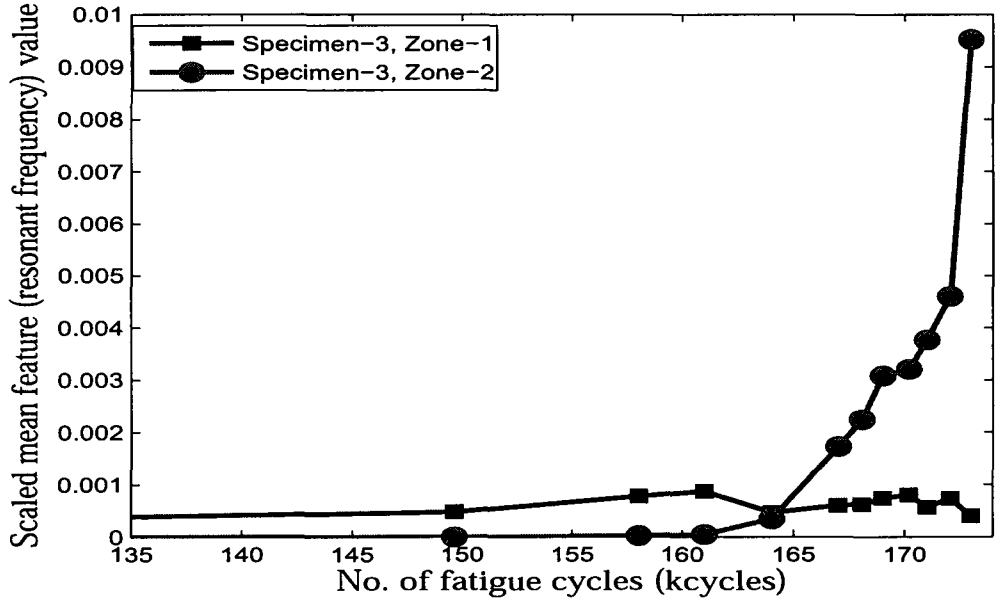

Fig. 5.21. Comparison of damage zone identifying metric for specimen 3.

but unlike the input space parameters (i.e., $\mathbf{x}_j$), at $j = 0, 1, \cdots, n-1, n^{th}$ damage levels, the output space parameter is a scalar. Before using the GP algorithm for online state estimation, the algorithm is trained with the data available from at least one sample over the entire fatigue loading envelope. This process helps the GP to learn the dynamics of crack propagation over the entire fatigue cycles range. For the present case, data from specimen 3 are used for training the online state estimation algorithm. As seen from Figure 5.3, the fatigue frame was stopped respectively 10, 10 and 7 times for specimen 1, specimen 2 and specimen 3. However, for the training of the online model, data from only specimen 3 are considered, because the sensor data from specimen 1 was found corrupted, due to the use of a faulty signal amplifier. The online state estimation model is validated against data found from specimen 2. It is noted that the higher the number of training data, the better is the learning of the GP algorithm and the better is the state estimation accuracy.

5.3.8. Information fusion and online state estimation

Information fusion is the process of combining information from multiple sources/sensors to enhance the fidelity of the overall prognostic system. In the present work information fusion is performed for the GP online state estimation model. As mentioned in the previous section, the GP input space is made of four different types of features: type-1 and type-2 are, respectively, the resonant frequency and signal variance based features found using the signals from sensor S3, and type-3 and type-4 are, respectively, the resonant frequency and signal variance based features found using the signals from sensor S4. These features are used to model the GP multivariate input space. The above mentioned input information is used in combination to estimate the GP hyperparameters. The hyperparameters are found by maximizing the negative log-likelihood function given

in Eq. (5.9). These hyperparameters for various combinations of input information have been estimated for further use in online state estimation of crack length or crack growth rate. Figure 5.22 shows a typical example of the convergence of the negative log-likelihood function optimization, while considering all four type of features for the GP input space. Based on the extracted signal features and optimized hyperparameters discussed above, the GP algorithm is used to estimate the unknown damage state for given input space information. The input space for both the training sample and the test sample are fed with the above mentioned four types of signal features. However, it is noted that unlike the GP training input space, the test input space is fed with features, as they become available, in real time. The test output at a given damage level has to be estimated using the $d \times 1$ feature vector extracted at that damage level. The comparison between estimated damage state (crack length) and the experiment value is depicted in Figure 5.23. From the figure it is found that, there is a good correlation between experiment and estimation, when the crack length is larger than 6 mm. The discrepancy between estimated and experiment increases as the crack length becomes smaller. This may be because the signal features are not sensitive to smaller cracks. This problem can be alleviated by using broadband and higher frequency input signals, which will be discussed in the next chapter. Also Table 5.1 shows the Mean Square Error (MSE) estimate between the estimated crack length and true crack length for various combination of input space information. It is found that the mean square error has its least value when all four types features are considered in the GP input space. The GP online estimation model (ref. Eq. 5.10) is also used to estimate the crack growth rate. The comparison between estimated crack growth rate and true crack growth rate is shown in Figure 5.24. From the figure it is seen that, there is a good correlation

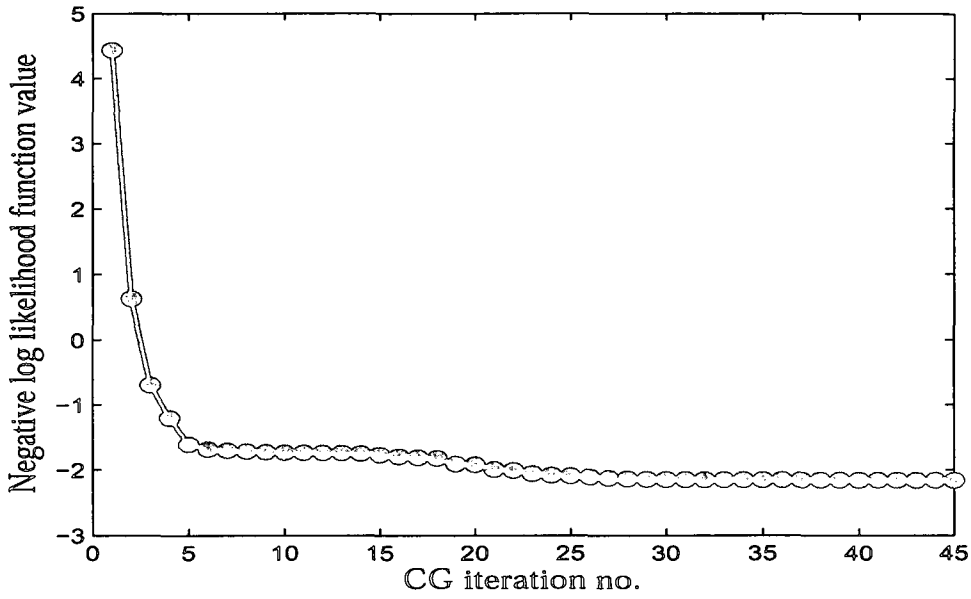

Fig. 5.22. Negative log-likelihood function value with respect to different Conjugate gradient iteration number

between estimated crack growth rate and the experimental value. In addition, Table 5.2 shows the MSE between estimated crack growth rate and true crack growth rate. From the table it is also found that MSE has its lowest value when all four signal features are used in the GP input space.

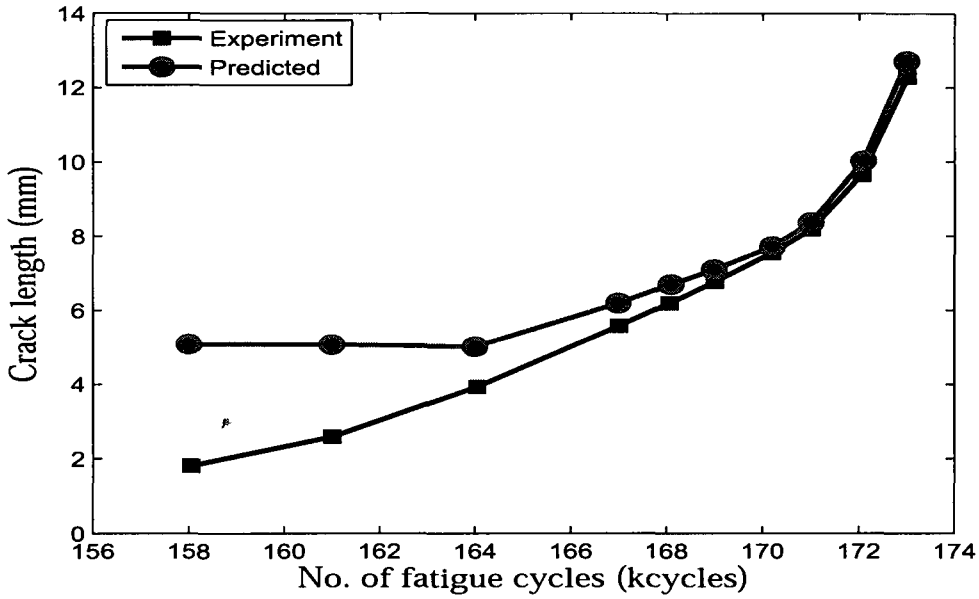

Fig. 5.23. Comparison of estimated crack length and true crack length using both resonant frequency (type-1) and signal variance (type-2) of signals from both sensor 3 and sensor 4

Fe. type (→) Sen. No. (↓)	Resonant frequency based feature (type-1)	Signal variance based feature (type-2)	Both resonant frequency and signal variance based feature
S3	23.645	5.0114	4.8541
S4	4.9254	6.9353	5.3749
both	2.8621	3.2096	**2.1303**

TABLE 5.1
MSE BETWEEN ESTIMATED CRACK LENGTH AND TRUE CRACK LENGTH FOR VARIOUS COMBINATION INPUT SPACE INFORMATION

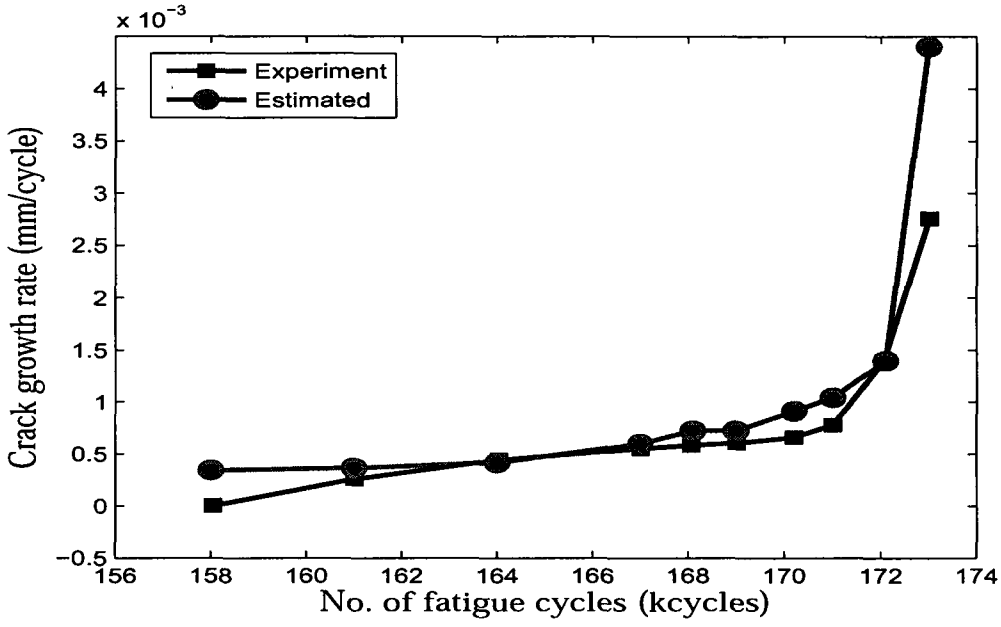

Fig. 5.24. Comparison of estimated crack growth rate and true crack growth rate using both resonant frequency (type-1) and signal variance (type-2) of signals from both sensor 3 and sensor 4

Fe. type (→) Sen. No. (↓)	Resonant frequency based feature (type-1)	Signal variance based feature (type-2)	Both resonant frequency and signal variance based feature
S3	5.82e-007	4.06e-007	3.27e-007
S4	3.39e-007	1.78e-006	7.31e-007
both	3.30e-007	3.43e-007	**3.06e-007**

TABLE 5.2

MSE BETWEEN ESTIMATED CRACK GROWTH RATE AND TRUE CRACK GROWTH RATE FOR VARIOUS COMBINATIONS OF INPUT SPACE INFORMATION

5.4. Conclusion

A GP supervised model is proposed to estimate the online damage states. The online damage states are estimated using real-time sensor measurements and a trained GP model. The approach is demonstrated on an Al-2024 Lug-joint subjected to constant cycle fatigue loading. The online damage state estimation shows that there is a good correlation between experiment and estimation when the crack length is larger than 6 mm. The estimation error for crack lengths smaller than 6 mm can be reduced by using higher frequency broadband active sensing, which will be discussed in the next chapter.

CHAPTER 6

Online Damage State Estimation Using Active Sensing and Unsupervised System Identification Approach

6.1. Introduction

In chapter 5 the supervised Gaussian process based online damage state estimation approach is discussed. However, most of the supervised pattern recognition algorithms like Gaussian process (GP) require large training data to extrapolate meaningful information for an unknown damage condition. In addition, the ultrasonic input based active sensing approach is highly sensitive to slight changes in boundary condition. In the earlier discussed supervised GP approach the online estimation model was based on a trained Gaussian process, which was trained using data from a different specimen. It is to be noted that, the training and test specimens, were tested under similar boundary conditions. Also the training and test specimen followed similar crack propagation path. However, it is not always possible to maintain the exact boundary condition and crack propagation path for both training and test structure. If there is not sufficient similarity between training and test condition, the supervised technique might give erroneous results. To circumvent the problem the use of unsupervised system identification technique can be explored. However, many of the available approaches on system identification [110], [111] are generally confined to low frequency based applications such as process and aircraft flight control identification. The research on low frequency structural damage identification, such as vibration-based damage identification has limitations [112] because of the larger power and actuator requirements to excite the low frequency, high power global structural modes. However, for local damage identification, smaller piezoelectric based actuators with low power requirements can be used to generate the required deterministic input signals for

effective use of system identification tools. The use of fairly matured system identification techniques can be extended for high frequency Lamb wave input signals in the range of kHz to MHz. For example, the high frequency response function [113] can be estimated at a particular damage condition and can be compared with the frequency response function of the other damage condition to evaluate the relative change in the structural health. However, the narrowband Lamb waves widely used in SHM have limited capability for persistence of excitation except around the central frequency of the chosen input signal. This lack of persistence excitation in a broader band of frequency limits the damage estimation capability of narrowband based SHM techniques. Input signals such as multisine [114] signal can be used for persistence excitation in a broader frequency band of interest. Under experimental conditions where noise is present, multiple cycles of the periodic input can be introduced until the variance in the model estimate is reduced to acceptable levels. In the present research, a broadband chirp [115] input is used to estimate the time series damage states. The chirp signal used is a type of multisine signal. The individual harmonics are not optimized, but linearly varied harmonics are selected in the required broadband frequency domain for simplicity. In addition, this chapter presents the use of two nonparametric system identification approaches such as frequency-domain based empirical transfer function estimation approach and time-domain based correlation analysis approach to estimate time series damage states. The real-time state identification algorithm is validated on an Al-2024 cruciform specimen undergoing biaxial cyclic loading.

6.2. Theoretical Approach

Real-time damage state estimation is an integral part of SHM and prognosis systems. Here, the condition of the structure has to be assessed at real time using sensor signals

acquired either continuously or discretely. As mentioned earlier, nonparametric system identification approaches based on ultrasonic deterministic input signals are explored to estimate the current state of a structure. In the present chapter the effectiveness of both narrow and broadband input signals are studied. It is noted that for low frequency identification applications, where the additive noise is independent of the deterministic input signal, the noise can be removed easily using correlation analysis. However, in the case of high frequency state identification applications usually the additive noise in the acquired signals contains the input dependent noise in addition to the input independent noise. Without proper knowledge of a time dependent noise transfer function, it is difficult to remove the input dependant noise from the measured outputs. To avoid this problem, two sensors are placed close together. Since both sensors receive the same input dependent and independent noise, it can be removed by taking the difference between the sensors measurements. In addition to the noise removal, the dual sensor configuration will also help to improve the spatial resolution in damage state estimation. If two sensors are placed adjacent to each other, ideally they would receive the same signal at a given damage condition. However, if there is a small change in damage, this will be reflected as large differential change in sensor signals received at the adjacent sensors. As the damage grows this differential change grows with respect to the healthy or reference condition. This phenomenon of large differential signal change for small change in damage condition can be used for improving the spatial resolution in damage state estimation. The dual sensor configuration block diagram is shown in Fig.6.1.

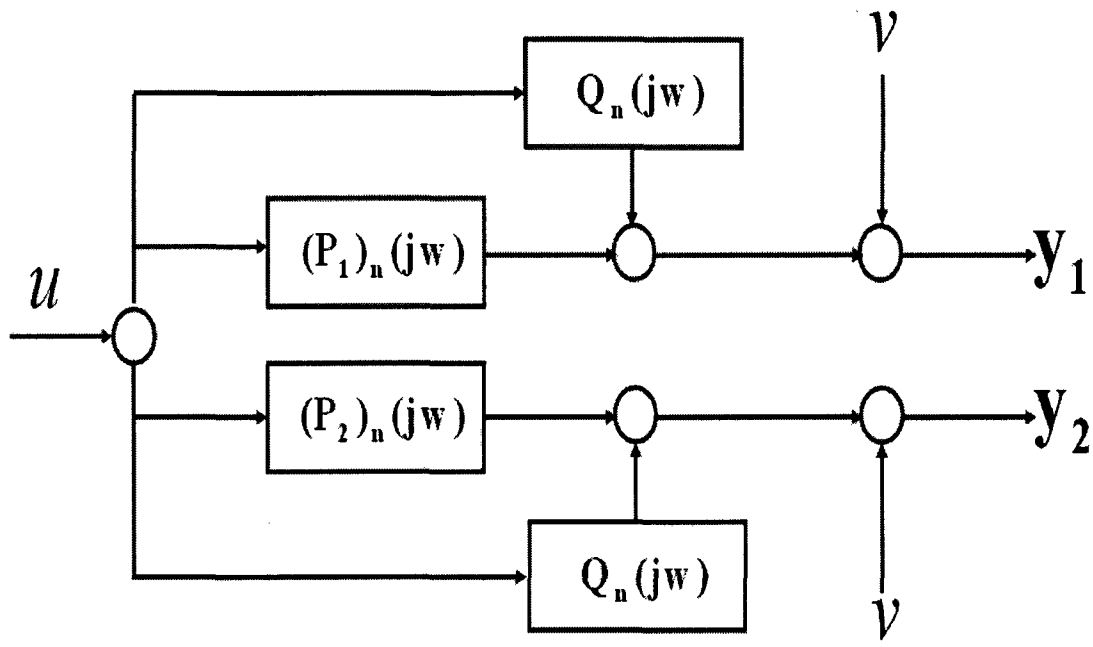

Fig. 6.1. Input-output block diagram for dual sensor configuration

In the figure, u is the deterministic narrow or broadband input signal, $(P_1)_n$ is the n^{th} damage level transfer function associated with input u and output y_1 from sensor 1. Similarly $(P_2)_n$ is the n^{th} damage level transfer function for sensor 2. It is noted that even though the two sensors are identical and placed nearby, the transfer function associated with sensor 1 will be different from the transfer function associated with sensor 2. This difference is because each sensor will be receiving different reflected signals from a propagating crack or damage. However, the input dependant noise transfer function Q_n is assumed to be the same for both sensors since it is usually due to electromagnetic interference and electromagnetic compatibility. In addition, the sensor might receive input independent noise, denoted as ν. With the above information, the measurement equation for both sensor 1 and 2 can

be written as:

$$y_1 = (P_1)_n(jw)u + Q_n(jw)u + \nu \tag{6.1}$$

$$y_2 = (P_2)_n(jw)u + Q_n(jw)u + \nu \tag{6.2}$$

6.2.1. Damage state estimation using empirical transfer function estimation (ETFE) approach

Subtracting Eq. (6.2) from Eq. (6.1),

$$y_1 - y_2 = ((P_1)_n(jw) - (P_2)_n(jw))u \tag{6.3}$$

Eq. (6.3) can be equivalently written as,

$$y = P_n(jw)u \tag{6.4}$$

where $y = y_1 - y_2$ and $P_n(jw) = (P_1)_n(jw) - (P_2)_n(jw)$. Using spectral analysis, the transfer function $P_n(jw)$ can be expressed as

$$P_n(jw) = \frac{S_{uy}(jw)}{S_{uu}(jw)} \tag{6.5}$$

where $S_{uy}(jw)$ and $S_{uu}(jw)$ are the cross-spectral density between u and y, and auto-spectral density of u respectively. These densities can be expressed in terms of cross-covariance coefficients $C_{uy}(m)$ and auto-covariance coefficients $C_{uu}(m)$ as

$$S_{uy}(jw) = \sum_{k=-L}^{L} C_{uy}\omega(k)e^{-j\omega k} \tag{6.6}$$

$$S_{uu}(jw) = \sum_{k=-L}^{L} C_{uu}\omega(k)e^{-j\omega k} \tag{6.7}$$

where $\omega(k)$ is the lag window used for smoothening and L is the truncation parameter for the window. Substituting $y_1 - y_2$ for y in Eq. (6.6) Eq. (6.5) can be rewritten as

$$P_n(jw) = \frac{S_{uy_1}(jw) - S_{uy_2}(jw)}{S_{uu}(jw)} = (P_1)_n(jw) - (P_2)_n(jw) \tag{6.8}$$

where

$$(P_1)_n(jw) = \frac{S_{uy_1}(jw)}{S_{uu}(jw)}; \quad (P_2)_n(jw) = \frac{S_{uy_2}(jw)}{S_{uu}(jw)} \tag{6.9}$$

The frequency response function $P_n(jw)$ represents the change in damage condition at n^{th} damage level. It is a vector and to directly compare the different damage conditions using this function is difficult. An equivalent root mean square deviation (RMSD) based novel damage index a_n is proposed. The damage index is normalized against the healthy condition frequency response function and is expressed as

$$a_n = \sqrt{\frac{\sum_{\omega=\omega_f}^{\omega=\omega_i}(P_n(j\omega) - P_0(j\omega))^2}{\sum_{\omega=\omega_f}^{\omega=\omega_i}(P_0(j\omega))^2}} \tag{6.10}$$

where $P_n(j\omega) = (P_1)_n(j\omega) - (P_2)_n(j\omega)$. Here, $n = 0$ represents the reference damage level. The n^{th} level damage index a_n is the equivalent change in output (from piezoelectric sensors) time-series against a fixed input (from the piezoelectric actuator) time-series measured at the n^{th} damage level.

6.2.2. Damage state estimation using correlation analysis (CRA) approach

The accuracy of the damage index estimated using the ETFE approach depends on how accurately the spectral densities S_{uy} and S_{uu} are estimated. The accurate estimation of the spectral densities depends on the accuracy of the Fourier transformation of the respective cross-covariance coefficients $C_{uy}(m)$ and auto-covariance coefficients $C_{uu}(m)$. To avoid errors in the frequency domain transformation, the time-domain cross-correlation and auto-correlation coefficients can be directly used to estimate the time-series damage indices a_n. For a deterministic, fixed input signal the auto-correlation coefficients $C_{uu}(m)$ are fixed for all damage conditions. Ignoring the contribution from the auto-correlation

coefficients $C_{uu}(m)$, the equivalent damage index can be evaluated as

$$a_n = \sqrt{\frac{\sum_{m=-M}^{m=M}((R_{uy})_n(m) - (R_{uy})_0(m))^2}{\sum_{m=-M}^{m=M}((R_{uy})_0(m))^2}} \tag{6.11}$$

where $(R_{uy})_n(m) = R_{uy_1}(m) - R_{uy_2}(m)$, $R_{uy_1}(m)$ and $R_{uy_2}(m)$ are the m^{th} lagged cross-correlation coefficients corresponding to sensor 1 and sensor 2 respectively. The m^{th} lagged cross-correlation coefficients $R_{uy_i}(m)$ are expressed in terms of the m^{th} lagged cross-covariance function $C_{uy_i}(m)$ as

$$R_{uy_i}(m) = \frac{C_{uy_i}(m)}{\sqrt{C_{uu}(m)}\sqrt{C_{y_iy_i}(m)}} \tag{6.12}$$

Where $n = 0$ represents the reference damage level. The damage index a_n is the representation of the n^{th} damage condition with respect to the reference ($n = 0$) or known damage condition. It is also important to mention that both the proposed damage index estimation approaches (ETFE and CRA) are valid for any complex structure and the validation of these approaches will be discussed in the following sections.

6.3. Numerical Results

To evaluate the performance of the damage index estimation at different damage conditions, both broadband and narrowband active signals are tested. To generate the output sensor signal against the broadband actuator input, a fatigue experiment is performed, whereas for generating the output sensor signal against the narrowband actuator input, a finite element simulation is performed. The finite element simulation is time consuming and the computational time and memory requirements increase significantly with an increase in the length of the input signal. In this work, finite element simulations are performed only for the narrowband input signal. The details of the fatigue experiment, finite element

simulation, and corresponding numerical evaluation of proposed damage index estimation approach are given below.

6.3.1. Fatigue experiment for broadband active sensing

To test the real-time state estimation algorithm, a fatigue test was performed on an Al-2024 cruciform specimen under biaxial loads. As shown in Figure 6.2, the cruciform specimen was loaded using a MTS biaxial/torsion test frame. The specimen was subjected to a constant amplitude fatigue load with amplitude $\sigma_{max} = 21.36$ kN, load ratio R=0.1, and frequency of 10 Hz. For damage state estimation at different damage levels, piezoelectric actuators and sensors were used. The instrumented cruciform specimen with different sensor configurations can be seen in Figure 6.3. After each 1500 cycles, the test frame was programmed to stop for 75 seconds and during this period, piezoelectric sensor signals were collected for a deterministic (or fixed) input signal. Images of the propagating damage were also collected using a high resolution camera. The data and image collection started at approximately 10 kcycles. The image and sensor data were collected at 95 different damage levels. It should be noted that to accelerate the crack initiation process, a circular hole (refer Figure 6.3) was made at the center of the web area. An EDM notch (in the bottom right quadrant of web area) of length 1 mm was made at the edge of the circular hole to accelerate crack initiation (Figure 6.3). A through crack started from the EDM notch at approximately 19 kcycles (refer Figure 6.4) and grew towards the bottom edge of the web area. Once the crack reached the bottom edge of the web, a second crack initiated at the upper boundary (along the vertical axis) of the central hole. The second crack grew up to the top boundary of the web before final catastrophic failure occurred. The second crack growth was rapid and occurred only within 6 kcycles before final failure

occurred at 151 kcycles. Out of the total 95 damage levels, the crack tip was in focus (of the high resolution camera) only for the first 48 images. The crack length measurement corresponding to different damage levels (or fatigue cycles) and different sequence of events can be seen in Figure 6.4. In the case of active sensing, the input signal considered for this study was a broadband chirp signal with frequency varying from 100 kHz to 300 kHz and is shown in Figure 6.5a. The persistence of excitation in the chosen band can be seen from the spectral density plot shown in Figure 6.5b. A representative sensor signal from sensor 1 (Ref. S1 in Figure 6.3) at the healthy condition is shown in Figure 6.5c, and the corresponding spectral density is shown in Figure 6.5d. From Figure 6.5d it can be seen that the output power spectral density, between 100 kHz to 300 kHz, is found to be persistently higher than -100dB/Hz. The persistence of excitation can also be seen from the spectrogram plots of the input and output signal shown in Figure 6.6a and 6.6b, respectively. This persistence of excitation of structural modes in the chosen frequency band is a good indicator for unbiased state estimation. It is noted that at each damage level, five sets of active signals were collected by exciting the piezoelectric actuator in five seconds intervals. These multiple sets of observations at a single damage level were collected to avoid any measurement loss due to false actuation and to quantify the error bound in the damage index estimation. The measured sensor signals at different damage levels are used to estimate the corresponding damage index. Details of the process are discussed below.

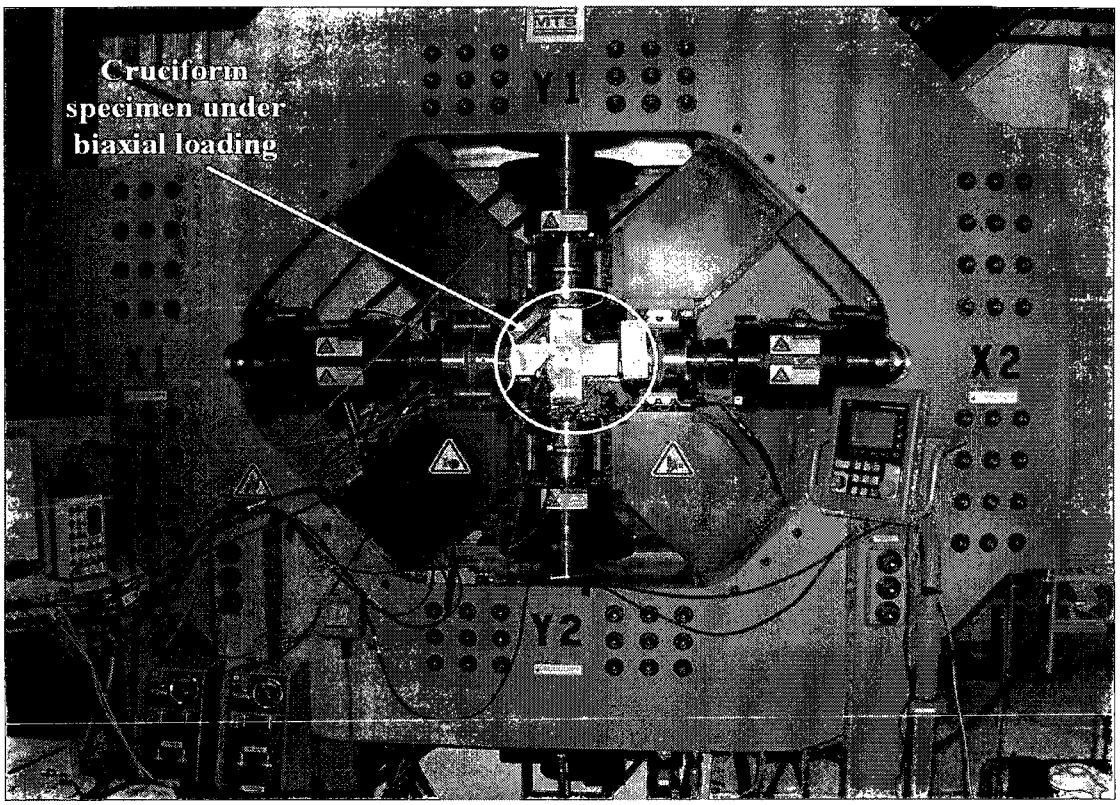

Fig. 6.2. Experimental setup with instrumented cruciform specimen.

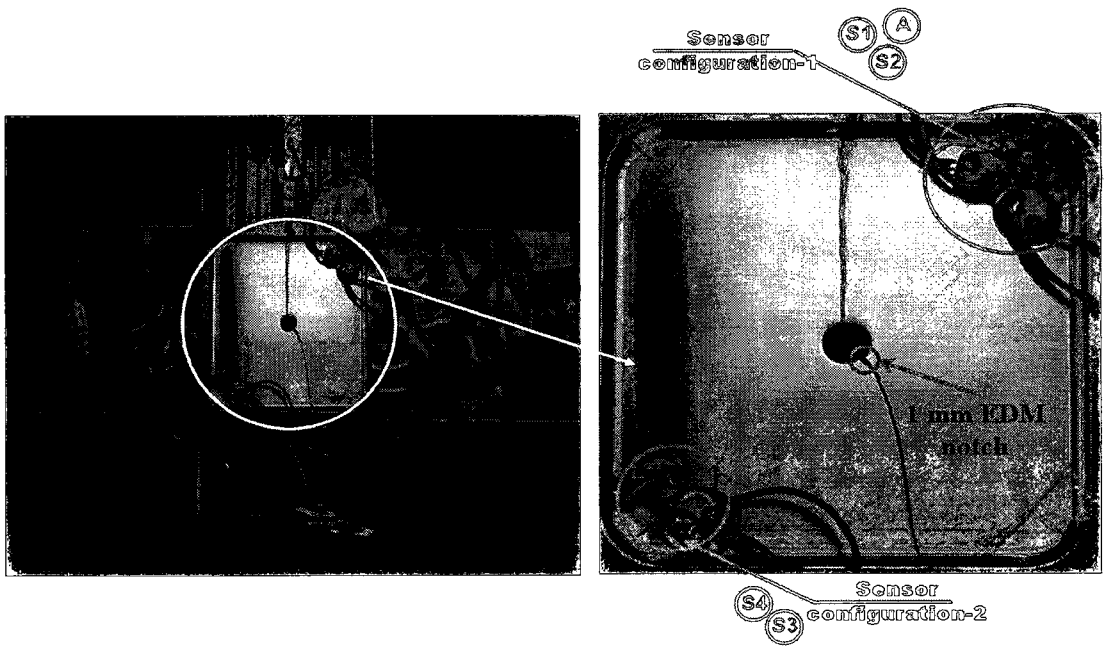

Fig. 6.3. Magnified cruciform specimen with different sensor configurations.

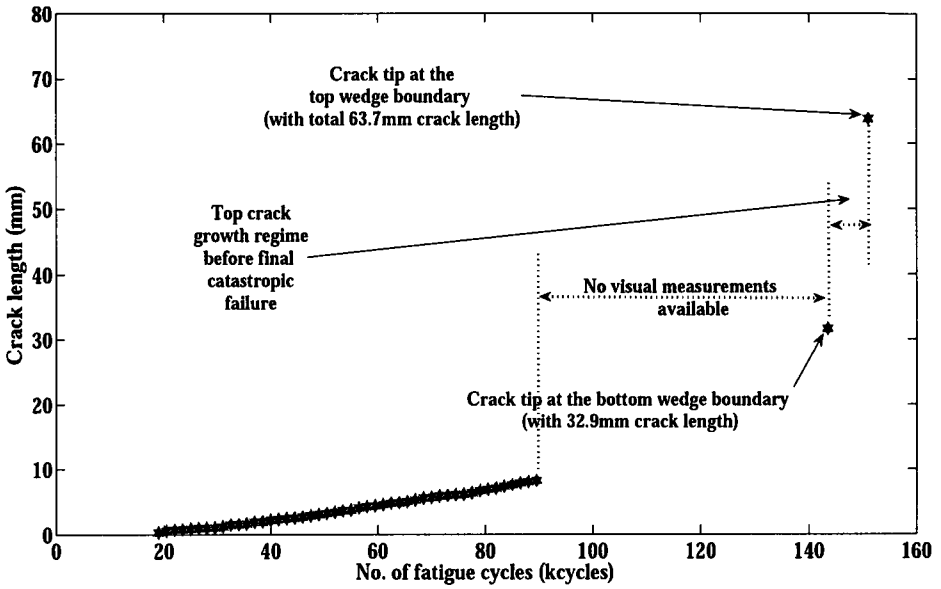

Fig. 6.4. Visual measurements with different sequence of events.

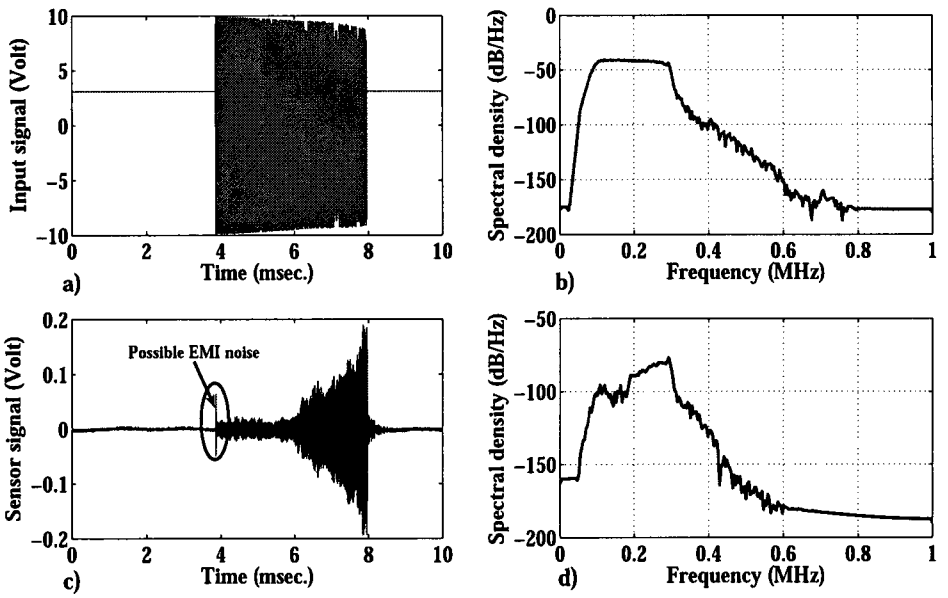

Fig. 6.5. a) Broadband chirp input with frequency sweep from 100 kHz to 300 kHz b) Power spectral density of the input signal c) Signal from sensor 1 at a typical damage level. d) Power spectral density of the sensor signal in c).

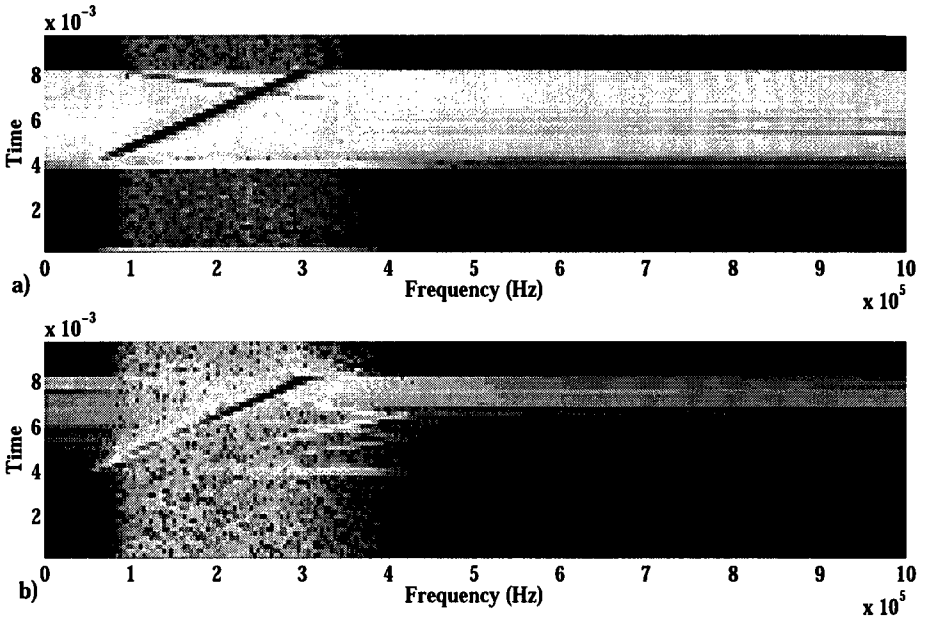

Fig. 6.6. Spectrogram of input and output signal shown in Figure 6.5a and c.

6.3.2. Finite element simulation for narrowband active sensing

To evaluate the performance of the damage index estimation against the narrowband burst signal, finite element (FE) simulations are performed. Ten different damage cases were considered. The details of the different damage cases are given in Table 6.1. The finite element model for a typical case (case 10) can be seen in Figure 6.7a. The piezoelectric actuator and sensors are located at the same positions as the experimental setup (Figure 6.3). A snapshot of the wave propagation simulation for damage case 10 can also be seen in Figure 6.7b. This wave propagation simulation study shows that due to the presence of a large crack in front of the actuator, sensors placed on the opposite side of the crack (e.g., sensor 3 and sensor 4 of sensor configuration 2) become blind to the traveling input waves. For all ten damage cases, the piezoelectric actuator is excited with a 230 kHz narrowband burst input as shown in Figure 6.8a. Figure 6.8b shows the power spectral density of the input signal. The sensor signal from sensor 1 and its power spectral density can be seen

Damage case	Crack size
1	Healthy condition (with 1 mm notch)
2	5 mm bottom crack
3	10 mm bottom crack
4	15 mm bottom crack
5	20 mm bottom crack
6	25 mm bottom crack
7	30 mm bottom crack
8	32 mm bottom crack
9	17 mm top (total crack length of 49 mm) crack
10	32 mm top (total crack length of 64 mm)

TABLE 6.1
DIFFERENT FE SIMULATED DAMAGE CASES

in Figure 6.8c and Figure 6.8d, respectively. In addition, Figures 6.9a and 6.9b show the spectrograms of the actuator and sensor signals shown in Figure 6.8. The simulated sensor signals at different damage levels are used to estimate the damage index.

6.3.3. Time-series damage state estimation

Sensor signals generated using the fatigue experiment and FE simulation are used for estimating the time-series damage index. The details of the results are explained in the following subsections.

6.3.3.1. *Damage index estimation using finite element simulated narrowband active sensing*

Damage indices based on both the empirical transfer function estimation approach and the correlation analysis approach are evaluated. The narrowband sensor signals are collected for the different FE simulated damage conditions discussed earlier. Using empirical transfer function estimation, the respective results for sensor configurations 1 and 2 are shown in Figure 6.10 and Figure 6.11. From Figure 6.10 it can be seen that there is a good trend in the damage index only from damage level 6, which is equivalent to 25 mm of crack length.

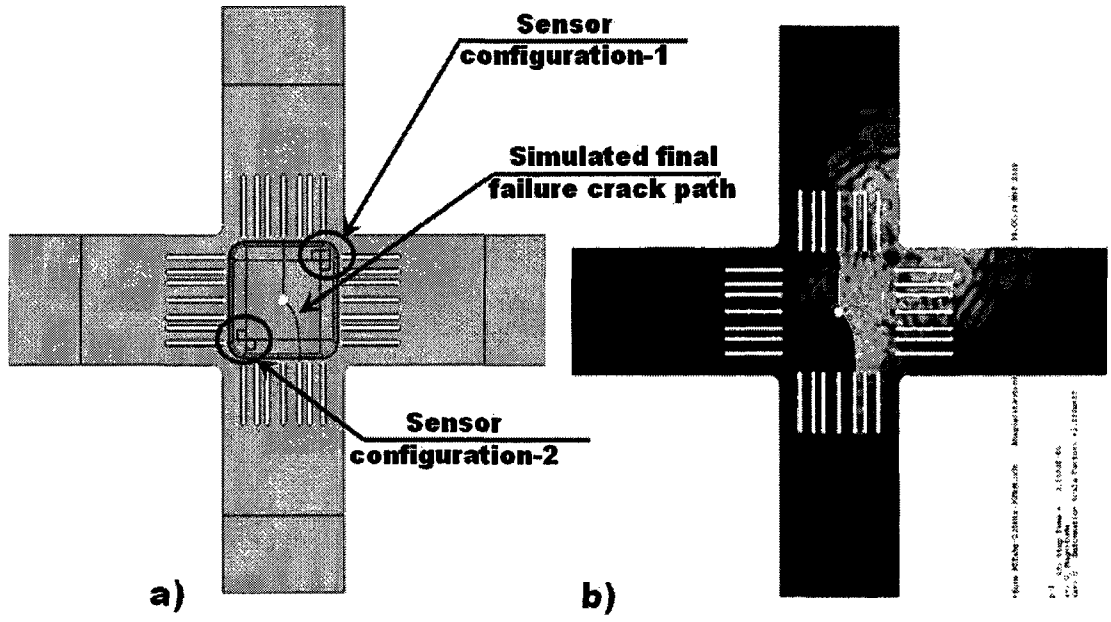

Fig. 6.7. a) Finite element simulation showing crack path during final catastrophic failure b) Snap shot of wave propagation with simulated crack path as shown in Figure a.

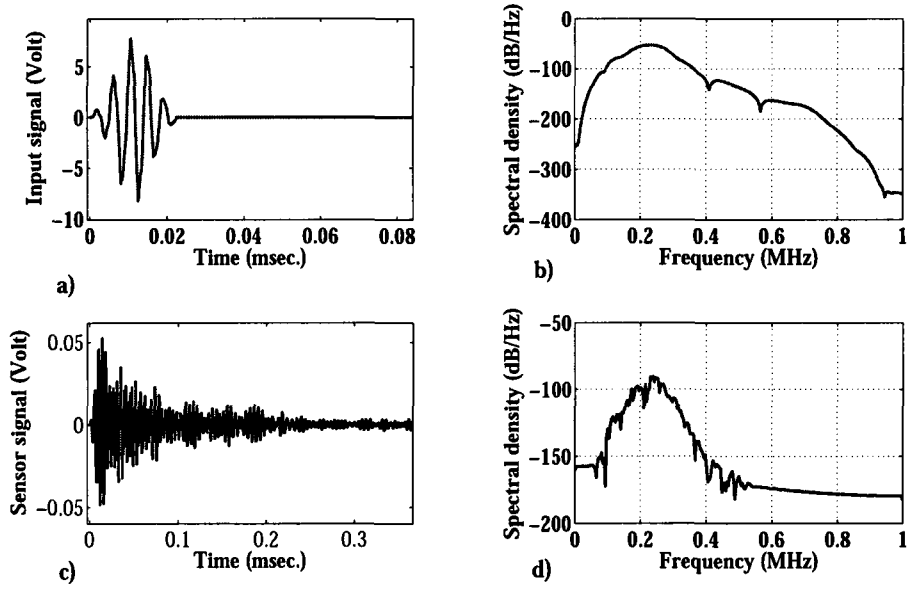

Fig. 6.8. a) Narrowband burst input with central frequency 230 kHz b) Power spectral density of the input signal c) Sensor signal from sensor 1 d) Power spectral density of the sensor signal in Figure c.

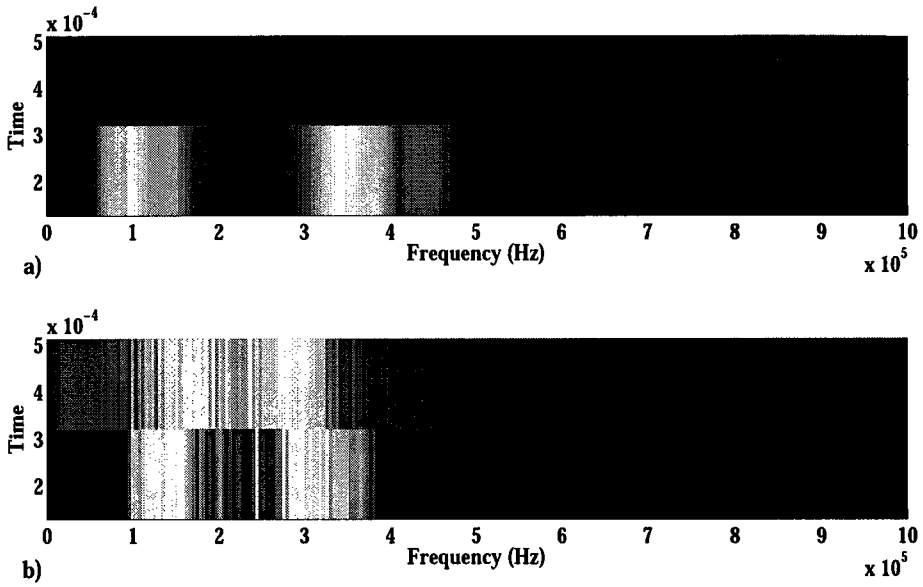

Fig. 6.9. Spectrogram of input and output signal shown in Figure 6.8a and 6.8c.

In case of sensor configuration 2 the damage index estimation is less accurate and there is no proper trend for the entire damage regime. Damage indices based on correlation analysis are evaluated for both sensor configurations 1 and 2 and are shown in Figure 6.12 and Figure 6.13. Compared to the damage indices estimated using empirical transfer function estimation, the correlation analysis based damage indices show a slightly better trend of cumulative damage growth. It is also seen that, similar to the empirical transfer function estimation approach, the correlation approach shows a better trend for sensor configuration 1 compared to sensor configuration 2. The poor performance of sensor configuration 2 is due to the development of a shadow region that is formed by the propagating cracks in front of the actuator. This leads to a poor damage signature in measurements from sensor configuration 2.

It is seen that the narrowband input based ETFE and CRA approaches show poor

performance of damage index estimation during smaller damage growth regime (i.e., below damage level 6 equivalently to 25mm crack length). It must be noted that signals based on FE simulation are noise free. Although the present narrowband based FE simulation signals are noise free, the damage index estimation using these signals fails to provide a clear trend of damage index growth throughout the fatigue life. A potential reason for the lack of trend in the damage index estimation is the narrowband signals central frequency, which may not necessarily be optimal for the chosen actuator and sensor location. Moreover, other structural modes (other than the structural mode associated with the central frequency of the narrowband signal) associated with the local damage are not persistently excited. This leads to a weaker signature in sensor signals. The above mentioned limitations in narrowband based SHM points to a need for exploring the usefulness of broadband active sensing, which is discussed in the following section.

6.3.3.2. *Damage index estimation using experimental broadband active sensing*

Unlike the case of narrowband input, for broadband input it is not required to tune its central frequency with the resonant frequency of the interrogated structure. Also, the tuned central frequency for narrowband input does not necessarily remain optimal as damage progresses. The broadband input consists of multiple sinusoids with different frequencies spread over a larger envelope that may be affected by damage. The multiple structural modes are affected by the damage and it is expected that a broadband input will excite those individual structural modes. Hence a broadband input does not require any frequency tuning of the input signal with the resonant frequency of the structure. Using the broadband chirp signals, the damage indices are estimated using Eq. (6.10) of the ETFE approach and

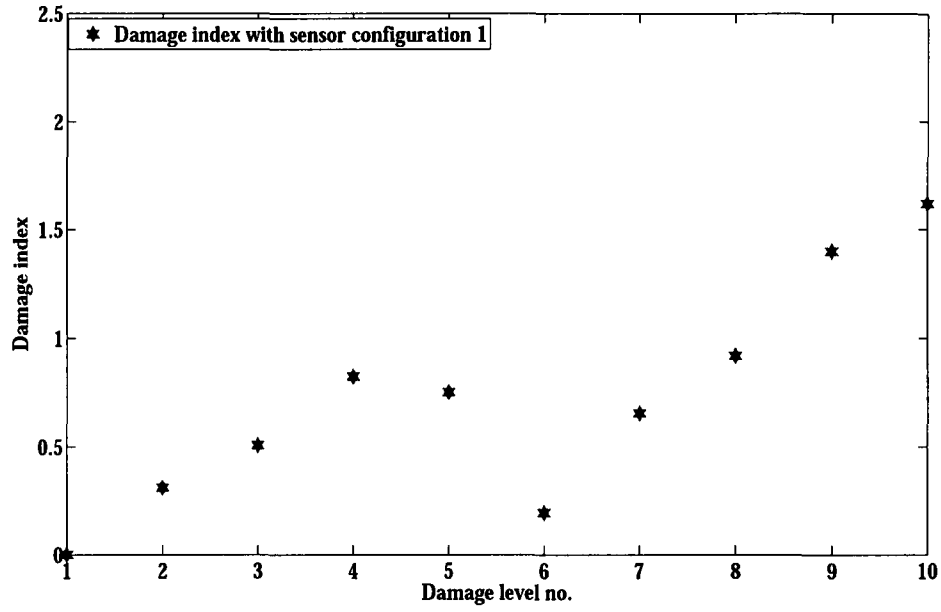

Fig. 6.10. Estimated damage index using ETFE approach and narrowband input signal from sensor configuration 1.

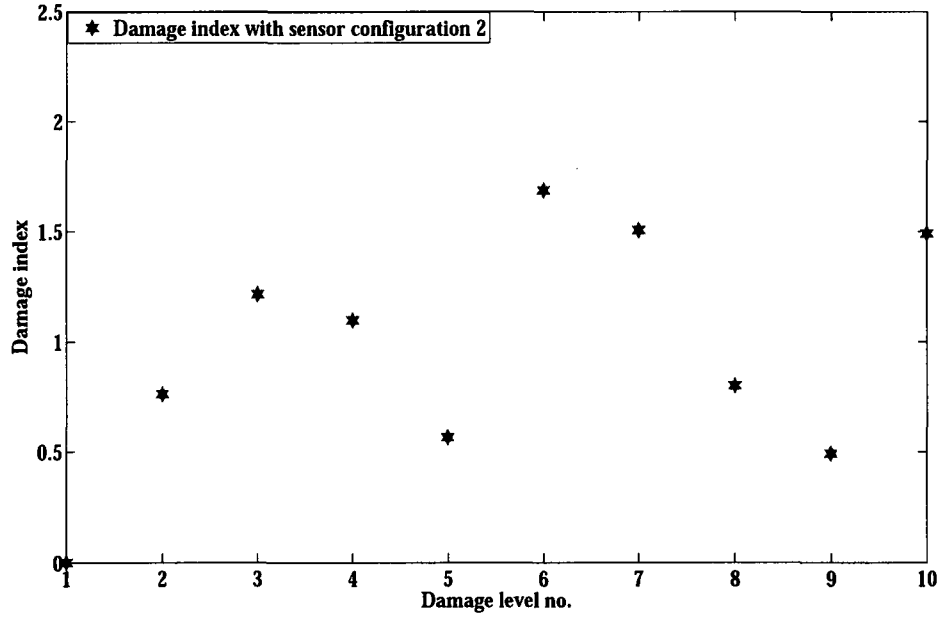

Fig. 6.11. Estimated damage index using ETFE approach and narrowband input signal from sensor configuration 2.

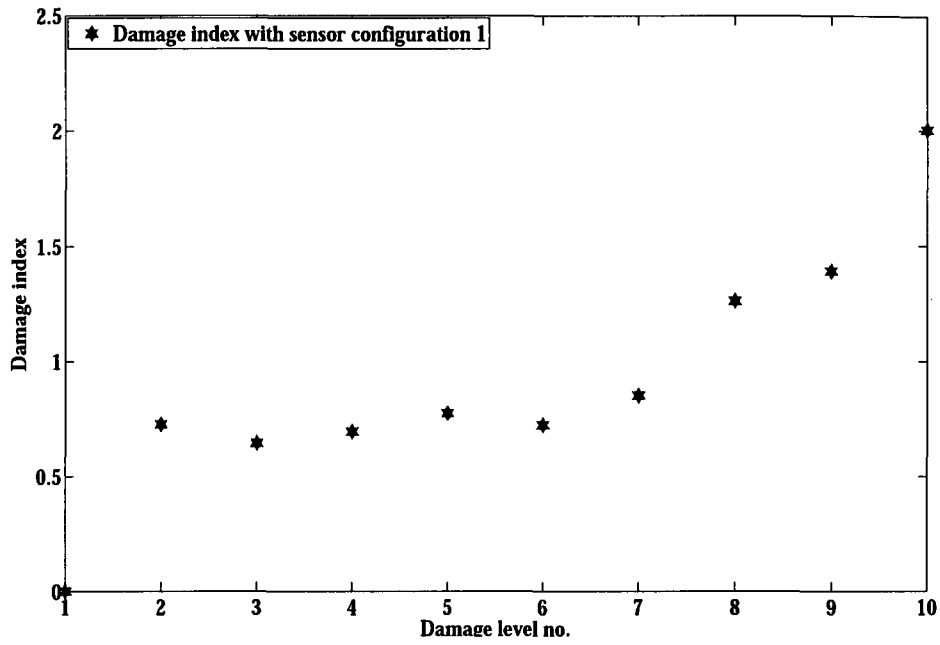

Fig. 6.12. Estimated damage index using correlation analysis approach and narrowband input signal from sensor configuration 1.

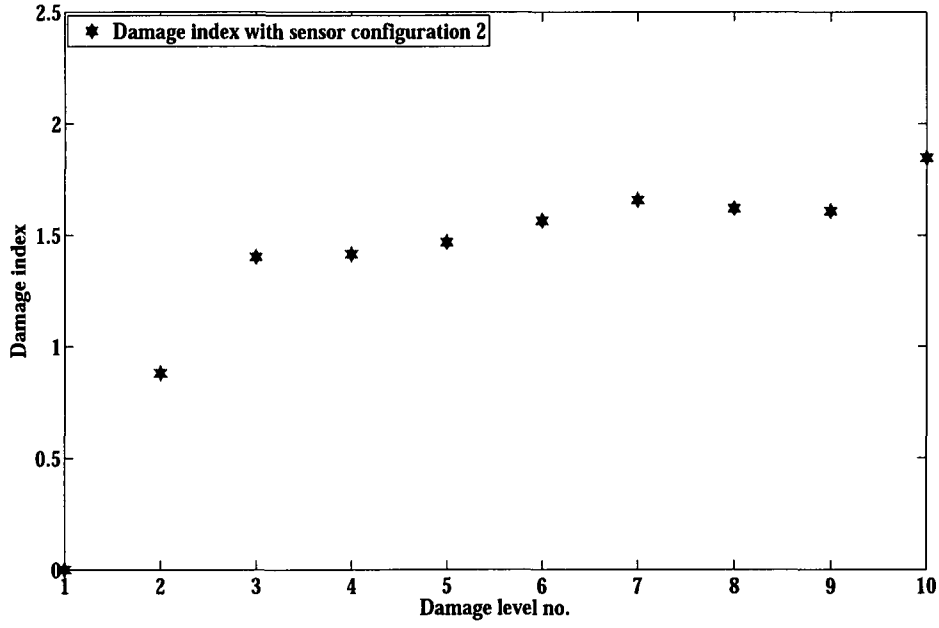

Fig. 6.13. Estimated damage index using correlation analysis approach and narrowband input signal from sensor configuration 2.

Eq. (6.11) of the CRA approach. For both sensor configurations the time series damage indices are estimated using the ETFE approach and shown in Figure 6.14 and Figure 6.15. For the CRA approach, the damage indices estimated using sensor configuration 1 and 2 are shown in Figure 6.16 and Figure 6.18. For each set of sensor signals, five different damage indices are estimated. Figure 6.14 to Figure 6.18 show the mean damage index and associated 2σ error bounds at different damage levels. For ETFE approach it is found that (Figure 6.14 and Figure 6.15) up to approximately 82 kcycles, there is a good correlation of cumulative damage growth between estimated damage index and available visual measurements (Figure 6.4) for both sensor configurations 1 and 2. However, after 82 kcycles it can be seen that (Figure 6.15) the damage index time series estimated using sensor configuration 2 does not show an increasing trend. This is due to the creation of a blind zone that leads to weaker signals being received by the sensors in configuration 2. On the other hand, for the entire fatigue loading regime, configuration 1 shows an increasing trend of damage index time series, which is evident in Figure 6.14. The increasing trend for sensor configuration 1 better resembles the physical phenomenon associated with cumulative damage growth.

In the case of the CRA based approach it is found that up to approximately 110 kcycles there is a continuous increasing trend of damage index time-series for both sensor configurations 1 and 2 (Figure 6.16 and Figure 6.18). However, after 110 kcycles it can be seen that the damage index time-series estimated using sensor configuration 2 (Figure 6.18) does not show continuous increasing trend. This is again due to the creation of a blind zone that leads to weaker signals being received by the sensors in configuration 2. On the other hand, for the entire fatigue loading regime, configuration 1 shows (Figure

6.16) an increasing trend of damage index time-series. This is more evident when Figure 6.16 is magnified as seen in Figure 6.17. It must be noted that although both approaches use the same sensor signals, in both sensor configurations the CRA based approach shows better trend in damage index growth compared to the ETFE based approach. For example, for sensor configuration 2, the ETFE based approach shows the cumulative damage index growth trend up to 82 kycles (Figure 6.15), whereas for CRA approach the corresponding trend is up to 110 kcycles (Figure 6.18). The higher accuracy of the damage index estimated using CRA approach is due to the direct use of cross-covariance coefficients $C_{uy}(m)$ and auto covariance coefficients $C_{uu}(m)$ (Eq. 6.12) rather than performing Fourier transformation of those (Eq. 6.6 and Eq. 6.7), while evaluating the damage index using ETFE based approach.

Figure 6.14 to Figure 6.18 also indicate that the rate of damage index growth is higher between 10 to 19 kcycles compared to that after 19 kcycles. This trend is observed for both sensor configurations 1 and 2 and with both damage index estimation approaches. The higher growth rate is possibly due to the creation of multiple surface cracks in front of the EDM notch (Figure 6.3). These surface cracks coalesce before forming a visible through crack at 19 kcycles. As seen from Figure 6.4 these surface cracks were not captured in the image either because the cracks were developed on the opposite side of the specimen (opposite to the camera) or due to lack of clarity in the captured image. For CRA based approach, similar trend in high damage index growth rate is also observed from 140.5 kcycles to 142 kcycles. From Figure 6.16 and 6.18 it can be seen that at 140.5 kcycles, when the top crack has not initiated (Figure 6.4 and 6.19a), the corresponding damage index was approximately 1.419 for sensor configuration 1 and 1.128 for sensor configuration 2. At 142

kcycles there is a sudden jump in damage index to 1.973 for sensor configuration 1 and to 1.23 for sensor configuration 2. From the acquired image shown in Figure 6.19b it is seen that there was no through crack at the top edge of the central hole. The jump in damage index again is possibly due to the development of multiple surface cracks. The snap-shot of the surface cracks coalescing (before the onset of a through crack at the top edge of the central hole) can be clearly seen from Figure 6.19c. Due to the development of multiple surface cracks, the signals received at the sensors are highly distorted and a jump or high growth in damage index is observed. From 140.5 kcycles to 142 kcycles this trend of high damage index growth rate is not observed (Figure 6.14 and 6.15) for ETFE based approach. This is because the ETFE based approach is not sensitive, as CRA approach, to distinguish between large crack opening and the corresponding precursory surface crack around it. It is also seen that the 2σ error bounds for correlation approach (Figure 6.16 and Figure 6.18) is significantly narrower compared to the ETFE based 2σ error bounds (Figure 6.14 and Figure 6.15). The lower 2σ error bounds in case of CRA approach compared to ETFE approach is due to the direct use of time response signals rather than Fourier transformed correlation coefficients used in ETFE approach.

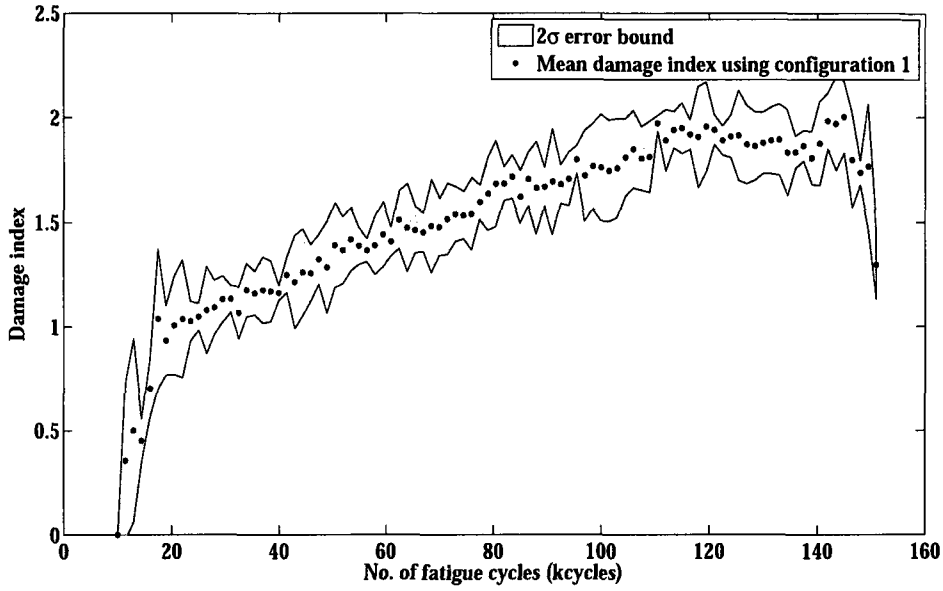

Fig. 6.14. Time series damage index estimated using ETFE approach and sensor configuration 1

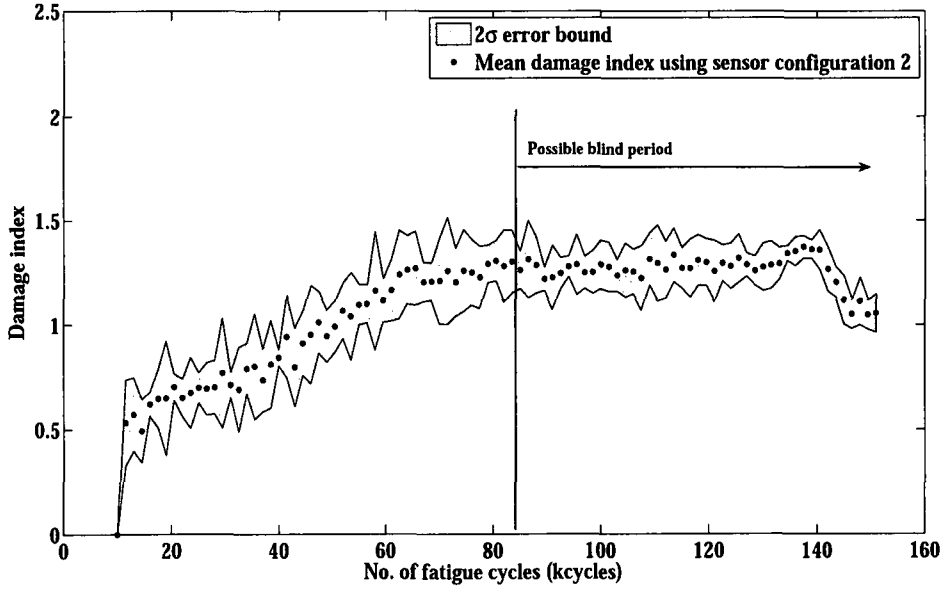

Fig. 6.15. Time series damage index estimated using ETFE approach and sensor configuration 2

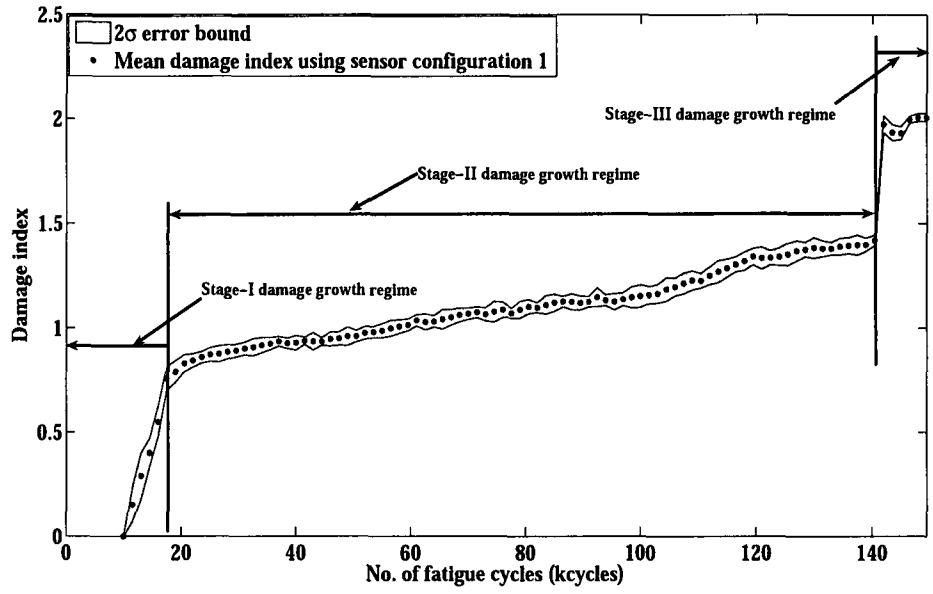

Fig. 6.16. Time series damage index estimated using correlation analysis approach and sensor configuration 1

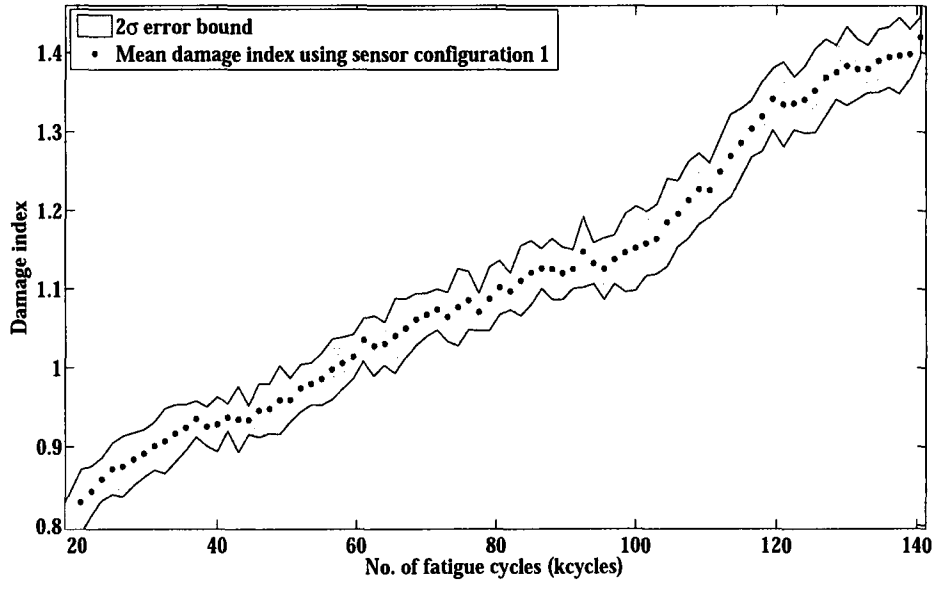

Fig. 6.17. Magnified (from 20 kycles to 140 kcycles) version of Figure 6.16

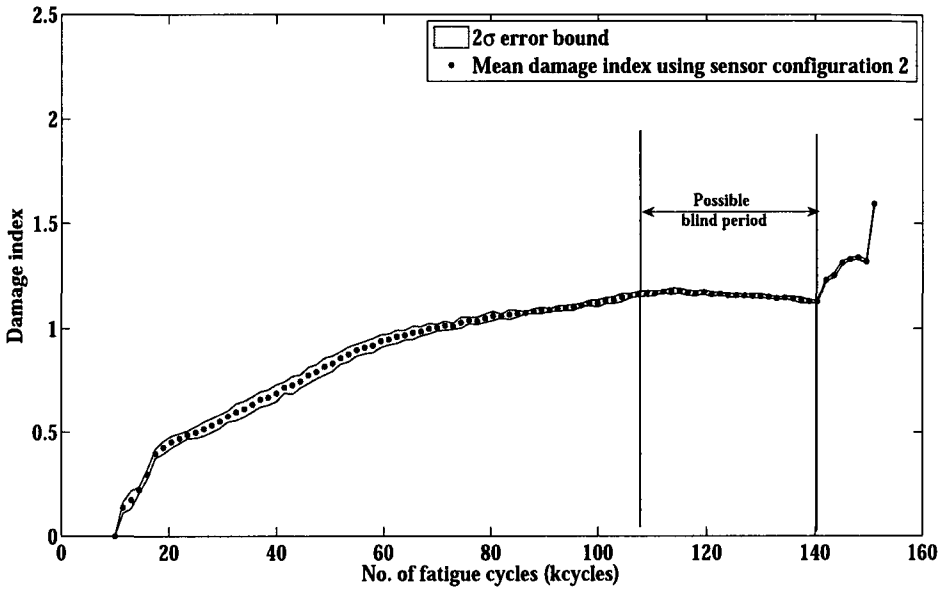

Fig. 6.18. Time series damage index estimated using correlation analysis approach and sensor configuration 2

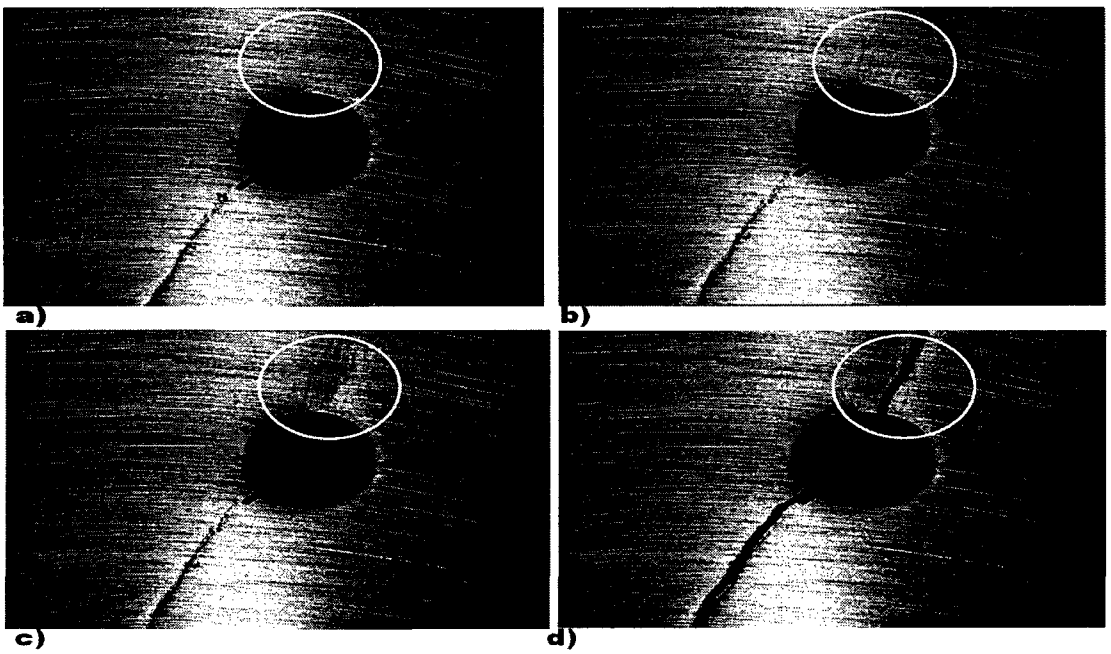

Fig. 6.19. Visual image snapshots at a) 140.5 kcycles b) 142 kcycles c) 149.5 kcycles d) 151 kcycles.

6.3.3.3. *Noise sensitivity evaluation*

The sensitivity of the damage index to noise is evaluated by estimating the index from 500 different sets of observations acquired at a particular damage level (in this case at the healthy condition). The 500 observation sets are collected at 2 second intervals by repeatedly exciting the actuator. The corresponding damage indices for ETFE based approach are plotted in Figure 6.20. It can be seen that the value of each damage index is restricted to 0.5 for all 500 sets of observations. This observation suggests that damage indices greater than 0.5 not only have the contribution from measurement noise but also have the contribution from the change in damage state. This sensitivity analysis also suggests that at a particular damage level, the maximum variation (due to electrical noise) of estimated damage index is limited to 0.5. The sensitivity information can also be correlated with the 2σ error bound presented in Figure 6.14 and Figure 6.15, which shows that the maximum variation in damage index about its mean damage level does not exceed 0.5. Similar sensitivity analysis is also performed for the CRA approach. The corresponding damage indices for 500 different sets of observations are estimated and are presented in Figure 6.21. It can be seen that the damage index value in this case is much smaller than the one obtained for the ETFE based approach. The damage index is restricted to a value of 0.1, except for a few outliers, for all 500 sets of observations. The above sensitivity analysis can also be correlated with the 2σ error bound, shown in Figure 6.16 and Figure 6.18, which shows that the maximum variation in the damage index (due to electrical noise) at any particular damage level is not more than 0.1. Comparison of the error bound and the sensitivity analysis results also shows that the CRA approach is less sensitive to noise compared to the ETFE based approach.

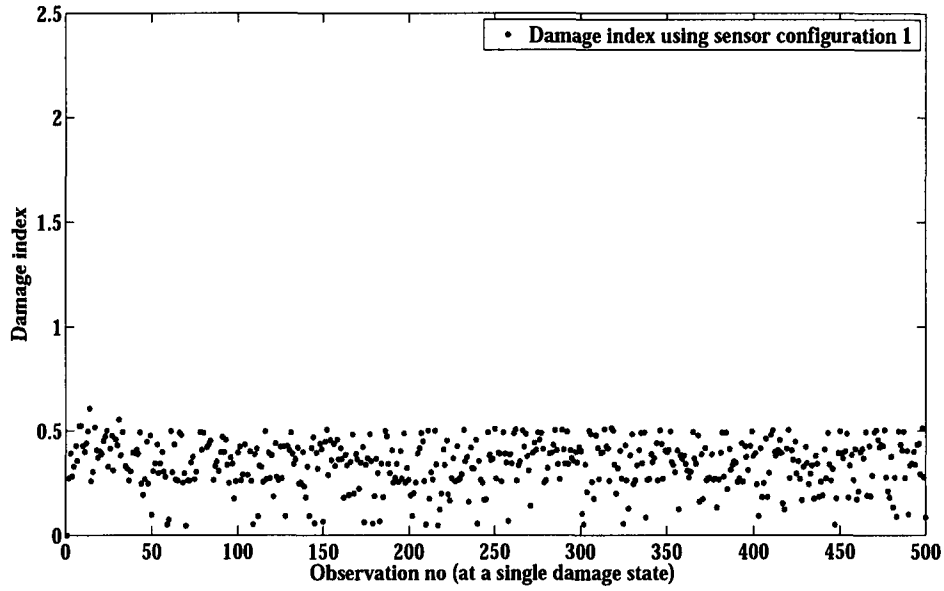

Fig. 6.20. Check of the sensitivity of the damage index estimation using ETFE approach and 500 different sets of observation collected at a particular damage level.

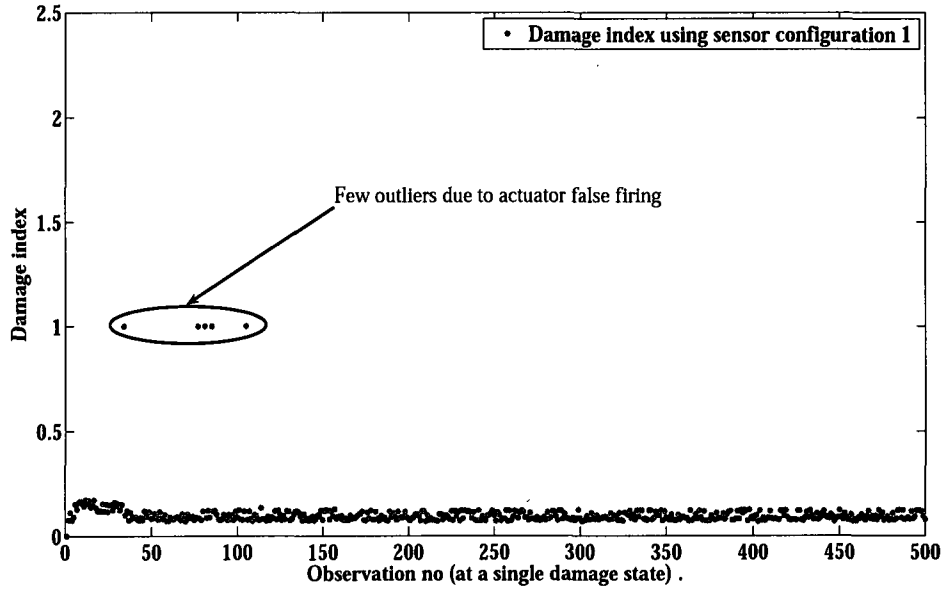

Fig. 6.21. Check of the sensitivity of the damage index estimation using correlation analysis and 500 different sets of observation collected at a particular damage level.

6.4. Conclusion

The use of two nonparametric system identification techniques namely, the empirical transfer function estimation approach and correlation analysis approach were investigated to estimate the time-series fatigue damage states. Novel dual sensing method is used to perform ultrasound input based system identification. From the numerical study it was found that the correlation based damage index estimation follows a better trend of cumulative damage growth compared to the empirical transfer function estimation based approach. The damage indices were estimated using both narrowband based burst input and broadband based chirp input. It was found that the damage index estimation based on the broadband chirp input outperforms the narrowband input based damage index estimation. Additionally, two different sensor configurations were studied. It was observed that the sensor configuration with sensors near the actuator was more effective for time series damage state estimation than the sensor configuration that had sensors placed away from the actuator. The time-series damage estimation approaches are validated on a complex Al-2024 cruciform specimen undergoing biaxial cyclic loading. The proposed unsupervised approaches can be useful for online health monitoring of any complex structure.

CHAPTER 7

Passive Sensing Based Online Damage State Estimation under Constant Cyclic Fatigue Loading

7.1. Introduction

Unsupervised broadband active sensing based techniques discussed, which can be used to estimate sub-millimeter level damage over the entire fatigue life including stage-I, II and III crack growth regimes have been discussed in chapter 6. The techniques can effectively be used to monitor critical structural hotspots such as the lug-joint that connects the fuselage with the main wing box. Although, active wave propagation based interrogation technique can estimate very small damage, it has the following major drawbacks. Specifically the sensing radius of an individual active sensing node is very small (in centimeters) and requires a large number of actuators and sensors to monitor a large structure. The need for a large number of sensors (in order of thousands) limits the usability of active sensing approach for large structures such as the entire wing of an aircraft. Also, the wave based techniques require an external excitation source, which is a major power driver. Furthermore, it is highly sensitive to reference boundary conditions. This sensitiveness can some times lead to false positive damage estimation if there is a little change in reference condition that does not necessarily affect the structural integrity. Based on the advantages and disadvantages of active sensing techniques it is practical to apply active wave based techniques for highly sensitive and tightly controlled structural hotspots (e.g., lug joint connectors that connect aircraft wing with the fuselage, landing gear, etc.). The overall structure on the other hand can be monitored using any vibration based passive sensing techniques ([116], [117]). The passive sensing technique has some advantages over active wave based techniques. For example passive techniques are more global and can monitor

a large structure if sensors are placed strategically. In addition, passive sensing techniques do not require any external power source as in case of active sensing. However, one of the major drawbacks in current passive sensing approach is hardware based, and specifically the type of sensor used. Though the use of different type of sensors are application specific, the accelerometer based damage monitoring approaches ([28], [118], [119]) are less sensitive for detecting smaller damage. In the above mentioned works the damage signatures are prominent only during the final failure regime. To alleviate the disadvantage of both wave based active sensing and accelerometer based passive sensing approaches, in the present work a novel strain gauge measurements based passive damage interrogations technique is developed. Though the strain gauge measurement is more local to accelerometer measurement, it is more global to wave based active sensing techniques. The strain gauges can be placed strategically in structural hotspots for passive and continuous monitoring of fatigue damage. It must also be noted that the strain gauge sensing techniques are more matured compared to wave based active sensing techniques. They neither require any external power source, nor are they sensitive to slight change in reference boundary conditions. The present chapter discusses a novel strain gauge measurements based passive sensing techniques that can estimate time-series damage states under constant cycle fatigue loading. The approach is demonstrated for an Al-6061 cruciform specimen subjected to biaxial and constant cycle fatigue loading.

7.2. Theoretical Approach

Aircraft structures and other structural system undergo fatigue loading. Two different locations of the structure experience different strain fields. There exists a particular correlation pattern between the dynamic strains fields measured at those locations. Due to

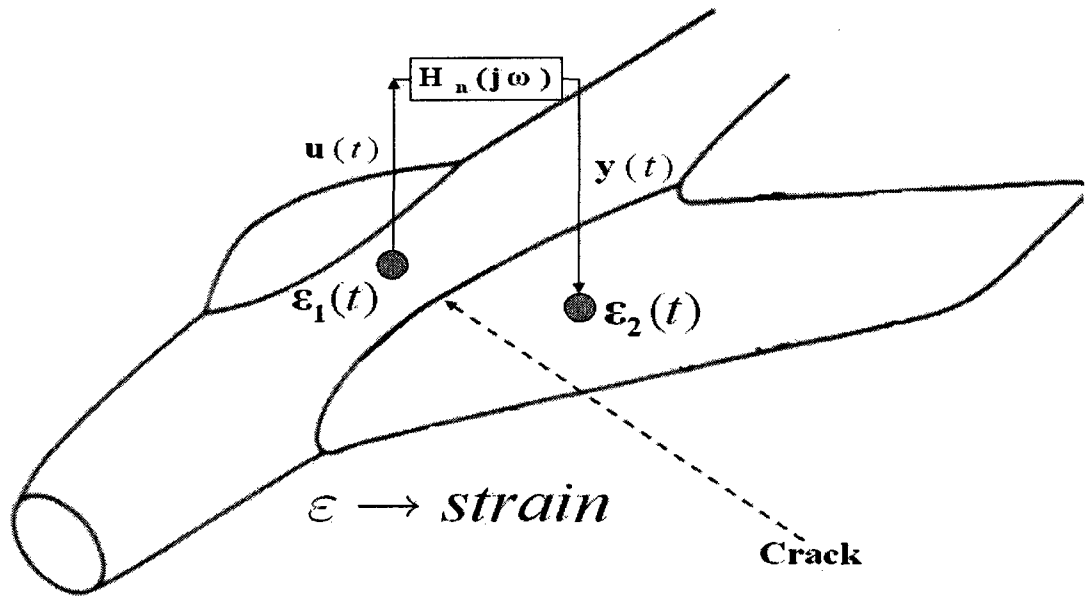

Fig. 7.1. Schematic showing strain at two points of a structure and related time-varying transfer function.

damage this correlation pattern changes. The change in correlation pattern can be mapped as a time-varying transfer function or can be a measure of time-varying damage condition. The schematic of the time-varying transfer function (H_n) between dynamic strain at two points is shown in Figure (7.1). In practical applications fatigue damage condition can be monitored in real-time by collecting online signals from passive sensors such as strain gauges. By using the strain measurements at two different locations the damage state of the structure between those two points can be estimated. To estimate the time-series damage states, the overall fatigue life can be divided into multiple short term discrete instances as shown in Figure (7.2). The strain measurements at those short term discrete instances can be used to estimate the corresponding damage states. The details of the damage state estimation approach is discussed in the following subsections.

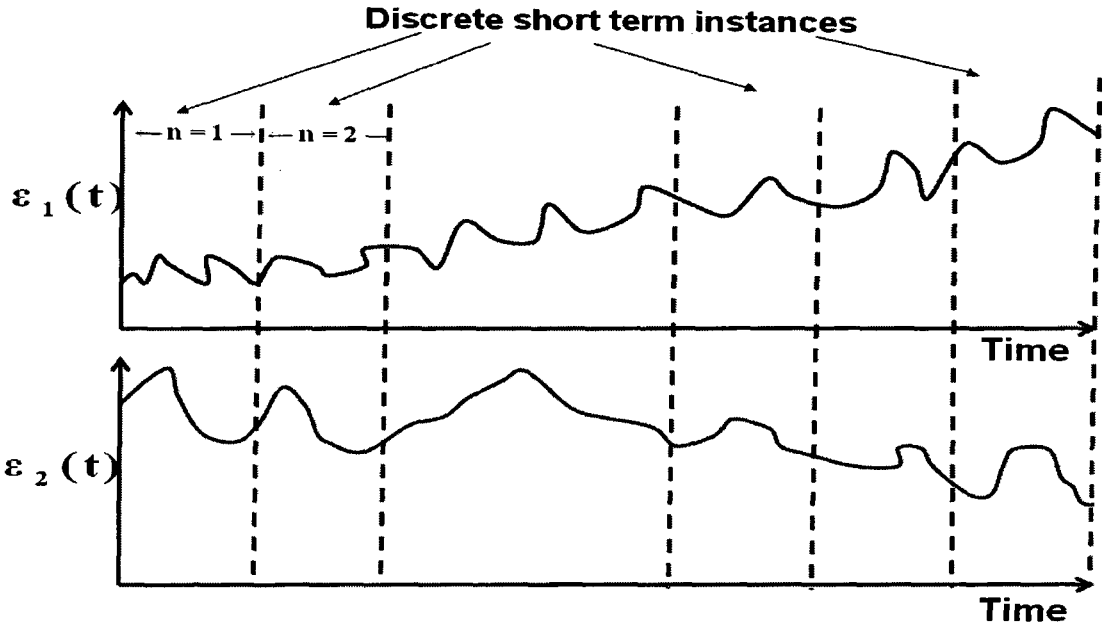

Fig. 7.2. Schematic showing the division of overall fatigue life to multiple discrete short term instances

7.2.1. Online n^{th} damage level transfer function estimation

At any particular damage level, the damage state of the structure is assumed to be unchanged and the corresponding output sensor measurement can be mapped with the input sensor measurement over a time invariant transfer function. As the state of the structure changes, the input-output mapping becomes time variant and the corresponding transfer function has to be estimated recursively. A typical n^{th} damage level block diagram that maps the input sensor measurements with the output sensor measurements is shown in Fig. 7.2. The fast scale z-domain transfer function $P(z)$ between input u and output y

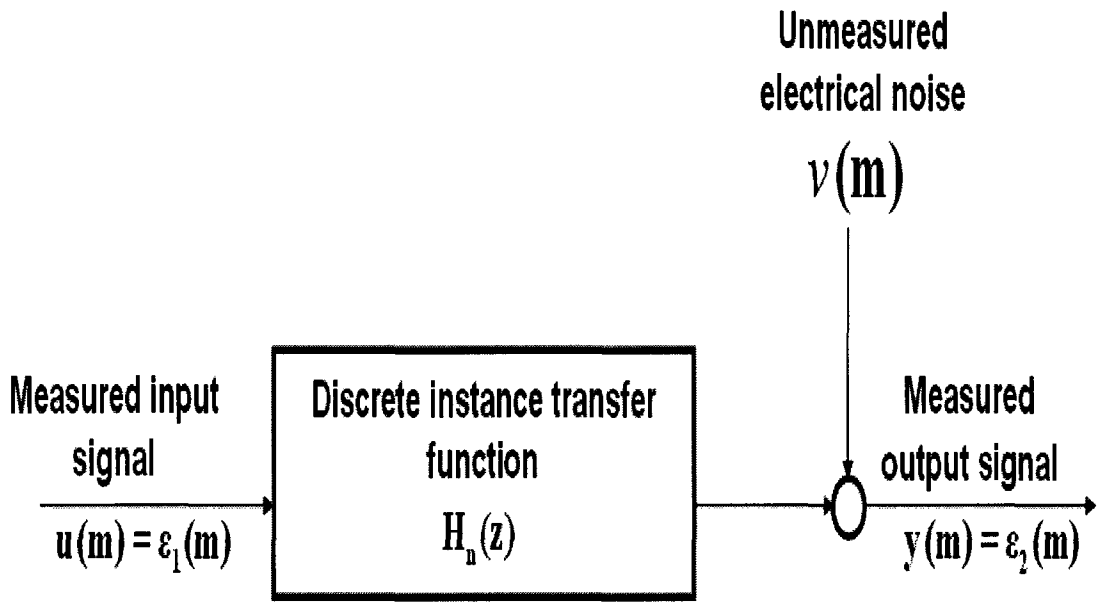

Fig. 7.3. Block diagram for fast scale transfer function. The transfer function is an instantaneous representation of the time degrading structure at any typical damage level. However as the damage grows the transfer function also changes leading to a time variant approach of system identification.

at n^{th} damage level can be represented as:

$$\begin{aligned} y(t) &= H_n(z)u(t) + \nu(t) \\ &= (b_0 + b_1 z^{-1} + b_2 z^{-2} + \ldots + b_M z^{-M})u(t) \\ &+ \nu(t) \end{aligned} \tag{7.1}$$

where $z^{-m}; m = 0, 1, \ldots M$ are the backspace operators of the pulse transfer function $P(z)$ and $b_m; m = 0, 1, \ldots M$ are the finite impulse response (FIR) [110, 111] coefficients. Eq. (7.1) can be rewritten in the discrete domain as

$$\begin{aligned} y(t) = b_0 u(t) &+ b_1 u(t-1) + b_2 u(t-2) \\ &+ \ldots + b_M u(t-M) + \nu(t) \end{aligned} \tag{7.2}$$

7.2.2. Online n^{th} damage level damage index estimation

The slow scale damage index, a_n, is the representative damage state obtained from n^{th} damage level fast-scale sensor measurements. The damage index can be derived by evaluating the m^{th} lagged output $y(t+m)$ from Eq. (7.2) and pre multiplying the input $u(t)$, obtaining

$$\begin{aligned} u(t)y(t+m) &= b_0u(t)u(t+m) + b_1u(t)u(t-1+m) \\ &+ b_2u(t)u(t-2+m) + \dots \\ &+ b_Mu(t)u(t-M+m) + u(t)\nu(t+m) \end{aligned} \tag{7.3}$$

Applying expectation operator to both sides of Eq. (7.3) and assuming independence between noise and the input signal, the m^{th} lagged cross-correlation coefficients can be expressed as

$$\begin{aligned} \gamma_{uy}(m) &= b_0\gamma_{uy}(m) + \gamma_{uy}(m-1) + b_2\gamma_{uy}(m-2) + \dots \\ &+ b_M\gamma_{uy}(m-M) \quad ; m = 0, 1 \dots, M \end{aligned} \tag{7.4}$$

With known input (u) and output (y) time series, the m^{th} lagged cross-correlation coefficients $\gamma_{uy}(m)$ and auto-correlation coefficients $\gamma_u(m)$, the FIR coefficients $b_m; m = 0, 1, \dots M$ can be estimated. To estimate $M+1$ FIR coefficients, $M+1$ algebraic equations, given by Eq. (7.4), need to be solved. The solution of $M+1$ equations involve inverting a $(M+1) \times (M+1)$ autocorrelation coefficient matrix, which becomes computationally expensive in the context of online applications. To circumvent this problem the damage state equivalent damage index can be estimated. Based on the cross-correlation coefficients

$\gamma_{uy}(m)$ a new damage index is formulated, which is expressed as follows:

$$a_n = \sqrt{\frac{\sum_{m=0}^{m=M}((\gamma_{uy})_n(m) - (\gamma_{uy})_0(m))^2}{\sum_{m=0}^{m=M}((\gamma_{uy})_0(m))^2}}; n = 1, 2 \ldots, N/\Delta N \tag{7.5}$$

where $(\gamma_{uy})_n(m)$ represents n^{th} damage level cross-correlation coefficients, and $(\gamma_{uy})_0(m)$ represents reference condition cross-correlation coefficients.

7.3. Numerical Results

7.3.1. Fatigue experiment and data collection

To numerically validate the developed methodology, fatigue test was performed on an Al-6061 cruciform specimen under biaxial loading. The loaded cruciform specimen in an MTS biaxial fatigue test frame can be seen in Fig.7.4. The specimen was subjected to a constant amplitude fatigue loading with maximum amplitude (σ_{max}) 4 kips and load ratio $R = 0.1$, and the biaxial machine actuator was operated with a frequency of 10 Hz. It should be noted that, the maximum stress amplitude was equal to two thirds the yield stress σ_Y. Based on nonlinear finite element analysis of cruciform specimen, the yield stress was approximated as $\sigma_Y = 6kips$. Also note that both the x-axis actuator and y-axis actuator of the biaxial frame were subjected to in-phase fatigue loading. For online state estimation, passive strain gauge sensors were used. One uniaxial strain gauge was mounted on the horizontal flange (Fig. 7.5b), and another on the vertical flange (Fig. 7.5b) and one biaxial rosette (with two strain gauges perpendicular to each other) strain gauge was mounted on the web area (Fig. 7.5a) of the cruciform specimen. In addition, a hole in the center of the specimen was made to create crack initiation in the web area of cruciform specimen. To accelerate damage growth, an EDM notch of 1 mm in length was made at left bottom quadrant boundary of the central hole (45^o to the vertical axis). A 48 channel

NI PXI system was used to collect the strain gauge signals and the measurements from the biaxial machine load cells. In addition, a high resolution SONY camera was used to visually monitor the crack growth. The data acquisition system and the computer capturing the visual image were synchronized with the biaxial machine controller to collect the time synchronized data/ image at a specified interval of $\Delta N = 1500 cycles$. The data and image collection started at approximately 11 kcycles. The image and sensor data were collected at 47 different time instances. For the first 44 instances, the signals and images were collected while the biaxial machine was running and during the last three instances the data were collected when the machine was stopped. This leads to a total of 44 different damage cases with the last damage state occurring at 75.5 kcycles. The proposed MATLAB based prognosis algorithm was also synchronized with the data acquisition system to estimate the current damage state, and to predict the future damage state and remaining useful life in real time.

7.3.2. Time-series damage state estimation

Strain gauge measurements were mapped as input and output. For example, the signal (ϵ_x^F) from the strain gauge mounted on the horizontal flange (or X-arm) of the cruciform specimen was considered as the input signal u, whereas the signal (ϵ_x^W) from the web mounted stain gauge was considered as output y. It should be noted that both the horizontal axis strain (ϵ_x^W) and the vertical axis strain (ϵ_y^W) were measured by two different strain gauges placed perpendicular to each other. Comparison of input strain (ϵ_x^F) and output strain (ϵ_x^W) at different damage level are shown in Fig. 7.6. The figure shows the comparison for four different damage cases, damage case 7 (at 20 kcycle), damage case 20

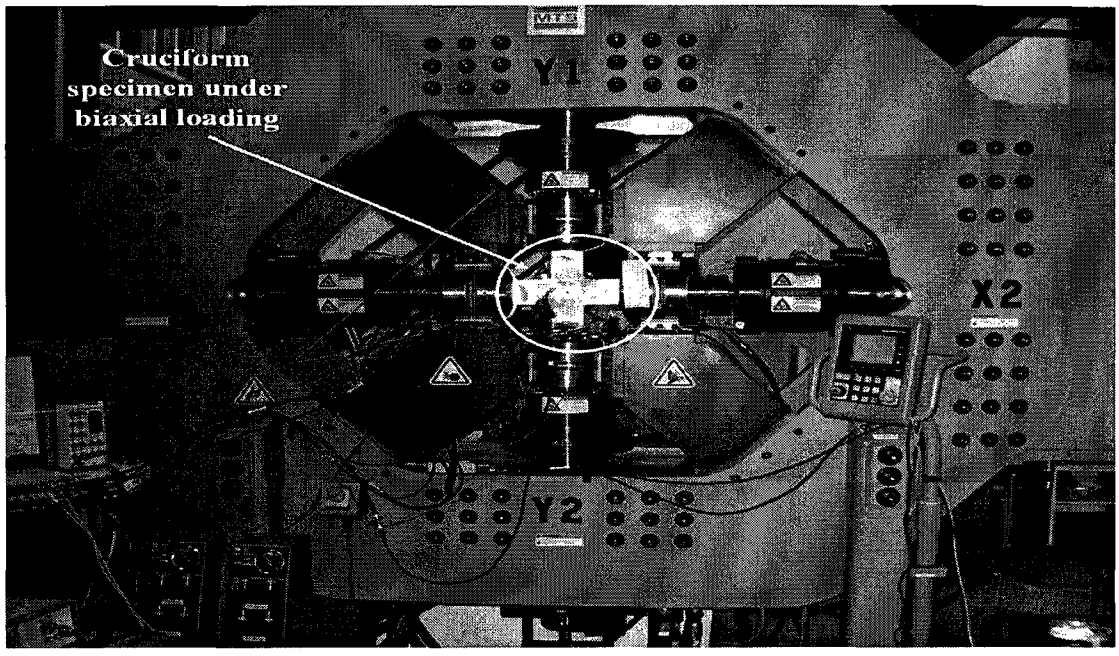

Fig. 7.4. Al-6061 cruciform specimen loaded in a MTS biaxial fatigue test frame.

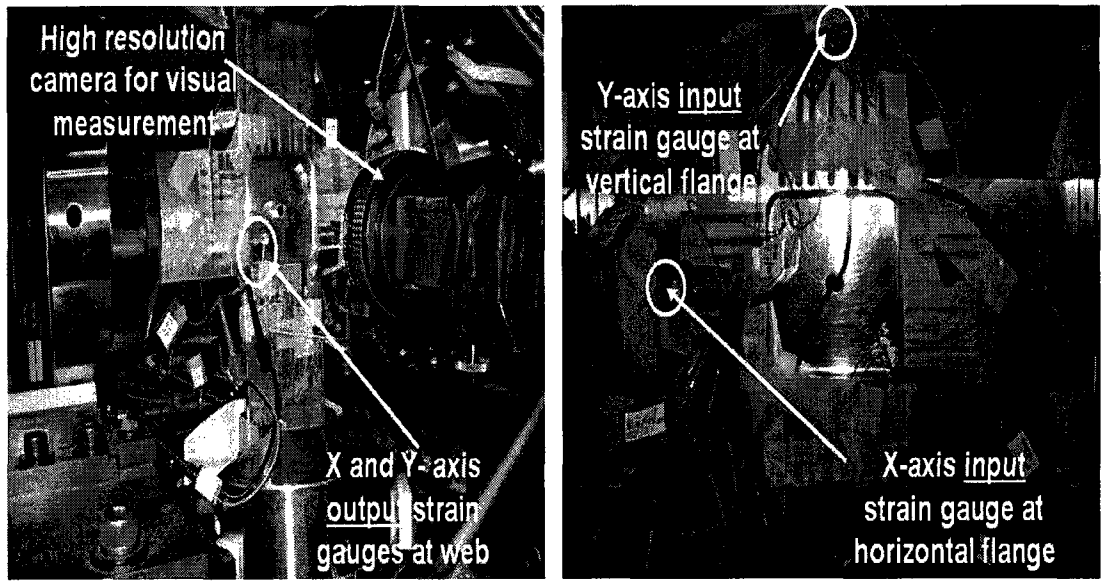

Fig. 7.5. Undamaged and damaged condition of cruciform specimen: a) shows the undamaged cruciform specimen. This rear view of the specimen also shows the location of two strain gauges mounted in the web area. b) shows the final damage condition (at 75.5 kcycles) of the cruciform specimen. This front view of the specimen also shows the location of two strain gauges: one mounted on horizontal arm and the other mounted on the vertical arm of the specimen.

(at 39.5 kcycle), damage case 42 (at 72.5 kcycle) and damage case 44 (at 75.5 kcycle). From the figure it can be seen that there is no clear trend between input and output strain at different damage levels. Rather than directly using the time series data for different damage case comparisons, using Eq. (7.4), the cross-correlation coefficient between input and output was found for different damage cases. The comparison of cross-correlation coefficients for damage level 1 (reference case at 11 k cycles) with cross-correlation coefficient at different damage levels are shown in Fig. 7.7. Figure 7.7a, 7.7b, 7.7c, and 7.7d, show the comparison of cross-correlation coefficients of damage case 1 with damage case 7, damage case 20, damage case 42 and damage case 44, respectively. It is to be noted that the results shown in Fig.7.7, the x-axis flange strain (ϵ_x^F) and x-axis web strain ϵ_x^W) are respectively taken as input u and output y. Also, from Fig.7.7 it can be seen that the cross-correlation plot shows a better trend of damage growth, compared to the direct time series measurements shown in Fig. 7.6. However, to compare the quantitative damage states between different damage levels, the scalar damage index shown in Eq. (7.5), was evaluated for the different damage states. Figure 7.8 shows the damage indices evaluated for two different output measurements, ϵ_x^W and ϵ_y^W, against input measurements ϵ_x^F from horizontal (x-axis) flange starain gauge. The figure shows a clear trend of damage growth with ϵ_x^W as output strain compared to ϵ_y^W as output strain. This is because the input signal ϵ_x^F is poorly correlated with the y-axis web strain (ϵ_y^W) measurements. Figure 7.8 also shows that with respect to ϵ_y^W as the output strain, except for final failure regime, there was no clear trend in damage growth. The higher damage indices during the final failure regime are possibly due to presence of shear strain components. Also from Fig. 7.8 a good correlation between normalized visual measurements and estimated damage indices (found with respect to ϵ_x^W

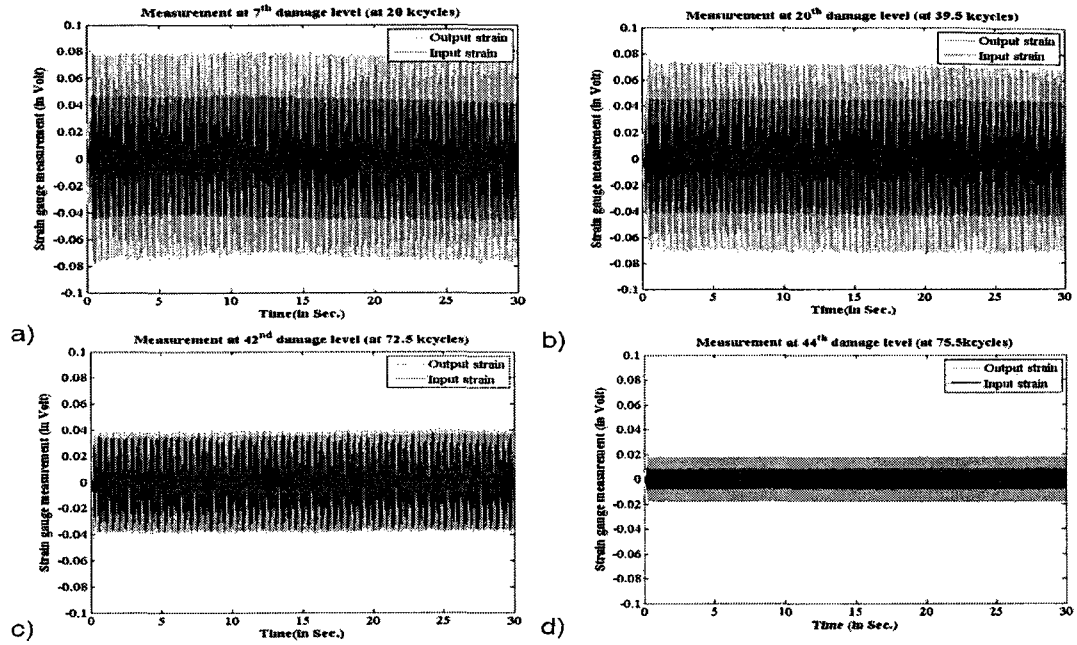

Fig. 7.6. Input output strain comparisons at different damage levels.

as output) is also observed. It must be noted that, the visual measurement is available up to damage level 29 (up to 53 kcycle). After the 29^{th} damage level, it was found that the camera went out of focus. In addition to the strain signal as input, damage indices were also obtained using biaxial frame load cell measurements (x-axis load cell). The corresponding damage indices are shown in Fig. 7.9, and a similar trend in damage index growth, as in the previous case (with x-axis flange strain measurement as input), can be observed. However, it is noted that in a real life scenario, it is hardly possible to directly measure the loads applied to the structure. On the other hand, it is realistic to mount strain gauges or small sensors at required locations without affecting the structural integrity of the host structure. Therefore the results presented in the subsequent sections are based only on the strain gauge based data.

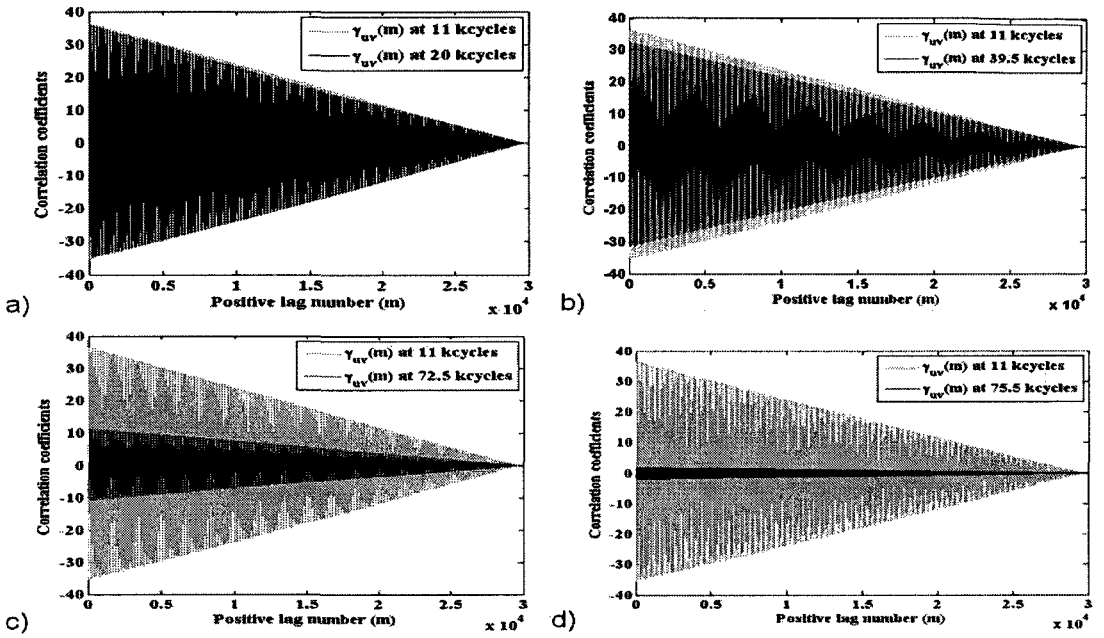

Fig. 7.7. Cross-correlation coefficient comparison at different damage levels with the reference level at 11 kcycles.

7.4. Conclusion

An online state estimation technique based on passive strain gauge measurements is proposed. A novel damage index based on correlation of dynamic strain measurements at two different locations of a structure is proposed. The proposed approach is validated on an Al-6061 cruciform specimen subjected to biaxial constant cycle fatigue loading. Numerical results showed good correlation between online estimated time-series damages states and the corresponding normalized visual measurements. It is to be noted that the proposed approach works well only when the applied cyclic load is constant. With this in mind the following two applications can be envisioned:

- For aircraft health monitoring (e.g connection between wing and fuselage), when the aircraft is in the ground, any particular subsystem (e.g wing) health at any discrete

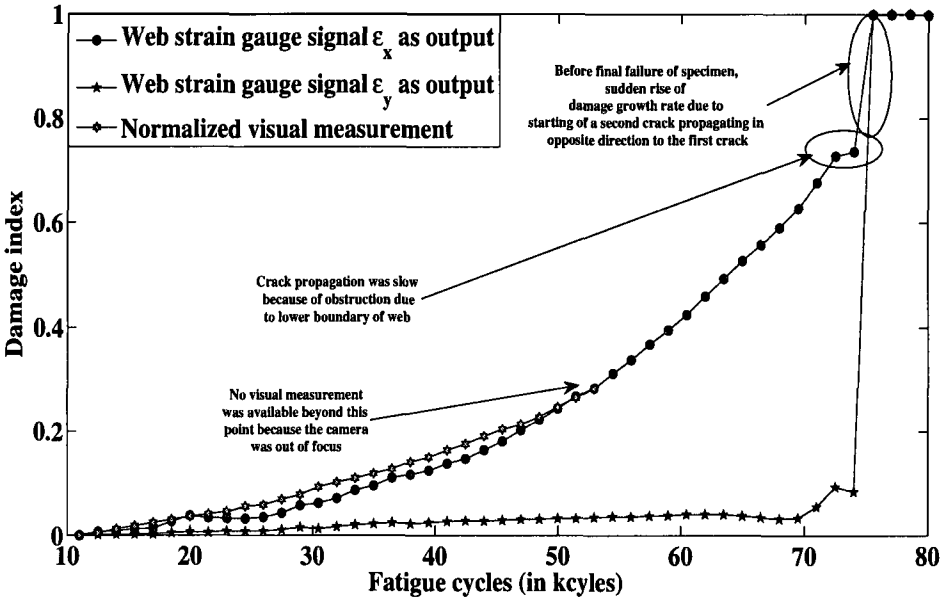

Fig. 7.8. Variation of damage index with fatigue cycle. Flange (x-axis) strain measurements were used as input and web (x and y-axis) strain measurements as output.

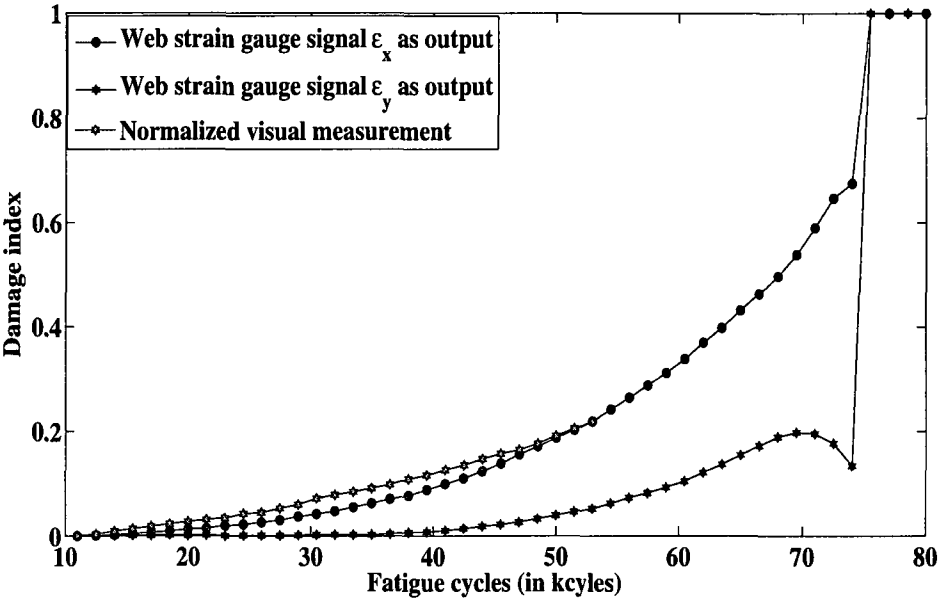

Fig. 7.9. Variation of damage index with fatigue cycle. Horizontal axis (or x axis) biaxial frame load-cell measurements as input and web (x and y-axis) strain measurements as output.

instances (or after specified flight hours) can be assessed by applying a fixed cyclic input load applied to that particular structure. The fixed load can be applied using any external source such as an electro dynamic shaker or using an internal source such as internal cabin pressurization or depressurization. Similar approach can also be followed in the time-series damage state estimation of rotorcraft systems (e.g., for the connection between rotor blade and hub).

- At present, many fatigue life models estimate the relation between fatigue crack growth rate and change in stress intensity factor. These laboratory condition relations are often estimated under constant cycle fatigue loading. To estimate the above relation, potential drop method is often used, but the potential drop method is suitable only for few specific geometries. However, the proposed dynamic strain measurement based damage state estimation approach is more versatile and can be applied to monitor damage in any complex geometry.

CHAPTER 8

Passive Sensing Based Online Damage State Estimation under Random Cyclic Fatigue Loading

8.1. Introduction

In the chapter 7, the use of strain gauge measurements for real-time damage state estimation under constant fatigue loading has been demonstrated. However, compared to damage interrogations under constant fatigue loading, damage estimation under random loading is more involved. The present chapter discusses a novel strain gauge measurement based passive sensing technique that can be used to estimate time-series damage states under random loading. The approach is demonstrated for an Al-2024 cruciform specimen subjected to biaxial random loading.

8.2. Theoretical Approach

Unlike the constant loading case passive sensing based damage state estimation under random loading condition is more complicated, due to the variation in the strain correlation (between two points) pattern with varying loads. This means it is not possible to identify whether the correlation pattern change is due to change in load or to damage. In the previous chapter, load information was not considered in the damage index formulation. However, for accurate damage state estimation under random loads, loading information in the damage index formulation needs to be considered. In addition to the loading information, other time varying input parameters such as temperature and humidity may also be included in the damage index formulation. Similar to the chapter 7, estimation of the time-series damage states, the overall fatigue damage process can be divided into multiple short term discrete instances as shown in Figure 8.1. However, unlike the chapter 7, at any discrete damage instances the transfer function mapping (Figure 8.2) between strain

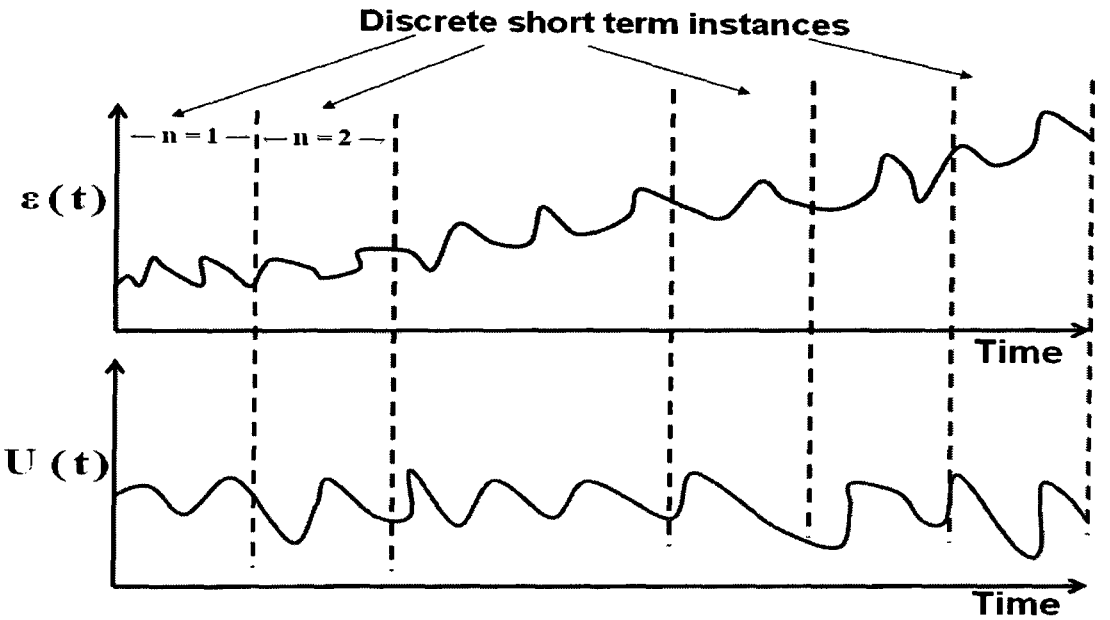

Fig. 8.1. Schematic showing the division of overall fatigue life to multiple discrete short term instances

measurements at two points is a function of applied random load. In Figure 8.2 $H_n(j\omega)$ represents the transfer function between input strain $u(= \epsilon_1)$ and output strain $y(= \epsilon_2)$ at location 1 and 2, respectively. Both the input and output strain measurements are function of applied random load U and damage condition of the structure at that point of time. Details of the damage index formulation are discussed in the following subsections.

8.2.1. Dynamic model estimation

One of the major steps in the proposed time-series damage state estimation approach is to estimate the nonlinear dynamic model using strain gauge and environmental load measurements. Two such models have to be estimated one between environmental loading U and input strain $u(= \epsilon_1)$ at location 1 and the other between environmental loading U and output strain $y(= \epsilon_2)$ at location 2. The following sections describe the procedure for dynamic model estimation.

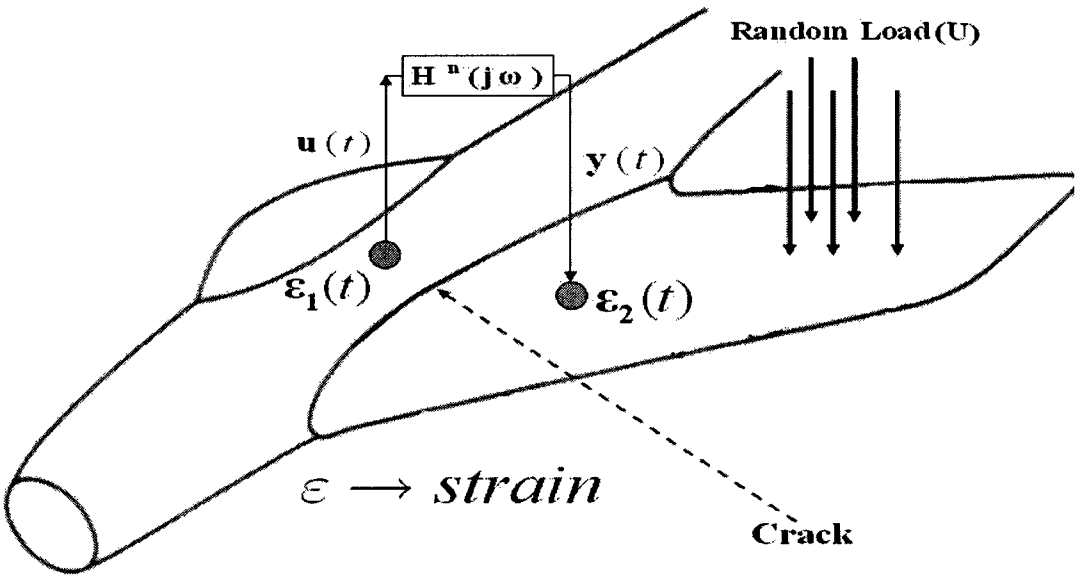

Fig. 8.2. Schematic showing strain at two points of a structure and related time-varying transfer function.

8.2.1.1. *Generic nonlinear dynamic model*

Assume that the $(n = N^{th})$ damage level can be described by sensor signals acquired between $n = N - \frac{\Delta N}{2}$ and $n = N + \frac{\Delta N}{2}$ fatigue cycle, where ΔN is the interval in fatigue cycles between which the damage state has to be estimated. It is assumed that during $n = N - \frac{\Delta N}{2}$ to $n = N + \frac{\Delta N}{2}$ fatigue cycle, the damage condition of the structure remains unchanged. The sensor measurements between $n = N - \frac{\Delta N}{2}$ and $n = N + \frac{\Delta N}{2}$ fatigue cycles are indexed by $m = 0, 1, \ldots, M$. The n^{th} damage level nonlinear dynamic model [120] between environmental input $U^n(m) = \{L^n(m), T^n(m), H^n(m)\}$ and input strain $u^n(= \epsilon_1)$ at location 1 can be expressed as

$$x^n(m) = g_u^n(x^n(m-1), U^n(m), d^n) \tag{8.1}$$

$$u^n(m) = h_u^n(x^n(m), U^n(m), d^n) \tag{8.2}$$

Similarly the n^{th} damage level nonlinear dynamic model between environmental input $U^n(m) = \{L^n(m), T^n(m), H^n(m)\}$ and output strain $y^n(= \epsilon_y)$ at location 2 can be expressed as

$$x^n(m) = g_y^n(x^n(m-1), U^n(m), d^n) \tag{8.3}$$

$$y^n(m) = h_y^n(x^n(m), U^n(m), d^n) \tag{8.4}$$

where the superscript n represents the n^{th} damage level, $x^n(\bullet)$ represents the n^{th} damage level hidden states, d^n is the quantitative value of damage condition at n^{th} damage level, $U^n(m) = \{L^n(m), T^n(m), H^n(m)\}$ represents the input environmental conditions with $L^n(m), T^n(m)$ and $H^n(m)$, represent the n^{th} damage level load, temperature and humidity, respectively, with lag coefficient m. $L^n(m)$ is a vector with input from multiple loading sources. In addition $g_{(\bullet)}^n$ and $h_{(\bullet)}^n$ are two nonlinear mapping functions. In the present work with laboratory test condition there is not much change in temperature and humidity. Because of this in numerical validation of the developed techniques the temperature and humidity variables will not considered. However, for generality temperature and humidity variables are included in the discussed theoretical formulation.

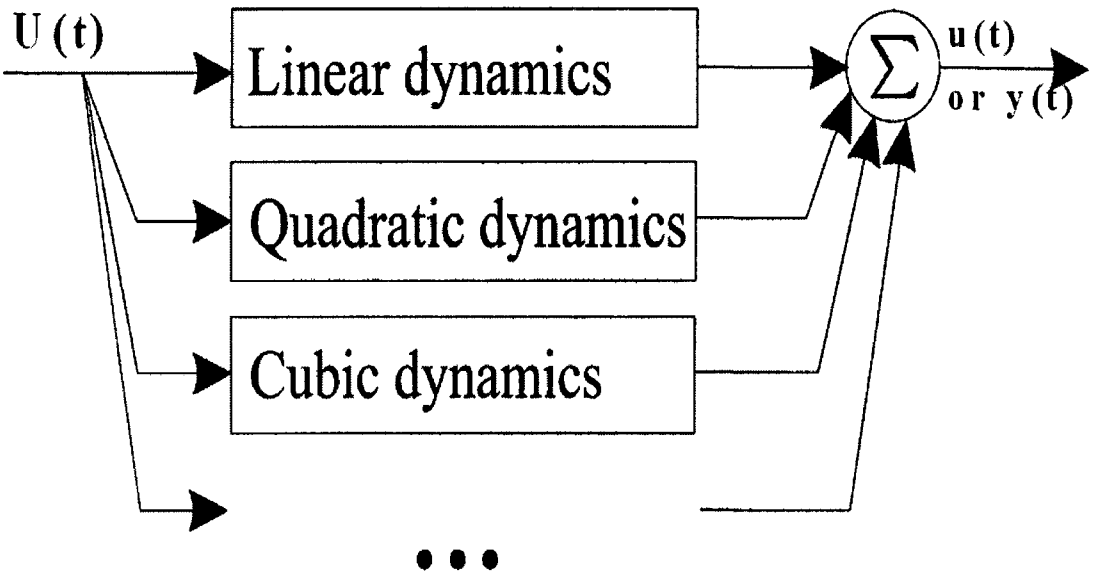

Fig. 8.3. Schematic showing various terms of Volterra series expansion [122].

8.2.1.2. *Nonlinear dynamic modeling using Volterra kernel*

Nonlinear dynamic modeling and signal processing have been gaining increased interest from researches in recent years. Numerous researchers [121] have contributed to the development and increased understanding of these fields. Examples of different nonlinearities are: smooth nonlinearities, multiple-values nonlinearities, e.g., hysteresis, non-smooth or nonlinearities with discontinuities. The smooth nonlinearities can be represented by polynomial models. To describe a polynomial nonlinear system with memory, the Volterra expansion has been the most widely used model for the last thirty years. The continuous-time Volterra filter model is based on Volterra series expansion. The output depends linearly on the Volterra series coefficients as shown in Figure (8.3). Using causal discrete-time Volterra filter the relation between environmental input $U^n(m)$ and input strain $u^n(= \epsilon_1)$ (Eq. 8.2) can be given as

$$u^n(m) = (h_u^n)_0 + \sum_{i_1=0}^{\infty}(h_u^n)_1(i_1)U(m-i_1) + \sum_{i_1=0}^{\infty}\sum_{i_2=0}^{\infty}(h_u^n)_2(i_1,i_2)U(m-i_1)U(m-i_2) + \ldots + \sum_{i_1=0}^{\infty}\cdots\sum_{i_p=0}^{\infty}(h_u^n)_p(i_1,\ldots,i_p)U(m-i_1)\ldots U(m-i_p) \quad (8.5)$$

Similarly the Volterra series relation between environmental input $U^n(m)$ and output strain $y^n(=\epsilon_1)$ (Eq. 8.4) can be given as

$$y^n(m) = (h_y^n)_0 + \sum_{i_1=0}^{\infty}(h_y^n)_1(i_1)U(m-i_1) + \sum_{i_1=0}^{\infty}\sum_{i_2=0}^{\infty}(h_y^n)_2(i_1,i_2)U(m-i_1)U(m-i_2) + \ldots + \sum_{i_1=0}^{\infty}\cdots\sum_{i_p=0}^{\infty}(h_y^n)_p(i_1,\ldots,i_p)U(m-i_1)\ldots U(m-i_p) \quad (8.6)$$

In Eq. (8.5 and 8.6) $(h_{(\bullet)}^n)_0$ is a constant and $\{(h_{(\bullet)}^n)_j(i_1,i_2,\ldots,i_j), 1 \leq j \leq \infty\}$ is the set of j^{th}-order Volterra kernel coefficients. Unlike the case of linear Volterra dynamic model, it is difficult to characterize the nonlinear Volterra dynamic model by the system unit impulse response. Also, as the order of the polynomial increases, the number of Volterra parameters increases rapidly, thus making the computational cost extremely high and uneconomical.

8.2.1.3. *Nonlinear dynamic modeling using Bayesian Gaussian Process*

The Volterra kernel nonlinear model discussed above is computationally intensive for highly nonlinear systems. In addition, polynomial type Volterra methods are more suitable

to model smooth nonlinearity. However fatigue damage consists of multiple-valued nonlinearity, e.g., hysteresis effect in stress-strain relation and requires a better robust approach to model it. The Bayesian Gaussian Process (GP) model [98, 83, 84] can be useful for modeling the nonlinear dynamics associated with the individual discrete damage instances. Using GP based high-dimensional kernel transformation, the nonlinear relation between the input environmental loading $U^n(m) = \{L^n(m), T^n(m), H^n(m)\}$ and the input/output strain (i.e $u^n(= \epsilon_1)$ or $y^n(= \epsilon_2)$ can first be mapped in a high-dimensional space. The high-dimensional transformation is performed using assumed kernel functions [98, 83, 84]. It is assumed that in the transformed high-dimensional space the input environmental load and the input/output strain follows a linear relation. In the high-dimensional space the mapping between the new transformed input $X = \Phi(U^n(m)) = \Phi(\{L^n(m), T^n(m), H^n(m)\}$, $u^n(= \epsilon_1)$ or $y^n(= \epsilon_2)$) and observed input/output strain (i.e $u^n(= \epsilon_1)$ or $y^n(= \epsilon_2)$ can be modeled as a Markovian model. It is to be noted that the high-dimensional mapping is performed in a subtle Bayesian framework and the mapped input-output relation cannot be directly visualize. With first order Markov dynamics assumption and considering process noise $\vartheta^n_{(\cdot)}$ the equivalent form of Eq. (8.1 and 8.2) for input strain $u^n(= \epsilon_1)$ at location 1 can be expressed as

$$X^n(m) = g^n_u(X^n(m-1), d^n; A^n_u) + \vartheta^n_X(m) \tag{8.7}$$

$$u^n(m) = h^n_u(X^n(m), d^n; B^n_u) + \vartheta^n_u(m) \tag{8.8}$$

and for output strain $y^n(= \epsilon_2)$ at location 2 can be expressed as

$$X^n(m) = g_y^n(X^n(m-1), d^n; A_y^n) + \vartheta_X^n(m) \tag{8.9}$$

$$y^n(m) = h_y^n(X^n(m), d^n; B_y^n) + \vartheta_y^n(m) \tag{8.10}$$

where $X^n(m) \in R^d$ denotes the d-dimensional latent coordinates at m^{th} lag coefficient of the n^{th} damage level. Also $\vartheta_{(\cdot)}^n$ is the zero-mean, white Gaussian process noise, $g_{(\cdot)}^n$ and $h_{(\cdot)}^n$ are nonlinear mapping functions parameterized by $A_{(\cdot)}^n$ and $B_{(\cdot)}^n$ respectively. The nonlinear mapping functions $g_{(\cdot)}^n$ and $h_{(\cdot)}^n$ at n^{th} damage level can be expressed as linear combination of basis functions ϕ and ψ and is expressed as below.

$$g_{(\cdot)}^n(X^n(m-1), d^n; A^n) = \sum_i A_i^n \phi_i^n \tag{8.11}$$

$$h_{(\cdot)}^n(X^n(m-1), d^n; B^n) = \sum_j B_j^n \psi_j^n \tag{8.12}$$

where $A^n = \{A_1^n, A_2^n, \ldots, A_M^n\}$ and $B^n = \{B_1^n, B_2^n, \ldots, B_M^n\}$ are weights. In order to fit the parameter of this model to training data, one must select an appropriate number of basis function i.e., in other way to select the proper order of the system. One must ensure that there is enough data to constrain the shape of the basis functions. Ensuring enough data and finding the proper order of the system can be very difficult in practice. However, from a Bayesian perspective, the specific form of mapping function $g_{(\cdot)}^n$ and $h_{(\cdot)}^n$ are incidental and therefore should be marginalized out. Following GP regression modeling [98, 83, 84], the discrete short term time-series measurements at n^{th} damage level can be modeled for the input strain $u^n(= \epsilon_1)$ as

$$f(\mathbf{u}^n|\{\mathbf{X}_m^n\}_{m=1,\ldots,M},\Theta_u^n) = \frac{1}{(2\pi)^{M/2}\sqrt{detK_u^n}} exp[-\frac{1}{2}(u^n-\mu_u)^T(K_u^n)^{-1}(u^n-\mu_u)] \quad (8.13)$$

Similarly for output strain $y^n(=\epsilon_2)$ as

$$f(\mathbf{y}^n|\{\mathbf{X}_m^n\}_{m=1,\ldots,M},\Theta_y^n) = \frac{1}{(2\pi)^{M/2}\sqrt{detK_y^n}} exp[-\frac{1}{2}(u^n-\mu_y)^T(K_y^n)^{-1}(u^n-\mu_y)] \quad (8.14)$$

where $\mathbf{u}^n = [u^n(m=1), u^n(m=2), \ldots, u^n(m=M)]$ or $\mathbf{u}^n = [\epsilon_1^n(m=1), \epsilon_1^n(m=2), \ldots, \epsilon_1^n(m=M)]$ is the short term input time series at n^{th} damage level. Similarly $\mathbf{y}^n = [y^n(m=1), y^n(m=2), \ldots, y^n(m=M)]$ or $\mathbf{y}^n = [\epsilon_2^n(m=1), \epsilon_2^n(m=2), \ldots, \epsilon_2^n(m=M)]$ is the short term output time series at n^{th} damage level. In addition K_u^n and K_y^n are $M \times M$ kernel matrices with respect to $X \rightarrow u$ and $X \rightarrow y$ mappings. The elements of kernel matrix can be found using assumed kernel functions. There are different types of kernel functions (e.g., constant kernel, Radial basis kernel, Multilayer perceptron kernel, etc.) [97]. Form the modeling point of view the choice of kernel should best suit our data. In the present application Multilayer perceptron kernel (MLP) kernel is used. The elements of n^{th} damage level kernel matrix can be found using MLP kernel function and is given as below.

$$\begin{aligned}(K_{(.)}^n)_{i,j} &= k(\mathbf{X}_i, \mathbf{X}_j) \\ &= (\theta_{(.)}^n)_p Sin^{-1} \frac{\mathbf{X}_i^T(\theta_{(.)}^n)_w \mathbf{X}_j}{\sqrt{(\mathbf{X}_i^T(\theta_{(.)}^n)_w \mathbf{X}_i + 1)(\mathbf{X}_j^T(\theta_{(.)}^n)_w \mathbf{X}_j + 1)}} + (\theta_{(.)}^n)_\vartheta\end{aligned} \quad (8.15)$$

In Eq. (8.15), $(\theta^n_{(\cdot)})_p$, $(\theta^n_{(\cdot)})_w$, $(\theta^n_{(\cdot)})_\vartheta$ are the process, width and noise hyperparameters, respectively. There are two sets of hyperparameters: $\Theta^n_u = \{(\theta^n_u)_p, (\theta^n_u)_w, (\theta^n_u)_b, (\theta^n_u)_\vartheta\}$ for $X \rightarrow u$ mapping and $\Theta^n_y = \{(\theta^n_y)_p, (\theta^n_y)_w, (\theta^n_y)_b, (\theta^n_y)_\vartheta\}$ for $X \rightarrow y$ mapping and can be found by minimizing the following two negative log-likelihood functions.

$$\Gamma^n_u = -\frac{1}{2} log det \mathbf{K}^n_u - \frac{1}{2}(\mathbf{u}^n)^T(\mathbf{K}^n_u)^{-1}\mathbf{u}^n - \frac{M}{2} log 2\pi \tag{8.16}$$

$$\Gamma^n_y = -\frac{1}{2} log det \mathbf{K}^n_y - \frac{1}{2}(\mathbf{y}^n)^T(\mathbf{K}^n_y)^{-1}\mathbf{y}^n - \frac{M}{2} log 2\pi \tag{8.17}$$

8.2.2. Time-series fatigue damage state estimation

Above subsection discussed how to estimate the nonlinear dynamic model for any individual damage instance. This subsection discusses how to estimate the time-series damage states at individual damage instances. It is to be noted that the estimation of dynamic model for any individual damage instance is a fast scale dynamical system identification problem. Compared to this, the time-series damage state estimation for entire fatigue life is a slow scale dynamical system identification problem. The step-by-step process for time-series damage state estimation for the entire fatigue life is discussed below.

8.2.2.1. *Reference model estimation*

Given the reference environmental condition $U^0(m) = \{L^n(m), T^n(m), H^n(m)\}$ and input strain $u^0(= \epsilon^0_1)$ and output strain $y^0(= \epsilon^0_2)$ the reference nonlinear dynamic models $H^0_{U\rightarrow u}$ (i.e to estimate Θ^0_u) and $H^0_{U\rightarrow y}$ (i.e to estimate Θ^0_y) can be estimated by minimizing the respective reference condition negative log-likelihood functions given below.

$$\Gamma_u^0 = -\frac{1}{2} log\ det\ \mathbf{K}_u^0 - \frac{1}{2}(\mathbf{u}^0)^T(\mathbf{K}_u^0)^{-1}\mathbf{u}^0 - \frac{M}{2} log 2\pi \tag{8.18}$$

$$\Gamma_y^0 = -\frac{1}{2} log\ det\ \mathbf{K}_y^0 - \frac{1}{2}(\mathbf{y}^0)^T(\mathbf{K}_y^0)^{-1}\mathbf{y}^0 - \frac{M}{2} log 2\pi \tag{8.19}$$

In Eq. (8.18 and 8.19) the kernel matrix can be written in the functional form as

$$\mathbf{K}_u^0 = \Omega(U^0, u^0, k(\mathbf{X}_i, \mathbf{X}_j), \Theta_u^0) \tag{8.20}$$

$$\mathbf{K}_y^0 = \Omega(U^0, y^0, k(\mathbf{X}_i, \mathbf{X}_j), \Theta_y^0) \tag{8.21}$$

In Eq. (8.20 and 8.21) $k(\mathbf{X}_i, \mathbf{X}_j)$ is the assumed kernel function given in Eq. (8.15).

8.2.2.2. *Current damage level dynamic strain mapping*

Once the reference (at $n = 0$) level dynamic models $H_{U\rightarrow u}^0$ and $H_{U\rightarrow y}^0$ are estimated, for a new environmental conditions $\mathbf{U}^n = [U^n(m = 1), U^n(m = 2), \ldots, U^n(m = M)]^T$, the corresponding input strain $\mathbf{u}_p^n = [u_p^n(m = 1), u_p^n(m = 2), \ldots, u_p^n(m = M)]$ and output strain $\mathbf{y}_p^n = [y_p^n(m = 1), y_p^n(m = 2), \ldots, y_p^n(m = M)]$ can be predicted using the probability density function (pdf)given below.

$$f(u_m^n|\Theta_u^0, \mathbf{K}_u^0, \mathbf{X}^n(m)) = \mathbf{N}\left[\mu_u(m), \sigma_u^2(m)\right]; m = 1, 2, \ldots, M \tag{8.22}$$

$$f(y_m^n|\Theta_y^0, \mathbf{K}_y^0, \mathbf{X}^n(m)) = \mathbf{N}\left[\mu_y(m), \sigma_y^2(m)\right]; m = 1, 2, \ldots, M \tag{8.23}$$

where $\mathbf{X}^n(m) = \Phi(\mathbf{U}^n(m))$ is the high dimensional transformation of the new environmental input $\mathbf{U}^n(m)$ at n^{th} damage level. $\mathbf{N}$ represents the Gaussian distribution with mean

$$\mu_u(m) = (\mathbf{k}_u^n(m))^T(\mathbf{K}_u^0)^{-1}\mathbf{u}^0 \ ; \ m = 1, 2, \ldots, M \tag{8.24}$$

$$\mu_y(m) = (\mathbf{k}_y^n(m))^T(\mathbf{K}_y^0)^{-1}\mathbf{y}^0 \ ; \ m = 1, 2, \ldots, M \tag{8.25}$$

and variance

$$\sigma_u^2(m) = \kappa_u^n(m) - (\mathbf{k}_u^n(m))^T(\mathbf{K}_u^0)^{-1}\mathbf{u}^0 \ ; \ m = 1, 2, \ldots, M \tag{8.26}$$

$$\sigma_y^2(m) = \kappa_y^n(m) - (\mathbf{k}_y^n(m))^T(\mathbf{K}_y^0)^{-1}\mathbf{y}^0 \ ; \ m = 1, 2, \ldots, M \tag{8.27}$$

where $(M \times M)$ $\mathbf{K}_{(\cdot)}^0$ matrix, $(M \times 1)$ $\mathbf{k}_{(\cdot)}^n(m)$ vector and scalar $\kappa_{(\cdot)}^n(m)$ can be found using the larger $(M+1 \times M+1)$ partitioned matrix given below.

$$\mathbf{K}_{(\cdot)}^n(m) = \begin{bmatrix} \mathbf{K}_{(\cdot)}^0 & \mathbf{k}_{(\cdot)}^n(m) \\ (\mathbf{k}_{(\cdot)}^n(m))^T & \kappa_{(\cdot)}^n(m) \end{bmatrix} \ ; \ m = 1, 2, \ldots, M \tag{8.28}$$

Following Eq. (8.22 - 8.28) the predicted input strain at n^{th} damage level can be rewritten as $\mathbf{u}_p^n = [\mu_u^n(m=1), \mu_u^n(m=2), \ldots, \mu_u^n(m=M)]$ and output strain given as $\mathbf{y}_p^n = [\mu_y^n(m=1), \mu_y^n(m=2), \ldots, \mu_y^n(m=M)]$

8.2.2.3. *Current damage level error signal estimation*

Due to damage the nonlinear dynamical model given by Eq. (8.1 to 8.4) will change from one damage level to other damage level. However if the dynamic model parameter kept fixed (as reference model parameter), the n^{th} damage level predicted input strain $\mathbf{u}_p^n$ will not be same as the actual input strain $\mathbf{u}_a^n$ (measured in real-time from the corresponding

sensors). Similar is the case for predicted output strain $\mathbf{y}_p^n$. The error in predicted signal and actual signal at a given damage level can be a measure of the damage state at that damage level. The error signals $e_{(\cdot)}^n$ for both the input and output strain are given as

$$e_u^n(m) = u_a^n(m) - u_p^n(m) \ ; \ m = 1, 2, \ldots, M \tag{8.29}$$

$$e_y^n(m) = y_a^n(m) - y_p^n(m) \ ; \ m = 1, 2, \ldots, M \tag{8.30}$$

8.2.2.4. *Time-series damage state estimation*

Once the error signal with respect to the input and output strain are estimated the corresponding scalar damage index a^n at n^{th} damage level can be estimated using either of the following two damage index formulations. The expression for root mean square error based damage index is given as,

$$a^n = \sqrt{\frac{1}{M} \sum_{m=1}^{m=M} [e_{(u \ or \ y)}^n(m)]^2} \ ; \ n = 1, 2, \ldots, N - \Delta N, N, N + \Delta N \tag{8.31}$$

where $e_{(\bullet)}^n(m)$ are the error signals as described in Eq. (8.29) and (8.30). This damage index formulation can depend on either the input error signal ($e_u^n(m)$) or the output error signal ($e_y^n(m)$). Another damage index formulation using both the input error signal ($e_u^n(m)$) and output error signal ($e_y^n(m)$) is described below. This damage index is based on previously discussed approach (chapter 7) for online damage state estimation under constant amplitude fatigue loading in which, the damage index was formulated by directly correlating the input dynamic strain ($u^n(m) = \epsilon_1^n(m)$) with the corresponding output dynamic strain ($y^n(m) = \epsilon_2^n(m)$). In contrast for the present random loading case, the damage index is

formulated by correlating the input error signal ($e_u^n(m)$) with output error signal ($e_y^n(m)$). The expression for the developed damage index is given below.

$$a^n = \sqrt{\frac{\sum_{m=-M}^{m=M}(\gamma_{e_u e_y}^n(m) - \gamma_{e_u e_y}^0(m))^2}{\sum_{m=-M}^{m=M}(\gamma_{e_u e_y}^0(m))^2}} \; ; \; n = 1, 2, \ldots, N - \Delta N, N, N + \Delta N \quad (8.32)$$

where $\gamma_{e_u e_y}^n(m)$ is the m^{th} lagged cross correlation coefficient between the error signal e_u and e_y. Also superscript 'n' and '0', represents the n^{th} and reference state damage levels respectively. It is to be noted that the reference damage level does not have to be the healthy condition of a structure.

8.3. Numerical Results

Validation of the numerical model discussed in the previous section is a complex task. The numerical prediction must to be validated by experimental results. Towards the validation goal, a fatigue test was conducted under biaxial random load. Using the real-time test data damage states were estimated at different fatigue damage levels. The details of the numerical exercise are discussed below.

8.3.1. Fatigue experiment and data collection

The experimental validation of the model developed was carried out using data from fatigue tests performed on an Al-2024-T351 cruciform specimen under biaxial random loading. The cruciform specimen loaded in an MTS biaxial fatigue test frame can be seen in Figure 8.4. The specimen was instrumented with strain gauges as shown in Figure 8.5A. Two strain gauge rosettes are placed at different locations to measure the input strain ϵ_1 and the output strain ϵ_2, respectively. In the present case the individual strain gauges of the 3-axis rosette gauges are aligned along the X-axis, 45^o to X-axis and Y-axis of the

MTS frame, respectively. Although in a typical application it is not necessary to follow any particular alignment direction, for better correlation of sensor signals the input and output rosettes should be placed parallel to each other. Figure 8.5A also shows the healthy condition of the cruciform specimen, while Figure 8.5B shows its failed condition. To accelerate the crack propagation, a 1.5 mm EDM notch was made at the bottom right boundary of the central hole. Also, to further accelerate the crack growth, the specimen was fatigued under constant cycle loading (maximum load of 4800 lbf and minimum load of 480 lbf), to achieve a visible crack (in front of the EDM notch) length of 1-2 mm. Then the specimen was tested under biaxial random loading. From the finite element based stress analysis results the yield load was found to be 7200 lbf. Based on this limiting yield load random load patterns were generated. The original patterns were generated using MATLAB and then coded to the MTS controller. Typical 1 block (equivalent of 300 cycles) of original random load pattern is shown in Figure 8.6. It is to be noted that for the present random loading case all the blocks are non-repetitive which means that each block is different from every other block. The random loading patterns were generated using MATLAB random number command with keeping maximum load limitation equal to 80 percent of the yield load and minimum load limited to 6.6 percent of the yield load. For each and every random loading block strain gauge signals and MTS load cell signals were acquired using a 48-channel NI-PXI (shown in Figure 8.4) data acquisition system. During testing both the X and Y-axis load frame actuators were programmed to operate at the same phase with a cyclic frequency of 10Hz. However, to capture high-frequency damage signatures, the strain gauge signals were acquired with 1000 Hz sampling frequency. In order to maintain same data length, the MTS X and Y-axis load cell signals were acquired with the same

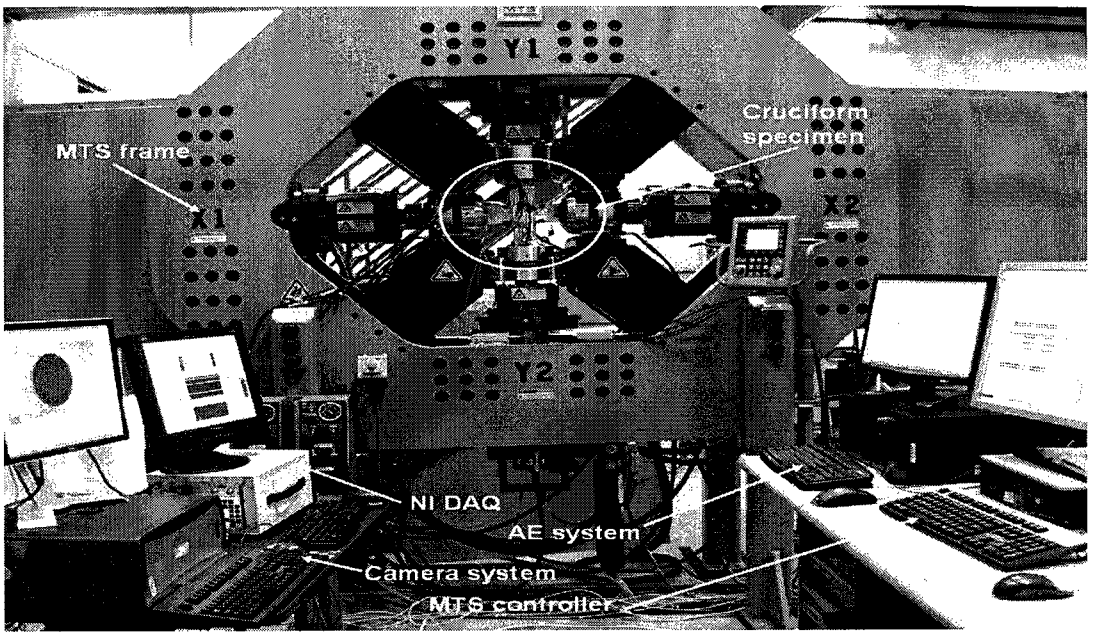

Fig. 8.4. Biaxial testing experimental setup. The figure shows a MTS biaxial/torsion frame mounted with an Al-2024 cruciform specimen.

sampling frequency. The load cell and strain gauge measurements for a typical (at healthy or reference state) random load block is shown in Figure 8.7. Part of the data based on Figure 8.7 is shown in Figure 8.8 in a magnified form. It is to be noted that, the present work a data driven state estimation approach that only requires the statistical correlation of different sensor signals. Hence it was not necessary to acquire the true strain field of the structure and so the strain gauges were not calibrated. Figures 8.7 and 8.8 show the uncalibrated strain signals.

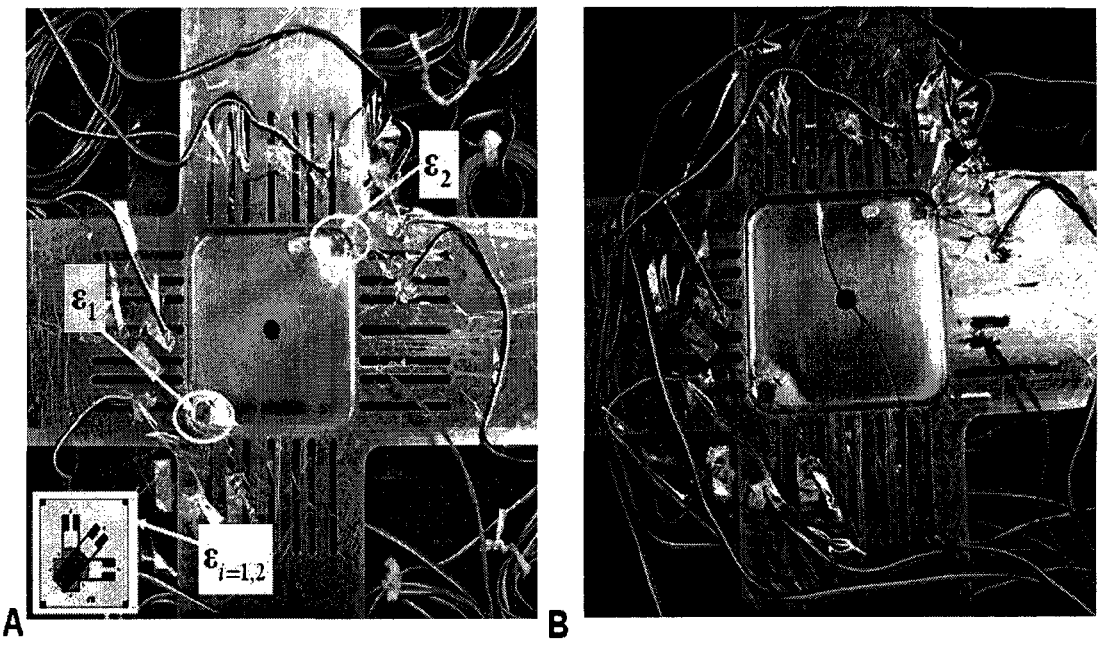

Fig. 8.5. A) Instrumented Al-2024 undamaged cruciform specimen. Two 3-axis rosette strain gauges were placed on both sides of the crack path to monitor dynamic strain. B) Damaged Al-2024 cruciform specimen.

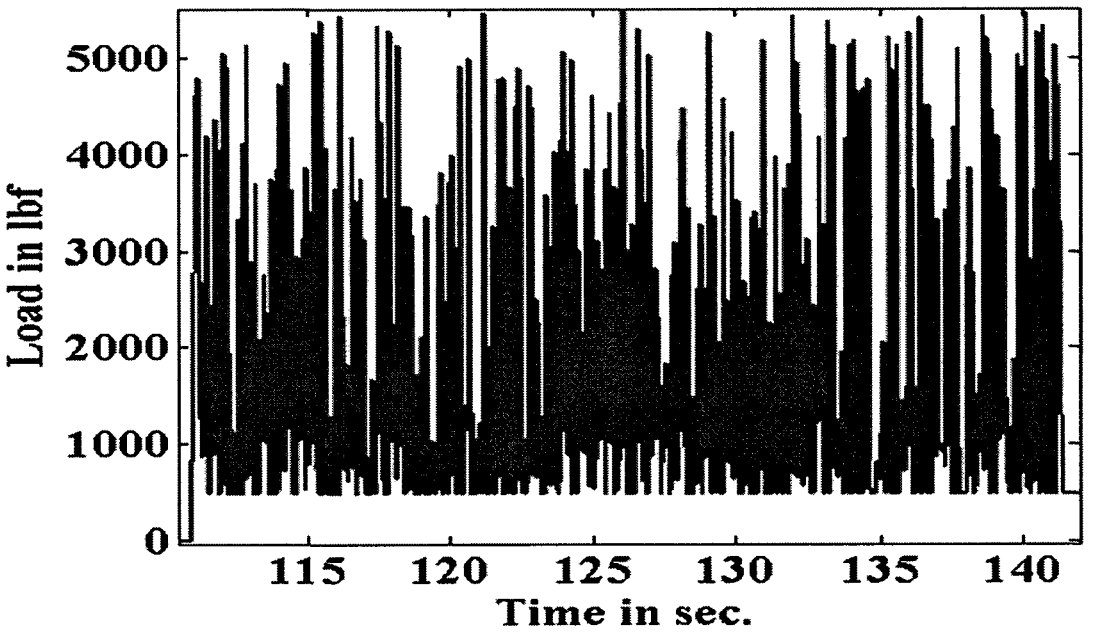

Fig. 8.6. 1-block of random load. Each block of random load is equivalent to 300 fatigue cycles. Individual random load blocks were generated using MATLAB random number generator.

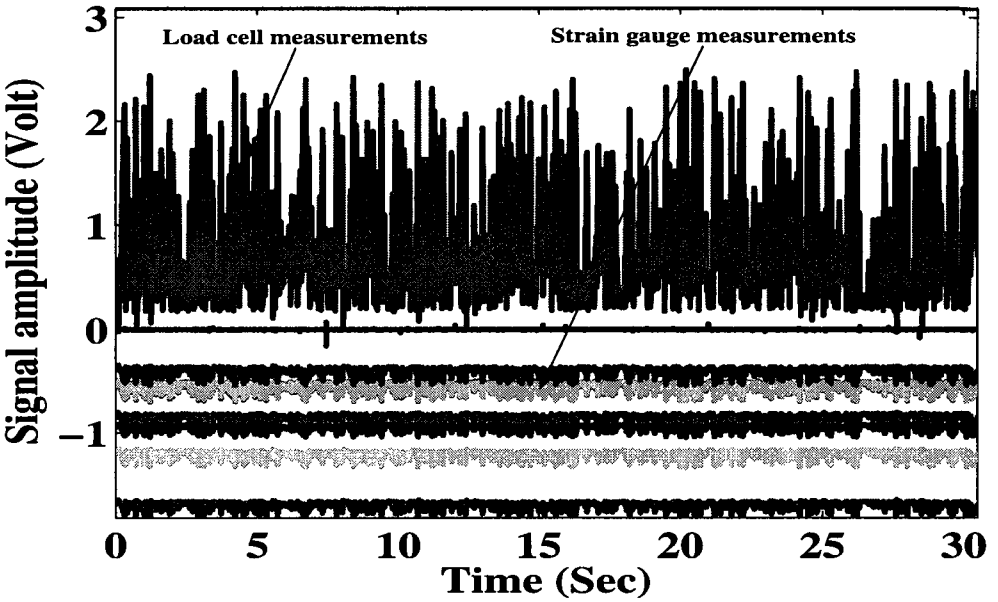

Fig. 8.7. Plot of the raw sensor signals collected at a typical (reference or healthy state) damage level. The plot shows both load cell (from MTS frame X and Y-axis load cells) measurements and signals from different strain gauges.

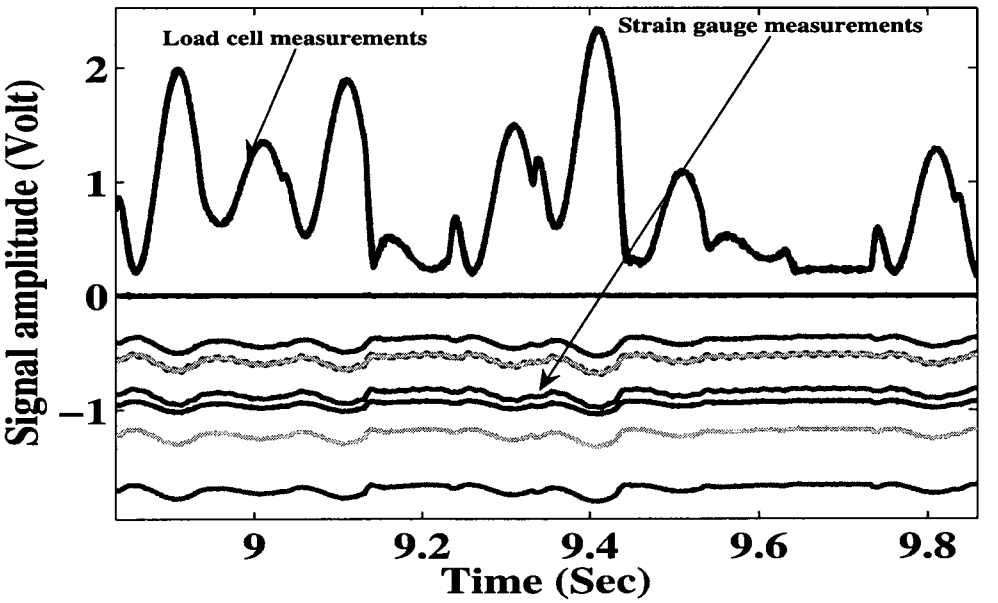

Fig. 8.8. Magnified version of the time-series signals shown in Figure 8.7

8.3.2. Reference nonlinear dynamic model estimation

To estimate the real-time damage state of the cruciform specimen at different damage levels, the dynamic model is estimated at reference or healthy condition first. The reference condition signals were collected during the 1^{st} random loading block. The nonlinear reference models that map both the reference input strain $u^0 = \epsilon_1^0$ and output strain $y^0 = \epsilon_2^0$ with the reference environmental parameters U^0, are estimated using Eq. (8.18-8.21). The present formulation is a multivariate formulation and can consider multiple fatigue affecting environmental parameters such as loading, temperature and humidity ($U^0(m) = \{L^0(m), T^0(m), H^0(m)\}$). However, for the numerical study temperature and humidity were not included in the damage estimation process due to the controlled climate condition in the laboratory. With the biaxial loading condition, only X and Y-axis load cell measurements are considered as input environmental parameters ($U^0(m) = \{L_x^0(m), L_y^0(m)\}$). The reference strain gauge measurements from individual rosettes were first converted to equivalent strain and then mapped against the input reference load $U^0(m)$. The equivalent strains $\epsilon_{eq}(m)$ for the individual rosettes are estimated using the following expression.

$$\epsilon_{eq}(m) = \frac{2}{3}\sqrt{\frac{3}{2}(\epsilon_x^2(m) + \epsilon_y^2(m)) + \frac{3}{4}\gamma_{xy}^2(m)} \; ; \; m = 1, 2, \ldots, M \tag{8.33}$$

where, $\epsilon_x(m)$ and $\epsilon_y(m)$ are the measurements from x and y axis strain gauges of individual rosettes and $\gamma_{xy}(m)$ are the corresponding shear strain components which can be evaluated using

$$\gamma_{xy}(m) = \sqrt{2\epsilon_{45}(m) - \epsilon_x(m) - \epsilon_y(m)} \; ; \; m = 1, 2, \ldots, M \tag{8.34}$$

Where, $\epsilon_{45}(m)$ represents the measurements from 45^o axis (to X-axis) strain gauge of individual rosettes. The relation between input load (or stress) and strain follows highly nonlinear hysteresis pattern and requires nonlinear model estimation approach as developed in Eq. (8.18-8.21). A typical hysteresis plot showing the relation between X-axis load cell measurements ($L_x^0(m)$) and X-axis input strain measurements ($(u^0)_x(m) = (\epsilon_1^0)_x(m)$) is shown in Figure 8.9. The corresponding hysteresis plot showing the relation between X-axis load cell measurements ($L_x^0(m)$) and X-axis output strain measurements ($(y^0)_x(m) = (\epsilon_2^0)_x(m)$) is shown in Figure 8.10. Based on the reference load measurements ($U^0(m) = \{L_x^0(m), L_y^0(m)\}$) and estimated equivalent input strain $u^0(m) = \epsilon_t^0(m)$ the multi input single output (MISO) reference input strain model $H_{U\rightarrow u}^0$ is estimated. The model estimation is performed to estimate the hyperparameters $\Theta_u^0 = \{(\theta_u^0)_p, (\theta_u^0)_w, (\theta_u^n)_\vartheta\}$ in Eq. (8.15). The hyperparameters are estimated by optimizing the negative log likelihood function Γ_u^0 given by Eq. (8.18). Optimization is performed using conjugate gradient optimization techniques. Similar procedure is also followed to estimate the model hyperparameters $\Theta_y^0 = \{(\theta_y^0)_p, (\theta_u^y)_w, (\theta_y^n)_\vartheta\}$ for the multi input single output (MISO) reference output strain model $H_{U\rightarrow y}^0$. Figure 8.11 and Figure 8.12 show the convergence history of Γ_u^0 and Γ_y^0 function value, respectively. During the optimization process, the hyperparameters are initialized to reasonable values and then the conjugate gradient method is used to search for their optimal values. To evaluate the accuracy of estimated models the reference level input strain ($(u^0)_x(m) = (\epsilon_1^0)_x(m)$) and output strain ($(y^0)_x(m) = (\epsilon_2^0)_x(m)$) are

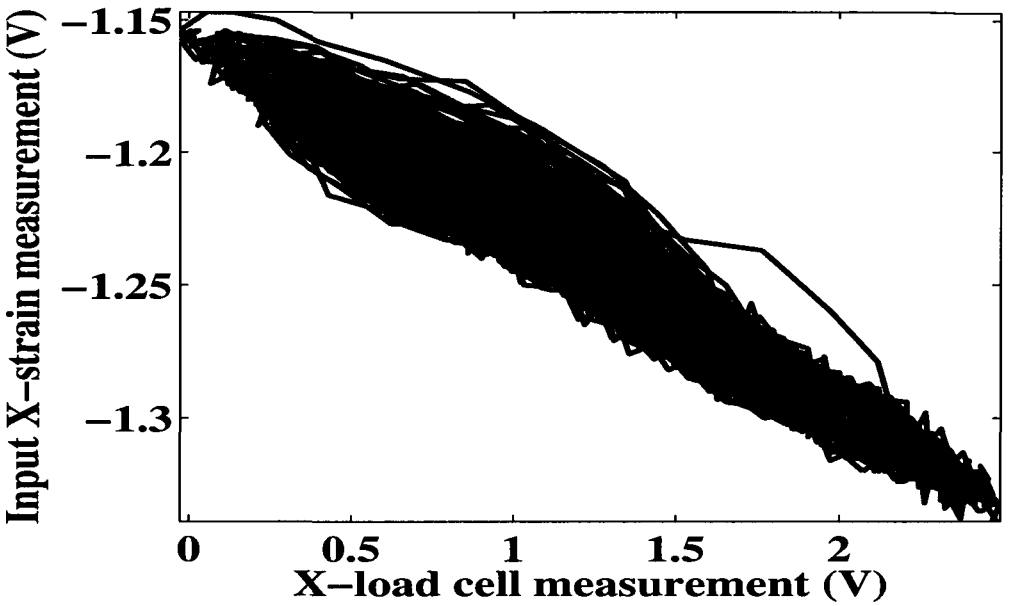

Fig. 8.9. X-axis load cell measurements versus X-axis input strain measurements

respectively regenerated using the estimated model parameters $\Theta_u^0 = \{(\theta_u^0)_p, (\theta_u^0)_w, (\theta_u^n)_\vartheta\}$ and $\Theta_y^0 = \{(\theta_y^0)_p, (\theta_u^y)_w, (\theta_y^n)_\vartheta\}$. These regeneration of strain time-series are performed against the reference load measurements ($U^0(m) = \{L_x^0(m), L_y^0(m)\}$). The comparison between actual input strain ($(u^0)_x(m) = (\epsilon_1^0)_x(m)$) and regenerated input strain time-series is shown in Figures 8.13 and 8.14. Similarly the comparison between actual output strain ($(y^0)_x(m) = (\epsilon_2^0)_x(m)$) and regenerated output strain time-series is shown in Figures 8.15 and 8.16. It can be clearly seen that there is a good match between predicted strains and actual strains. The mean square error (MSE) between the predicted and actual strain for models $H_{U\to u}^0$ and $H_{U\to y}^0$ was found to be 3.8255e-005 and 2.8006e-005, respectively. The MSE can be further reduced by using better signal processing and global optimization techniques.

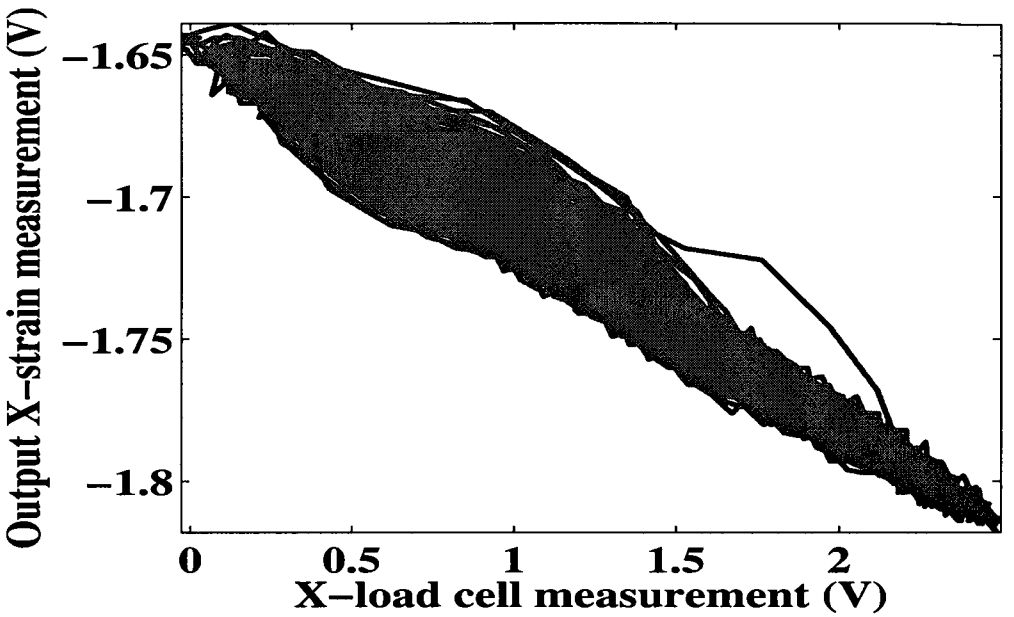

Fig. 8.10. X-axis load cell measurements versus X-axis output strain measurements

8.3.3. Current damage level dynamic strain mapping

Once the reference model parameters are estimated using Eq. (8.22-8.28), the current stage (n^{th} damage level) input dynamic strain ($(u^n)_x(m) = (\epsilon_1^n)_x(m)$) and output dynamic strain ($(y^n)_x(m) = (\epsilon_2^n)_x(m)$) are predicted. The predictions are performed using the reference level models $H^0_{U\rightarrow u}$ and $H^0_{U\rightarrow y}$ discussed in the previous subsection and using the current level load measurements ($U^n(m) = \{L_x^n(m), L_y^n(m)\}$).

The comparisons of predicted and actual input dynamic strain for four typical damage levels is shown in Figure 8.17. The figure shows the prediction at different crack lengths of 4.1621 mm, 12.917 mm, 46.573 mm, and 70.939mm. Also, the comparison of predicted and actual output dynamic strain for the four damage levels are shown in Figure 8.18. The crack lengths are estimated from the images captured by a high-resolution camera. From Figures 8.17 and 8.18, it is clear that as the damage or crack grows the mismatch between

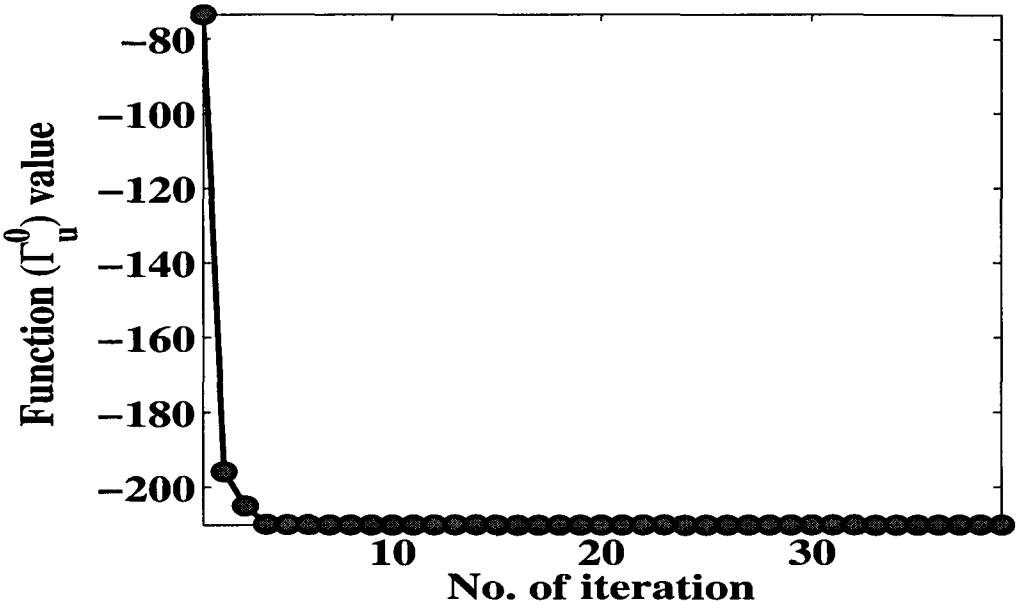

Fig. 8.11. Conjugate gradient optimization of negative log likelihood function Γ_u^0

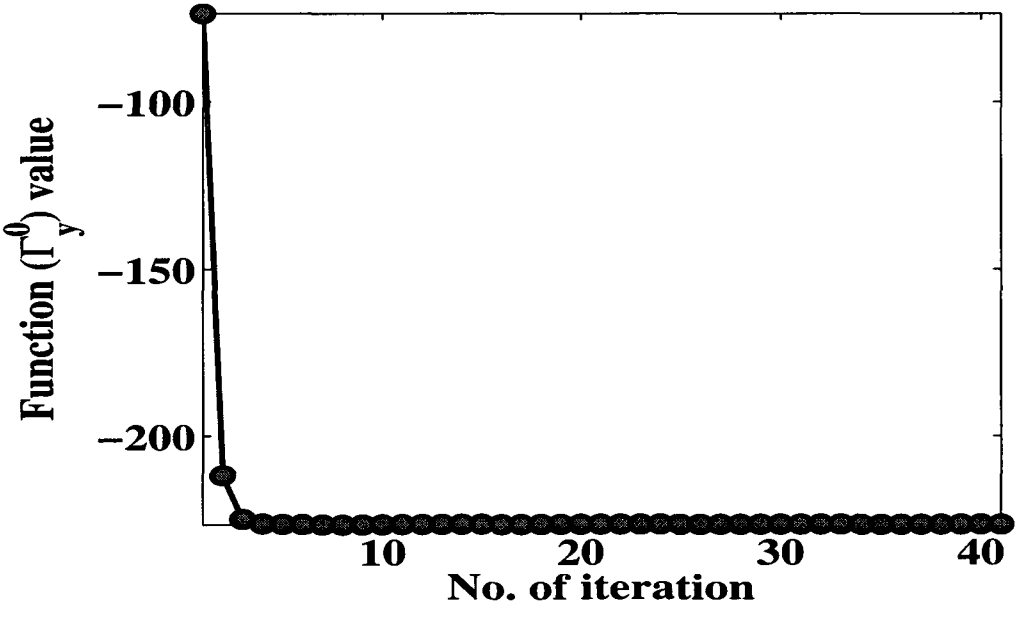

Fig. 8.12. Conjugate gradient optimization of negative log likelihood function Γ_y^0

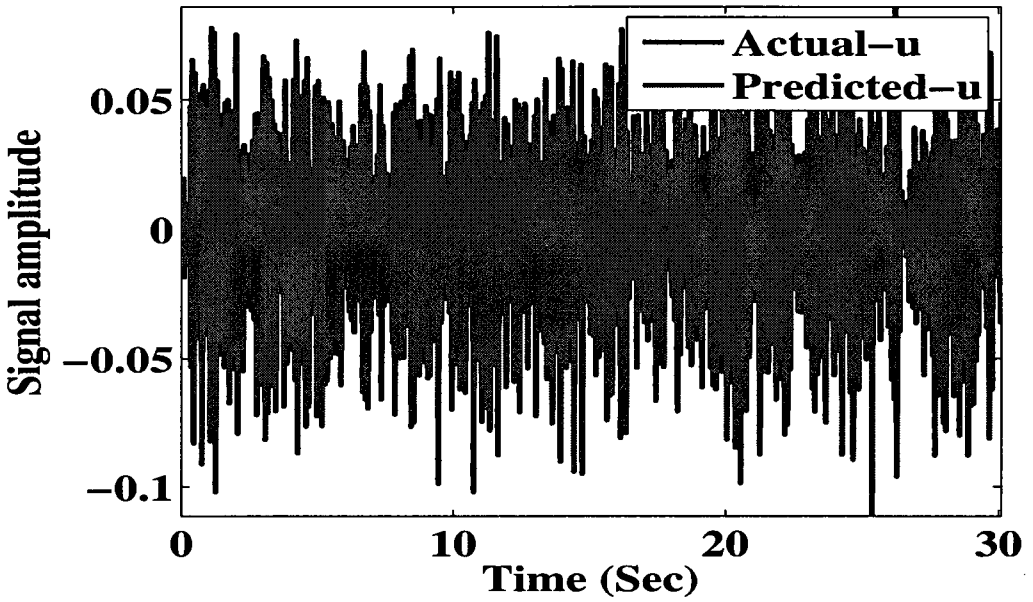

Fig. 8.13. Predicted versus actual input dynamic strain at reference (healthy stage) damage condition.

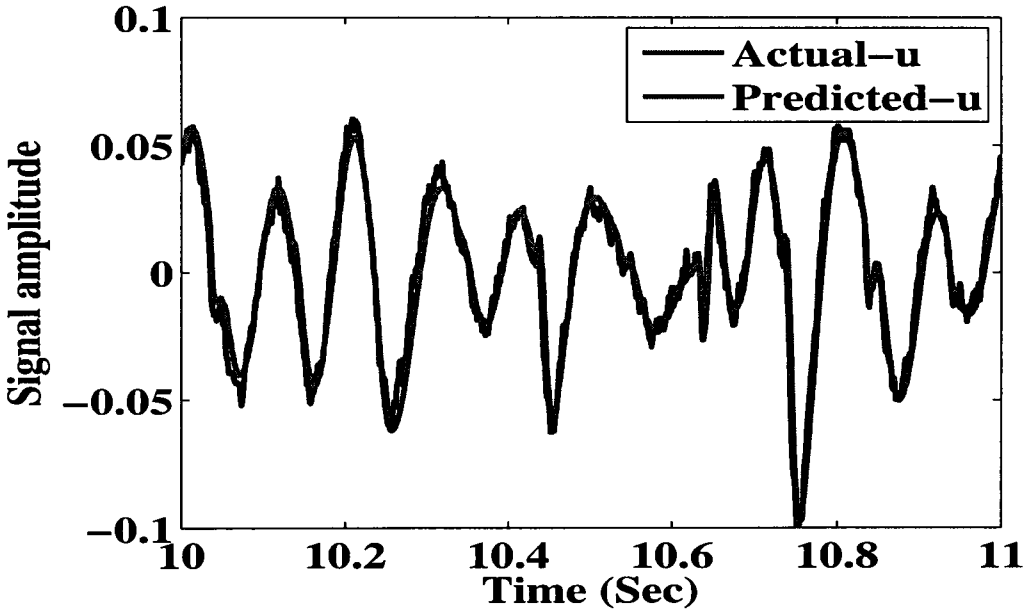

Fig. 8.14. Magnified version of the time-series signals shown in Figure 8.13.

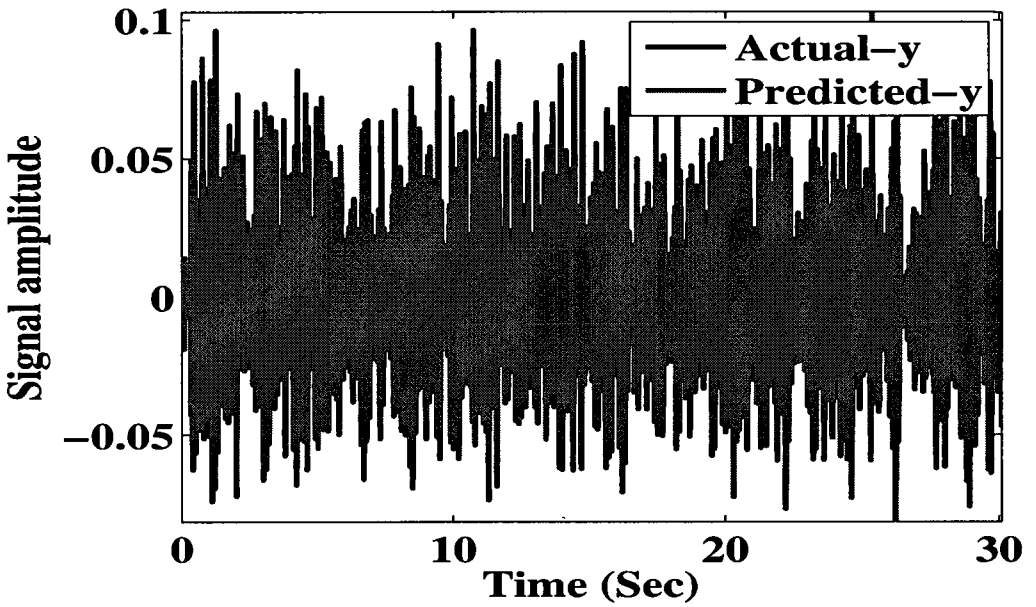

Fig. 8.15. Predicted versus actual output dynamic strain at reference (healthy stage) damage condition.

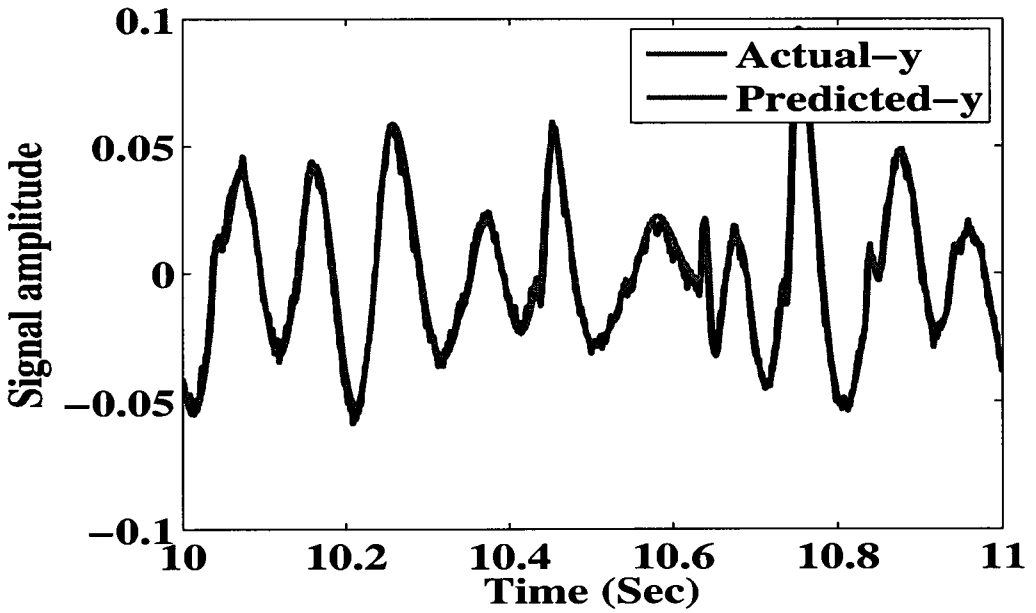

Fig. 8.16. Magnified version of the time-series signals shown in Figure 8.15.

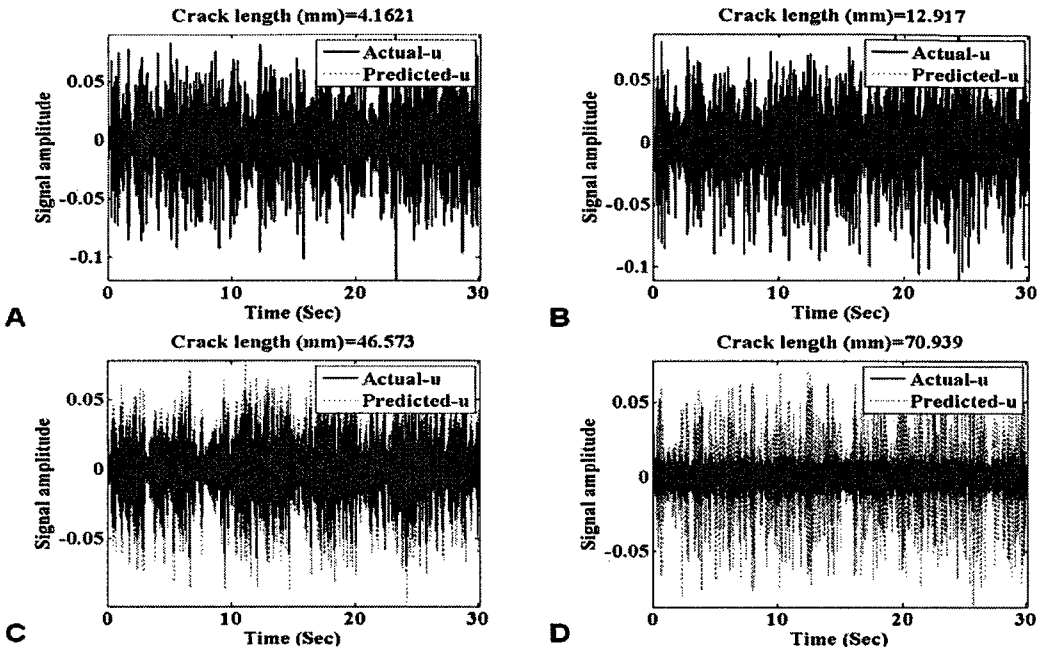

Fig. 8.17. Predicted versus actual input dynamic strain at different damage levels.

the predicted and actual dynamic strain increases. If there had been no damage, ideally there should be a good match between predicted and actual dynamic strains. However, the estimated n^{th} damage level nonlinear dynamic models $H^n_{U\to u}$ and $H^n_{U\to y}$ will no longer be the same as the reference condition models $H^0_{U\to u}$ and $H^0_{U\to y}$ because of change in the internal dynamics of the structure due to damage. Since fixed (reference stage parameters) model parameters are used to estimate the current damage stage dynamic strains (for a new random load $U^n(m) = \{L^n_x(m), L^n_y(m)\}$), the predicted dynamic strain will not match its actual value. The difference increases as the severity of damage grows.

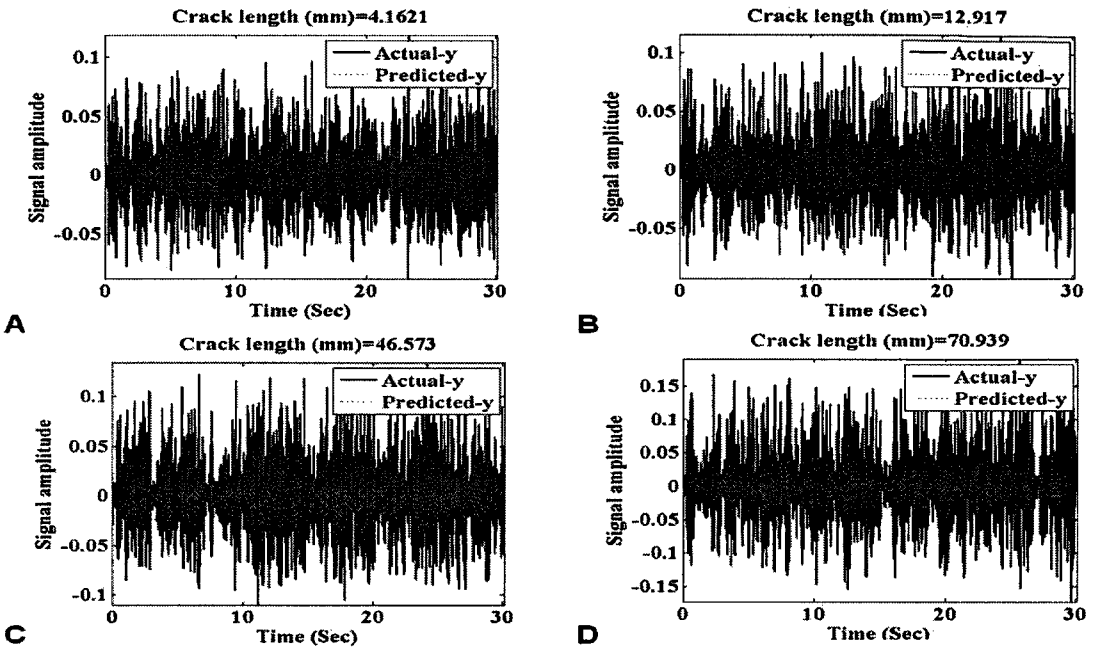

Fig. 8.18. Predicted versus actual output dynamic strain at different damage levels.

8.3.4. Current damage level error signal estimation

Once the current damage level dynamic strains are estimated, the corresponding error signal can be estimated using Eq. (8.29-8.30). The estimated error signals for the input dynamic strain predictions are shown in Figure 8.19 for four typical damage levels: crack length of 4.1621 mm, 12.917 mm, 46.573 mm and 70.939mm. The corresponding error signals for output dynamic strain predictions are shown in Figure 8.20. There is a clear trend developing as the damage level get higher.

8.3.5. Time-series damage state estimation

A discussion on how to estimate the current damage level (n^{th} damage level) input and output error signals was presented before. The estimated error signals at different damage levels can be used to estimate the corresponding scalar damage states. The individual damage states can be estimated either using the root mean square error (RMSE) based

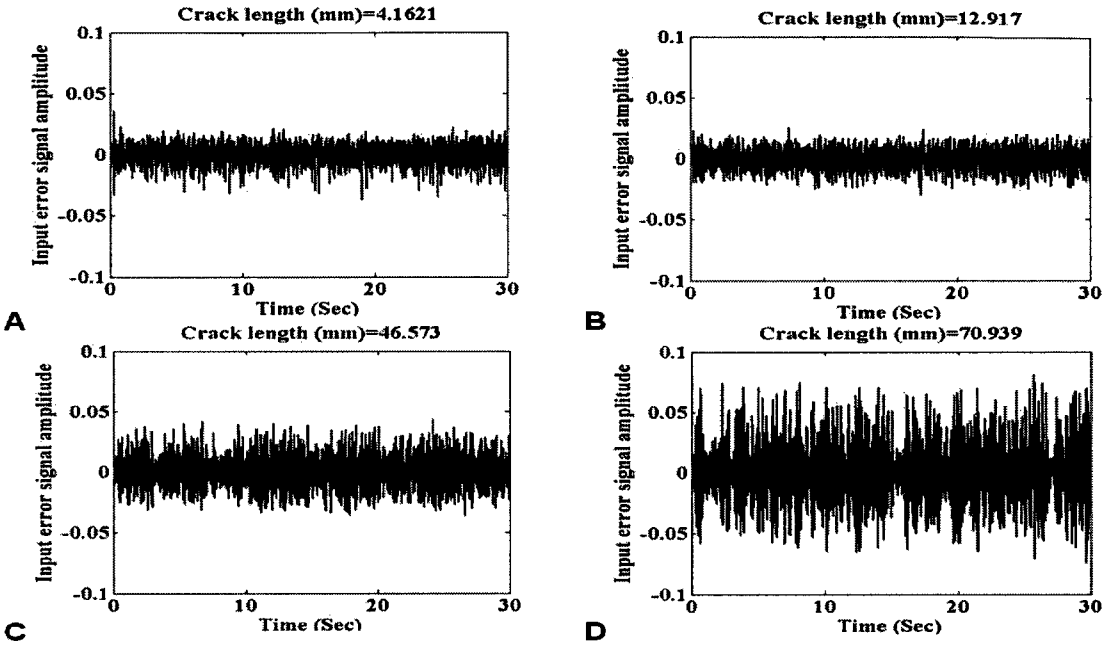

Fig. 8.19. Time-series input error signal at different damage levels

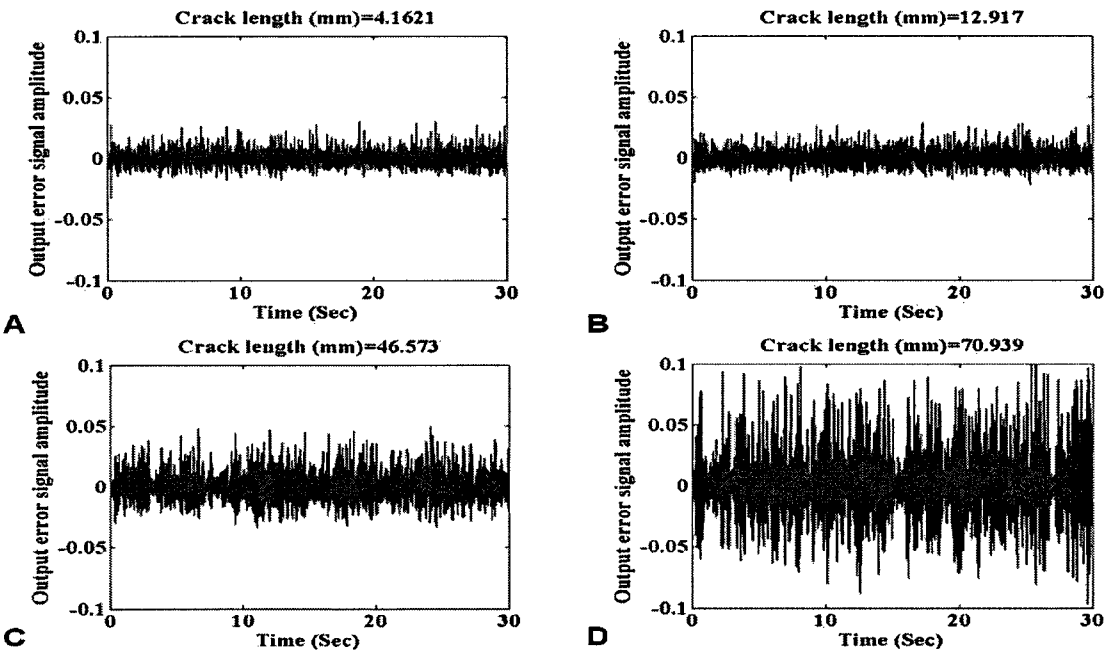

Fig. 8.20. Time-series output error signal at different damage levels

damage index or using the correlation analysis (CRA) based damage index given in Eq. (8.31) and Eq. (8.32), respectively. The normalized damage states estimated using root mean square error based damage index formulation is shown in Figure 8.21. The figure shows the normalized damage states estimated using both input strain error signal as well as output strain error signal. In addition, the figure shows the normalized crack length estimated from the visual image captured by a high resolution camera. It is to be noted that the random loading fatigue test was started with a precracked (with 1.5 mm crack in front of 1.5mm EDM notch) specimen. In the precracked specimen a stable crack grew up to the bottom wedge boundary resulting in a total length of 43.1 mm (refer Figure 8.5B) then a second crack started at the top edge of the central hole. The stable crack (equivalent of 43.1 mm crack length) reached the bottom boundary of the central wedge in approximately 380680 fatigue cycles. Whereas, the second crack growth was unstable and the crack grew to a total length of 28 mm (Figure 8.5B) within 3320 fatigue cycles. Figure 8.21 only shows the time-series damage state estimation in the stable crack growth regime. For proper comparison the estimated damage states from both sensor signals and from visual image are normalized against their maximum value. From Figure 8.21 it can be seen that, the estimated damage states using the input strain error signal follows a similar trend as that of estimated damage states using the output strain error signal. However, it can be seen that, except during the end of stable crack growth regime, the estimated damage states do not follow the trend of normalized visual measurements. The clear trend in estimated damage states only during the final failure regime is also observed by other works [28, 119]). However it is clear that it is better to identify the fault trend long before the final failure regime. The correlation analysis based damage state estimation given by

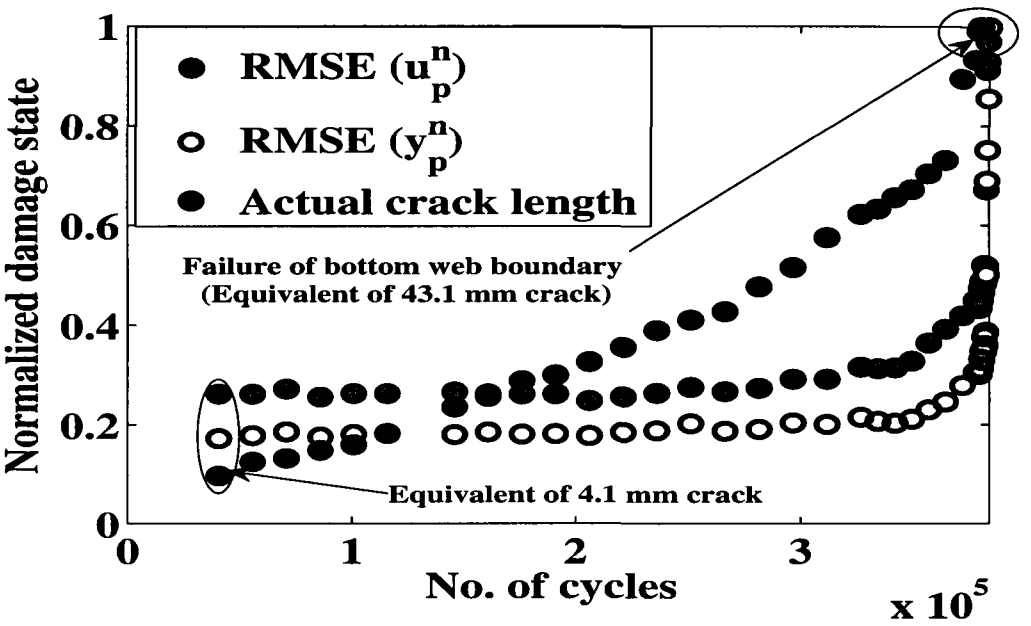

Fig. 8.21. Time-series damage states using root mean square error (rmse) based damage index

Eq. (8.32) can be used to improve the prediction horizon. The estimated damage states using Eq. (8.32) is shown in Figure 8.22. It can be seen that there is a very good correlation between predicted damage states and normalized visual measurements. The accuracy and applicability of the proposed approach can be further improved by using advanced signal processing algorithm.

8.4. Conclusion

A passive sensing based SHM technique that can be useful to estimate the real-time fatigue damage state of any complex structure subjected to random fatigue loading has been introduced. The predicted and actual dynamic strains at two different locations are considered. It is assumed that these two locations will ideally be positioned on opposite sides of the damage path. First, individual reference condition dynamic models are

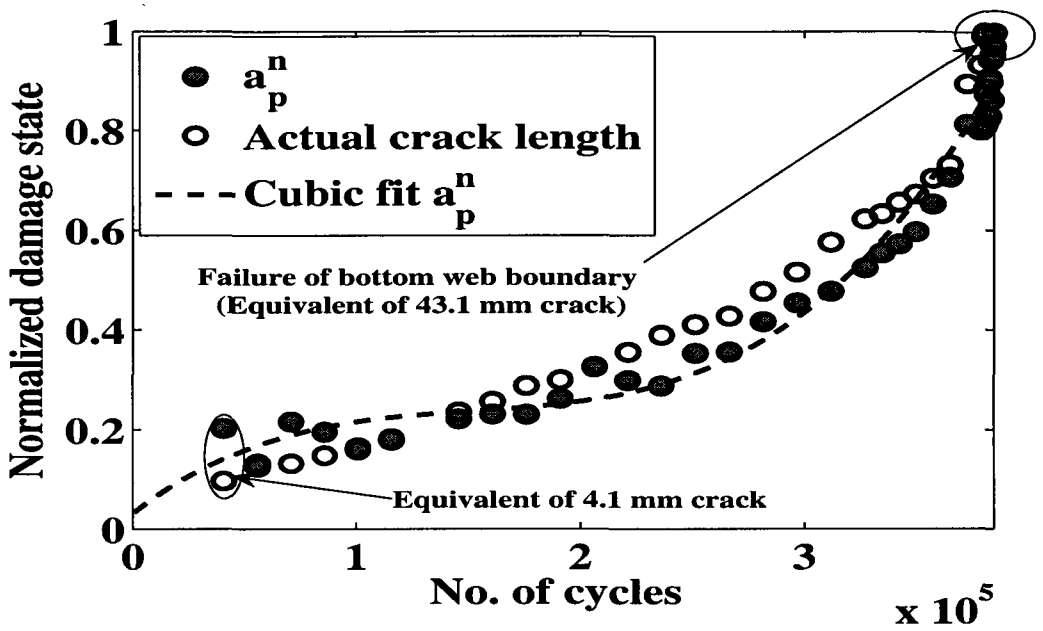

Fig. 8.22. Time-series damage states using correlation analysis (CRA) based damage index

estimated by mapping the reference condition applied load with the reference condition estimated equivalent strain. The reference condition equivalent strains are estimated using the measurements from 3-axis strain gauge rosettes placed at the corresponding locations. The reference condition dynamic models are estimated using Bayesian Gaussian process approach. Once the reference models are estimated, the dynamic strains are predicted for any applied load at any given instant of time using these models. The predicted strains are compared with the actual sensor measurements to estimate the corresponding error signals. Finally the error signals at the two locations are correlated to estimate the corresponding fatigue damage state. The approach is demonstrated for time-series damage state estimation of the complex geometry of an Al-2024 cruciform structure subjected to biaxial random loading. To verify the accuracy of the approach, the predicted damage states are compared with the actual damage states estimated using visual images. From the com-

parison it is found there is a good correlation between the predicted and actual time-series damage states. Further improvement of the prediction accuracy can be achieved by using global optimization and advanced signal processing techniques.

CHAPTER 9

Condition Based Fatigue Damage Prognosis and Residual Useful Life Estimation

9.1. Introduction

The conventional damage prediction approach uses either a deterministic physics based approach or a stochastic data driven approach, in order to predict the future progression of the damage and to estimate the residual remaining life of the structure. In either of these methods the damage tolerance and fatigue life predictions are obtained based on assumed structural flaws, regardless of whether they actually occur in service (i.e the prognosis is made before the diagnosis). Consequently, a large degree of conservatism is incorporated into structural designs due to these uncertainties. In realty, keeping track of the damage growth in a complex structural component manually is quite difficult and requires automatic damage state estimation. The availability of effective online (or autonomous) damage state estimation techniques offers adaptive damage state prediction and residual useful life assessment. The real-time damage state information from online state estimation model can be used as input to a predictive model to update the residual useful life estimation in the event of a new prevailing situation on a regular basis. The offline state prediction model (chapter 3 and 4) and online state estimation model (chapter 5 to 8) have been discussed before. The interrelations between the two models have not been discussed. The present chapter discusses the use of an integrated prognosis model, which combines the previously discussed online state estimation model with the offline predictive model. The aim of the integrated model is to estimate the condition based future damage states and the corresponding residual useful life.

9.2. Theoretical Approach

The integrated prognosis model is an adaptive model that works in conjunction with real time sensor measurements. As shown in Figure 9.1, the integrated prognosis architecture has two distinct sub modules, the online state estimator and the offline state predictor. The online state estimator infers the current state of the structure from real time sensor measurements. Once the current state information becomes available, it is fed to the offline predictive model to predict the future states and the corresponding residual useful life is estimated. The estimated current state updates the initial condition of the predictive model. The condition based damage prediction methods can be divided in to two groups based on the techniques followed for online state estimation. For active sensing based damage state estimation the estimated time-series damage indices (or direct sensor signal features) using Eq. (5.14), Eq. (6.10) and Eq. (6.11) do not follow exponential damage growth trend as in case of visual crack growth measurement. This is evident from the time-series damage indices shown in Figures 5.18, 5.19, 6.14, and 6.16. From these figures it can be seen that the estimated damage indices curve do not follow an exponential growth pattern as in case of visual crack growth measurements (Figure 5.3). This feature based damage cannot be directly fed to the offline predictive model for initial condition updating. It is to be noted that the offline prognosis model is largely based on the physics of damage propagation which would follow exponential damage growth patterns as in the case of visual crack growth measurement. To use the active sensing based approach for condition based damage prognosis first the time-series damage features have to be mapped to global damage states (such as crack length) using a supervised approach as discussed in chapter 5. The active sensing based condition based prognosis approach will be discussed in the

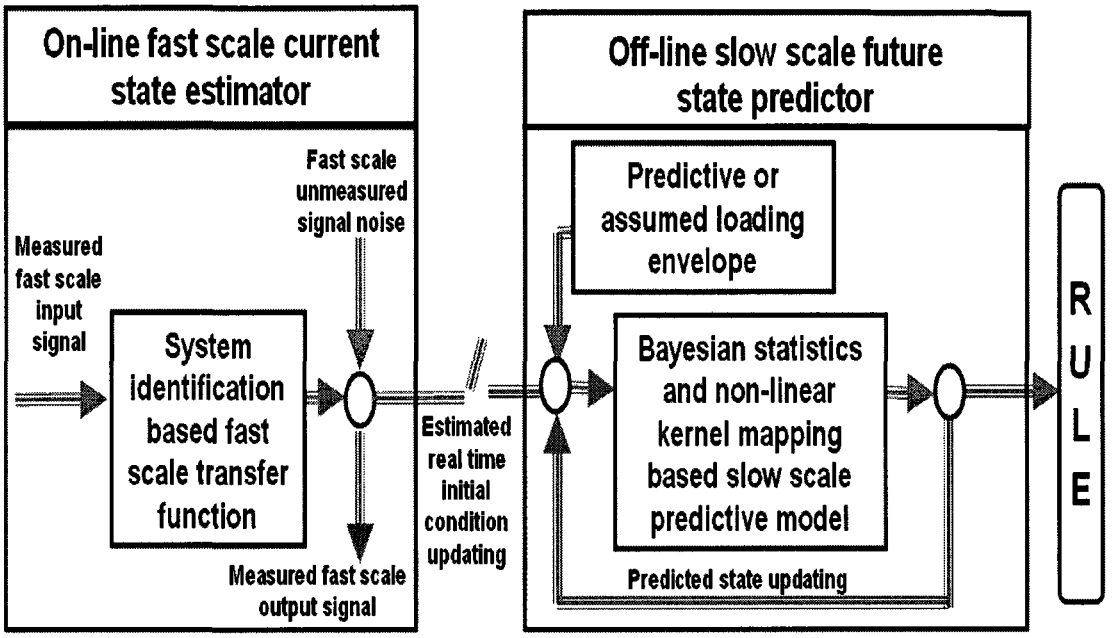

Fig. 9.1. Schematic of the integrated prognosis model

following subsections. Contrary to the active sensing approach, the passive sensing based approach is more global. The estimated time-series damage indices from passive sensing approach follow exponential damage growth patterns as in case of visual crack growth measurement. This is evident from Figure 7.8 and 7.9 of chapter 7 and from Figure 8.22 of chapter 8. Hence the passive sensing based estimated damage indices can directly be fed to a prognosis model for condition based future damage state prediction. The passive sensing based condition based prognosis approach will be discussed in the following subsections. For the previously discussed offline prediction (chapters 3 and 4), Bayesian based GP data driven approach is followed. Note that an on-board prognosis system should be based on a data driven approach as it takes less computational time compared to finite element based physics model. Also to use the physics based prognosis model, the crack path needs to be known in priory, and therefore it is not suitable for on-board applications.

9.2.1. Condition based damage prognosis using passive sensing

In previous chapters online state estimation model and offline state prediction model, were described individually. The present chapter discusses how the estimated online state information is linked to the offline model to reassess the future state and the corresponding residual useful life estimate (RULE). The estimated damage states are fed into the offline predictive model, as the online state information becomes available. As discussed in the previous subsection, the current condition damage states can be estimated either using the supervised active sensing based approach or using the unsupervised passive sensing approach. In the present chapter only the passive sensing based condition based damage prognosis is demonstrated. For the offline prediction, the previously discussed (chapters 3 and 4) Gaussian process is used. Unlike the previous case of supervised GP model, in the present case a self supervised GP model is used. Here, "supervised" means that the GP model is trained with history test data from previously tested specimen(s). In the present self-supervised case, to predict the future damage of the test structure, the GP model is trained with the history data of the test structure it self. At a given instant the available time-series damage states estimated using the online model is used to train the GP model. In the present case constant cyclic fatigue loading is considered. For the purpose the damage index given by Eq. (7.5) can be used for the online damage state estimation. However, for passive sensing based damage state estimation under random loading Eq. (8.32) given in chapter 8 must be used. For the offline model a multivariate GP model is used. The

one-step ahead GP prediction model is given below.

$$\begin{aligned} f(a_{n+1}|D &= \{\mathbf{x}_i, a_i\}, \mathbf{x}_{n+1}, k_{ij}(x_i, x_j, \Theta)_{i,j=1,2,..n}) \\ &= \sqrt{\frac{det(\mathbf{K}_n)}{(2\pi)det(\mathbf{K}_{n+1})}} exp(-\frac{(a_{n+1}-\mu_{n+1})^2}{2\sigma_{n+1}^2}) \end{aligned} \tag{9.1}$$

where μ_{n+1} is the one-step ahead predicted mean at damage level $n+1$ and is given by

$$\mu_{n+1} = \mathbf{k}^T \mathbf{K}_n^{-1} \mathbf{a}_n; \quad k_i = k(\mathbf{x}_{n+1}, \mathbf{x}_i)_{i=1,2,...n} \tag{9.2}$$

σ_{n+1}^2 is the one-step ahead predicted variance at damage level $n+1$ and is given by

$$\sigma_{n+1}^2 = \kappa - \mathbf{k}^T K_n^{-1} \mathbf{k}; \quad k_i = k(\mathbf{x}_{n+1}, \mathbf{x}_i)_{i=1,2,...n};$$

$$\kappa = k(\mathbf{x}_{n+1}, \mathbf{x}_{n+1}) \tag{9.3}$$

The individual elements of the kernel matrix K_n in Eq. (9.2 and 9.3) are based on the assumed multi layer perceptron (MLP) [97] based kernel function given as

$$k_f(\mathbf{x}_i, \mathbf{x}_j, \Theta) = \theta_n^p Sin^{-1}$$

$$\frac{\mathbf{x}_i^T \theta_n^w \mathbf{x}_j}{\sqrt{(\mathbf{x}_i^T \theta_n^w \mathbf{x}_i + 1)(\mathbf{x}_n^T \theta_n^w \mathbf{x}_n + 1)}} + \theta_n^\vartheta \tag{9.4}$$

The individual hyperparameters $\theta_n^{(\cdot)}$ in Eq. (9.4) can be evaluated using the procedure discussed in chapter 3. The one-step ahead GP model given in Eq. (9.1), recursively updates it parameter at each damage level. The update is performed for both the online and offline cases. For example, when a new online estimated state is available (say at n^{th} damage level), then it is included in the previous damage level (at $n-1^{th}$ damage level) training data set of the GP model. Accordingly a new set of hyperparameters (Θ) are estimated. Based on this new trained GP model and n^{th} damage level online or true condition the $(n+1)^{th}$ damage level damage state is forecasted in offline. Similar to the

case of online data updates, the $(n+1)^{th}$ damage level forecasted state is included in the previous damage level (at n^{th} damage level) training data set of the GP model, resulting in a new set of hyperparameters Θ being estimated to forecast the next level i.e., the $n+2^{nd}$ level damage state. This parameter update and current and future state estimation process is performed recursively as shown in Figure 9.1. The details of the input-output data set used in the parameter update are described below.

9.2.1.1. *Input-output data set for single step ahead prediction*

For single step ahead prediction, the Gaussian process prediction model given by Eq. (9.1), predicts the single step ahead damage index. For prediction of the $(n+1)^{th}$ damage index, the training data set D and test input vector $\mathbf{x}_{n+1}$ can be stated as,

$$D = \left[\mathbf{x}_i \mid a_i \right]_{i=d,\ldots,n}$$

$$= \begin{bmatrix} \overbrace{\begin{matrix} a_0 & a_1 & \ldots & a_{d-1} \\ a_1 & a_2 & \ldots & a_d \\ \vdots & \vdots & \ldots & \vdots \\ a_{n-d} & a_{n-d+1} & \ldots & a_{n-1} \end{matrix}}^{Training\ data\ matrix} & \overbrace{\begin{matrix} a_d \\ a_{d+1} \\ \vdots \\ a_n \end{matrix}}^{Target\ vector} \end{bmatrix} \tag{9.5}$$

$$\mathbf{x}_{n+1} = \begin{bmatrix} \overbrace{\begin{matrix} a_{n-d+1} & a_{n-d+2} & \ldots & a_n \end{matrix}}^{Test\ input\ data\ vector} \end{bmatrix} \tag{9.6}$$

In Eq. (9.5 and 9.6) the subscript n symbolizes the n^{th} damage instance or damage level, up to which the last online data was available, and d represents the dimension of the input space.

9.2.1.2. *Input-output data set for multi step ahead prediction*

For multi step ahead prediction, the GP model given by Eq. (9.1) recursively predicts the future state after the last online data available. However, unlike the single step ahead prediction model, the multi step ahead training data set D and test input vector $\mathbf{x}_{n+\tilde{n}}$ are adaptively updated with offline predicted damage indices rather than online estimated damage indices. For prediction of the $n+\tilde{n}^{th}$ damage index the training data set D and test input vector $\mathbf{x}_{n+\tilde{n}}$ can be written as

$$D = \left[\mathbf{x}_i \mid a_i \right]_{i=d,\ldots,n-1+\tilde{n}}$$

$$= \left[\overbrace{\begin{matrix} a_0 & a_1 & \cdots & a_{d-1} \\ a_1 & a_2 & \cdots & a_d \\ \vdots & \vdots & \cdots & \vdots \\ a_{n-d} & a_{n-d+1} & \cdots & a_{n-1} \\ a_{n-d+1} & a_{n-d+2} & \cdots & a_n \\ a_{n-d+2} & a_{n-d+3} & \cdots & a^p_{n+1} \\ \vdots & \vdots & \cdots & \vdots \\ a^p_{n-d-1+\tilde{n}} & a^p_{n-d+\tilde{n}} & \cdots & a^p_{n-2+\tilde{n}} \end{matrix}}^{Training\ data\ matrix} \overbrace{\begin{matrix} a_d \\ a_{d+1} \\ \vdots \\ a_n \\ a^p_{n+1} \\ a^p_{n+2} \\ \vdots \\ a^p_{n-1+\tilde{n}} \end{matrix}}^{Target\ vector} \right] \tag{9.7}$$

$$\mathbf{x}_{n+\tilde{n}} = \left[\overbrace{\begin{array}{cccc} a^p_{n-d+\tilde{n}} & a^p_{n-d+\tilde{n}+1} & \cdots & a^p_{n-1+\tilde{n}} \end{array}}^{Test\ input\ data\ vector} \right] \tag{9.8}$$

Where the subscript n symbolizes the damage instance up to which the last online data is available, and the subscript $\tilde{n}$ represents the damage instance number after the last online data available, and the superscript p symbolizes predicted damage index from the offline module, as opposed to being estimated from the online model.

9.2.1.3. *Residual useful life estimation (RULE)*

The residual useful life estimation can be defined as the difference between the number of fatigue cycles at which the predicted damage index becomes critical, i.e reaches its critical value (a^*), and the number of fatigue cycles at which the last online data is available. The RULE can be defined as:

$$RULE = (n + \tilde{n}^*)\Delta N + N_0 - (n)\Delta N - N_0 = \tilde{n}^*\Delta N \tag{9.9}$$

where ΔN is the number of fatigue cycle increments per each increment of damage instance and $\tilde{n}^*$ corresponds to the number of damage instances for the damage index to become critical after the last available online data.

9.3. Numerical Results

To validate the integrated prognosis algorithm, fatigue test was performed on an Al-6061 cruciform specimen under biaxial loading. The loaded cruciform specimen in an MTS biaxial fatigue test frame can be seen in Fig.7.4. The test was conducted under constant cyclic fatigue loading. Details regarding fatigue test can be found in section 7.3.1 of chapter 7. The online states are estimated based on Eq. (7.5) and using passive sensor

signals acquired from two sensors, one is considered as input and the other is considered as output. As discussed earlier (section 7.3.2 of chapter 7), to evaluate the damage index, the signal (ϵ_x^F) from the strain gauge mounted on the horizontal flange (or X-arm) of the cruciform specimen was considered as the input signal u, whereas the signal (ϵ_x^W) from the web mounted stain gauge was considered as output y. The magnified view of the cruciform specimen can be seen in Figure 7.5. Based on the online estimated damage states and using the self-supervised GP model discussed in previous section the condition based future states are predicted. The details of the numerical results are discussed in the following subsections.

9.3.1. Single step ahead state forecasting

Figure 9.2 shows the comparison between single step ahead forecasted state and actual damage state (or damage index) with online data available up to the previous damage level. The prognosis algorithm starts predicting from damage level 7. The dimension d of the Gaussian process input was chosen as 6. Therefore the prognosis algorithm requires at least six damage states to obtain the 1×6 test input vector (see Eq. 9.6). Also, due to the unavailability of any training data set D (Eq. 9.5), to predict the 7^{th} damage state, the initial hyperparameters (Eq. 9.4) are chosen as: $\theta_n^p = \theta_n^w = 1$ and $\theta_n^\vartheta = 0.1$. There is a large mismatch between the 7^{th} level predicted damage index and the actual damage index. However, for predicting damage state levels eight and beyond, the training input data matrix (Eq. 9.5) and target vectors (Eq. 9.6) are recursively updated. For each recursive updating, a new set of hyperparameters were obtained using the conjugate gradient optimization method. Once the hyperparameters are estimated, the one-step ahead damage index was predicted for the immediate ahead damage level. Figure 9.2 shows a clear correlation between one-step ahead predicted damage index and the actual damage index.

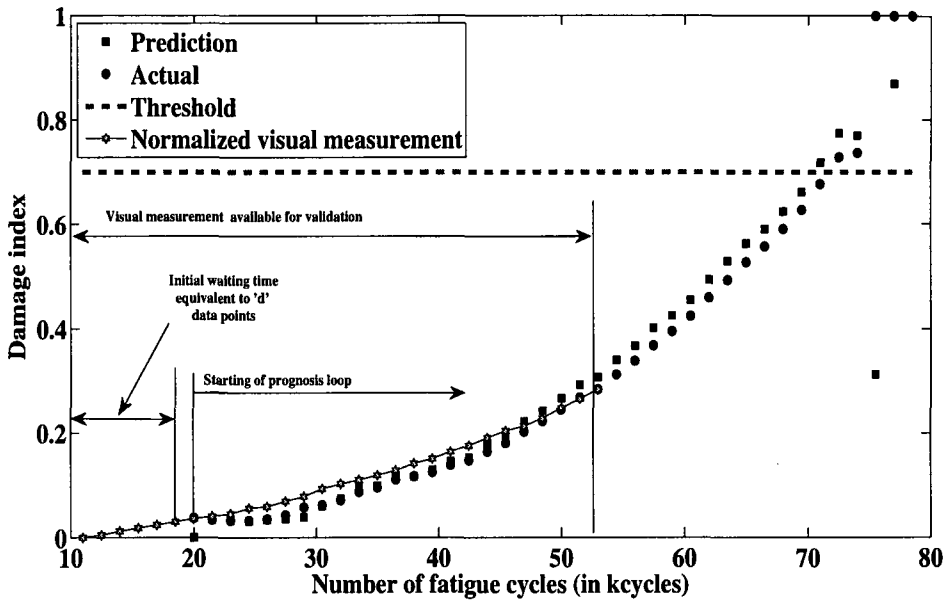

Fig. 9.2. One-step ahead damage state prediction using offline predictive model

It must be noted that the actual damage indices are the online damage states (or damage index) which were directly estimated from the sensor signals. The threshold value of 0.7 is 70% of the final damage index value of 1. From Eq. (7.5) (chapter 7) the damage index reaches its final value of 1 when there is no cross-correlation between the input u and y. This is because the specimen has undergone complete failure. It should be noted that the critical damage index value of 0.7 was selected based on the results from previously performed similar experiments.

9.3.2. Multi step ahead prediction

Unlike the single step ahead prediction, the multi step ahead prediction recursively predicts the damage state multiple steps ahead of the damage level at which last online data was available. Figure 9.3 shows the multi step ahead state prediction. Similar to single step ahead prediction process, the prognosis algorithm was started after the 6^{th} damage

level (i.e., at 18.5 kcycles). From the 7^{th} damage level (20kcycles), damage indices were predicted and then fed back to the prognosis model to update the Gaussian process training data matrix (Eq. 9.7) and the test input vector (Eq. 9.8). The feedback process and the corresponding future state predictions were continued recursively as long as the predicted damage index did not reach its critical value of 0.7. It is to be noted that unlike the single step ahead prediction, the training data matrix and the corresponding test input vector were updated with offline model predicted states, rather than being updated with online model estimated states, which could not be available in real time. It can be seen from Fig. 9.3 that, with online data available up to damage level 23 (at 44 kcycles), the multi step ahead predicted states fails to reach the critical value of 0.7. This is because the predictive model was unable to learn the damage growth dynamics. It is also to be noted that if the predictive model does not learn the damage growth dynamics it keeps on running with only predicting unvarying damage indices. The predicted unvarying damage indices time series can also be seen from the Fig. 9.3. Without satisfying the threshold criteria, the prediction of unvarying damage indices could have continued indefinitely. However to reduce the computational expenses, the prognosis algorithm was stopped at certain times. The criteria for stopping the algorithm was if the rate of damage index growth was not greater than $1 \times 10^{-7}/cycles$ for six consecutive damage levels, the offline predictive model had to be terminated. This was because, if the damage growth was slow enough, the predicted damage index, would never reach the critical value even if the algorithm had to run indefinitely. From Figure 9.3 it is also seen that, the first multi step ahead prediction curve, that reaches the critical value starts from damage level 24 (from 45.5 kcycles). Beyond this damage level, the multiple step ahead prediction increasingly converges with the actual damage index.

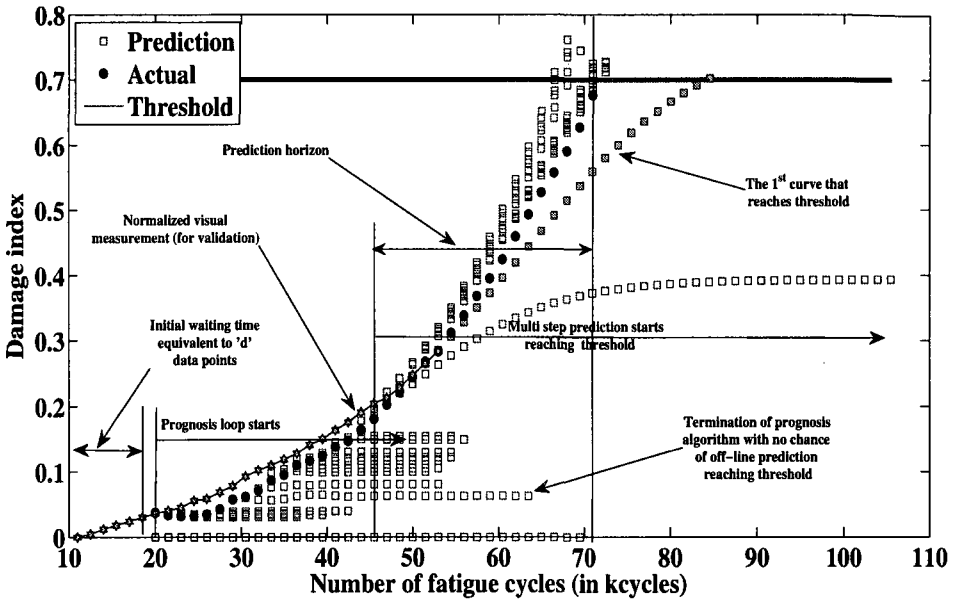

Fig. 9.3. Multi-step ahead damage state prediction using offline predictive model.

From the above mentioned observations, it can be assumed that the prediction horizon (or the true positive regime) was between damage level 24 (45.5 kcycles) and damage level 42 (72.5 kcycles), during which, the predicted damage states reached its critical value.

9.3.3. Residual useful life estimation (RULE) and mean square error evaluation

Using Eq. (9.9), the residual useful life at any given damage level (up to the last online data available) was estimated. Figure 9.4 shows the comparison of predicted RULE and actual RULE. From the figure it can be seen that, there is a good correlation between predicted and actual RULE in the true positive regime i.e., between 45.5 kcycles and 72.5 kcycles. Also as more and more online data becomes available, better correlation between predicted RULE and actual RULE is observed. Figure 9.5 shows the mean square error between predicted RULE and estimated RULE. It can be seen that during the true positive

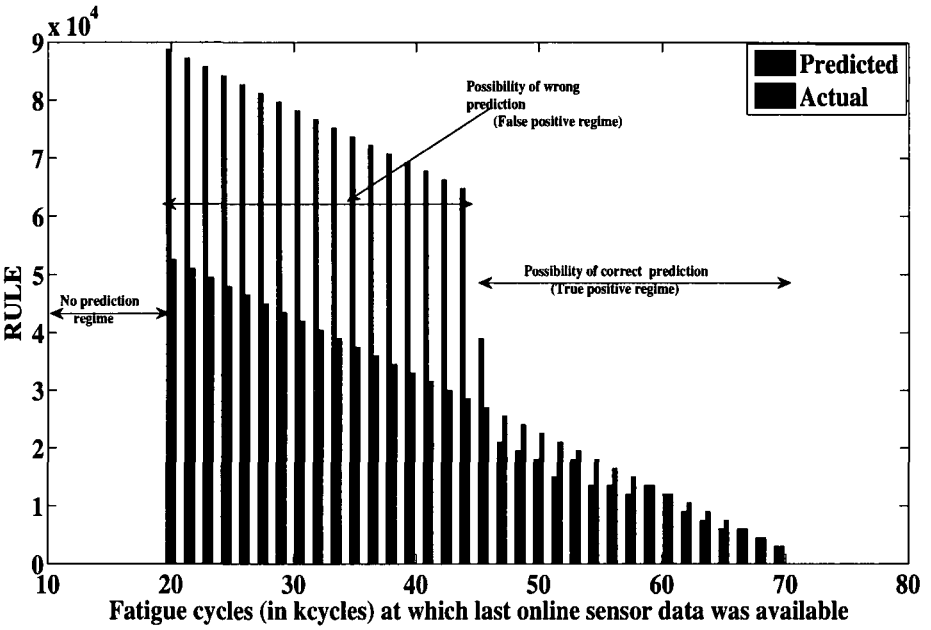

Fig. 9.4. Comparision of predicted RULE and actual RULE.

regime, the mean square error is substantially lower than the mean square error during the false positive regime.

9.4. Conclusion

An online-offline prognosis model is proposed for adaptive future damage state prediction and residual useful life estimation. The proposed prognosis model combines an online state estimation model with an offline predictive model to adaptively estimate the residual useful life of an Al-6061 cruciform specimen under biaxial loading. The online model was based on passive sensing approach (chapter 7), which estimates the current damage states. Once the current damage state was available from the online model, the information was fed to an offline predictive model to obtain the future states and remaining useful life estimation (RULE). The offline predictive model is a high-dimensional kernel function based Gaussian process model (previously discussed in chapter 3). The future states are

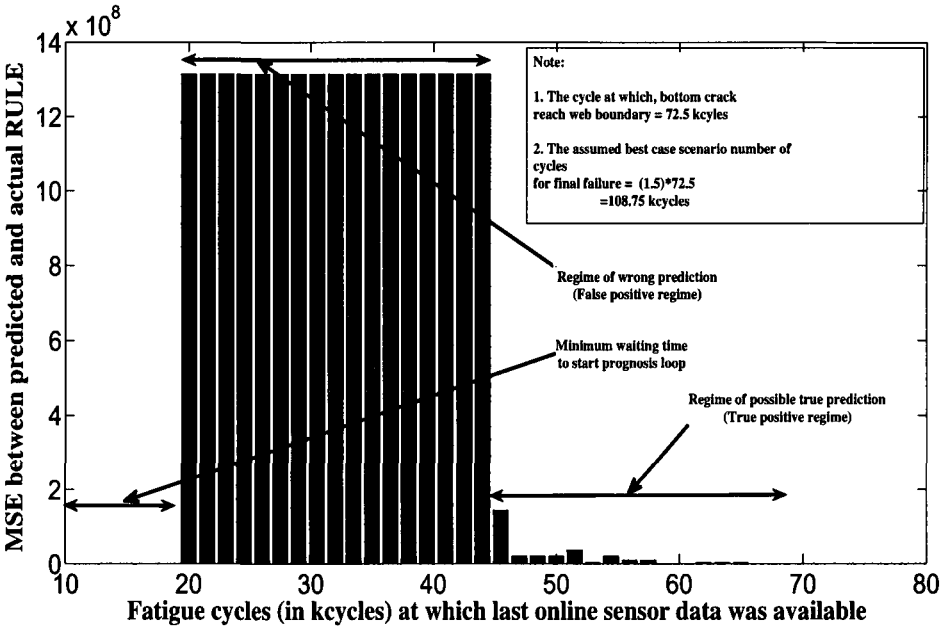

Fig. 9.5. Mean square error between predicted RULE and actual RULE.

recursively predicted by feeding back the previous predicted states to the offline model. Also, the model parameters (Gaussian process hyperparameters) were updated with recursively. Good correlation was also observed between actual damage states and predicted future damage states well before the final failure occurred. Furthermore, a good correlation between predicted RULE and actual RULE is also observed during which, the predicted damage index reached its critical value.

CHAPTER 10

Summary and Future Works

A real-time framework has been developed for condition based fatigue damage state estimation and residual useful life prediction. The developed framework consists of both online structural health monitoring (SHM) model for current damage state estimation and offline prognosis model for future damage state prediction. State awareness models have been developed through SHM using strain gauge based passive sensing measurements as well as using guided wave propagation based active sensor measurements. Both SHM models estimate time-series damage condition using real-time sensor measurements. In addition to forecasting the future damage states, an offline prognosis has been developed using Gaussian process (GP). The integrated online-offline framework is illustrated for condition based fatigue damage state prediction and remaining useful life estimation. The approach is validated against monitoring and predicting fatigue damage of complex Al-2024/6061 structures. In this chapter, a general summary of the research is presented, along with some thoughts on future work.

10.1. Summary

The major contribution of this work is to develop an integrated condition based damage prognosis model. The integrated framework comprises the following three critical elements.

1. Offline damage prognosis
2. Online state estimation using active sensing
3. Online state estimation using passive sensing
4. Condition based adaptive prognosis

The major observations from these studies are summarized in the following sections.

10.1.1. Offline damage prognosis

A one-step ahead Bayesian Gaussian process (GP) predictive model has been developed to forecast damage under constant, random and flight profile fatigue loading. The GP model is based on high-dimensional kernel transformation that can perform nonlinear pattern reorganization. Based on history of fatigue damage information, the GP model uses a Bayesian framework to predict the future fatigue damage states for any future anticipated load. The important observations from the offline GP model are as follows.

1. Compared to the conventional fracture mechanics approach the proposed data driven approach does not require the use of any approximated coupon geometric function that is necessary in the case of conventional Paris law based fracture mechanics approach to model the stress intensity factor. This indicates that, the developed GP model can be useful for fatigue modeling of real-life complex geometry and is expected to give better prediction performance compared to the fracture mechanics type model.

2. The approach is computationally less intensive, compared to FE models and therefore can be suitable for on-board applications.

3. The numerical validation under random and flight profile fatigue load shows that prediction under a particular load spectrum can be performed very accurately by training the GP model with the fatigue test data obtained under same loading condition.

4. Prediction under a different loading spectrum can be performed fairly accurately if the GP model has been trained with a fatigue test data set that contains majority of the test case load patterns (e.g., the load ratios). In the present case this is illustrated with an example where the GP model is trained using random load fatigue test data

and prediction is made for flight profile load.

From the above discussion, it can be summarized that the proposed approach can effectively be used in practical applications. It is assumed that each aircraft manufactures performs at least one full-scale fatigue test to validate the structural integrity. During this testing, required data can be collected and can be used to train the GP model. It is anticipated that this trained GP model can then be used in the on-board system to predict damage in real-time for any new anticipated load at any given instant of time.

10.1.2. Online state estimation using active sensing

The online damage state estimation estimates the current health of the structure based on real-time sensor measurements. Both active and passive sensor measurements based on-line estimation models have been developed. For active sensor measurement two different approaches have been developed, such as supervised and unsupervised state estimation model. A GP supervised model is developed to estimate the online damage states. The online damage states are estimated using real-time sensor measurements and a trained GP model. The active sensing based approach is based on piezoelectric sensor signals, which are acquired using a narrowband input applied to piezoelectric actuator. To estimate the damage states for a particular specimen previous test data were used to train the GP model. From previous test, sensor signal features such as change in signal variance and change in central frequency of the applied input signal was used to construct the GP input matrix. For the corresponding output, the visually measured crack length was used. The GP model was trained using the input-output history data. The trained GP model was used to estimate the unknown damage state at any given instant of time if the corresponding sensor

signals were available. The developed approach is demonstrated on an Al-2024 Lug-joint damaged under uniaxial fatigue loading. The online damage state estimation showed that there is a good correlation between experiment and estimation when the crack length is larger than 6 mm.

The supervised GP model may not be feasible for all practical applications since it is require measuring the training case damage conditions by visual measurements. The visual measurements may not be always possible as in case of monitoring unassailable regions such as in undercarriages. To avoid this problem of visual measurements in supervised approach an unsupervised approach is preferred. Different unsupervised system identification models are developed for online damage state estimation. Two nonparametric system identification techniques, empirical transfer function estimation (ETFE) approach and correlation analysis approach (CRA), have been presented for estimating the time-series fatigue damage states. Broadband ultrasonic input was used as opposed to narrowband ultrasonic input. The broadband input helps estimating smaller damage. Novel dual sensing method was used for better noise removal and to improve spatial resolution in time-series damage state estimation. The time-series damage estimation approaches have been validated on a complex Al-2024 cruciform specimen damaged under biaxial fatigue loading. The important observations from the broadband input based unsupervised models are as follows.

1. The developed approach estimates very small damage such as micro cracks in front of plastic zones.

2. The procedure is capable of estimating time-series damage states encompassing all three fatigue damage regimes, such as stage-I, II and III crack growth stages.

3. Numerical study shows that the correlation based damage index estimation follows a better trend of cumulative damage growth compared to the empirical transfer function estimation based approach.

4. The damage index estimation based on the broadband chirp input outperforms the narrowband input based damage index estimation.

5. In the pulse-echo configuration, with sensors placed near the actuator, was more effective for time series damage state estimation than the pitch-catch configuration, where the sensors were placed away from the actuator.

6. The unsupervised approaches showed good validation on complex cruciform geometry.

10.1.3. Online state estimation using passive sensing

Active sensing approach requires external power source to excite the piezoelectric actuator. To avoid this limitation a passive sensor measurement based approach has also been developed. An online state estimation technique based on correlation of dynamic strain measurements at two different location of a structure has been developed. The approach has been validated on an Al-6061 cruciform specimen subjected to biaxial but constant cycle fatigue loading. The numerical results showed good correlation between online estimated time-series damages states and the corresponding normalized visual measurements. The proposed approach can be useful for monitoring of rotary components such as rotor blades, hubs, transmission shafts of helicopter or aircraft engines. With maintaining a particular reference speed the above mentioned components can be subjected to a constant cyclic loading either in grounded condition or in-flight condition. And by following the developed approach, the instantaneous health of the mentioned rotary components can be estimated.

A passive sensor measurement based dynamic strain mapping model has also been developed. Passive sensor measurement based correlation analysis model works well only when the applied cyclic load is constant. Therefore, a passive sensing based model that can be useful for damage state estimation under random loading has also been developed. The model uses, dynamic strain at two different locations. Individual reference condition dynamic models are estimated my mapping the reference condition applied load with the reference condition measured dynamic strain. The reference condition dynamic models are estimated using Bayesian Gaussian process approach. Once the reference models are estimated, using these models the dynamic strains are predicted for any applied load at any given instant of time. The predicted strains are compared with the actual sensor measurements at the above mentioned locations to estimate the corresponding error signals. Finally the error signals at these two locations are correlated to estimate the corresponding fatigue damage state. The developed model was validated for time-series damage state estimation of a complex geometry Al-2024 cruciform structure subjected to biaxial random loading. The predicted damage states have been compared with the actual damage states estimated using visual images. From the comparison it is found there is a good correlation between the predicted and actual time-series damage states. It is expected that the developed approach can be useful for monitoring the real-time health of any real-life complex structure under any complex random loading conditions.

10.1.4. Condition based adaptive prognosis

An integrated framework of online SHM model and offline prognosis model has been developed for condition based damage state prediction. The developed framework combines an online state estimation model with an offline predictive model to adaptively estimate the

residual useful life. The online model estimates the current damage states using real-time sensor measurements. Once the current damage state was estimated, it was fed to the offline model to update new initial conditions. Based on this new condition, time-series future states were recursively predicted. Also, the model parameters (Gaussian process hyperparameters) were updated recursively. The developed approach has been demonstrated on a complex Al-2024 cruciform structure. Good correlation was observed between actual damage states and the predicted future damage states well before final failure occurred. Furthermore, a good correlation between predicted and actual RULE was also observed. From the above observations, it is expected that the developed methodology can be useful for any practical applications.

10.2. Future Works

As mentioned earlier, the overall objective of this research work was to develop an integrated framework for condition based damage state estimation. Based on the present study, some improvements and new concepts are suggested as follows,

1. The multivariate GP model discussed for the complex cruciform geometry was trained using only one previous test data set. Using only one data set for training the GP model does not give the statistical nature of crack growth attributed from the microstructural variability. Generating training data sets by fatiguing real structures is time consuming and costly. It is developed to perform physics based multiscale FE simulation to avoid costly and highly time consuming experiments. With different microstructure representative volume element (RVE), offline fatigue simulation must be performed to generate the crack growth history. Different simulated crack growth

histories should be generated under different loading conditions and using different microstructure RVE. These crack growth histories along with corresponding loading histories must be used for training the GP model. Then the GP predictive model will be statistically robust compared to the present model. The proposed GP model only depends on data, and it is not necessary to run a FE model in real-time. Rather, offline FE simulated data can be stored as a library in the on-board computer for real-time condition based damage prediction.

2. In this work the online damage sate estimation was performed for a smaller structure. However, real-life structural components are often larger in dimension. These large structures can not be monitored using a single sensor network as used in the current work. A suitable framework has to be developed for monitoring large structures using multiple sensor networks. The issue of large scale data storage and information fusion has to be addressed properly.

3. A single component structure is studied in this work. However, real-life structural assemblies are more complex concatenated systems with multiple subcomponents. To perform condition monitoring of such large systems, the developed approach may not be useful directly. A suitable hierarchical system must be developed for condition based life estimation of the overall system.

REFERENCES

[1] "Aloha Airlines Aircraft Accident Investigation", *National Transportation Safety Board*, Jun. 1989.

[2] "Columbia Crew Survival Investigation Report", *http* : *//www.nasa.gov/pdf/*298870*main*$_S$*P* − 2008 − 565.*pdf*, 2008, NASA report no. NASA/SP-2008-565

[3] "Ways and options for aircraft structural health management", *Journal of Smart Mater. Struct*, 10 (2001) 432-440

[4] *ICAO Digest of Statistics*, 517 Series F 2002

[5] Latorella, K.A.,Prabhu,P.V. ., "A review of human error in aviation maintenance and inspection", *International Journal of Industrial Ergonomics*,2000, Vol. 26, pp. 133-161

[6] "Continental express flight 2574 in-flight structural breakup, 1991", *National transportation safety board report, Report number: NTSB/AAR-92/04*

[7] *Structural health monitoring of civil infrastructure systems*, Edited by Vistasp M. Karbhari and Farhad Ansari, 2009, Woodhead Publishing Limited and CRC Press LLC

[8] Silverman, H., "T-HUMS-AH64 Lead the fleet (LTF) summary and glimpse at hermes 450 MT-HUMS," *AIAC Conference* Melbourne, 2005 , Paper 151.

[9] McColl, J., "HUMS in the era of CAA, JAA, EASA and ICAO,", *AIAC Conference*, Melbourne, 2005, Paper 112.

[10] LaRiviere S G and Thompson J , "Development of reliable NDI procedures for airframe inspection", *NATO RTO Meeting Proc. 10: Airframe Inspection Reliability under Field/Depot Conditions paper 7*, 1998.

[11] Achenbach, J.D., "Quantitative nondestructive evaluation,", *International Journal of Solids and Structures*,2000, Vol. 37, pp.13-27.

[12] Achenbach, J.D., "Structural health monitoring - What is the prescription?,", *Mechanics Research Communications*,2009, Vol. 36, pp. 137-142.

[13] Achenbach, J.D., 1992. Measurement models for quantitative ultrasonics. J. Sound and Vibration 159, pp. 385-401.

[14] Siegel, M.W., Kaufman, W.M., and Alberts, C.J., "Mobile robots for difficult measurements in difficult environments: Application to aging aircraft inspection," *Robotics and Autonomous Systems* pp. 11, 1993, pp. 187-194.

[15] Siegel M, Gunatilake P and Podnar G , "Robotic assistance for aircraft inspectors", *IEEE Instrum. Meas. Mag.* 1998, March 16-30.

[16] Farrar, C.R. and Doebling, S.W., "Damage detection II: field applications to large structures," *In: Silva, J.M.M. and Maia, N.M.M. (eds.), Modal Analysis and Testing, Nato Science Series*, 1999, Dordrecht, Netherlands: Kluwer Academic Publishers.

[17] Montalvo, D.,Maia N.M.M., and Ribeiro, A.M.R., "A Review of Vibration-based Structural Health Monitoring with Special Emphasis on Composite Materials," *The Shock and Vibration Digest*, Vol. 38, 2006, pp. 295-324

[18] Maia, N.M.M. and Silva, J.M.M. , *Theoretical and Experimental Modal Analysis.*, 1997, England: Research Studies Press Ltd.

[19] West, W. M, "Illustration of the Use of Modal Assurance Criterion to Detect Structural Changes in an Orbiter Test Specimen,", *Proceedings of the Air Force Conference on Aircraft Structural Integrity*, 1984, 1-6.

[20] Chattopadhyay, A. and Dragomir-Daescu, D., "An Investigation of Delaminated Smart Composite Plates for Damage Detection", *Proceedings of the International Mechanical Engineering Congress and Exposition Winter Annual Meeting of ASME*,1998,Anaheim, CA, pp. 122-132.

[21] Swann, C., Chattopadhyay, A., and Ghoshal, A., "Characterization of Delamination by Using Damage Indices", *Journal of Reinforced Plastics and Composites*, Vol. 24, 2005, pp.699-711

[22] Scanning laser vibrometer, $http://www.polytec.com/int/158_321.asp$ [cited 2010]

[23] Chattopadhyay, A., Thornburgh, R. , and Ghoshal, A., "Transient analysis of smart structures using a coupled piezoelectricmechanical theory", *IUTAM Symposium on Dynamics of Advanced Materials and Smart Structures*,May 2002, Yamagata, Japan.

[24] Chattopadhyay, A., Kim, H. S., and Ghoshal, A.,"Nonlinear vibration analysis of smart composite structures with delamination using a refined layerwise theory", *International Conference on Adaptive Structures (ICAST)*, October 2002, Berlin, Germany.

[25] Kim, H. S., Zhou, X., and Chattopadhyay, A., "Interlaminar stress analysis of shell structures with piezoelectric patch including thermal loading", *AIAA J*, Vol. 40, No. 12, 2002, pp. 2517-2525.

[26] Kim, H. S., Ghoshal, A.,Chattopadhyay, A.,and Prosser, W. H., "Development of Embedded Sensor Models in Composite Laminates for Structural Health Monitoring", *Journal of Reinforced Plastics and Composites*, Vol. 23, 2004, pp. 1207-1240.

[27] Ghoshal, A.,Kim, H. S.,Chattopadhyay, A.,and Prosser, W. H., "Effect of delamination on transient history of smart composite plates", *Finite Elements in Analysis and Design Journal*, Vol. 41, 2005, pp. 850-874.

[28] Williams, T., Ribadeneira, X., Billington , S., and Kurfess T., "Rolling element bearing diagnostics in run-to-failure lifetime testing," *Mechanical Systems and Signal Processing*, Vol. 15, No. 5, 2001, pp. 979-993.

[29] Qiu, H., Lee, J., Lin, J., and Yu, G., "Wavelet filter-based weak signature detection method and its application on rolling element bearing prognostics," *Journal of Sound and Vibration*, Vol. 289 , 2006, pp. 1066-1090.

[30] Carden, E. P., and Fanning , P., "Vibration Based Condition Monitoring: A Review," *Structural Health Monitoring*, Vol. 3, No. 4, 2004, pp. 355-377

[31] Wang, F., and Mechefske, C. K., "Adaptive modeling of transient vibration signals," *Mechanical Systems and Signal Processing*, Vol. 20 , 2006, pp. 825-842.

[32] Raghavan, A., and Cesnik, C. E. S., "Review of Guided-wave Structural Health Monitoring," *The Shock and Vibration Digest*, Vol. 39, No. 2, March 2007, pp. 91-114

[33] Giurgiutiu, V., *Structural Health Monitoring with Piezoelectric Wafer Active Sensors*, Academic Press,2008.

[34] Worlton, D. C., "Experimental Confirmation of Lamb Waves at Megacycle Frequencies," *Journal of Applied Physics*, Vol. 32, No. 6, 1961, pp. 967-971.

[35] Giurgiutiu, V., " Lamb Wave Generation with Piezoelectric Wafer Active Sensors for Structural Health Monitoring", *Proceedings of the SPIE's 10th Annual International Symposium on Smart Structures and Materials and 8th Annual International Symposium on NDE for Health Monitoring and Diagnostics*,SPIE, 2-6 March 2002,San Diego, CA.

[36] Hay , T R., Royer, R. L., Gao, H., Zhao, X. and Rose, J. L., "A comparison of embedded sensor Lamb wave ultrasonic tomography approaches for material loss detection," Smart Mater. Struct. Vol. 15 , 2006, pp. 946-951

[37] Yang, J., and Fu-Kuo Chang, F. K., "Detection of bolt loosening in C-C composite thermal protection panels: I. Diagnostic principle," *Smart Mater.* Struct. 15 , 2006, pp. 581-590

[38] Monnier , T., "Lamb Waves-based Impact Damage Monitoring of a Stiffened Aircraft Panel using Piezoelectric Transducers," *Journal of Intelligent Material Systems and Structures*, Vol. 17, 2006, pp. 411-421

[39] SomaSekhar, B. V., Balasubramaniam, K., and Krishnamurthy, C.V., "Structural Health Monitoring of Fiber-reinforced Composite Plates for Low-velocity Impact Damage using Ultrasonic Lamb Wave Tomography", *Structural Health Monitoring*, Vol. 5, 2006, pp. 243-253

[40] Zhao, X., Gao, H., Zhang, G., Ayhan, B., Yan, F., Kwan, C., and Rose, J. L., "Active health monitoring of an aircraft wing with embedded piezoelectric sensor/actuator network: I. Defect detection, localization and growth monitoring," *Smart Mater. Struct*, Vol. 16, 2007, pp. 1208-1217

[41] Olson, S. E., DeSimio, M. P., and Derriso, M. M., "Beam Forming of Lamb Waves for Structural Health Monitoring," *Transactions of the ASME*, Vol. 129, 2007, pp. 730-738

[42] Michaels, J. E., and Michaels, T. E., "Guided wave signal processing and image fusion for in situ damage localization in plates," *J. of Wave Motion* Vol. 44, 2007, pp. 482-492

[43] Yu, L., and Giurgiutiu, V., "In situ 2-D piezoelectric wafer active sensors arrays for guided wave damage detection", *J. of Ultrasonics*, Vol. 48, 2008, pp. 117-134

[44] Kim, S. B., and Sohn, H., "Instantaneous reference-free crack detection based on polarization characteristics of piezoelectric materials," *Smart Mater. Struct*, Vol. 16, 2007, pp. 2375-2387

[45] Qing, X. P., Beard, S. J., Kumar, A., Sullivan, K., Aguilar, R., Merchant, M., and Taniguchi, M., "The performance of a piezoelectric-sensor-based SHM system under a combined cryogenic temperature and vibration environment," *Smart Mater. Struct.*, Vol.17, 2008, pp. 1-11

[46] Das, S., Chattopadhyay, A., and Zhou, Xu, "Acoustic Based Structural Health Monitoring for Composites Using Optimal Sensor Placement: Analysis and Experiments", *Journal of Reinforced Plastics and Composites* Vlo. 28, 2009, pp. 83-97.

[47] Kostson E., and Fromme, P., "Fatigue crack growth monitoring in multi-layered structures using guided ultrasonic waves," *Journal of Physics: Conference Series* Vol. 195, 2009, pp. 1-10

[48] Chakraborty, D., Kovvali, N., Wei, J., Papandreou-suppappola, A., Cochran, D., and Chattopadhyay, A.,"Damage Classification Structural Health Monitoring in Bolted Structures Using Time-frequency Techniques", *Journal of Intelligent Material Systems and Structures*, Online published on March 23, 2009 as doi:10.1177/1045389X08100044

[49] Doyle, D., Zagrai, A., Arritt, B., Akan, H. C., "Damage Detection in Bolted Space Structures", *Journal of Intelligent Material Systems and Structures*, Vol. 21, pp. 251-264

[50] Palmgren, A., "Ball and Roller Bearing Engineering,"SKF Industries,Inc., Philadelphia, 1945, pp. 82-83.

[51] Miner, M.A., "Cumulative Damage in Fatigue", *Journal of Applied Mechanics*, ASME, Vol.12, Sept. 1945, pp. A-159-164.

[52] Jacoby, G., "Comparison of Fatigue Life Estimation Processes For Irregularly Varying Loads", *Proceedings of 3rd conference on Dimensioning*, Budapest 1968.

[53] Arden, R.W., "Hypothetical Fatigue Life Problem, presented at the Specialists Meeting on Helicopter Fatigue Methodology", *Midwest Region of the American Helicopter Society*, preprint no. 18, 1980.

[54] Gallagher, J.P.; Giessler, F.J.; and Berens, A.P., "Guidelines for the Analysis and Design of Damage Tolerant Aircraft Structures", *USAF Damage Design Handbook*, Air Force Wright Aeronautical Laboratory, AFWAL-TR- 82-3073, 1984.

[55] Everett, R. A., Jr, "A Comparison of Fatigue Life Prediction Methodologies for Rotorcraft," *NASA Technical Memorandum*, Accession Number : ADA239840, 1990, NASA Langley Research center, Hampton, VA

[56] Ghonem, H., and Dore, S. 1987, "Experimental Study of the Constant Probability Crack Growth Curves Under Constant Amplitude Loading ," Engineering Fracture Mechanics., 27(1):1-25

[57] Suresh, S. 1991, Fatigue of Materials, Cambridge University Press, Cambridge, U.K

[58] Broek, D. 2002, *Elementary Engineering Fracture Mechanics*, Kulwer Academic Publishers, Dordrecht, The Netherlands

[59] Newman, J.C., Jr. 1982, "Prediction of fatigue crack growth under variable-amplitude and spectrum loading using a closure model". ASTM STP 761: 255-277

[60] Newman, J.C. Jr. 1984. A crack-opening stress equation for fatigue crack growth. International Journal of Fracture 24, R131-R135.

[61] Newman, J.C. Jr.1992. FASTRAN-II - A Fatigue Crack Growth Structural Analysis Program. NASA Technical Memorandum 104159, Langley Research Center.

[62] Harter, J.A. 1999, AFGROW Users' Guide and Technical Manual. Report No. AFRL-VA-WP-1999-3016, Air force Research Laboratory.

[63] Ray, A., Patankar, R.P.,2001, "Fatigue Crack Growth Under Variable Amplitude Loading-Part-I: Model Formulation in State-Space Setting," J. of Applied Mathematical Modeling, 25(11), pp. 979-994.

[64] Ray, A., Patankar, R.P.,2001, "Fatigue Crack Growth Under Variable Amplitude Loading-Part-II: Code Development and Model Validation," J. of Applied Mathematical Modeling, 25(11), pp. 995-1013.

[65] Patankar, R., Qu, R. 2005, "Validation of the state-space model of fatigue crack growth in ductile alloys under variable-amplitude load via comparison of the crack-opening stress data," Int J. of Fracture., 131(4):337-349

[66] QU, R.1; Patankar, R. P.; Rao, M. D. 2006, "A third-order state-space model for fatigue crack growth ", Fatigue Fract Engng Mater Struct, 29(12):1045-1055

[67] Iyyer, N.; Sarkar, S.; Merrill, R.; Phan, N., "Aircraft life management using crack initiation and crack growth models - P-3C Aircraft experience," *Int. J. of Fatigue*, Vol. 29, 2007, pp. 1584-1607.

[68] ASTM Standards, 1981, ASTM E 399-81, PART-10.

[69] Giner E., Sukumar, N., Tarancon J. E.,and Fuenmayor F. J.,"An Abaqus implementation of the extended finite element method," *Engineering Fracture Mechanics*, 2008

[70] Schwabacher, M. A. "A Survey of Data-Driven Prognostics", *Proceedings of the AIAA Infotech Aerospace Conference*, 26 - 29 September 2005, Arlington, Virginia

[71] Jardine, A. K.S., Lin, D., and Banjevic, D., "A review on machinery diagnostics and prognostics implementing condition-based maintenance," *Mechanical Systems and Signal Processing*, Vol. 20, 2006, pp. 1483-1510

[72] Farrar, C. R., and Lieven, N .A. J., "Damage prognosis: the future of structural health monitoring," *Phil. Trans. R. Soc.* Vol. A 365, 2007, pp. 623-632

[73] DiUlio, M., Savage, C., Finley, B. & Schneider, E. , "Taking the integrated condition assessment system to the year 2010,". *13th Int. Ship Control Systems Symposium*, 2003, Orlando, FL.

[74] Anon. , *In Proc. 13th Int. Congress on Condition Monitoring and Diagnostic Eng. Management*, 2000, Houston, TX.

[75] Virkler DA, Hillberry BM, Goel PK. "The statistic nature of fatigue crack propagation," *ASME J Engng Mater Technol*, Vol. 101, 1979, pp. 148-153.

[76] Yao, JTP., Kozin, F., Wen, Y. K.,Yang, J. N.,Schueller G. I. and Ditlevsen, O. "Stochastic fatigue, fracture and damage analysis", 1986, *Journal of Structural Safety*, Vol. 3, pp. 231-67

[77] Yang J. N., Hsi W. H.,and Manning S. D., "Stochastic crack propagation with applications to durability and damage tolerance analyses", *USA Airforce Technical report, Flight Dynamics Laboratory, Wright-Patterson Air Force Base*, 1985, AFWAL-TR-85-3062.

[78] Yang J. N., and Manning S. D., "A simple second order approximation for stochastic crack growth analysis," *Engng Fract Mech*, Vol. 53, 1996, pp. 677-86.

[79] Ray, A., and Tangirala, A., "Stochastic Modeling of Fatigue Crack Dynamics for On-Line Failure Prognostics," *IEEE Transactions on Control Systems Technology*, Vol. 4, No. 4, 1996, pp. 443, 451

[80] Wu, W. F.; Ni, C. C., "Probabilistic models of fatigue crack propagation and their experimental verification," *Probabilistic Engineering Mechanics*, Vol. 19, 2004, pp. 247-257.

[81] MacKay, D., "Bayesian Interpolation," *Neural Computation*, Vol. 4, 1992, pp. 415-447.

[82] MacKay, D., "Introduction to Gaussian Processes," *Neural Networks and Machine Learning*, Vol. 168, 1998, pp.133-165.

[83] MacKay, D., *Information Theory, Inference, and Learning Algorithms*, 2003, Cambridge university press.

[84] Rasmussen, C. and Williams, C. 2006. , *Gaussian Processes for Machine Learning*, The MIT Press, Cambridge, MA.

[85] Paris, P.C., "The growth of fatigue cracks due to variations in load," PhD. Thesis, Leigh University, 1962

[86] Paris, P.C., Gomez, M.P. and Anderson, W.E., "A rational analytic theory of fatigue," *The trend in Engineering*, Vol. 13, 1961, pp 9-14.

[87] Erdogan, F., "Crack propagation theories," *NASA Report*, 1967, NASA-CR-901.

[88] Elber, W., "The significance of fatigue crack closure," *ASTM Standard*, 1971, ASTM STP 486, pp. 230-242

[89] Sander, M., and Richard, H.A., "Experimental and numerical investigations on the influence of the loading direction on the fatigue crack growth," *International Journal of Fatigue*, Vol. 28, 2006, pp. 583-591.

[90] AFGROW 4.0004.12.10, AFRL/VASM, 2001.

[91] NASGRO v3.0.20, May 2002.

[92] J. Schijve, M. Skorupa , A. Skorupa, T. Machniewicz, P. Gruszczynski, "Fatigue crack growth in the aluminum alloy D16 under constant and variable amplitude loading," *International Journal of Fatigue*, Vol. 26, 2004, pp. 1-15.

[93] Neal,R. M.1993. "Probabilistic Inference Using Markov Chain Monte Carlo Method ", Technical Report CRG-TR-93-1, Dept. of Computer Science, University of Toronto.

[94] Aizerman, M.; Braverman, E. and L. Rozonoer, 1964. "Theoretical foundations of the potential function method in pattern recognition learning". *J. of Automation and Remote Control* vol. 25, pp. 821-837.

[95] Cortes, C. and Vapnik, V., 1995, "Support vector networks", *J. of Machine Learning*, vol. 20, pp. 273-297.

[96] Courant, R. and Hilbert, D. 1953. , *Methods of Mathematical Physics*, volume 1, Interscience Publishers Inc., New York.

[97] Christopher K. I. Williams., "Computing with infinite networks," Edited by Michael C. Mozer, Michael I. Jordan, and Thomas Petsche, *Advances in Neural Information Processing Systems*, Vol. 9., 1997, MIT Press, Cambridge, MA.

[98] Gibbs, M.N. 1997. "Bayesian Gaussian Processes for Regression and Classification," PhD thesis, Department of Physics, University of Cambridge.

[99] Liu, Y.; Mahadevan, S., 2007,"Stochastic fatigue damage modeling under variable amplitude loading", *Int. J. of Fatigue*, vol. 29, pp. 1149-1161.

[100] I.P. Bond, I.R. Farrow, "Fatigue life prediction under complex loading for XAS/914 CFRP incorporating a mechanical fastener," *International Journal of Fatigue*, Vol. 22, 2000, PP. 633-644.

[101] Schijve, J., Vlutters, A M., Ichsan, and Kluit, J C. P., "Crack growth in aluminum alloy sheet material under flight-simulation loading," *Int. J. Fatigue*, Vol.7, No. 3, 1985, pp. 127-136.

[102] Jonge, D., Schutz, J. B., Lowak, D. H., and Schijve, J., "A standardized load sequence for flight simulation tests on transport aircraft," *TR-73029, National Aerospace Laboratory*, NLR, The Netherlands, 1973, FB-106 (LBF Report. Darmstadt. FRG)

[103] "FALSTAFF Description of a fighter aircraft loading standard for fatigue evaluation," *Joint Publication of F+W. Switzerland*, LBF. Germany. NLR. The Netherlands and IABG. Germany, 1976.

[104] *ASTM Standard Test Method for Measurement of Fatigue Crack Growth Rates*, American Society of Testing Materials, West Conshohocken (PA). ASTM Standard E 647-00, pp. 1-42.

[105] Sukumar N, Chopp DL, Moran B., "Extended finite element method and fast marching method for three-dimensional fatigue crack propagation," *Engg. Fracture Mech*,Vo. 70, No. 1, 2003, pp. 29-48.

[106] Farrar, C.R., Sohn, H., Hemez, F.M., Anderson, M.C., Bement, M.T., Cornwell, P.J., Doebling, S. W, Schultze, J.F., Lieven, N., and Robertson, A.N., 2003, "Damage Prognosis: Current Status and Future Needs", Los Alamos Report No. LA-14051-MS

[107] Farrar, C.R., Worden, K., Todd, M.D., Park, G., Nichols, J., Adams, D.E., Bement, M.T., Farinholt, K., 2007, "Nonlinear System Identification for Damage Detection", Los Alamos Report No. LA-14353.

[108] Rao, C.R. "The Use and Interpretation of Principal Component Analysis in Applied Research", *Sankhya*, 1964, Vol. A 26, pp. 329-358.

[109] Smith, L., "A tutorial on Principal Component Analysis", [*onlinedatabase*], *URL* : *http* : *//www.cs.otago.ac.nz/cosc*453/*student*$_t$*utorials/principal*$_c$*omponents.pdf*, [*cited*2002].

[110] Ljung, L., *System Identification: Theory for the User*, Prentice-Hall, Cambridge, MA, 1999, 2nd Edition,ISBN 0-13-656695-2.

[111] Klein, V.,and Morelli, E. A.,*Aircraft System Identification: Theory and Practice*, AIAA Education Series,AIAA,USA, 2006, 1st Edition,ISBN-10: 1-56347-832-3.

[112] Giurgiutiu, V.,and Cuc, A., "Current Issues in Vibration-Based Fault Diagnostics and Prognostics", *Proceedings of the SPIE's 9th Annual International Symposium on Smart Structures and Materials and 7th Annual International Symposium on NDE for Health Monitoring and Diagnostics*,SPIE, 2002, 17-21 March,San Diego, CA.

[113] Park, G., "High-Frequency Response Functions for Composite Plate Monitoring with Ultrasonic Validation", *IAA Journal*, 2005, 43(11), pp:2431-2437.

[114] Rivera, D. E.,Lee, H.,Mittelmann, H.D., and Barun, M.W.,"High-Purity Distillation - Using plant-friendly multisine signals to identify a strongly interactive process", *IEEE Control Systems Magazine*, 2007, 27(5), pp:72-89.

[115] Xiang-Gen, X.,"System identification using chirp signals and time-variant filtersin the joint time-frequency domain", *IEEE Transactions on Signal Processing*, 1997, 45(8), pp:2072 - 2084.

[116] Fugate, M. L., Sohn, H., and Farrar, C. R., "Vibration-Based Damage Detection Using Statistical Process Control", *Mechanical Systems and Signal Processing*, 2001, 15 (4) pp.707-721.

[117] Sohn, H., and Farrar, C. R., "Damage Diagnosis Using Time Series Analysis of Vibration Signals", *Journal of Smart Materials and Structures*, 2001, 10, pp. 446-451. 118

[118] Qiua, H; Leea, J; Linb, J; Yu, G., "Wavelet filter-based weak signature detection method and its application on rolling element bearing prognostics", 2006, *Journal of Sound and Vibration*, Vol. 289, pp. 1066-1090

[119] Lewicki,D. G.; Dempsey,P. J.; Heath, G. F.; Shanthakumaran, P., "Gear Fault Detection Effectiveness As Applied To Tooth Surface Pitting Fatigue Damage", 2009, *U.S. Army research laboratory report*, Number ARL-RP-0247

[120] Witczak, M., *Modelling and estimation strategy for fault diagnosis of non-linear systems: From analytical to soft computing approaches*, Springer-Verlag, Berlin Heidelberg, 2007.

[121] Ogunfunmi, T., *Adaptive Nonlinear system identification: The Volterra and Winer model approaches*, Springer Publishing, New York, 2007.

[122] Nmeth, J. G., Kollr, I., and Schoukens, J. ,"Identification of Volterra Kernels Using Interpolation", *IEEE Transactions on instrumentation and measurement*, 2002, vol-51(4), pp.770-775.

[123] Scott, M. B., Herseberg, H., Li, H., and Thomson, R., 2005, "Structural Health Monitoring-The Future of Advanced Composite Structures", *Structural Health Monitoring*,Edited by Fu-Kuo Chang, Vol. 1, pp. 107-121